Measurement of the CKM angle gamma with the Lambda _b -> D p K decay and commissioning of the Upstream Tracker at the LHCb experiment

Chiara Mancuso

To cite this version:

Chiara Mancuso. Measurement of the CKM angle gamma with the Lambda _b -> D p K decay and commissioning of the Upstream Tracker at the LHCb experiment. High Energy Physics - Experiment [hep-ex]. Université Paris-Saclay; Università degli studi (Milan, Italie), 2024. English. NNT : 2024UPASP084 . tel-04828160

HAL Id: tel-04828160
https://theses.hal.science/tel-04828160v1
Submitted on 9 Dec 2024

Measurement of the CKM angle γ with the $\Lambda_b^0 \to D^0 p K^-$ decay and commissioning of the Upstream Tracker at the LHCb experiment

Mesure de l'angle γ de la matrice CKM avec la désintégration $\Lambda_b^0 \to D^0 p K^-$ et commissioning de l'Upstream Tracker à l'expérience LHCb

Thèse de doctorat de l'Université Paris-Saclay et de l'Università degli Studi di Milano

École doctorale n° 576, Particules, Hadrons, Énergie et Noyau: Instrumentation, Imagerie, Cosmos et Simulation (PHENIICS)
Spécialité de doctorat: Physique des particules
Graduate School : Physique
Référent: Faculté des sciences d'Orsay

Thèse préparée dans l'unité de recherche **IJCLab** (Université Paris-Saclay, CNRS) et **INFN Sezione di Milano** (Università degli Studi di Milano), sous la direction de **Patrick ROBBE**, Directeur de recherche, et la direction de **Nicola NERI**, Professeur Associé

Thèse soutenue à Paris-Saclay, le 23 Septembre 2024, par

Chiara MANCUSO

Composition du jury

Membres du jury avec voix délibérative

Achille STOCCHI Professeur des universités, Université Paris-Saclay / IJCLab	Président
Jolanta BRODZICKA Chercheur (équiv. HDR), Polish Academy of Science / IFJ PAN	Rapporteuse & Examinatrice
Arantza OYANGUREN CAMPOS Professeur, Institute of Corpuscular Physics / University of Valencia	Rapporteuse & Examinatrice
Giancarlo FERRERA Professeur, Università degli Studi di Milano	Examinateur
Emi HONG-KOU Directrice de recherche, Université Paris-Saclay / IJCLab	Examinatrice
Elisa MINUCCI Docteur, INFN Laboratori Nazionali di Frascati	Examinatrice

THESE DE DOCTORAT

NNT: 2024UPASP084

université
PARIS-SACLAY

ÉCOLE DOCTORALE
Particules, hadrons, énergie et noyau :
instrumentation, imagerie, cosmos
et simulation (PHENIICS)

Titre: Mesure de l'angle γ de la matrice CKM avec la désintégration $\Lambda_b^0 \to D^0 p K^-$ et commissioning de l'Upstream Tracker à l'expérience LHCb

Mots clés: violation de CP, baryon, beaute, experience LHCb, physique des saveurs

Résumé: La violation de la Parité de Charge (CP) est un phénomène bien documenté décrit par le Modèle Standard (MS) de la physique des particules. La compréhension de la violation de CP peut expliquer pourquoi la matière a prévalu sur l'antimatière après le Big Bang, ce qui explique essentiellement notre existence. De nombreuses prédictions théoriques ont été observées expérimentalement, à commencer par la découverte en 1964 de la violation de CP dans le système du kaon neutre par James Cronin et Val Fitch. Depuis lors, de nombreuses expériences de physique des saveurs ont enrichi nos connaissances, observation après observation. Aujourd'hui, alors que la violation de CP dans les systèmes de mésons a été largement étudiée, la violation de CP dans les systèmes de baryons reste largement inexplorée. Cette thèse contribue à ce domaine en tirant parti de la capacité unique de l'expérience LHCb à produire des baryons en quantités suffisantes pour des études détaillées de la saveur. L'accent est mis sur la particule Λ_b^0, qui se désintègre en un état final à trois corps, $D^0 p K^-$, le méson D^0 se désintégrant ensuite en deux hadrons. L'ensemble de données comprend 9 fb^{-1} de collisions pp collectées entre 2011 et 2018 à des énergies de centre de masse de 7, 8 et 13 TeV. L'état final D^0 a été sélectionné en choisissant la technique adoptée plus tard dans la recherche : la méthode GLW (Gronau, London, Wyler), qui se concentre sur les états propres paires de CP, en particulier deux kaons ou deux pions. Une asymétrie entre l'état final et son opposé dans le miroir pourrait être utilisée pour mesurer, par la méthode GLW, l'angle γ CKM (Cabibbo-Kobayashi-Maskawa), un paramètre fondamental décrivant la violation de CP dans le MS. L'étude utilise de nouveaux algorithmes d'apprentissage automatique (ML) pour optimiser les candidats au signal, améliorant ainsi le rendement du signal même dans les canaux précédemment explorés par la collaboration. Cette analyse est complétée par un travail sur le détecteur Upstream Tracker (UT), installé après le Long Shutdown 1 (LS1) et opérationnel lors du Run 3 du LHC. Positionné en amont de l'aimant dipolaire de LHCb, l'UT améliore la résolution en quantité de mouvement des particules chargées et réduit le taux de traces fantômes. Elle fournit des mesures spatiales de haute précision, contribuant à la reconstruction précise des traces, aux côtés du localisateur de vertex (VELO) et du traqueur de fibres scintillantes (SciFi). Cette thèse détaille les différentes phases de la mise en service de l'UT, depuis l'installation et le test des cartes de contrôle des détecteurs (DCB) jusqu'au contrôle de l'acquisition des données et à la caractérisation des capteurs en silicium. Les tests ont consisté à s'assurer de la bonne alimentation des cartes et du fonctionnement des liaisons optiques. La caractérisation était cruciale pour identifier et masquer les pics de bruit anormaux dans les capteurs et assurer le bon fonctionnement de la chaîne d'amplification. Enfin, le contrôle des données en temps réel pendant les essais est essentiel pour vérifier le bon fonctionnement du détecteur et intervenir en cas de dysfonctionnement.

université PARIS-SACLAY

ÉCOLE DOCTORALE
Particules, hadrons, énergie et noyau :
instrumentation, imagerie, cosmos
et simulation (PHENIICS)

Title: Measurement of the CKM angle γ with the $\Lambda_b^0 \to D^0 p K^-$ decay and commissioning of the Upstream Tracker at the LHCb experiment

Keywords: CP violation, baryon, beauty, LHCb experiment, flavour physics

Abstract: Charge Parity (CP) violation is a well-documented phenomenon described by the Standard Model (SM) of particle physics. Understanding CP violation can explain why matter prevailed over antimatter after the Big Bang, essentially explaining our existence. Many theoretical predictions have been experimentally observed, starting with the 1964 discovery of CP violation in the neutral kaon system by James Cronin and Val Fitch. Since then, numerous flavour physics experiments have enriched our knowledge, observation after observation. Today, while CP violation in meson systems has been extensively studied, CP violation in baryon systems remains largely unexplored. This thesis contributes to this field, leveraging the LHCb experiment's unique capability to produce baryons in sufficient quantities for detailed flavour studies. The focus is on the Λ_b^0 particle, which decays into a three-body final state, $D^0 p K^-$, with the D^0 meson further decaying into two hadrons. The dataset comprises 9 fb^{-1} of pp collisions collected between 2011 and 2018 at center-of-mass energies of 7, 8, and 13 TeV. The D^0 final state has been selected choosing the technique later adopted in the research: the GLW (Gronau, London, Wyler) method, which focuses on CP-even eigenstates, specifically two kaons or two pions. An asymmetry between the final state and its mirror-opposite could be used to measure through the GLW method the CKM (Cabibbo-Kobayashi-Maskawa) angle γ, a fundamental parameter describing CP violation within the SM. The study employs new Machine Learning (ML) algorithms to optimise signal candidates, enhancing signal yield even in channels previously explored by the collaboration. Complementary to this analysis is a work on the Upstream Tracker (UT) detector, installed after Long Shutdown 1 (LS1) and operational in Run 3 of the LHC. Positioned upstream of the LHCb dipole magnet, the UT improves the momentum resolution of charged particles and reduces the rate of ghost tracks. It provides high-precision spatial measurements, contributing to accurate track reconstruction alongside the Vertex Locator (VELO) and the Scintillating Fibre Tracker (SciFi). This thesis details various phases of the UT commissioning, from installing and testing the Detector Control Boards (DCBs) to monitoring data acquisition and characterising silicon sensors. Tests involved ensuring the correct powering of boards and the functioning of optical links. Characterisation was crucial to identify and mask anomalous noise peaks in sensors and ensure proper operation of the amplification chain. Finally, real-time data monitoring during runs is essential to verify the detector's correct functioning and intervene in case of malfunctioning.

Contents

Acknowledgements

What this document won't talk about are the people who walked the harsh road of the PhD with me, with whom I have shared laughs and tears, and who deserve a heartfelt thank you. For this reason, these few lines are for you.

I would first like to thank the researchers who kindly agreed to be reviewers of this thesis, Jolanta Brodzicka and Arantza Oyanguren. Thank you for the time spent reading my work and writing the reports, both full of kind words and thoughtful comments, which have helped me improve the quality of what I am presenting to you today. I would also like to thank the other members of the jury, Achille Stocchi, Giancarlo Ferrera, Emi Kou, and Elisa Minucci, for being here today and for the enriching experience of exchanging comments and working together over the past years. You all have shown me different facets of being involved in research.

Patrick, je tiens à te remercier sincèrement pour ces années passées ensemble, au cours desquelles tu m'as guidée à travers les défis que la physique nous impose, tout en me procurant le soutien moral dont j'avais tant besoin. Comme cet été, quand, pedant un appel, submergée par le larmes, tu m'as conseillé de ne pas abandonner, assurant que tout finirait par s'arranger. Pour cela, je te suis profondément reconnaissante. Merci pour tout ce que tu m'as appris, pour les nombreuses opportunités que tu m'as offertes, notamment en me mettant en relation avec les bonnes personnes selon les besoins du projet, et pour m'avoir permis de voyager aux quatre coins du monde, de la Californie à la Chine. Enfin, merci de m'avoir montré que la durée d'un vol Paris-Pékin est amplement suffisante pour préparer un séminaire, lire une thèse de doctorat, et pourquoi pas, profiter d'une bonne nuit de sommeil. En définitive, le temps est relatif.

Grazie anche a te, Nicola. Questa cotutela non sarebbe stata possibile, in primo luogo, senza il tuo sostegno alla folle idea di una studentessa magistrale che arrivava sempre con quei tre minuti di ritardo a lezione. Grazie per i tuoi consigli sempre puntuali e per avermi permesso di mantenere un contatto importante con l'esperienza in laboratorio. Ho imparato tanto su come si costruisce un rivelatore da zero, ma anche un intero esperimento. Buona fortuna per Aladdin!

While working on this thesis over the past three years, I had the pleasure and honor of being part of two incredible LHCb groups. Despite everything starting during the pandemic, and only meeting my doppelganger months after we had both begun, the entire IJCLab group bonded over laughter, food, and (sometimes terrible) jokes. Interacting with everyone has been one of the most enriching experiences of my life—I learned about different cultures and countries, which completely turned upside-down the few certainties I had. I wish you all the best for now and the future—you truly deserve all the good things coming your way. Sharing the days in Orsay with you made me feel like a very lucky PhD student. Gaelle, Piera, Marie, Janina, Seva, Guillaume, Valeriia, Yuya, Felicia, Bo, Elisabeth—thank you for being there.

The second group, no less important but only later in time, was the Milano group. Gio, Sara, quando mi sentivo persa, nostalgica, quando volevo parlare e (a vostro malgrado) fare polemiche, voi ci siete state. Siete state il seme che ha fatto crescere il sentimento di casa anche in un paesino sperduto della campagna francese, con cui condividere la prima partita di calcio mai giocata, ma anche lunghe passeggiate delle vigne. Super Gio e super Sara!

Labs are made of permanent researchers too, an I was lucky enough to exchange also with them. MH, Yasmine, Sergey, Guy and Frédéric, you are all very different and have very different areas of expertise, but one thing in common, how open you are to anyone coming to ask you question and help, you are irreplaceable.

Paris has been home, has been family. I've met people who found their way into my heart, for whom I'd do anything, and whose unwavering support I have constantly felt. We bonded over COVID in a student residence, and now we are young adults, with almost everything pulled together (let's pretend it's like that). I can't begin to count the amazing memories I share with all of you, and the happiness and love I feel when I'm around you. You've seen me through my highest highs and my lowest lows—you were there when I told you I was leaving, and I hope you'll be there when I tell you I'm coming back. Clod, Cri, Cate, Edo, Hussam, Ross, Fra, Giulio, Jack, Dani, Gio, Leo—words aren't enough to express how grateful I am to have had you all in my life.

I cannot forget that my french experience started as a Master's student, and it is indeed crazy to think that even if we attended half of the classes online, we still managed to connect and still be there after so many years. Ari, with you I started climbing, I started running, Renaud, with you I started swimming, I beg you all please stop making me discover new amazing sports. Lucas, Andres, Tunç, Gilles, Noémie, Olekseii, and everyone really, I could have not asked for better classmates.

Even though I was initially supposed to spend some time in Milan, I eventually found myself quite often at CERN, until I fully relocated—with all my plants—to the French countryside. Rebuilding a routine from scratch was challenging in its own way, but being surrounded by incredibly kind and welcoming people made everything much easier. From pasta workshops to building snowmen, from wild parties to hiking in the Jura, I owe a big thank you to all the amazing people I shared these moments with over the past 10 months. Starting with my roommates, who I think still hate me for the idea of Monday's HIIT & Eat sessions—Florian, Lukas, Vicky—the moments we shared in that house will always hold a special place in my heart. Chiarelli, FedeB, Shini, Pietro, Lori, Eugenia (Speedy), AndreVilla, Scarab, Simo, FedeF, Davide, Valerio, Paolo, Sofia, Elena—you all helped fill the huge void that leaving Paris created, and thanks to you, it doesn't hurt as much anymore.

Quando, quattro anni fa, sono partita, non sapevo cosa avrei trovato, ma sapevo cosa, o meglio, chi stavo lasciando: gli amici di una vita. Abbiamo passato anni insieme, dai "banchi" dell'asilo, ai banchi del liceo, alla vita a Milano. Le colazioni al bar, le gite fuori porta, i giri in moto—quante cose abbiamo condiviso! Ci sono stati periodi in cui è stato difficile tenerci in contatto, ma come ogni cosa bella, prima o poi si trova la quadra. Ciò che mi scalda il cuore ancora di più è poter condividere un altro traguardo insieme: Fede, Ale, Dario, persone su cui ho sempre potuto contare, che appoggiano le mie folli idee di partire per l'Islanda gelida o di venire a Parigi per camminare 15 km al giorno. Grazie per esserci sempre.

Non posso certo dimenticare quelle persone che mi hanno "vissuto" diventare dottoressa ormai per la terza volta, con cui abbiamo condiviso pranzi, partite a carte e ore di studio, ma anche gite sugli sci e passeggiate per Milano e Parigi. Sara, Ale, Tommi, grazie per tutto ciò che abbiamo condiviso e che condivideremo; so che c'è ancora tanto da vivere insieme.

Ho cominciato questo percorso non nel miglior stato mentale, ma là dove non riuscivo io a trovare come tirarmi su, avevo dietro di me il sostegno della mia famiglia. La mamma che ha sempre cercato di far si che tutto mi fosse possibile, il papà che ancora non mi ha tirato (troppi) accidenti per i milioni di traslochi attraverso cui è passato insieme a me per tutta l'Europa, il mio fratellino, che ormai è fratellone, che mi manca, e spero ogni giorno non ce l'abbia con me troppo per essermene andata. So che non parliamo tanto, ma so anche che ci vogliamo bene, e che non ce lo diciamo abbastanza spesso, ma eccoci qua, nero su bianco.

One thing I have learned in these years abroad is that love is measured in couches—the couches you can sleep on when you have friends to visit, or when you want to scatter around the world. The second thing I learned is that of these couches, I have a lot, and even if I haven't named them all, I am grateful for each one of them.

Now yes, now we can start to talk about physics.

Synthèse

Le Modèle Standard (MS) est le cadre théorique le plus complet dont on dispose pour comprendre les particules fondamentales de l'univers et leurs interactions. Élaboré au cours du XXe siècle, le MS combine trois des quatre forces fondamentales, à savoir les forces électromagnétique, faible et nucléaire forte, à l'exception de la gravité, qui reste décrite par la relativité générale. Le MS est né d'une série de découvertes et d'avancées théoriques cruciales, en particulier celles qui ont conduit à la mécanique quantique et à la théorie quantique des champs. Les premières découvertes, comme celle du neutron et du neutrino, ont considérablement élargi notre compréhension des particules au-delà des protons et des électrons. L'électrodynamique quantique (QED), une théorie qui a réussi à intégrer la mécanique quantique à l'électromagnétisme, a jeté les bases des développements ultérieurs. Dans les années 1960 et 1970, l'introduction du modèle des quarks a transformé la compréhension des protons et des neutrons, en établissant que ces particules étaient composées d'entités plus petites appelées quarks, qui sont maintenues ensemble par la force forte médiée par les gluons. Cela a conduit à la création de la chromodynamique quantique (QCD), qui décrit les interactions entre quarks et gluons au sein du modèle fort.

Parallèlement, la théorie électrofaible a été élaborée pour unifier les forces électromagnétiques et nucléaires faibles, ce qui a abouti à la prédiction puis à la découverte des bosons $W^{\pm}$ et Z [1] [2] en tant que médiateurs des interactions faibles. La dernière pièce du MS a été la découverte du boson de Higgs en 2012 [3], qui a confirmé que le mécanisme de Higgs est le processus par lequel les particules acquièrent une masse. Cette découverte a marqué la réalisation des principales prédictions du modèle de masse. Cependant, en dépit de son succès, le MS reste incomplet. Il n'intègre pas la gravité et ne peut expliquer des phénomènes tels que la matière noire, l'énergie noire ou les masses non nulles des neutrinos. Ainsi, bien qu'il constitue un cadre puissant et précis pour la physique des particules, il souligne la nécessité d'élaborer des théories qui dépassent son champ d'application actuel.

Les particules élémentaires du MS sont classées en fermions, constituants de la matière, et en bosons, porteurs de force. Les fermions sont divisés en quarks et en leptons, chacun étant à son tour classé en familles. Les quarks, qui constituent les protons, les neutrons et les autres hadrons, présentent des charges électriques fractionnaires et sont liés entre eux par la force forte par l'intermédiaire des gluons. Il existe six types de quarks : up, down, charm, strange, top et bottom, chacun ayant des propriétés uniques. Les leptons, qui comprennent les particules électron, muon et tau ainsi que les neutrinos correspondants, ne participent pas à la force forte et interagissent plutôt par le biais des forces électromagnétique et faible. Les neutrinos, particulièrement énigmatiques en raison de leurs taux d'interaction extrêmement faibles et de leurs petites masses, continuent de défier les prédictions du MS, car leurs masses et leur comportement oscillatoire impliquent une physique au-delà du MS.

Les interactions au sein du MS sont médiées par des bosons de Gauge, avec des photons pour la force électromagnétique, des bosons $W^{\pm}$ et Z pour la force faible, et des gluons pour la force forte. Chaque type d'interaction est régi par une symétrie décrite dans le lagrangien du MS, une formulation mathématique qui dicte la dynamique des interactions entre particules. Les termes électrofaibles et QCD du lagrangien représentent les interactions faible, électromagnétique et forte. Le lagrangien est basé sur les principes de l'invariance de Gauge locale sous les symétries SU(2), U(1) et SU(3), correspondant aux forces fondamentales du MS. Ce cadre permet d'obtenir une description hautement structurée et mathématiquement cohérente des interactions entre particules et jette les bases du calcul des propriétés physiques telles que les masses des particules, les taux de désintégration et les sections

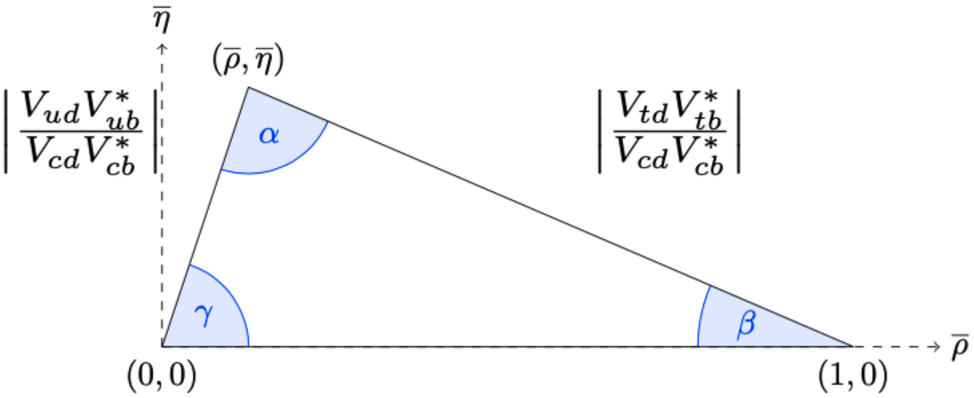

Figure 1: Esquisse de l'un des triangles d'unitarité qui peuvent être extraits en imposant la condition d'unitarité à la matrice CKM, et qui sont utilisés dans cette analyse.

efficaces d'interaction.

Un phénomène central du MS pour cette thèse est la violation de *CP*, qui se réfère à une différence de comportement entre les particules et leurs antiparticules sous des transformations combinées de conjugaison de charge (*C*) et de parité (*P*). La violation de *CP* est importante car elle permet de comprendre le déséquilibre observé entre la matière et l'antimatière dans l'univers. Elle peut être classée en trois catégories principales : la violation directe de *CP*, la violation de *CP* dans le mélange et la violation de *CP* dans l'interférence entre les processus de mélange et de désintégration. La violation directe de *CP* se produit lorsqu'une particule et son antiparticule ont des probabilités de désintégration inégales dans certains états finaux, se manifestant directement dans le processus de désintégration lui-même par une différence mesurable dans les taux de désintégration. La violation de *CP* dans le mélange se produit spécifiquement pour les mésons neutres, qui peuvent osciller entre les états de particule et d'antiparticule. Dans ces cas, les états propres de masse diffèrent dans leurs valeurs propres de *CP*, et la transition entre les états peut créer des asymétries observables. Enfin, la violation de *CP* dans l'interférence entre le mélange et la désintégration est observée dans les systèmes où le mélange et la désintégration directe contribuent tous deux à l'état final. Cette forme de violation de *CP* est caractérisée par l'asymétrie résultant de l'interférence entre ces processus, particulièrement pertinente dans les systèmes de mésons neutres où une particule peut se transformer en son antiparticule et vice versa avant de se désintégrer. La violation de *CP* est quantitativement décrite par des observables dérivées des différences d'amplitude, en particulier les éléments de matrice Cabibbo-Kobayashi-Maskawa (CKM) [4], [5] dans le MS, qui décrivent les transitions de changement de saveur des quarks pour chaque élément de matrice, rapporté dans ce qui suit avec sa paramétrisation Wolfensein [6]:

$$V_{CKM} = \begin{pmatrix} V_{ud} & V_{us} & V_{ub} \\ V_{cd} & V_{cs} & V_{cb} \\ V_{td} & V_{ts} & V_{tb} \end{pmatrix} = \begin{pmatrix} 1-\frac{\lambda^2}{2} & \lambda & A\lambda^3(\rho - i\eta) \\ -\lambda & 1-\frac{\lambda^2}{2} & A\lambda^2 \\ A\lambda^3(1-\rho-i\eta) & -A\lambda^2 & 1 \end{pmatrix} + \mathcal{O}(\lambda^4). \tag{1}$$

L'unitarité de la matrice CKM implique l'existence de triangles dans le plan complexe, qui sont utilisés pour mesurer la violation de *CP*, en particulier à travers des angles qui reflètent le degré d'asymétrie entre les processus de matière et d'antimatière, une représentation peut être trouvée dans la figure 1. Les mesures de la violation de *CP*, impliquant des mésons tels que les kaons et les mésons B, ont été poursuivies par des collaborations mondiales, avec des expériences notables dans des collaborations telles que BaBar [7], LHCb [8], Belle [9] et BelleII [10]. Plusieurs techniques ont été développées pour étudier la violation de *CP* dans les désintégrations de mésons B, notamment les méthodes Gronau-London-Wyler (GLW) [11], Atwood-Dunietz-Soni (ADS) [12] et Dalitz plot [13]. La méthode GLW utilise les états propres *CP* du méson D, produit dans les désintégrations du méson B, et examine les asymétries dans les taux de désintégration pour extraire les observables de la violation de *CP*. La méthode ADS exploite les interférences entre les canaux de désintégration favorisés par Cabibbo et ceux doublement supprimés par Cabibbo, améliorant la sensibilité à γ en utilisant des états finaux spécifiques du méson D qui maximisent les effets d'interférence. Les analyses du graphe de Dalitz sont utilisées lorsque les produits de désintégration comprennent des états finaux à trois corps, ce qui permet une étude détaillée des structures de résonance et des régions de l'espace de phase. Ces méthodes fournissent des observables *CP* qui contribuent à la mesure précise de l'angle CKM γ. Cette thèse a étendu les études de la collaboration LHCb aux désintégrations de baryons Λ_b^0, comme le canal $\Lambda_b^0 \to D^0 p K^-$, où les mesures de violation de *CP* peuvent être effectuées en adaptant les méthodes basées sur les mésons aux baryons, notamment la méthode GLW en réadaptant les observables de la méthode de la manière suivante :

$$\begin{aligned}\mathcal{A}_{CP} &= \frac{\Gamma(\Lambda_b^0 \to D_{CP} f) - \Gamma(\overline{\Lambda}_b \to D_{CP} \overline{f})}{\Gamma(\Lambda_b^0 \to D_{CP} f) + \Gamma(\overline{\Lambda}_b \to D_{CP} \overline{f})} \\ &= \frac{2\kappa r_{\Lambda_b^0} \sin\delta_{\Lambda_b^0} \sin\gamma}{1 + r_{\Lambda_b^0}^2 + 2\kappa r_{\Lambda_b^0} \cos\delta_{\Lambda_b^0} \cos\gamma},\end{aligned} \tag{2}$$

$$\begin{aligned}\mathcal{R}_{CP} &= \frac{\Gamma(\Lambda_b^0 \to D_{CP} f) + \Gamma(\overline{\Lambda}_b \to D_{CP} \overline{f}))}{\Gamma(\Lambda_b^0 \to D f) + \Gamma(\overline{\Lambda}_b \to D \overline{f}))} \\ &= 1 + r_{\Lambda_b^0}^2 + 2 r_{\Lambda_b^0} \cos\delta_{\Lambda_b^0} \cos\gamma,\end{aligned} \tag{3}$$

ayant κ, $r_{\Lambda_b^0}$, $\delta_{\Lambda_b^0}$ et γ, représentant respectivement le facteur de cohérence, le rapport d'amplitude entre les deux désintégrations, la phase forte et la phase faible. Les désintégrations de Λ_b^0 constituent un cas intéressant en raison de la dynamique différente des désintégrations de baryons par rapport aux mésons, comme l'absence de facteurs de suppression de la couleur, ce qui conduit à des rapports d'amplitude plus importants et à des signaux violant *CP* potentiellement plus forts. Les observables dans les désintégrations de Λ_b^0 dépendent également des termes d'interférence impliquant des différences de phase faibles et fortes, et l'augmentation prévue des statistiques avec l'amélioration du LHCb permettra d'améliorer la précision de l'observation de ces effets dans les baryons. Mesurer la violation de *CP* dans les baryons présente des défis uniques, car ces particules sont plus difficiles à produire en grandes quantités que les mésons. Toutefois, les récentes améliorations apportées à l'expérience LHCb devraient permettre d'augmenter considérablement les données sur ces désintégrations de baryons, ce qui permettra d'obtenir des mesures plus précises et de réduire les incertitudes statistiques.

Cette thèse contient une analyse approfondie du processus de désintégration $\Lambda_b^0 \to D^0 p h^-$, où h représente un hadron tel que K ou π. L'analyse s'appuie sur les données de collisions proton-proton enregistrées par le détecteur LHCb, avec une luminosité intégrée de 9 fb^{-1} collectées à des énergies de centre de masse de 7, 8 et 13 TeV. Ce travail vise à étudier les spectres de masse invariante précédemment non observés pour ces processus de désintégration et présente la première tentative de mesure de la violation de *CP* dans ce canal. Le traitement des données commence par une étape initiale appelée stripping, au cours de laquelle de grands volumes de données brutes sont réduits en appliquant des critères spécifiques pour identifier les événements contenant des désintégrations de signaux possibles. Cette première étape de filtrage permet à l'expérience de traiter le volume important de données générées par le détecteur, en isolant les signaux potentiels et en écartant les données moins pertinentes. Les événements sélectionnés sont ensuite soumis à une nouvelle sélection hors ligne, qui améliore la précision de l'analyse en maximisant une Figure de Mérite (FoM). Cette mesure quantifie l'équilibre entre la sensibilité du signal et la suppression du bruit de fond en guidant les choix effectués lors des premières étapes du traitement des données afin de garantir une extraction efficace des événements du signal à partir d'un bruit de fond. Les simulations de Monte Carlo (MC) jouent un rôle essentiel dans cette analyse, car elles permettent de modéliser les comportements attendus des processus de signal et de bruit de fond. Ces simulations permettent d'estimer l'efficacité de la détection, de modéliser les contributions de de bruit de fond et d'interpréter les résultats expérimentaux. Les simulations MC sont largement utilisées pour tester différents critères de sélection, développer des algorithmes de classification et comprendre les effets de la réponse des détecteurs sur les données observées. Grâce à des outils tels que Gauss [14], EvtGen [15] et Geant4 [16], la collaboration LHCb génère des échantillons de MC qui simulent les interactions entre les particules, les chaînes de désintégration et les réponses des détecteurs. Pythia [17] modélise les collisions proton-proton initiales et les pluies de partons qui s'ensuivent, tandis qu'EvtGen simule les désintégrations des hadrons de saveur lourde. Geant4 modélise les interactions de ces particules lorsqu'elles traversent les matériaux du détecteur, ce qui permet d'obtenir des estimations précises des trajectoires des particules et des schémas de dépôt d'énergie. Les événements MC générés sont ensuite traités par les mêmes algorithmes de reconstruction que les données réelles, ce qui permet des comparaisons directes entre les données simulées et observées. Ce cadre de simulation est utilisé pour développer et valider les critères de sélection utilisés tout au long de l'analyse. Une partie importante de l'analyse est consacrée à la suppression du bruit de fond afin d'isoler les événements du signal pour la désintégration $\Lambda_b^0 \to D^0 p h^-$. La suppression du bruit de fond est réalisée à l'aide d'algorithmes de classification avancés, notamment les arbres de décision boostés (BDT), qui sont largement utilisés en physique des hautes énergies pour distinguer les événements du signal de ceux du bruit de fond sur la base de caractéristiques discriminantes spécifiques. Dans cette analyse, les BDT sont entraînés à reconnaître les modèles et les caractéristiques des événements de bruit de fond et à les séparer du signal. En identifiant des différences subtiles dans les variables cinématiques et géométriques, les BDT permettent une discrimination efficace entre le signal et le bruit de fond, ce qui permet à l'analyse de conserver une sensibilité élevée au signal tout en réduisant de manière significative le bruit de fond. Les performances des BDT sont évaluées à l'aide de mesures telles que les courbes ROC (Receiver Operating Characteristic), qui représentent le taux de vrais positifs (efficacité du signal) par rapport au taux de faux positifs (rejet du bruit de fond) pour différents seuils de décision. L'aire sous la courbe ROC (AUC) sert à mesurer l'efficacité du classificateur, les valeurs proches de 1 indiquant une excellente discrimination.

L'un des objectifs de cette analyse est de mesurer les asymétries *CP* pondérées par l'efficacité dans les désintégrations d'intérêt. Cette approche pondérée tient compte des variations de l'efficacité de détection dans les différentes régions de l'espace des phases, ce qui garantit que l'asymétrie mesurée reflète fidèlement la physique sous-jacente. Dans le cas présent, l'accent est mis sur le baryon Λ_b^0 et ses désintégrations en un méson D^0 et un proton, le D^0 se désintégrant ensuite dans des canaux tels que K^-K^+ ou $\pi^-\pi^+$. La formule de l'asymétrie *CP*, donnée par

$$A = \frac{\sum_i w_i^{\mathrm{GLW},\Lambda_b^0}/\epsilon_i^{\mathrm{GLW},\Lambda_b^0} - \sum_i w_i^{\mathrm{GLW},\overline{\Lambda}_b^0}/\epsilon_i^{\mathrm{GLW},\overline{\Lambda}_b^0}}{\sum_i w_i^{\mathrm{GLW},\Lambda_b^0}/\epsilon_i^{\mathrm{GLW},\Lambda_b^0} + \sum_i w_i^{\mathrm{GLW},\overline{\Lambda}_b^0}/\epsilon_i^{\mathrm{GLW},\overline{\Lambda}_b^0}}. \tag{4}$$

ayant $w_i^{\mathrm{GLW},\Lambda_b^0}$ and $w_i^{\mathrm{GLW},\overline{\Lambda}_b^0}$ sont les *sWeights* [18] extraits de le fit de la désintégration respective de Λ_b^0 et de son antiparticule, et $\bar{\Gamma}_i$ représentent les taux de désintégration de la particule et de l'antiparticule, et ϵ_i désigne le poids d'efficacité, permettant une mesure précise qui incorpore les effets du détecteur. La mesure est effectuée dans l'espace des phases complet et dans un espace restreint, en supprimant les contributions provenant des résonances Λ_c^*, appliquant ainsi une coupure de masse de $m(pD^0) > 3000$ Mev/c^2.

L'analyse utilise un canal de contrôle, $\Lambda_b^0 \to D^0 p\pi^-$, qui sert de référence pour valider la stratégie d'analyse et évaluer les incertitudes systématiques. En examinant ce canal de contrôle, l'analyse peut tester divers critères de sélection et techniques de suppression du bruit de fond dans un mode de désintégration étroitement lié. Cette approche permet de s'assurer que les méthodes utilisées pour le canal du signal sont fiables et que les biais potentiels ou les effets systématiques sont minimisés. Le canal de contrôle permet également une comparaison plus solide des distributions du signal et du bruit de fond, ce qui constitue une vérification croisée précieuse des résultats obtenus pour le canal de désintégration primaire.

L'un des principaux défis de cette analyse est la modélisation précise des processus de bruit de fond, en particulier ceux qui résultent d'une mauvaise identification des particules et d'événements partiellement reconstruits. On parle de bruit de fond de mauvaise identification lorsqu'une particule est incorrectement identifiée comme un autre type de particule en raison de similitudes dans les signatures de leurs détecteurs. Par exemple, un pion peut être identifié à tort comme un kaon, ce qui entraîne une contamination de l'échantillon sélectionné. Pour remédier à ce problème, l'analyse applique des exigences strictes en matière des variables des identification des particules (PID), en utilisant les données d'étalonnage des détecteurs RICH pour estimer les taux d'identification erronée et corriger les biais dans les données reconstruites. En outre, un veto est appliqué pour supprimer les événements pour lesquels des plages de masse invariante spécifiques suggèrent des particules mal identifiées.

Les antécédents partiellement reconstruits représentent un autre défi important, en particulier dans les désintégrations impliquant plusieurs particules à l'état final, dont certaines peuvent échapper à la détection. Dans ces cas, l'analyse repose sur des simulations MC pour modéliser la distribution des événements partiellement reconstruits, en utilisant des techniques spécialisées pour corriger les écarts entre les données simulées et observées. La repondération des échantillons MC sur la base des distributions observées est cruciale pour modéliser avec précision ces bruit de fond, car elle garantit que les données simulées s'alignent sur les conditions expérimentales réelles.

Les incertitudes systématiques sont soigneusement évaluées tout au long de l'analyse afin de quantifier leur impact sur les résultats finaux. Ces incertitudes proviennent de diverses sources, notamment des critères de sélection, de l'efficacité du PID, de la résolution du détecteur et de la modélisation des processus de bruit de fond. Par exemple, les incertitudes dans l'étalonnage du PID peuvent affecter la précision de l'identification des particules, tandis que les variations dans l'alignement et la résolution du détecteur peuvent introduire des biais dans les spectres de masse invariants reconstruits. Pour évaluer ces effets, l'analyse effectue de multiples vérifications croisées et études de sensibilité, en ajustant les critères de sélection et en réévaluant les résultats pour déterminer la robustesse des mesures. Les incertitudes systématiques sont ensuite intégrées dans les estimations d'erreur finales, ce qui permet une évaluation complète de la fiabilité de l'analyse. Dans la dernière étape de l'analyse, les spectres de masse invariants pour les candidats à la désintégration Λ_b^0 sélectionnés sont ajustés pour extraire le rendement du signal et mesurer les asymétries de *CP*. La procédure d'ajustement est effectuée sur plusieurs échantillons de données, ce qui permet de comparer les résultats pour différentes énergies de centre de masse et périodes de prise de données. L'ajustement incorpore des modèles de bruit de fond développés par des simulations MC et des techniques de repondération, garantissant que le rendement du signal observé est séparé avec précision des contributions de buit de fond. Le résultat de ces études est visible dans les figures 2 et 3 pour les cas $D^0 \to K^-K^+$ et $D^0 \to \pi^-\pi^+$ respectivement. Les résultats obtenus sont énumérés ci-dessous, d'abord dans l'espace de phase complet

$$A_{\text{CP}}^{K^-K^+}(\Lambda_b^0) = -0.15 \pm 0.07^{+0.03}_{-0.02}$$

$$A_{\text{CP}}^{\pi^-\pi^+}(\Lambda_b^0) = 0.07 \pm 0.10 \pm 0.03$$

$$A_{\text{CP}}^{K^-K^+}(\Xi_b^0) = -0.16 \pm 0.13^{+0.03}_{-0.02}$$

$$A_{\text{CP}}^{\pi^-\pi^+}(\Xi_b^0) = 0.20 \pm 0.27 \pm 0.03,$$

et pour l'espace de phase restreint :

$$A_{\text{CP}}^{K^-K^+}(\Lambda_b^0) = -0.13 \pm 0.14^{+0.03}_{-0.02}$$

$$A_{\text{CP}}^{\pi^-\pi^+}(\Lambda_b^0) = -0.11 \pm 0.19 \pm 0.03,$$

la première incertitude étant statistique et la seconde systématique.

Complémentaire à l'analyse, cette thèse inclut également la contribution à le commissioning de l'Upstream Tracker (UT), un détecteur installé pendant le Long Shutdown et désormais en fonctionnement dans le Run 3. L'UT a été installé en remplacement du Tracker Turicensis (TT) afin de répondre aux exigences d'une luminosité accrue et de taux d'interaction plus élevés. L'UT est un détecteur à microstrip de silicium, conçu avec quatre couches de détection disposées selon une configuration $x-u-v-x$, comme il est montré en Figure 4. Chaque couche est constituée de capteurs avec des

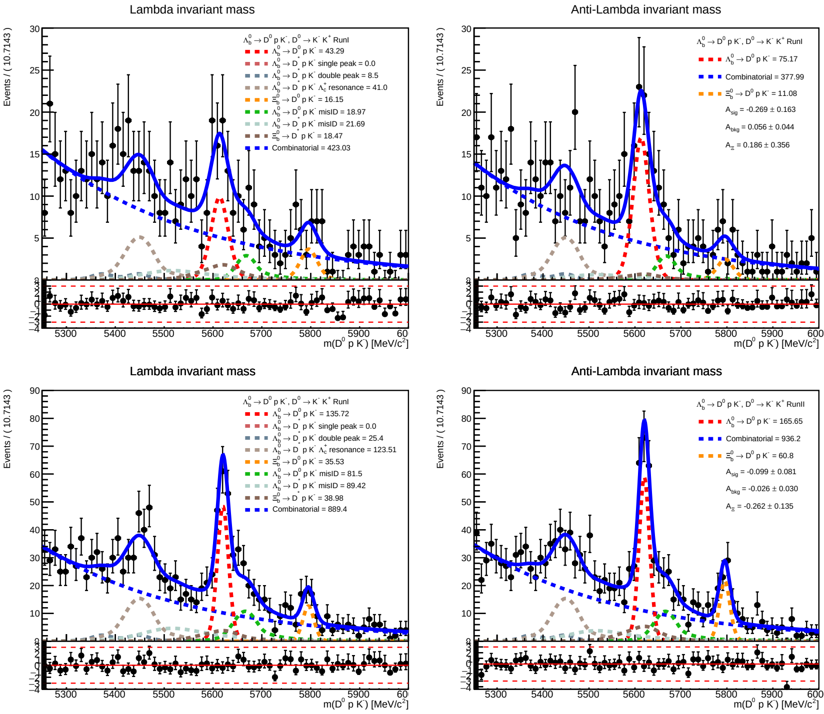

Figure 2: Simultaneous unbinned maximum-likelihood fit for $\Lambda_b^0 \to [K^-K^+]_{D^0}pK^-$ decays, on the left column, the results for Λ_b^0-type are shown, on the right column, the results for $\overline{\Lambda}_b^0$-type are shown. Top row is for Run I results, bottom row for Run II.

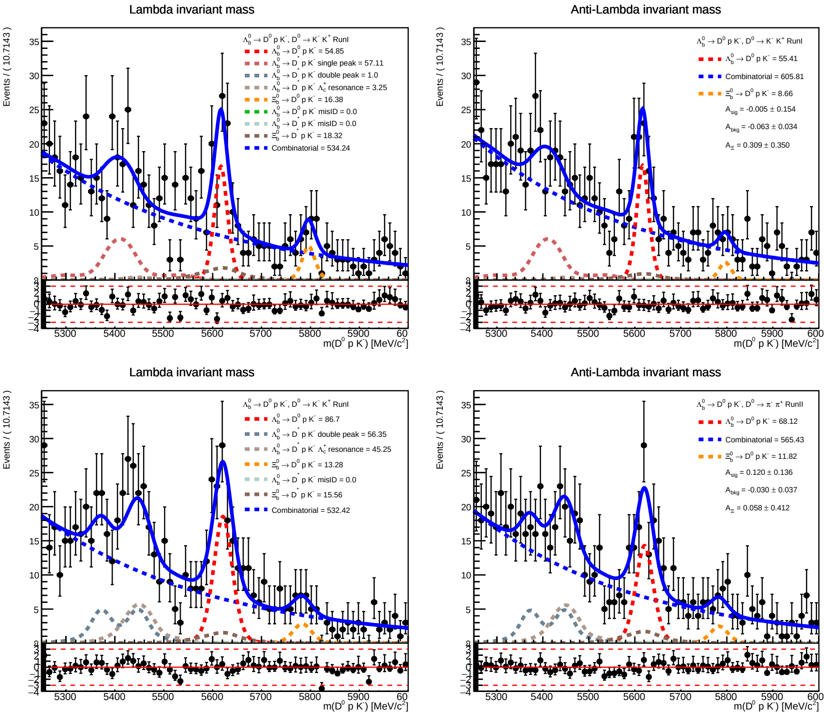

Figure 3: Simultaneous unbinned maximum-likelihood fit for $\Lambda_b^0 \to [\pi^-\pi^+]_{D^0}pK^-$ decays, on the left column, the results for Λ_b^0-type are shown, on the right column, the results for $\overline{\Lambda}_b^0$-type are shown. Top row is for Run I results, bottom row for Run II.

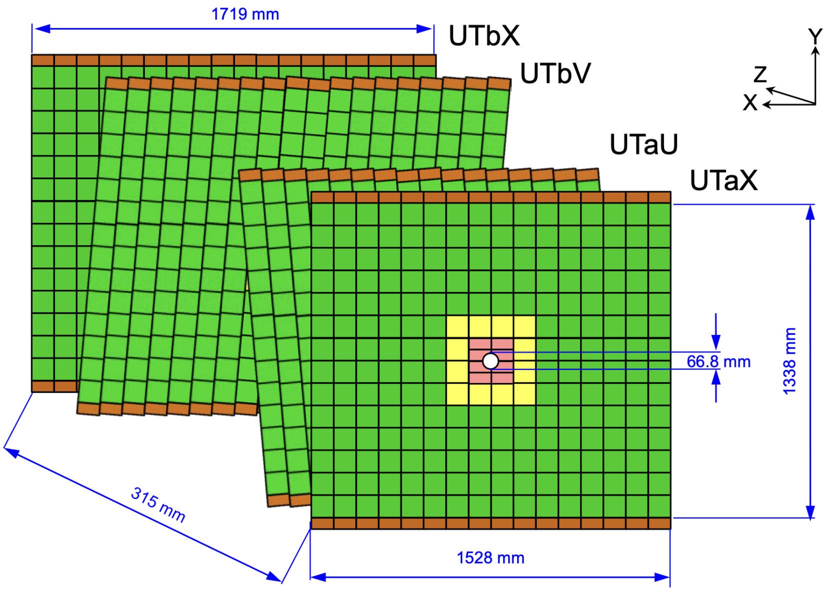

Figure 4: Vue d'ensemble de la géométrie de l'UT en regardant en aval

pas variés, allant de 93,5 μm près de la ligne de faisceau à 187,5 μm dans les régions à plus faible occupation. Une partie majeure de ce travail a concerné l'assemblage et le test des Data Concentrator Boards (DCBs), des composants essentiels du système d'acquisition de données (DAQ) de l'UT. Les DCBs consolident les données provenant de l'électronique frontale et les transmettent via des fibres optiques aux cartes TELL40 dans les salles de comptage. Le processus d'assemblage a permis d'assurer l'installation correcte des cartes mezzanine avec des émetteurs-récepteurs polyvalents (VTRx) et des émetteurs jumelés (VTTx), en fonction des exigences spécifiques de chaque couche. La fonctionnalité de chaque carte a été testée afin de garantir une communication sans erreur avec les futurs staves. L'installation physique des DCBs dans le cadre de l'UT a été réalisée avec une grande minutie, les cartes étant positionnées dans les emplacements assignés en fonction de leurs configurations spécifiques et connectées au backplane pour l'alimentation électrique et la transmission des données. Des tests supplémentaires utilisant des émulateurs ont confirmé une communication correcte entre les DCBs et les staves du détecteur. Les études de bruit ont constitué un autre aspect de ce travail, menées à la fois dans la clean room et après l'installation du détecteur dans la caverne de l'expérience LHCb. Ces études visaient à identifier et atténuer les sources de bruit, telles que le bruit électronique, le bruit induit par les radiations et les interférences électromagnétiques. Le comportement du bruit a été analysé à plusieurs niveaux, y compris au niveau des ASICs individuels, des staves et des modules. Les valeurs de pédestal, le bruit moyen de mode commun et les valeurs des convertisseurs analogique-numérique (ADC) ont été soigneusement évalués pour garantir une intégrité optimale du signal. Les canaux présentant un bruit supérieur à cinq écarts-types par rapport à la distribution attendue ont été signalés comme anormaux, et des actions correctives appropriées ont été mises en œuvre. Des analyses comparatives entre les données issues de la clean room et celles de la caverne ont démontré que les niveaux de bruit sont restés stables après l'installation, validant la robustesse de la conception et des processus d'assemblage du détecteur. Cette comparaison est observable à la Figure 5. La fonctionnalité d'amplification des ASICs SALT a également été testée dans le cadre de la mise en service. Ces puces incluent un générateur interne d'impulsions de test, permettant l'injection d'une charge connue équivalente à celle d'une particule minimum ionisante (MIP). En analysant les résultats, des problèmes ont été identifiés dans les canaux où l'amplification était absente ou incohérente, et ils ont été résolus. Les résultats ont confirmé un comportement uniforme de l'amplification à travers les ASICs, ce qui est essentiel pour la précision du détecteur. En outre, des contributions ont été apportées au développement de logiciels de surveillance. Le cadre de surveillance de LHCb, Monet, a été utilisé pour créer des outils de visualisation des données en temps réel et d'assurance qualité. Le système de

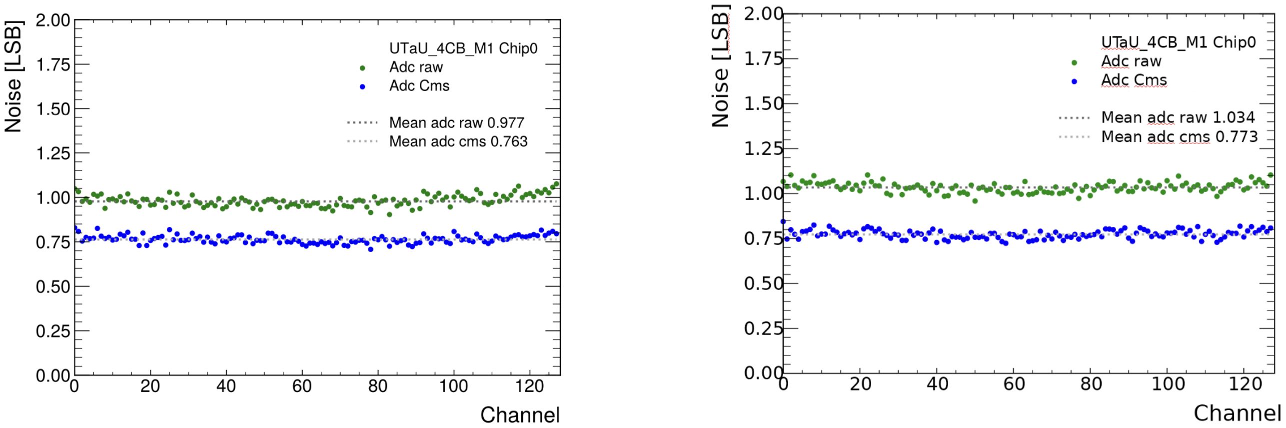

Figure 5: Distribution du bruit par canal de l'ASIC 0 du sensor UTaU 4CB M1, dans la clean room à gauche, et dans la caverne à droite

surveillance génère des histogrammes des impacts dans l'UT, affichés en temps réel dans la salle de contrôle pour fournir un retour immédiat pendant les périodes de prise de données. Ces outils permettent de détecter efficacement les anomalies et de maintenir une acquisition de données de haute qualité.

Après l'installation, l'alignement et la calibration de l'UT ont été effectués pour garantir son intégration avec les autres sous-détecteurs, tels que le VELO et le SciFi. Le processus d'alignement a impliqué des ajustements grossiers et fins, tandis que des séries de calibrations utilisant des rayons cosmiques et des sources de particules connues ont permis d'optimiser la réponse des capteurs ainsi que les réglages de gain et de seuil de l'électronique de lecture. Ces efforts ont abouti à un détecteur bien calibré, capable de fournir des données de suivi de haute précision.

L'évaluation des performances de l'UT en 2024 a fourni des informations cruciales sur ses capacités opérationnelles. Les premières prises de données ont démontré la stabilité des opérations du système d'acquisition de données (DAQ) et l'alignement avec les autres sous-détecteurs de LHCb. Les études d'efficacité ont indiqué que l'UT atteignait environ 95 % d'efficacité pour les longues trajectoires, avec une marge d'amélioration grâce à des optimisations du firmware et des réparations des régulateurs basse tension. La grande granularité et la précision de l'UT ont permis de réduire de manière significative les trajectoires fantômes et d'améliorer la résolution en impulsion des particules chargées, contribuant ainsi à la performance globale du détecteur LHCb.

1

Introduction

The Standard Model (SM) of particle physics stands as an established framework that describes the fundamental particles and their interactions. This theory well defines the nature of elementary particles, such as quarks, and their assembly into composite particles like baryons (comprising three quarks) and mesons (consisting of a quark and an antiquark). Among baryons, protons and neutrons are the building blocks of ordinary matter. The SM also comprehensively describes the forces governing these particles. Despite its success and the numerous accurate predictions it has made, the SM falls short in explaining certain phenomena, particularly the pronounced imbalance between matter and antimatter in the Universe. This disparity is not adequately addressed within the SM's framework. One area of interest is the violation of charge and parity symmetries, known as CP violation, which might offer insights into the dominance of matter over antimatter. However, the extent of CP violation observed so far is insufficient to account for the observed asymmetry. The quest to understand CP violation extends to studying various particle decays, such as those well-explored of mesons, but also including those of baryons. Investigating CP violation in baryons might reveal new physics beyond the Standard Model and enhance our understanding of the matter-antimatter asymmetry. Among the different baryon decays, the decay of the Λ_b^0 baryon into a D^0 meson, a proton (p), and a kaon (K^-) is of particular interest. This decay channel is significant as it enables the measurement of the CKM angle γ, which is one of the least precisely known parameters of the Cabibbo-Kobayashi-Maskawa (CKM) matrix. The CKM matrix, which describes the mixing between different quark flavors, is at the base to the SM's explanation of CP violation. The LHCb experiment at the Large Hadron Collider (LHC) provides a robust platform for studying heavy baryon decays. Specifically designed to probe the decays of particles containing b and c quarks, LHCb excels in producing and detecting baryons, allowing for high-precision measurements of their decay properties and CP-violating effects. The experiment's advanced detection systems and substantial data collection capacity make it particularly suited for these investigations.

This thesis focuses on measuring the CKM angle γ using the $\Lambda_b^0 \to D^0 p K^-$ decay at the LHCb experiment. The importance of this measurement comes from the fact that it offers an independent determination of γ, thereby contributing to a deeper understanding of CP violation and the consistency of the CKM framework. By utilizing the dataset of Λ_b^0 decays gathered by LHCb from pp collisions at a center-of-mass energy of 7 TeV, 8 TeV and 13 TeV from 2011 to 2018, this study aims to achieve a first CP violation measurement in baryons and, furthermore, attempt the measurement of γ. This study seeks to identify any deviations from SM predictions, which could indicate the presence of new physics phenomena. Such findings would enhance our comprehension of the fundamental forces and particles that constitute our universe, contributing significantly to the broader effort of addressing the enduring mysteries of CP violation and the imbalance between matter and antimatter. The work towards this measurement is presented in this document, organized as follows: in Chapter 2, a more punctual description of the SM and of the theoretical concepts behind this analysis can be found, along with considerations about how the absence of polarization of the Λ_b^0 could interfere with the study. Chapter 3 describes the experimental setup where the analysed data are collected. Chapters 5 and 6, finally, describe the methods adopted for the data analysis and present the results obtained.

Along with the effort studying the Λ_b^0 and its decays, this document also collects the contribution made to the commissioning of the Upstream Tracker (UT) of the LHCb experiment. From 2018 to 2022, the experiments on the LHC underwent major upgrades to prepare for Run 3, in which pp collisions at the record center-of-mass energies of 13.6 TeV are foreseen to happen. Run 3 is scheduled until 2025, with an expected luminosity five times higher than in the previous runs. To cope with the increased amount of events, a key change, among others, has been to install a brand new tracker upstream of the magnet. With its increased granularity and reduced material budget compared to the previous tracking detectors, it allows for better resolution in the measurement of particle trajectories. Also, its improved spatial resolution leads to better momentum resolution for charged particles. Last but not least, its design ensures high hit efficiency and robustness against radiation damage, which is particularly important given the increased luminosity and data rates expected. In Chapter 4, the contribution to the commissioning of the detector is detailed: from the population of the Detector Control Boards (DCBs) with the Versatile Transceivers (VTRx) and Twin-Transmitters (VTTx), the communication/powering tests performed and the installation of the components in the detector frame, to the noise characterization of the sensors, to finally implement the monitoring for the data taking.

2

Theoretical and experimental overview

2.1 The Standard Model of particle physics

The Standard Model (SM) of particle physics stands as a cornerstone in our understanding of the fundamental constituents of the universe. This framework, developed over the second half of the 20th century, provides a comprehensive theory that describes the interactions of subatomic particles with remarkable precision. It elegantly combines three of the four known fundamental forces – the electromagnetic, weak, and strong nuclear forces – leaving out only gravity, which is currently described by General Relativity.

The birth of the SM can be traced back to the early 20th century, which was marked by groundbreaking discoveries and theoretical advancements and the introduction of quantum mechanics with its probabilistic nature. In the 1930s, the discovery of the neutron [19] and the proposition of the neutrino hypothesized the existence of a family of particles beyond the protons and electrons known at the time. This period also saw the development of Quantum Electrodynamics (QED), a theory that successfully merged quantum mechanics with electromagnetism and accurately described the interactions between charged particles and photons, the quanta of light.

The subsequent decades witnessed a rapid expansion in our understanding of particle physics. The 1960s and 1970s were marked by the development of the quark model, which proposed that protons and neutrons were not elementary particles but were composed of quarks, held together by the strong force, mediated by particles called gluons. This theory evolved into Quantum Chromodynamics (QCD), a part of the SM that describes the interactions between quarks and gluons.

Parallel to the development of QCD, the electroweak theory emerged, unifying the electromagnetic and weak nuclear forces. Pioneered by Sheldon Glashow [20], Abdus Salam [21], and Steven Weinberg [22], this theory introduced the W and Z bosons, particles that mediate the weak force, responsible for nuclear processes like β decay. The electroweak theory's success was bolstered by the predicted existence of the Higgs boson [3], a particle associated with the mechanism that imparts mass to other particles.

The confirmation of the SM's predictions came through a series of high-energy particle experiments. The first happened in January 1983, when the signal of W boson was observed by UA1 and UA2 detectors [1] in the Super Proton Synchrotron (SPS) at the European Council for Nuclear Research (CERN). It was the first accelerator that, at that time, could accelerate particles to reach the energy of such a massive boson, i.e. 80.379 GeV/c^2. A few months later, in

Generation		Q(e)	m (MeV/c^2)	
I	u	$+2/3$	$2.16^{+0.49}_{-0.26}$	$I_3 = +1/2$
	d	$-1/3$	$4.67^{+0.48}_{-0.17}$	$I_3 = -1/2$
II	c	$+2/3$	1270±20	$C = +1$
	s	$-1/3$	93^{+11}_{-5}	$S = -1$
III	t	$+2/3$	$(172.76\pm0.30)\cdot10^3$	$T = +1$
	b	$-1/3$	4180^{+30}_{-20}	$B = -1$

Table 2.1: Elementary particles: quarks. They are divided following the generation they belong to, but also the electric charge Q and their mass are reported. The last column is the flavour quantum number of each quark.

May 1893, the *Z* boson was discovered in the same facilities [2] by its experimental signature of high-energy lepton-anti-lepton. The discovery of the top quark followed in 1995 [23] by the CDF and D0 collaborations at Fermilab's Tevatron collider, completing the third generation of the SM's quark sector. The crowning achievement came in 2012 with the discovery of the Higgs boson at the Large Hadron Collider (LHC) at CERN, confirming the last major prediction of the SM.

Despite its triumphs, the SM is not without limitations. It does not incorporate gravity and fails to explain the dark matter and dark energy that seem to dominate the universe's mass-energy content. Moreover, it cannot account for the neutrino masses, which are experimentally observed but not predicted by the original framework. It is a beautiful but yet incomplete theory, a robust framework for understanding the fundamental particles and their interactions, yet it also points to new physics beyond its scope.

2.1.1 Particles, the bricks of the theory

As with every well-established theory, SM also has its own fundamental constituents, from which laws and interactions then develop: the fermions. These are the fundamental constituents of matter, subdivided into quarks and leptons, each group containing six particles, classified according to their charge, and divided into families for historical but also for hierarchical reasons.

Quarks are the subatomic particles making up protons and neutrons, and in general, hadrons. There are six flavours of quarks: up (u), down (d), charm (c), strange (s), top (t), and bottom/beauty (b). They exhibit fractional electric charges: up, charm, and top quarks carry a charge of $+2/3|q_e|$, while down, strange, and bottom quarks have a charge of $-1/3|q_e|$. Quarks are perpetually confined within the particles they are constituents of due to the strong force mediated by gluons, which makes isolating individual quarks impossible. This confinement leads to the concept of "colour charge," property quarks possess that is analogous to electric charge but for the strong interaction, ensuring quarks are always bound together. Fundamental to describe these particles are their quantum numbers, which, besides the already mentioned electric charge, are colour charge, spin, and more nuanced ones like isospin, charm, strangeness, topness, and bottomness. The reader can find a complete report in Table 2.1. "Lepton" is a label that can be given to six particles: electrons, muons, taus, and their corresponding neutrinos. They are distinguished from their counterpart quarks by their inability to participate in the strong nuclear force, instead, they interact via electromagnetic and weak nuclear force. Electrons are the first discovered particles, while muons and taus are heavier cousins of the electron, identical in charge and spin but with significantly greater mass. It is possible to find a summary of their most

Generation		Q(e)	m (MeV/c^2)	
I	e	-1	0.511	$\ell_e = 1$
	ν_e	0	$< 1.1 \cdot 10^{-3}$	$\ell_e = 1$
II	μ	-1	105.658	$\ell_\mu = 1$
	ν_μ	0	< 0.19	$\ell_\mu = 1$
III	τ	-1	1776.84	$\ell_\tau = 1$
	ν_τ	0	< 18.2	$\ell_\tau = 1$

Table 2.2: Elementary particles: leptons. They are divided following the generation they belong to, but also the electric charge Q and their mass are reported. The last column is the lepton quantum number, the only ones that are not null are those of the flavour of the particle. The masses of the neutrinos are considered to be zero in the SM, so the listed values are those measured experimentally.

relevant properties in Table 2.2. They are unstable, decaying into lighter particles shortly after being produced in high-energy processes, such as cosmic ray interactions in the atmosphere. Neutrinos, the neutral counterparts to the charged leptons, are perhaps the most enigmatic particles. They interact only via the weak nuclear force, making them incredibly elusive; billions pass through our bodies every second without any noticeable effect. Neutrinos have a very small mass, which was a major discovery since the SM initially predicted them to be massless. Their mass and the phenomenon of neutrino oscillation (the property of neutrinos to switch between different types) are still under investigation, providing insights into physics beyond the SM.

2.1.2 Interactions, the glue

What is a theory, a model, if it does not describe the processes in which its constituents are involved in? As in the previous paragraph the particles were described, the main focus here will be how they interact with each other, and which are the carriers of these interactions.

The electromagnetic force is one of the four fundamental forces of nature, responsible for interactions between particles with an electric charge. Governed by the theory of QED, it is mediated by photons, massless bosons that travel at the speed of light and do not carry an electric charge, enabling them to mediate electromagnetic interactions over infinite distances. In the quantum field theoretical framework, charged particles interact by exchanging photons, manifesting as the electromagnetic force. This force is responsible for a vast array of phenomena, from binding electrons to atoms to underpinning the operations of electrical and magnetic devices. Its strength is determined by the fine-structure constant, a dimensionless quantity characterizing the strength of electromagnetic interactions, called $\alpha_{em} = \frac{1}{137}$.

The weak nuclear force, though short-ranged, plays a crucial role in the universe, most notably in the nuclear processes that fuel the sun. This force is responsible for radioactive decay and hydrogen fusion, phenomena essential to the life cycles of stars. The theory describing this force, known as the electroweak theory, unifies the weak force with electromagnetism at high energy levels but shows distinct behaviours at low energies. This force is mediated by three massive bosons: $W^\pm$ and Z. Unlike photons, these bosons can carry an electric charge ($W^\pm$) or be neutral (Z), and their substantial mass limits the force's range to subatomic distances ($\sim 10^{-18}$m). The weak force is unique in its ability to change the flavour of quarks, enabling processes like β decay where a neutron transforms into a proton, electron, and electron antineutrino, but also main protagonist in the processes studied in this thesis.

The strong nuclear force is the *strongest* force among the four fundamental forces, but it operates over the shortest range. It is responsible for holding quarks together within protons and neutrons and keeping protons and neutrons bound within atomic nuclei. QCD is the theory that details the strong force, with gluons acting as the force mediators. Gluons are massless particles that carry the "colour charge", which is, as previously said, analogous to electric charge in electromagnetism but relevant to the strong interaction. Unlike photons, gluons can interact with each other due to their colour charge, leading to the unique property of the strong force known as confinement: quarks cannot be isolated individually and are always found in hadrons. Under the category of hadrons, it is possible to find colourless particles, combination of a quark and an antiquark, called mesons ($q\overline{q}$), groups of three quarks, named baryons (qqq). More recently, researchers have discovered other configurations, such as tetraquarks and pentaquarks. Tetraquarks are particles made up of four quarks, typically arranged as two quarks and two antiquarks ($qq\overline{q}\overline{q}$), while pentaquarks are composed of five quarks, typically four quarks and one antiquark ($qqqq\overline{q}$). These exotic hadrons challenge and expand our understanding of quark confinement and the ways quarks can combine within the strong force framework, providing deeper insight into the complexity of the strong interaction.

Last but not least, central to the SM is the Englert-Higgs mechanism [24] [3], which explains how particles acquire mass. The Higgs field permeates the universe, and particles gain mass through their interaction with this field. The Higgs boson, a scalar particle discovered in 2012, is a manifestation of this field. While not a force carrier in the traditional sense, the Higgs boson is integral to the structure of the SM, affecting the masses of the *W* and *Z* bosons and thereby influencing the weak force's properties.

2.1.3 The Lagrangian of the Standard Model

After a brief description of the phenomenology of the SM, it follows the mathematical description of the processes and interactions of the previous section. All the interactions forehead mentioned and their dynamics are described by equations of motion that are deduced from the Lagrangian density of each theory, that combined together form the Lagrangian of the SM. Before describing the components of interest, it is important to recall that the SM is built on the principle of local gauge invariance, which is expressed by the $SU(2)_I \times U(1)_Y \times SU(3)_C$ gauge group, where I is the weak isospin, Y is the hypercharge and C the colour charge. This symmetry dictates the form of the interactions and the inclusion of gauge bosons, the photon, *W* and *Z* bosons, and gluons, as mediators of the previously treated forces and mathematically, the generators of these groups. The $SU(2)_L \times U(1)_Y$ term is associated to the electroweak interactions, i.e. describes the electromagnetic and the weak forces. This component introduces the concept of spontaneous symmetry breaking through the Higgs mechanism, giving mass to the *W* and *Z* bosons while leaving the photon massless. The $SU(3)_C$ term is the component associated to the colour symmetry group, which is the one describing the QCD. The symmetries together lead to a formulation of the SM Lagrangian density invariant under local transformation. Finally, it is possible to write the SM Lagrangian density $\mathcal{L}_{SM}$ as

$$\mathcal{L}_{SM} = \mathcal{L}_{EW} + \mathcal{L}_{QCD} + \mathcal{L}_H + \mathcal{L}_Y \tag{2.1}$$

where, in order, the electroweak, QCD, Higgs and Yukawa Lagrangian densities are summed up.

Electroweak Lagrangian density It is considered a free Dirac particle, described by a Lagrangian of a spinor field Ψ, with spin 1/2

$$\mathcal{L}_0 = i\overline{\Psi}\gamma^\mu\partial_\mu\Psi - m\overline{\Psi}\Psi, \tag{2.2}$$

where γ^μ are the Dirac matrices [25]. Such a Lagrangian is invariant under global U(1) transformation, but when considering local gauge transformation, in which the phase transformation depends on the space–time coordinate, $\Psi(x) \to e^{iq\lambda(x)}\Psi(x)$, the invariance does not hold anymore. Hence, an extra term is needed to preserve this property, a new spin-1 field A_μ, which represents the four-vector electromagnetic potential. The modification is lead by the local transformation, under which the recently introduced field transforms as $A_\mu \to A_\mu + \partial_\mu\lambda(x)$. The last remark to preserve the invariance is the replacement of the derivative by a covariant derivative D_μ, defined as $D_\mu = \partial_\mu - iqA_\mu$. The Lagrangian density now becomes

$$\mathcal{L}_A = \overline{\Psi}(i\gamma^\mu D_\mu - m)\Psi = \mathcal{L}_0 - j^\mu A_\mu, \tag{2.3}$$

where the last term represents the interaction between the Dirac particle and the electromagnetic field, and j^μ is defined as $q\overline{\Psi}\gamma^\mu\Psi$, representing the conserved electromagnetic current. The gauge principle has generated an interaction between the Dirac spinor and the gauge field A_μ, which corresponds to the vertex of QED. Furthermore, it is necessary for A_μ to be a propagating field, and to achieve so, a gauge-invariant kinetic term is added, $-\frac{1}{4}F_{\mu\nu}F^{\mu\nu}$, where $F_{\mu\nu} = \partial_\mu A_\nu - \partial_\nu A_\mu$, is the electromagnetic field strength. The unification between QED and weak forces comes in a similar way asking for the local gauge invariance under the group $SU(2)_I \times U(1)_Y$. The weak theory describes several fermionic flavours, left- and right-handed fields which should appear in doublets, but also massive gauge bosons $W^\pm$ and Z in addition to the photon. The simplest group with doublet representations is $SU(2)$. Electroweak interactions are described by weak isospin doublets of left-handed fermions and right-handed spinor singlets. This time, the local transformations correspond to $\Psi_L \to e^{ig\alpha_k(x)\tau^k + ig'\frac{Y}{2}\lambda(x)}\Psi_L$ for left-handed fermions and $\Psi_R \to e^{ig'Y\lambda(x)}\Psi_R$ for right-handed fermions, where g and g' are the coupling constants of $SU(2)_I$ and $U(1)_Y$ respectively and τ^k are the Pauli matrices multiplied by a factor 1/2, with $k \in 1, 2, 3$. The Pauli matrices, σ^1, σ^2, and σ^3, are defined as follows:

$$\sigma^1 = \begin{pmatrix} 0 & 1 \\ 1 & 0 \end{pmatrix}, \quad \sigma^2 = \begin{pmatrix} 0 & -i \\ i & 0 \end{pmatrix}, \quad \sigma^3 = \begin{pmatrix} 1 & 0 \\ 0 & -1 \end{pmatrix}.$$

These matrices satisfy the commutation relations

$$[\sigma^i, \sigma^j] = 2i\epsilon_{ijk}\sigma^k,$$

where ϵ_{ijk} is the Levi-Civita symbol, and are used in the representation of the $SU(2)$ symmetry, where they act as generators when scaled by 1/2. Considering the gauge fields coming from $SU(2)_I$, W^k_μ and B_μ from $U(1)_Y$, the covariant derivatives can be written as $D_\mu = \partial_\mu - ig'\frac{Y}{2}B_\mu - ig\tau^k W^k_\mu$. The W and B bosons are massless, so they do not yet correspond to those of the electroweak theory. To finally obtain them, one needs to consider the different manner of interacting that right- and left-handed fermions have. The result for the photon, Z-boson and $W^\pm$-boson fields respectively, follows:

$$\begin{aligned} A_\mu &= \sin\theta_W W^3_\mu + \cos\theta_W B_\mu, \\ Z_\mu &= \cos\theta_W W^3_\mu - \sin\theta_W B_\mu, \\ W^\pm_\mu &= \frac{1}{2}(W^1_\mu \pm W^2_\mu), \end{aligned} \tag{2.4}$$

where θ_W is called the weak mixing angle.

QCD Lagrangian density As already mentioned, QCD describes strong interactions having as mediators the 8 different types of gluons G_μ. The theory is based on a $SU(3)$ color symmetry, and again, it has to be invariant under local transformation, in order for the physics not to be dependent from color charge. The covariant derivative that in this case ensures the invariance is $D_\mu = \partial_\mu - ig_s G^a_\mu T_a$, where g_s is the strong coupling constant and T_a are the group generators, the Gell-Mann matrices [26] multiplied by a factor 1/2. The dynamics of the gluon fields themselves are described by the gluon field strength tensor, which accounts for the kinetic energy of the gluons and their self-interactions, $G^a_{\mu\nu} = \partial_\mu G^a_\nu - \partial_\nu G^a_\mu - g_s f_{abc} G^b_\mu G^c_\nu$, with f_{abc} the $SU(3)$ structure constants. The Lagrangian of the strong interaction is then expressed as

$$\mathcal{L}_{\text{QCD}} = \sum_q \overline{\psi}_q (i\gamma^\mu D_\mu - m_q)\psi_q - \frac{1}{4} G^a_{\mu\nu} G^{\mu\nu}_a, \tag{2.5}$$

with m_q the mass of the corresponding quark to the field ψ_q. As said, quarks and gluons do carry color, but only observations of colourless combinations have been done up-to-now. Isolated color-charged particles do not seem to exist freely; rather, they must join with others to form color-neutral entities known as hadrons. This characteristic is clear by examining the variation of the strong coupling constant α_s (proportional to the square of the strong force coupling constant g_s) with the energy scale, denoted by Q. At low Q values, which correlate with greater distances, the coupling constant is significantly large. On the other side, at high Q values it diminishes. Thus, at high energies or shorter distances, quarks and gluons exhibit weaker interactions, behaving almost like free particles, a phenomenon termed asymptotic freedom that is unique to QCD. At low energies or larger distances, they are forced to create bound states, the hadrons. When the coupling constant is small, such as in the 100 GeV to 1 TeV energy range hovering around 0.1, QCD calculations become simpler and can be conducted using perturbative techniques (pQCD). However, at higher coupling constant values (below 1 GeV), more complex methods like lattice QCD are required for calculations.

Higgs Lagrangian density The gauge bosons described previously should be massless according to the symmetries of the SM theory. However, the *W* and *Z* bosons are observed to be quite massive. The Higgs mechanism reconciles this discrepancy by introducing an additional field, now known as the Higgs field, permeating all of space. The mass of bosons was not mentioned because if a term like $m\overline{\psi}\psi$ is added, then right- and left-handed mixed terms would arise, breaking the built gauge invariance. The Higgs field is a scalar field consisting into a Lagrangian expressed as:

$$\mathcal{L}_{\text{Higgs}} = (D^\mu \Phi)^\dagger (D_\mu \Phi) - V(\Phi), \tag{2.6}$$

where the first term is the kinetic component and the potential $V(\Phi)$ is defined as $V(\Phi) = \mu^2 \Phi^\dagger \Phi + \lambda(\Phi^\dagger \Phi)^2$, with μ^2 the mass parameter, < 0, and λ the coupling constant, > 0, allowing for spontaneous symmetry breaking and ensuring the potential to be bounded from below, resulting in vacuum stability. The Higgs field is an $SU(2)$ doublet composed of two complex scalar fields, ϕ^+, the charged component of the Higgs field, and ϕ^0, the neutral component. After spontaneous symmetry breaking, the neutral component of the doublet acquires a nonzero vacuum expectation value (VEV). This can be expressed as

$$\phi^0 = \frac{1}{\sqrt{2}} \begin{pmatrix} 0 \\ v \end{pmatrix}, \tag{2.7}$$

where $v = \sqrt{-\mu^2/\lambda}$ is the VEV and is approximately 246 GeV. The field can then be written in terms of its fluctuations around the vacuum expectation value as:

$$\Phi(x) = \frac{1}{\sqrt{2}} \begin{pmatrix} 0 \\ v + h(x) \end{pmatrix}. \tag{2.8}$$

The gauge boson masses are obtained by evaluating the Higgs Lagrangian with the just-found Higgs field. The kinetic term becomes:

$$(D_\mu \Phi)^\dagger (D^\mu \Phi) = \frac{1}{2}(\partial_\mu h)(\partial^\mu h) + \frac{g^2}{4}(v+h)^2 W_\mu^+ W^{-\mu} + \frac{1}{8}(g^2 + g'^2)(v+h)^2 Z_\mu Z^\mu, \tag{2.9}$$

with the potential

$$V(\Phi) = \frac{\mu^2}{2}(v+h)^2 + \frac{\lambda}{4}(v+h)^4. \tag{2.10}$$

Knowing the bosons we are looking for, we can classify them as "neutral currents" mediated by the *Z* boson, and "charged currents" mediated by the charged bosons $W^\pm$. From the kinetic term they appear as

$$W_\mu^\pm = \frac{1}{\sqrt{2}}(W_\mu^1 \pm i W_\mu^2), \tag{2.11}$$

$$Z_\mu = \frac{-g' B_\mu + g W_\mu^3}{\sqrt{g^2 + g'^2}}, \tag{2.12}$$

$$A_\mu = \frac{g B_\mu + g' W_\mu^3}{\sqrt{g^2 + g'^2}}. \tag{2.13}$$

Expressing them as above and looking at Equation 2.4, it is clear that the weak mixing angle can be defined via the coupling constants of $SU(2)$ and $U(1)$ groups, indeed its cosine is $cos\theta_w = \frac{g}{\sqrt{g^2+g'^2}}$. Retrieving the masses from the earlier obtained Lagrangian density, the final result is

$$M_W^2 = \frac{1}{4} g^2 v^2, \tag{2.14}$$

$$M_Z^2 = \frac{1}{4}(g^2 + g'^2) v^2, \tag{2.15}$$

$$M_A = 0, \tag{2.16}$$

$$M_{\text{Higgs}} = \sqrt{2\lambda} v. \tag{2.17}$$

Only one piece of the puzzle is missing to complete the theory, as also fermions have mass. They acquire it in the same way the bosons do, by interacting with the Higgs field. The Lagrangian density that describes this process is the Yukawa Lagrangian, as through the Yukawa couplings quantify the scalar interactions between the fermion and the Higgs fields. It follows:

$$\mathcal{L}_Y = -Y_{ij}^D \overline{Q}_{Li} \phi D_{Rj} - Y_{ij}^U \overline{Q}_{Li} \phi^* U_{Rj} - Y_{ij}^L \overline{L}_{Li} \phi E_{Rj} + \text{h.c.}, \tag{2.18}$$

where Y_{ij}^D, Y_{ij}^U, and Y_{ij}^L are the Yukawa coupling matrices running over i, j fermion generations for down-type quarks, up-type quarks, and leptons, respectively; $\overline{Q}_{Li}$, $\overline{L}_{Li}$ are the left-handed quark and lepton doublets; D_{Rj}, U_{Rj}, E_{Rj} are the right-handed down-type quark, up-type quark, and lepton singlets and h.c. stands for Hermitian conjugate, which denotes the conjugate transpose of all preceding terms. To conclude, the mass of the fermions is computed as $m_i = y_i \frac{v}{\sqrt{2}}$, where y_i is the Yukawa coupling for the fermion i. Yukawa couplings are "free parameters" in the sense that the SM does not predict their values, they must be determined by experiment.

2.2 Discrete symmetries and *CP* Violation

Symmetries play an important role in elementary particle physics, mainly thanks to Noether's theorem [27] which states that whenever there is a symmetry, a conserved quantity comes along. This allows us to describe a dynamic system even if not all its variables are available. There are two categories of symmetries, the discrete and the continuous ones. The continuous distinguish from the discrete by the set of continuous parameters from which they are characterized. There is a particular interest into discrete ones, the Parity (*P*), Charge conjugation (*C*) and Time reversal (*T*). The adjective discrete is associated with them as they force the system to a non-continuous change, a swap, for example. Parity operation indeed reverses the spatial coordinates of any positional vector, i.e. $(\mathrm{t}, \mathbf{x}) \xrightarrow{\hat{\mathrm{P}}} (\mathrm{t}, -\mathbf{x})$, leaving the angular momentum untouched. Charge Conjugation acts on the charges, taking one particle to its antiparticle, the particle with the same mass and spin but opposite electrical charge and other quantum numbers, and vice versa. Time reversal, instead, inverses the time direction; the spatial coordinates are unchanged but the direction of momenta is reversed. If the system is invariant under the transformation one of the operators carries out, it is possible to talk about symmetry conservation, otherwise, it is a symmetry breaking. Requiring the conservation of one of these three symmetries, or the combination of two of them, for a physics process results in the prohibition of certain transitions to occur in nature. It was clear since the beginning that taking into account P or C separately, these transformations were not conserved in weak interactions, while a more significant violation was obtained observing the C and P transformations acting together, which initially seemed to leave the system invariant. An important breakthrough in this context was provided by an experiment conducted by Chien-Shiung Wu in 1956 [28]. Wu's experiment, carried out at the National Bureau of Standards, demonstrated the violation of parity conservation in the weak decay of cobalt-60. This experiment showed that the distribution of electrons emitted in the β decay of cobalt-60 nuclei was not symmetrical, providing clear evidence that parity is not conserved in weak interactions. This discovery was pivotal as it challenged previously held beliefs about symmetry in fundamental interactions. Following this, an experiment carried out at Brookhaven raised further doubts about the symmetry in weak interactions. In 1956, the oscillation of the neutral Kaon to its antiparticle was observed, providing an optimal experiment to test *CP* violation. In 1964, Cronin and Fitch [29] measured a small but significant amount of *CP* violation, which was accommodated in the Standard Model as an effect of the Cabibbo-Kobayashi-Maskawa (CKM) [4], [5] mechanism for the mixing of quarks. So far, *CPT* symmetry is upheld as an exact symmetry in nature, with no observed deviations. This symmetry emerges from local Lorentz invariance, one of the fundamental principles of contemporary quantum field theory. Should *CPT* symmetry be compromised, it would signify a failure of the Standard Model.

2.2.1 CKM Matrix

The concept of quark mixing, i.e. the transition probability from a quark family to another, originated from the need to explain certain experimental results in weak decay processes that could not be accounted for by the then-existing theory. The weak force, responsible for processes like β decay, has the unique property of changing quark flavour, leading to quark mixing. In the 1960s, Nicola Cabibbo first introduced the idea that the weak interaction eigenstates of the quarks are not aligned with their mass eigenstates. He posited a mixing angle, now known as the Cabibbo angle, to describe the mixing between the up-to-then observed quarks, the u and d

as a doublet, and the s as a singlet. This phenomenon is represented as a rotation matrix of the Cabibbo angle, $\theta_C \sim 13^\circ$, as

$$\begin{pmatrix} d' \\ s' \end{pmatrix} = \begin{pmatrix} \cos\theta_C & \sin\theta_C \\ -\sin\theta_C & \cos\theta_C \end{pmatrix} \begin{pmatrix} d \\ s \end{pmatrix} = \begin{pmatrix} d \cdot \cos\theta_C + s \cdot \sin\theta_C \\ -d \cdot \sin\theta_C + s \cdot \cos\theta_C \end{pmatrix} \tag{2.19}$$

where the primed quarks are the weak interaction eigenstates while the not-primed are the mass ones. This result, though, had the issue of allowing Flavour Changing Neutral Currents (FCNC), i.e. $d \to s$ transitions, which were not observed in nature. It was the introduction of another mechanism, by Glashow, Iliopoulos and Maiani (GIM) [30], that proposing the existence of a fourth quark, hence having 2 doublets, that solved the issue and forbid the existence of FCNCs. It was in 1973 when two scientists, Kobayashi and Maskawa [31], proposed a third family of quarks, t and b, to explain *CP* violation in the kaon sector. To accomodate this addiction, the Cabibbo matrix was extended into the Cabibbo-Kobayashi-Maskawa (CKM) matrix, obtained from the Cabibbo one, and fully describing the mixing between three families of quarks. The CKM matrix can be written as:

$$V_{CKM} = \begin{pmatrix} V_{ud} & V_{us} & V_{ub} \\ V_{cd} & V_{cs} & V_{cb} \\ V_{td} & V_{ts} & V_{tb} \end{pmatrix} = \begin{pmatrix} 1 - \frac{\lambda^2}{2} & \lambda & A\lambda^3(\rho - i\eta) \\ -\lambda & 1 - \frac{\lambda^2}{2} & A\lambda^2 \\ A\lambda^3(1 - \rho - i\eta) & -A\lambda^2 & 1 \end{pmatrix} + \mathcal{O}(\lambda^4) \tag{2.20}$$

Each V_{ij} matrix element indicates the probability for the transition between the named quarks to occur. The last equality is written using the Wolfenstein parametrization [6], in which the following substitution are applied: $\lambda = \frac{|V_{us}|}{\sqrt{|V_{ud}|^2 + |V_{us}|^2}} = \sin\theta_C$, $A\lambda = |\frac{V_{cb}}{V_{us}}|$ and $A\lambda^3(\rho - i\eta) = V_{ub}$. The parametrization is an approximation of the real values; as can be noticed, it is reported up to the third order in λ, and this particular parametrization is chosen because the higher the order of λ is, the lower in the hierarchy in terms of probability for the transition to happen, they are.

The condition that the CKM matrix is a unitary matrix, i.e. $V_{CKM}V^\dagger_{CKM} = I$, with I used to identify the identity matrix, imposes $\sum_i V_{ij}V^*_{ik} = \delta_{jk}$ and $\sum_j V_{ij}V^*_{kj} = \delta_{ik}$. The six vanishing combinations, which are illustrated as triangles in the complex plane of (ρ, η), serve to quantify *CP* violation. Despite having identical areas, indicative of non *CP* conservation, these triangles exhibit diverse shapes owing to variations in the magnitudes of the V_{ij} coefficients. The most commonly used unitarity triangle is given by

$$V_{ud}V^*_{ub} + V_{cd}V^*_{cb} + V_{td}V^*_{tb} = 0, \tag{2.21}$$

from which it is possible to identify three angles

$$\alpha = \arg\left(-\frac{V_{td}V^*_{tb}}{V_{ud}V^*_{ub}}\right), \qquad \beta = \arg\left(-\frac{V_{cd}V^*_{cb}}{V_{td}V^*_{tb}}\right), \qquad \gamma = \arg\left(-\frac{V_{ud}V^*_{ub}}{V_{cd}V^*_{cb}}\right). \tag{2.22}$$

These angles belong to the triangle pictured in the complex plane $(\overline{\rho}, \overline{\eta})$ in Figure 2.1, the two parameters are defined as $\overline{\rho} = \rho(1 - {}^{\lambda^2}\!/_2 + ...)$ and $\overline{\eta} = \eta(1 - {}^{\lambda^2}\!/_2 + ...)$.

2.2.2 *CP* Violation and γ from $B^\pm$ Meson Decays

Measuring *CP* violation provides crucial insights into the asymmetries between matter and anti-matter, offering a window into understanding why the universe is dominated by matter despite

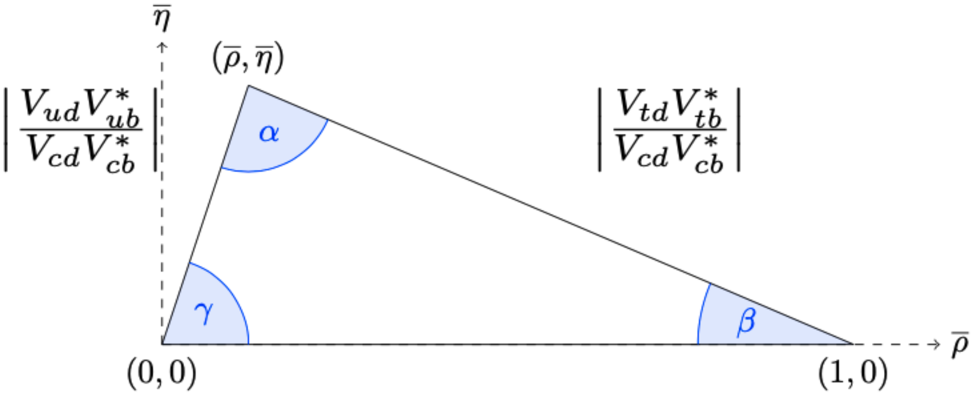

Figure 2.1: Sketch of the unitarity triangle of the CKM matrix, angles defined as in Equation 2.22

the theoretical expectation of equal amounts of matter and antimatter produced during the Big Bang, the cosmological event that marks the origin of the universe from an extremely dense and hot state. Experimental investigations of *CP* violation involve studying the behaviour of particles and antiparticles in various processes, such as decay and scattering, to identify differences in their properties. These differences manifest as observable deviations from the predictions of *CP* symmetry, indicating the presence of *CP* violation. Experimental efforts to measure *CP* violation have been highly successful, particularly in experiments involving mesons such as neutral kaons and B mesons. In the world, several facilities have been or are investigating these decays, notably BaBar [7], LHCb [8], Belle [9] and BelleII [10] in Japan. When investigating *CP* violation, it is necessary to distinguish which typology of this phenomenon is being observed. Indeed, three categories exist:

- Direct *CP* violation: it occurs in the decay itself for both charged and neutral parent particles. It occurs when the probability of a particle and its corresponding antiparticle decay to different final states, one the *CP* transformation of the other. In other words, the decay rates of a particle and its antiparticle are asymmetrical. This violation directly affects the decay process itself, leading to observable differences in the final state particle distributions.

- *CP* violation in mixing: it occurs in the mixing of neutral particles, which can oscillate to their antiparticle and back, in particular when the two neutral mass eigenstates cannot be *CP* eigenstates. The first observation of *CP* violation, i.e. the Kaon system, belongs to this category.

- *CP* violation in interference between the decay and the oscillation amplitude: it occurs when the interference between mixing and decay processes leads to differences in decay rates for particle-antiparticle pairs that decay into *CP* eigenstates. In these systems, particles can transform into their antiparticles and vice versa through the process of mixing, which involves oscillations between different flavour eigenstates. The asymmetry in decay rates arises from the interference between mixing and decay rather than from the decay process itself.

In the context of this thesis, particular emphasis will be placed on the investigation of *CP* violation in decay processes. Within the LHCb experiment, numerous analysis focusing on *CP* violation have been performed, hence, the initial focus will be on elucidating the well-established methodologies employed for B meson decays, then continuing the discussion on the particular decay channel under scrutiny in this analysis.

The starting point is the definition of the amplitudes under study. Indeed, defining as $|A_n|$ the module of the n-th decay magnitude contributing to the total amplitude, δ_n the strong phase and ϕ_n the weak phase, the total amplitude of a process can be described as $A = \sum_n |A_n| e^{i(\delta_n + \phi_n)}$. Applying the *CP* operation, the result is $\overline{A} = \sum_n |A_n| e^{i(\delta_n - \phi_n)}$. To have *CP* violation in decay, at least two contributing amplitudes are required, so for the sake of simplification, it follows the computation for the measurement only in the lower bound case: $|A|^2 - |\overline{A}|^2 = -4|A_1||A_2|\text{sin}(\delta_1 - \delta_2)\text{sin}(\phi_1 - \phi_2)$. It is clear that in order to observe *CP* violation, both $\Delta\delta$ and $\Delta\phi$ need to be different from zero, i.e. it is mandatory to have interfering decay amplitudes with different phases. For decays in which $b \to c$ and $b \to u$ transitions interfere, the difference between the weak phases could be conveniently substituted by the CKM angle γ, which is a notable parameter when talking about the CKM matrix and *CP* violation in general as it is not depending on the t quark. Notably, the processes from which γ is extracted involve only tree diagrams, basic Feynman diagrams representing the leading-order interactions without loops, ensuring that the measurement of this parameter is quite clean and has small theoretical uncertainties. The techniques developed to complete the measurement can be of different typologies: time-dependent, time-integrated or Dalitz plot analyses. The time-dependent techniques are used when the decay analyzed has a *CP* violation in mixing and direct decay, so the observables depend on the particle oscillation frequency, decay width difference and the time at which the decay occurs. Time-integrated techniques, instead, are used when there is no need to perform sophisticated flavour tagging methods [32], which retrieve the flavour of the signal particle at the moment of its production before decaying since the flavour of the particle at the time of its decay is known by looking at the final state. Dalitz plot analyses are performed when the final state is a three-body final state, on which a Dalitz plot [13], or a double Dalitz plot can be performed. This document will give a detailed explanation of time-independent techniques for the study. Two methods can be found in this category: the Gronau, London and Wyler (GLW) method and the Atwood, Dunietz and Soni (ADS) method.

GLW This method [11] of measuring the angle γ was formulated for $B^+ \to DK^{(*)+}$ meson decays, and the D meson further decaying into a *CP* eigenstate, either even $\frac{D^0 + \overline{D}^0}{\sqrt{2}}$, as K^+K^- and $\pi^+\pi^-$, or odd $\frac{D^0 - \overline{D}^0}{\sqrt{2}}$, as $K^0_S\pi^0$ and $K^0_S\phi$. The observables of this method are obtained with a clear dependence on γ:

$$\begin{aligned}\mathcal{A}_{CP} &= \frac{\Gamma(B \to D_{CP} f) - \Gamma(\overline{B} \to D_{CP}\overline{f})}{\Gamma(B \to D_{CP} f) + \Gamma(\overline{B} \to D_{CP}\overline{f})} \\ &= \frac{2\kappa r_B \text{sin}\delta_B \text{sin}\gamma}{1 + r_B^2 + 2\kappa r_B \text{cos}\delta_B \text{cos}\gamma},\end{aligned} \tag{2.23}$$

$$\begin{aligned}\mathcal{R}_{CP} &= \frac{\Gamma(B \to D_{CP} f) + \Gamma(\overline{B} \to D_{CP}\overline{f}))}{\Gamma(B \to D f) + \Gamma(\overline{B} \to D\overline{f}))} \\ &= 1 + r_B^2 + 2 r_B \text{cos}\delta_B \text{cos}\gamma,\end{aligned} \tag{2.24}$$

with r_B the amplitude ratio between the B meson decays, defined as $\frac{1}{3}\frac{|V_{ub}||V^*_{cs}|}{|V_{cb}||V^*_{us}|}$ in the forehead case, with the factor 1/3 coming from the colour suppression, and δ_B the corresponding relative strong phase. In the last expression, D indicates the Cabibbo favoured mode, $D \to K\pi$. The $\mathcal{A}_{CP}$ observable provides a direct quantification of the amount of *CP* violation in this decay mode, while $\mathcal{R}_{CP}$ indicates the sensitivity of the method. From the *CP* observables just defined, it is possible to notice that there are two discrete ambiguities in γ: one is the sign of the weak phase, i.e. γ itself, the other is the possibility of confusing γ with the final state phase difference, $\delta_2 - \delta_1$. The sign ambiguity of γ results in four different solutions for sin(γ), which have different magnitudes due to the different rates of the decay processes. Anyway, increasing the statistics, given that each decay has a different $\delta_2 - \delta_1$ value, it resolves the ambiguity of confusing γ and the final state phase difference. The ambiguity in the sign of sin(γ), instead, is intrinsic to the method, but in the SM.

ADS Even though the GLW method is effective in measuring γ, some difficulties can be encountered: for example, the decay amplitudes of $B \to D^0 h$ and $B \to \overline{D}^0 h$ are quite different, and interference is found in D_{CP} decay, resulting in an expected small value of $\mathcal{A}_{CP}$. To overcome this problems, another method can be used, which is the ADS [12]. It does not use *CP* eigenstates of D, instead, it takes in account the Cabibbo-favoured $D^0 \to K^-\pi^+$ and the doubly Cabibbo-suppressed $D^0 \to K^+\pi^-$ decays. In computing the observables of this method, two more parameters have to be taken into account, which are the amplitude ratio r_D, defined as $\frac{|V^*_{ud}||V_{cs}|}{|V^*_{cd}||V_{us}|}$, and the corresponding relative strong phase δ_D:

$$\begin{aligned}\mathcal{A}_{ADS} &= \frac{\Gamma(B \to [K^+\pi^-]_D f) - \Gamma(\overline{B} \to [K^-\pi^+]_D \overline{f})}{\Gamma(B \to [K^-\pi^+]_D f) + \Gamma(\overline{B} \to [K^-\pi^+]_D \overline{f})} \\ &= \frac{2r_B r_D \text{sin}(\delta_B - \delta_D)\text{sin}\gamma}{r_B^2 + r_D^2 + 2r_B r_D \text{cos}(\delta_B - \delta_D)\text{cos}\gamma}\end{aligned} \tag{2.25}$$

$$\begin{aligned}\mathcal{R}_{ADS} &= \frac{\Gamma(B \to [K^+\pi^-]_D f) + \Gamma(\overline{B} \to [K^-\pi^+]_D \overline{f})}{\Gamma(B \to [K^-\pi^+]_D f) + \Gamma(\overline{B} \to [K^+\pi^-]_D \overline{f})} \\ &= \frac{r_B^2 + r_D^2 + 2r_B r_D \text{cos}(\delta_B - \delta_D)\text{cos}\gamma}{1 + r_B^2 r_D^2 + 2r_B r_D \text{cos}(\delta_B + \delta_D)\text{cos}\gamma}\end{aligned} \tag{2.26}$$

2.3 *CP* Violation in Λ_b^0 decays

In this work, the interest is in the decays of Λ_b^0, in order to observe a direct *CP* violation for the baryon with final state $D^0 pK^-$, with the D^0 decaying in *CP* even eigenstates, i.e. K^-K^+ and $\pi^+\pi^-$. In this section, the theories and the methods previously explained are going to be readapted to the study-case. The relevance of the measurement is given by the fact that although *CP* violation is described by SM, it has never been observed in baryons because of the limiting uncertainties that come with the measurements, as their production is more difficult than B mesons. With the Upgrade that LHCb is carrying on, at the end of the next Run it is expected to have about five times the number of events than at the end of the previous Run, which would sensibly reduce the statistical uncertainties.

2.3.1 Decay phenomenology and Feynman diagrams

In order to better frame the analysis, an overview of the particles that are going to be studied is given. In Table 2.3 a summary of the parent, daughter and grand-daughter particles is given. There are only a few Feynman diagrams possible at the lowest order showing how Λ_b^0 can decay to $D^0 pK^-$ at the quark level. Increasing the order, inevitably new vertexes are added, making

		m (MeV/c^2)	Lifetime τ	$I(J^P)$
Λ_b^0	$\vert udb\rangle$	5619.60 ± 0.17	1.471 ± 0.009 10^{-12}s	0(1/2$^+$)
p	$\vert uud\rangle$	938.2720813(58)	> 3.6 × 10^{29}yr	1/2(1/2$^+$)
D^0	$\vert c\overline{u}\rangle$	1864.84 ± 0.05	410.1 ± 1.5 10^{-15}s	1/2(0$^-$)
K^-	$\vert s\overline{u}\rangle$	493.677 ± 0.013	1.2379 ± 0.0021 10^{-8}s	1/2(0$^-$)
π^-	$\vert d\overline{u}\rangle$	139.57039 ± 0.00017	2.6033 ± 0.0005 10^{-8}s	1(0$^-$)

Table 2.3: Particles involved in the analysis and their properties.

the process less probable. In Figure 2.2, the tree-level diagrams of the contributing processes of the study are shown. It also follows the representation of the Ξ_b^0 diagrams with the same Λ_b^0 final states in Figure 2.3. Figure 2.4 presents the Feynman diagrams of the decays of interest of D^0.

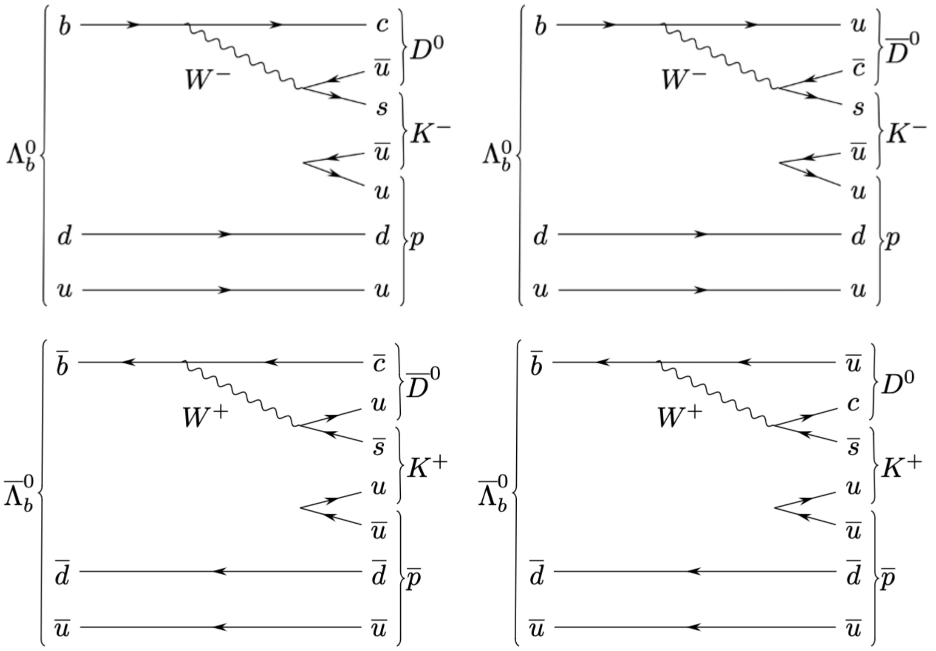

Figure 2.2: Feynman diagrams of lowest order for the decay $\Lambda_b^0 \to D^0 pK^-$.

2.3.2 *CP* observables

Following the methods previously described, also with the baryon Λ_b^0 is possible to measure the angle γ of the CKM matrix through its *CP* observables. There is an advantage in using Λ_b^0 rather than a B meson, as the ratio between the two amplitudes does not hold the factor 1/3 coming from the two decays being one colour suppressed and the second no, but it is just $r_{\Lambda_b^0} = \frac{|V_{ub}||V_{cs}^*|}{|V_{cb}||V_{us}^*|} \sim 0.4$. To better understand the physics behind the measurement, the computation for the observables follows. The first step is defining the amplitudes of the Feynman diagrams in Figure 2.2.

$$\mathrm{A}(\Lambda_b^0 \to D^0 pK^-) = |\mathrm{A}_1|e^{i\delta_1}, \tag{2.27}$$

$$\mathrm{A}(\overline{\Lambda}_b^0 \to \overline{D}^0 \overline{p}K^+) = |\mathrm{A}_1|e^{i\delta_1}, \tag{2.28}$$

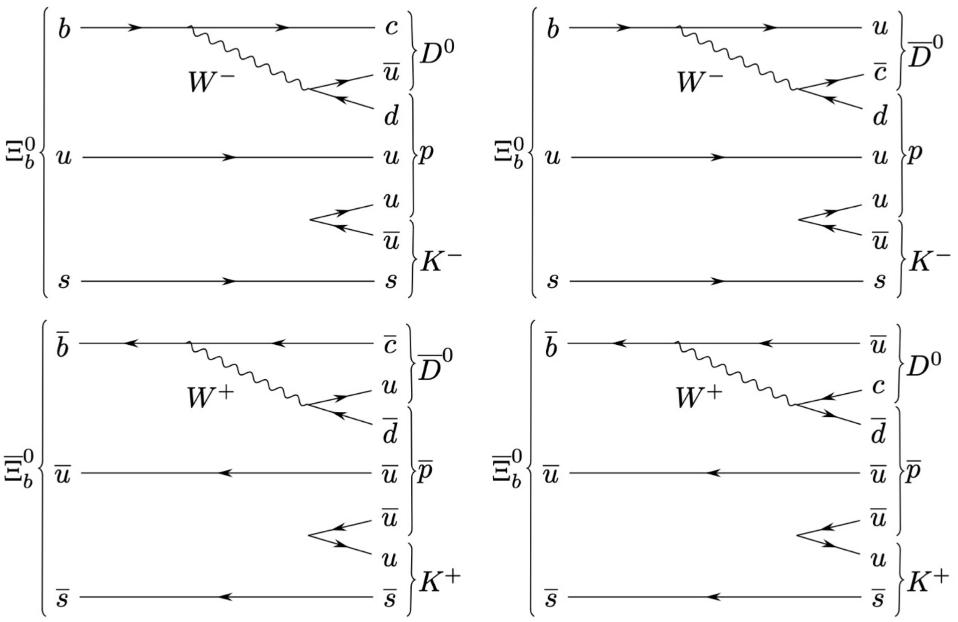

Figure 2.3: Feynman diagrams of lowest order for the decay $\Xi_b^0 \to D^0 p K^-$.

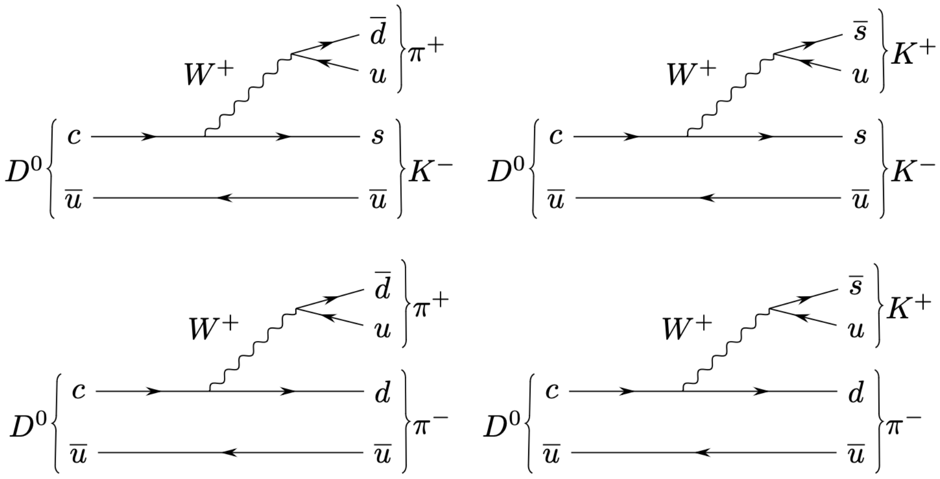

Figure 2.4: Feynman diagrams of lowest order for the decay $D^0 \to h^- h^+$, with $h = K, \pi$.

$$\mathrm{A}(\Lambda_b^0 \to \overline{D}^0 p K^-) = |\mathrm{A}_2| e^{i(\delta_2 - \gamma)}, \tag{2.29}$$

$$\mathrm{A}(\overline{\Lambda}_b^0 \to D^0 \overline{p} K^+) = |\mathrm{A}_2| e^{i(\delta_2 + \gamma)}. \tag{2.30}$$

By substituting the CKM matrix elements and adopting the Wolfenstein parametrization, the amplitudes now become:

$$\mathrm{A}(\Lambda_b^0 \to D^0 p K^-) = |V_{cb}||V_{us}^*| e^{i\delta_1} = A\lambda^3 e^{i\delta_1}, \tag{2.31}$$

$$\mathrm{A}(\overline{\Lambda}_b^0 \to \overline{D}^0 \overline{p} K^+) = |V_{cb}^*||V_{us}| e^{i\delta_1} = A\lambda^3 e^{i\delta_1}, \tag{2.32}$$

$$\mathrm{A}(\Lambda_b^0 \to \overline{D}^0 p K^-) = |V_{ub}||V_{cs}^*| e^{i(\delta_2 - \gamma)} = A(1 - \lambda^2/2)\lambda^3 \sqrt{\rho^2 + \eta^2} e^{i(\delta_2 - \gamma)}, \tag{2.33}$$

$$\mathrm{A}(\overline{\Lambda}_b^0 \to D^0 \overline{p} K^+) = |V_{ub}^*||V_{cs}| e^{i(\delta_2 + \gamma)} = A(1 - \lambda^2/2)\lambda^3 \sqrt{\rho^2 + \eta^2} e^{i(\delta_2 + \gamma)}. \tag{2.34}$$

Obtaining the decay rate from these amplitudes and simplifying them appropriately, it is possible to write the *CP* asymmetry as

$$\begin{aligned}\mathcal{A}_{CP} &= \frac{\Gamma(\Lambda_b^0 \to D_{CP} p K^-) - \Gamma(\overline{\Lambda}_b^0 \to D_{CP} \overline{p} K^+)}{\Gamma(\Lambda_b^0 \to D_{CP} p K^-) + \Gamma(\overline{\Lambda}_b^0 \to D_{CP} \overline{p} K^+)} \\ &= \frac{2(1 - {\lambda^2}/{2})\sqrt{\rho^2 + \eta^2}\kappa \sin\delta_{\Lambda_b} \sin\gamma}{1 + (1 - {\lambda^2}/{2})^2(\rho^2 + \eta^2) + 2(1 - {\lambda^2}/{2})\sqrt{\rho^2 + \eta^2}\kappa \cos\delta_{\Lambda_b} \cos\gamma}\end{aligned} \tag{2.35}$$

It follows that $r_{\Lambda_b} = (1 - {\lambda^2}/{2})\sqrt{\rho^2 + \eta^2}$ and the same formula as for the B mesons is obtained. From the data analysis, also Ξ_b^0 decaying to the same final state of Λ_b^0 is visible. It could be worth estimating the expected level of *CP* violation in this case. The amplitudes in this case would be

$$\mathrm{A}(\Xi_b^0 \to D^0 p K^-) = |V_{cb}||V_{ud}^*|e^{i\delta_1} = A\lambda^2(1 - {\lambda^2}/{2})e^{i\delta_1}, \tag{2.36}$$

$$\mathrm{A}(\overline{\Xi}_b^0 \to \overline{D}^0 \overline{p} K^+) = |V_{ub}^*||V_{cd}|e^{i\delta_1} = -A\lambda^4 e^{i\delta_1}, \tag{2.37}$$

$$\mathrm{A}(\Xi_b^0 \to \overline{D}^0 p K^-) = |V_{ub}||V_{cd}^*|e^{i(\delta_2 - \gamma)} = -A\lambda^4 e^{i(\delta_2 - \gamma)}, \tag{2.38}$$

$$\mathrm{A}(\overline{\Xi}_b^0 \to D^0 \overline{p} K^+) = |V_{ud}||V_{cb}^*|e^{i(\delta_2 + \gamma)} = A\lambda^2(1 - {\lambda^2}/{2})e^{i(\delta_2 + \gamma)}. \tag{2.39}$$

And again, the *CP* asymmetry would be:

$$\begin{aligned}\mathcal{A}_{CP} &= \frac{\Gamma(\Xi_b^0 \to D_{CP} p K^-) - \Gamma(\overline{\Xi}_b^0 \to D_{CP} \overline{p} K^+)}{\Gamma(\Xi_b^0 \to D_{CP} p K^-) + \Gamma(\overline{\Xi}_b^0 \to D_{CP} \overline{p} K^+)} \\ &= \frac{-2\lambda^2(1 - {\lambda^2}/{2})\sqrt{\rho^2 + \eta^2}\kappa \sin\delta_{\Xi_b} \sin\gamma}{(1 - {\lambda^2}/{2})^2 + \lambda^4(\rho^2 + \eta^2) - \lambda^2(1 - {\lambda^2}/{2})\sqrt{\rho^2 + \eta^2}\kappa \cos\delta_{\Xi_b} \cos\gamma}\end{aligned} \tag{2.40}$$

The parametrization in this case imposes that $r_{\Xi_b} = \frac{\lambda^2\sqrt{\rho^2+\eta^2}}{(1-{\lambda^2}/{2})}$ and a rough estimation allows to conclude that the expected *CP* asymmetry is around 3%. Considering the statistics at disposal while performing the analysis, such a small asymmetry is not visible due to the consequently large statistical uncertainties.

Before beginning the next paragraph, it could be of use the introduction of the coherence factor κ. In particle decays, it is introduced to quantify the degree of coherence between the decay amplitudes of a particle and its antiparticle, and it ranges from 0 to 1. In this context, it is used to describe how the mother particle and its anti-particle interfere while decaying, as the interference between the amplitudes of different decay paths can enhance or suppress certain decay modes. The interferences generate multiple intermediate states that then contribute to the final state. Regarding the $\Lambda_b^0 \to D^0 p K^-$ decay, the possible resonances are

- $\Lambda_b^0 \to \Lambda_c^{*+} K^-$, with $\Lambda_c^{*+} \to D^0 p$
- $\Lambda_b^0 \to D^0 \Lambda^*$, with $\Lambda^* \to p K^-$
- $\Lambda_b^0 \to D_s^- p$, with $D_s^- \to D^0 K^-$

The only resonance path that preserves the interference in the $D^0 - \overline{D}^0$ mesons is the second, which is therefore the one with the highest sensitivity to *CP* violation.

2.4 Polarization effect in the measurement

A long-standing doubt about the feasibility of a γ measurement using baryons regards their polarization. As at LHCb Λ_b^0 is produced with null polarization [33], the intent of the following sections is to demonstrate to the reader that in such a case, even if the polarization of the baryon is zero, it would still be possible to perform such a measurement.

2.4.1 Formalism

With respect to the previous parametrization given to the Λ_b^0 decays, some changes are placed. The amplitudes are expressed as:

$$\mathcal{A}(\Lambda_b^0 \to D^0 p K^-) = \mathrm{A}_c e^{i\delta^c_{\Lambda_b^0}} = \mathrm{A}_{\Lambda_b^0} \tag{2.41}$$

$$\mathcal{A}(\overline{\Lambda}_b^0 \to \overline{D}^0 \overline{p} K^+) = \mathrm{A}_c e^{i\delta^c_{\Lambda_b^0}} = \mathrm{A}_{\Lambda_b^0} \tag{2.42}$$

$$\mathcal{A}(\Lambda_b^0 \to \overline{D}^0 p K^-) = \mathrm{A}_u e^{i(\delta^u_{\Lambda_b^0} - \gamma)} = \mathrm{A}_{\Lambda_b^0} r_{\Lambda_b^0} e^{i(\delta_{\Lambda_b^0} - \gamma)} \tag{2.43}$$

$$\mathcal{A}(\overline{\Lambda}_b^0 \to D^0 \overline{p} K^+) = \mathrm{A}_u e^{i(\delta^u_{\Lambda_b^0} + \gamma)} = \mathrm{A}_{\Lambda_b^0} r_{\Lambda_b^0} e^{i(\delta_{\Lambda_b^0} + \gamma)} \tag{2.44}$$

where $\delta_{\Lambda_b^0} = \delta^u_{\Lambda_b^0} - \delta^c_{\Lambda_b^0}$, and $r_{\Lambda_b^0} = \frac{\mathrm{A}_u}{\mathrm{A}_c}$. At first, amplitudes and widths will be computed considering the decay $\Lambda_b^0 \to \Lambda^* D^0$, with $\Lambda^* \to pK^-$, as it is the most sensitive region to γ. The formalism used, comes from the LS coupling, soon to be explained. The unpolarized partial decay rate of a particle of mass M in an initial state $|i\rangle$ decaying in some n-body final state $|f\rangle$ is given in its rest frame by [34]:

$$d\Gamma \approx \frac{(2\pi)^4}{2M} |\mathcal{M}|^2 d\Phi_n(P; p_1, p_2, ..., p_n) \tag{2.45}$$

where $d\Phi_n$ is an element of the n-body phase space and the matrix element $\mathcal{M}$ describes the amplitude of the process, where the squared of the amplitude gives the decay probability. For a three-body decay, the matrix serving this purpose is the helicity amplitude $\mathcal{A}_{\mathcal{M},\lambda_1,\lambda_2,\lambda_3}$ which is written via defined spin states $|i\rangle = |J, M\rangle$ and $|f\rangle = |\vec{p}_1, \vec{p}_2, \vec{p}_3; \lambda_1, \lambda_2, \lambda_3\rangle$. To take into account the possibility for the Λ_b^0 to be polarized and how this could possibly enter computations, the probability written above needs to be modified, as it is not suitable for particles described by a mixture of states. Calling $|\chi\rangle$ the mixed state, it can be written as a coherent sum of pure states $|e_i\rangle$ occurring with a statistical weights p_i (where $\sum_i p_i = 1$). The expectation value of an observable A can then be written as [35]

$$\langle A\rangle = \sum_i p_i \langle\chi_i| A |\chi_i\rangle = \sum_{j,k} \langle e_j| A |e_k\rangle \sum_i \langle e_k|\chi_i\rangle p_i \langle\chi_i|e_j\rangle = \sum_{j,k} a_{jk}\rho_{kj} \tag{2.46}$$

where $a_{jk} = \sum_{j,k} \langle e_j| A |e_k\rangle$ and $\rho_{kj} = \sum_i \langle e_k|\chi_i\rangle p_i \langle\chi_i|e_j\rangle$. It is easy to see that as it is defined, ρ_{kj} represents the density matrix. The diagonal elements ρ_{kk} represent the probability of finding the system in a pure state $|e_k\rangle$, so that the expectation value of A can be written as

$$\langle A\rangle = \sum_{j,k} a_{ij}\rho_{kj} = \mathrm{Tr}(A\rho) \tag{2.47}$$

Therefore, the spin orientation of an ensemble of spin j particles is described by a $(2j+1)(2j+1)$ density matrix containing $(2j+1)^2-1$ independent real parameters, with $|e_i\rangle = |s,m\rangle$. In the case presented in this note, i.e. $\Lambda_b^0 \to D^0 pK^-$, $j=\frac{1}{2}$ hence ρ is a 2×2 matrix parametrized by 3 real numbers. The most general way to write ρ is using the Pauli matrices σ_i and the identity matrix $\mathcal{I}$ is

$$\rho = \frac{1}{2}(\mathcal{I} + \vec{P}\cdot\vec{\sigma}) = \begin{bmatrix} \rho_{\frac{1}{2},\frac{1}{2}} & \rho_{\frac{1}{2},-\frac{1}{2}} \\ \rho_{-\frac{1}{2},\frac{1}{2}} & \rho_{-\frac{1}{2},-\frac{1}{2}} \end{bmatrix} = \frac{1}{2}\begin{bmatrix} 1+P_z & P_x - iP_y \\ P_x + iP_y & 1-P_z \end{bmatrix} \tag{2.48}$$

Inverting the equation and using the properties of Pauli matrices, $\vec{P}$ is obtained:

$$\vec{P} = \mathrm{Tr}(\rho\vec{\sigma}) \tag{2.49}$$

$\vec{P} = \{P_x, P_y, P_z\}$ is the polarization vector representing the degree and direction of the state's spin orientation. The condition $\mathrm{tr}(\rho^2) \leq 1$ ensures that $|\vec{P}| \leq 1$. A pure state corresponds to a state fully polarized with $P = \pm 1$. Introducing the spin density matrix, the decay width becomes:

$$d\Gamma(\Omega) \propto \sum_{\{\lambda_i\}} \sum_{m,m'} \rho_{m,m'} \mathcal{A}_{m,\lambda_1,\lambda_2,\lambda_3} \mathcal{A}^*_{m',\lambda_1,\lambda_2,\lambda_3} \tag{2.50}$$

where Ω describes the phase space, and m is the spin projection along the polarization axis, i.e. z.

Partial amplitude for $\Lambda_b^0 \to [pK^-]_{\Lambda^*} D^0$ The parameters characterizing this decay chain are

- $s_R = s_{\Lambda^*}$
- $\lambda_R = \lambda_{\Lambda^*}$
- $\lambda_1 = \lambda_p = \pm\frac{1}{2}$
- $\lambda_2 = \lambda_{K^-} = 0$
- $\lambda_3 = \lambda_{D^0} = 0$
- $J = J_{\Lambda_b^0} = \frac{1}{2}$

By s, we call the spin of the particle, by λ, the helicity, and finally J is the total angular momentum. Then we can substitute these parameters into the two-body decay amplitude formula, which from a generic form

$$\begin{aligned} \mathcal{A}_{M,\lambda_1,\lambda_2,\lambda_3}(a \to 1+2+3) = \sum_{\lambda_1} & D^{*J}_{M,\lambda_R-\lambda_3}(\phi_1,\theta_1,-\phi_1) D^{*s_R}_{\lambda_R,\lambda_1-\lambda_2}(\phi_3,\theta_3,-\phi_3)\times \\ & \times H^{a\to R,3}_{\lambda_R,\lambda_3} H^{R\to 1,2}_{\lambda_1,\lambda_2}, \end{aligned} \tag{2.51}$$

where $H^{a\to R,3}_{\lambda_R,\lambda_3}$ are the helicity couplings for the decay of the mother particle to the resonance R and $H^{R\to 1,2}_{\lambda_1,\lambda_2}$ the one for the decay of the resonance R to its decay products, becomes

$$\begin{aligned} \mathcal{A}_{m,\lambda_p} = B_{\Lambda^*}(M_{pK}) \times \sum_{s_{\Lambda^*}} \sum_{\lambda_{\Lambda^*}} & D^{s_{\Lambda^*}}_{\lambda_{\Lambda^*},\lambda_p}(\phi'_p,\theta'_p,-\phi'_p) D^{\frac{1}{2}*}_{m,\lambda_{\Lambda^*}}(\phi_{\Lambda^*},\theta_{\Lambda^*},-\phi_{\Lambda^*})\times \\ & \times H^{\Lambda^*\to pK^-}_{\lambda_p,\lambda_{K^-}} H^{\Lambda_b^0\to\Lambda^* D^0}_{\lambda_{\Lambda^*},\lambda_{D^0}} \end{aligned} \tag{2.52}$$

where the factor $B_{\Lambda^*}(M_{pK})$ is the relativistic Breit-Wigner function for Λ^*. Fundamental to the description of the amplitude is the D-matrix, rotation matrices and representations of the SU(2) group. These are defined as $D^j_{m',m}(\alpha,\beta,\gamma) = \langle jm'|e^{-i\alpha J_z}e^{-i\beta J_y}e^{-i\gamma J_z}|jm\rangle = e^{-i\alpha m'}d^j_{m',m}(\beta)e^{-i\gamma m}$, where $d^j_{m',m}(\beta)$ are the Wigner d-matrix elements. The angles are computed each time in the rest frame of the decaying particle, thus θ_1 and ϕ_1 are computed in the rest frame reached from the laboratory frame and θ_3 and ϕ_3 are computed in the *R* rest frame reached from the *a* rest frame. The most general formula, runs over all the possible Λ^* resonances, to simplify the computation, we are considering only the major contribution $\Lambda(1520)$. Some considerations follow: the projection of the total angular momentum of the $D^0\Lambda^0_b$ system on the axis defined by the momentum of D^0 is $\lambda_{\Lambda^*} - \lambda_{D^0} = \lambda_{\Lambda^*}$ (the projection of the orbital angular momentum is 0). Here again, since the total angular momentum $J_{\Lambda^0_b} = \frac{1}{2}$ is conserved, the projection λ_{Λ^*} can only take the values $+\frac{1}{2}$ or $-\frac{1}{2}$, whatever the value of $J_{\Lambda^0_b}$ is. This reduces the number of allowed terms in Equation 2.52. Furthermore, considering the parity conservation in the strong decay $\Lambda^* \to pK^-$, it is possible to reduce the number of allowed couplings

$$\begin{aligned} H^{\Lambda^*\to pK^-}_{\lambda_p,\lambda_{K^-}} &= \eta_{\Lambda^*}\eta_p\eta_{K^-}(-1)^{s_p+s_{K^-}-s_{\Lambda^*}}H^{\Lambda^*\to pK^-}_{-\lambda_p,-\lambda_{K^-}}(-1)^{2\lambda_{K^-}} \\ &= \eta_{\Lambda^*}(-1)^{\frac{3}{2}-s_{\Lambda^*}}H^{\Lambda^*\to pK^-}_{-\lambda_p,-\lambda_{K^-}} \end{aligned} \tag{2.53}$$

where $\eta_{K^-} = -1$ and $\eta_p = 1$, calling η the eigenvalues of the parity operator. The conclusion arising from this computation is $H^{\Lambda^*\to pK^-}_{\lambda_p,0} = \pm H^{\Lambda^*\to pK^-}_{-\lambda_p,0}$, where the sign is determined by the spin of the resonance. In the following table, the allowed couplings are reported.

		λ_{Λ^*}	
		$\frac{1}{2}$	$-\frac{1}{2}$
λ_p	$\frac{1}{2}$	$H^{\Lambda^*\to pK^-}_{\frac{1}{2},0}H^{\Lambda^0_b\to\Lambda^*D^0}_{\frac{1}{2},0} \equiv G_1$	$H^{\Lambda^*\to pK^-}_{\frac{1}{2},0}H^{\Lambda^0_b\to\Lambda^*D^0}_{-\frac{1}{2},0} \equiv G_2$
	$-\frac{1}{2}$	$\pm H^{\Lambda^*\to pK^-}_{\frac{1}{2},0}H^{\Lambda^0_b\to\Lambda^*D^0}_{\frac{1}{2},0} \equiv \pm G_1$	$\pm H^{\Lambda^*\to pK^-}_{\frac{1}{2},0}H^{\Lambda^0_b\to\Lambda^*D^0}_{-\frac{1}{2},0} \equiv \pm G_2$

A remark is needed, the way helicity couplings are defined depends on the specific convention adopted for the phase of the second particle of the decay. When using the so-called no-phase convention, the helicity couplings are denoted by capital H, whereas for the convention that includes the phase of particle 2, they are denoted by lowercase h. The relationship between these two sets of couplings is described as follows:

$$h^{R\to j}_{\lambda_i,\lambda_j} = H^{(j)}_{\lambda_i,\lambda_j}(-1)^{j-\lambda_j}, \quad h^{a\to R,k}_{\lambda_R,\lambda_k} = H^{a\to(j),k}_{\lambda_R,\lambda_k}(-1)^{j_k-\lambda_k} \tag{2.54}$$

One can derive amplitudes with the Partial Wave (PW) basis, which automatically includes parity conservation. It is possible to pass from the helicity basis to the PW basis through the relation

$$\begin{aligned} h^{a\to R,3}_{\lambda_R,\lambda_3} = \sum_{S=|J_R-J_3|}^{J_R+J_3}\sum_{J=|L-S|}^{|L+S|} h^{a\to R,3}_{LS}\sqrt{\frac{2L+1}{2J+1}}\langle j_R,\lambda_R;j_3,-\lambda_3|S,\lambda_R-\lambda_3\rangle\times \\ \times\langle L,0;S,\lambda_R-\lambda_3|J,\lambda_R-\lambda_3\rangle \end{aligned} \tag{2.55}$$

where the first Clebsch-Gordan coefficient is for the coupling of j_R and j_3 to a spin S which is the total spin of the system (J_RJ_3) and the second one for the coupling of L and S to the total angular momentum $J = J_R + J_3$. The same relation holds for the isobars. This relation, gives us the tools to rewrite the couplings of Λ_b^0 decay to the Λ^* resonances in the *LS* basis separating the parity conserving and the parity violating part. Recalling Eq. 2.55, in this case the parameters assume the values of $J_3 = J_{D^0} = 0$, the spins of the system $(\Lambda^* D^0)$ can only be $S = S_{\Lambda^*}$ and since $J = \frac{1}{2}$ by conservation of the total angular momentum, L is constrained by $|\frac{1}{2} - S_{\Lambda^*}| < L < |\frac{1}{2} + S_{\Lambda^*}|$, thus

$$\begin{aligned} h_{\lambda_{\Lambda^*},\lambda_{D^0}}^{\Lambda_b^0 \to \Lambda^* D^0} &= \sum_{L=|\frac{1}{2}-S_{\Lambda^*}|}^{|\frac{1}{2}+S_{\Lambda^*}|} h_{LS}^{\Lambda_b^0 \to \Lambda^* D^0} \sqrt{\frac{2L+1}{2}} \langle j_R, \lambda_R; 0, 0 | S_{\Lambda^*}, \lambda_{\Lambda^*} \rangle \times \\ &\qquad \times \langle L, 0; S_{\Lambda^*}, \lambda_{\Lambda^*} | J = \frac{1}{2}, \lambda_{\Lambda^*} \rangle \end{aligned} \tag{2.56}$$

where $\sqrt{\frac{2L+1}{2}} \langle j_R, \lambda_R; 0, 0 | S_{\Lambda^*}, \lambda_{\Lambda^*} \rangle$ is a constant term and λ_{Λ^*} can only take values $\pm\frac{1}{2}$

$$\langle L, 0; S_{\Lambda^*}, \lambda_{\Lambda^*} \mid J = \frac{1}{2}, \lambda_{\Lambda^*} \rangle = F_{L,S_{\Lambda^*},\lambda_{\Lambda^*}}, \tag{2.57}$$

$$\sqrt{\frac{2L+1}{2}} \langle j_R, \lambda_R; 0, 0 | S_{\Lambda^*}, \lambda_{\Lambda^*} \rangle = e_L, \tag{2.58}$$

then the decomposition would look like

$$h_{\lambda_{\Lambda^*},\lambda_{D^0}}^{\Lambda_b^0 \to \Lambda^* D^0} = \sum_L h_{LS}^{\Lambda_b^0 \to \Lambda^* D^0} \times F_{L,S_{\Lambda^*},\lambda_{\Lambda^*}} e_L. \tag{2.59}$$

It implies a sum over all possible waves, $S(L=0), P(L=1), ...$, weighted by the Clebsch-Gordan coefficients $F_{L,S_{\Lambda^*},\lambda_{\Lambda^*}}$. Following the parity conservation relation

$$\eta_{\Lambda_b^0} = \eta_{\Lambda^*} \eta_{D^0} (-1)^L = \eta_{\Lambda^*} (-1)^{L+1} \tag{2.60}$$

it is possible to identify which values of L correspond to parity violating and parity conserving couplings.

As an example, we continue the computation for $\Lambda(1520)$, which we know has $J^P = \frac{3}{2}^-$. Even L corresponds to the parity conserving (PC) couplings, odd L to parity violating (PV) ones. The possible values for the orbital angular momentum are $L = 1, 2$, which implies as possible Clebsch-Gordan coefficients: $C_{1,3/2,\pm 1/2} = -\sqrt{1/3}$ and $C_{2,3/2,\pm 1/2} = \pm\sqrt{1/5}$.

$$\begin{aligned} h_{\lambda_{\Lambda^*},0}^{\Lambda_+^+ \to \Lambda^* D^0} &= \sqrt{2} \left(h_{1,3/2}^{\Lambda_b^0 \to \Lambda^* D^0} \times C_{1,3/2,\lambda_{\Lambda^*}} + h_{2,3/2}^{\Lambda_b^0 \to \Lambda^* D^0} \times C_{2,3/2,\lambda_{\Lambda^*}} \right) = \\ &= \sqrt{\frac{3}{2}} \left(h_{1,3/2}^{\Lambda_b^0 \to \Lambda^* D^0} \left(-\sqrt{\frac{1}{3}} \right) + \sqrt{\frac{5}{2}} h_{2,3/2}^{\Lambda_b^0 \to \Lambda^* D^0} \left(\pm\sqrt{\frac{1}{5}} \right) \right). \end{aligned} \tag{2.61}$$

Defining $h_{\text{PC}}^{\Lambda^*} \equiv h_{2,3/2}^{\Lambda_b^0 \to \Lambda^* D^0}$ and $h_{\text{PV}}^{\Lambda^*} \equiv h_{1,3/2}^{\Lambda_b^0 \to \Lambda^* D^0}$, one obtains:

$$\begin{cases} h_{\frac{1}{2},0}^{\Lambda_b^0 \to \Lambda^* D^0} &= -\sqrt{\frac{1}{2}} \left(h_{\text{PC}}^{\Lambda^*} + h_{\text{PV}}^{\Lambda^*} \right) \\ h_{-\frac{1}{2},0}^{\Lambda_b^0 \to \Lambda^* D^0} &= -\sqrt{\frac{1}{2}} \left(h_{\text{PC}}^{\Lambda^*} - h_{\text{PV}}^{\Lambda^*} \right) \end{cases} \tag{2.62}$$

Coming back to definition of total decay width, this can be written, taking into account the density matrix, as

$$\begin{aligned}\Gamma =&\rho_{\frac{1}{2},\frac{1}{2}}\left(\left|\mathcal{A}_{\frac{1}{2},\frac{1}{2}}\right|^2+\left|\mathcal{A}_{\frac{1}{2},-\frac{1}{2}}\right|^2\right)\\&+\rho_{\frac{1}{2},-\frac{1}{2}}\left(\mathcal{A}_{\frac{1}{2},\frac{1}{2}}\mathcal{A}^*_{-\frac{1}{2},\frac{1}{2}}+\mathcal{A}_{\frac{1}{2},-\frac{1}{2}}\mathcal{A}^*_{-\frac{1}{2},-\frac{1}{2}}\right)\\&+\rho_{-\frac{1}{2},\frac{1}{2}}\left(\mathcal{A}_{-\frac{1}{2},\frac{1}{2}}\mathcal{A}^*_{\frac{1}{2},\frac{1}{2}}+\mathcal{A}_{-\frac{1}{2},-\frac{1}{2}}\mathcal{A}^*_{\frac{1}{2},-\frac{1}{2}}\right)\\&+\rho_{-\frac{1}{2},-\frac{1}{2}}\left(\left|\mathcal{A}_{-\frac{1}{2},\frac{1}{2}}\right|^2+\left|\mathcal{A}_{-\frac{1}{2},-\frac{1}{2}}\right|^2\right)\end{aligned} \tag{2.63}$$

and by applying parity conservation for the production of Λ_b^0 which is done via strong interactions (contribution of the production via weak interactions is negligible, 0.1%), the cross terms $\rho_{\frac{1}{2},+\frac{1}{2}}(...)$ and $\rho_{-\frac{1}{2},\frac{1}{2}}(...)$ are zero. The final differential rate for the $\Lambda_b^0 \to \Lambda^* D^0$ decay is:

$$d\Gamma \propto (1+P_z)\left(\left|\mathcal{A}_{\frac{1}{2},\frac{1}{2}}\right|^2+\left|\mathcal{A}_{\frac{1}{2},-\frac{1}{2}}\right|^2\right)+(1-P_z)\left(\left|\mathcal{A}_{-\frac{1}{2},\frac{1}{2}}\right|^2+\left|\mathcal{A}_{-\frac{1}{2},-\frac{1}{2}}\right|^2\right). \tag{2.64}$$

Using the $D(\phi,\theta,0)$ convention, we can write the amplitudes as

$$\mathcal{A}^{\Lambda^*}_{m,\lambda_p}=B_{\Lambda^*}\left(M_{pK}\right)\times\sum_{\Lambda^*}\sum_{\lambda_{\Lambda^*}}D^{s_{\Lambda^*}}_{\lambda_{\Lambda^*},\lambda_p}\left(\phi'_p,\theta'_p,0\right)D^{\frac{1}{2}*}_{m,\lambda_{\Lambda^*}}\left(\phi_{\Lambda^*},\theta_{\Lambda^*},0\right)H^{\Lambda^*\to pK^-}_{\lambda_p,\lambda_{K^-}}H^{\Lambda_b^0\to D^0\Lambda^*}_{\lambda_{\Lambda^*},\lambda_{D^0}} \tag{2.65}$$

Assuming we will then integrate on ϕ and θ, we focus on the dependency of $\mathcal{A}^{\Lambda^*}_{m,\lambda_p}$ on the helicity couplings.

$$\begin{aligned}&(1+P_z)\left(\left|\mathcal{A}_{\frac{1}{2},\frac{1}{2}}\right|^2+\left|\mathcal{A}_{\frac{1}{2},-\frac{1}{2}}\right|^2\right)+(1-P_z)\left(\left|\mathcal{A}_{-\frac{1}{2},\frac{1}{2}}\right|^2+\left|\mathcal{A}_{-\frac{1}{2},-\frac{1}{2}}\right|^2\right)\\&=(1+P_z)\left(\left|H^{\Lambda^*\to pK^-}_{\frac{1}{2},0}H^{\Lambda_b^0\to D^0\Lambda^*}_{\frac{1}{2},0}+H^{\Lambda^*\to pK^-}_{\frac{1}{2},0}H^{\Lambda_b^0\to D^0\Lambda^*}_{-\frac{1}{2},0}\right|^2+\right.\\&\left.+\left|\pm H^{\Lambda^*\to pK^-}_{-\frac{1}{2},0}H^{\Lambda_b^0\to D^0\Lambda^*}_{\frac{1}{2},0}\pm H^{\Lambda^*\to pK^-}_{-\frac{1}{2},0}H^{\Lambda_b^0\to D^0\Lambda^*}_{-\frac{1}{2},0}\right|^2\right)+\\&+(1-P_z)\left(\left|H^{\Lambda^*\to pK^-}_{\frac{1}{2},0}H^{\Lambda_b^0\to D^0\Lambda^*}_{\frac{1}{2},0}+H^{\Lambda^*\to pK^-}_{\frac{1}{2},0}H^{\Lambda_b^0\to D^0\Lambda^*}_{-\frac{1}{2},0}\right|^2+\right.\\&\left.+\left|\pm H^{\Lambda^*\to pK^-}_{-\frac{1}{2},0}H^{\Lambda_b^0\to D^0\Lambda^*}_{\frac{1}{2},0}\pm H^{\Lambda^*\to pK^-}_{-\frac{1}{2},0}H^{\Lambda_b^0\to D^0\Lambda^*}_{-\frac{1}{2},0}\right|^2\right)\\&=(1+P_z)\left(\left|G_1+G_2\right|^2+\left|\pm G_1\pm G_2\right|^2\right)+(1-P_z)\left(\left|G_1+G_2\right|^2+\left|\pm G_1\pm G_2\right|^2\right)\\&=2\left(\left|G_1+G_2\right|^2+\left|\pm G_1\pm G_2\right|^2\right)=4\left|G_1+G_2\right|^2\\&=4\left|H^{\Lambda^*\to pK^-}_{\frac{1}{2},0}H^{\Lambda_b^0\to D^0\Lambda^*}_{\frac{1}{2},0}+H^{\Lambda^*\to pK^-}_{\frac{1}{2},0}H^{\Lambda_b^0\to D^0\Lambda^*}_{-\frac{1}{2},0}\right|^2=\mathrm{A}_{\Lambda_b^0}.\end{aligned} \tag{2.66}$$

The result is obtained by applying the parity conservation and the equalities shown above. The computation continues checking the interferences between the amplitudes

$$\begin{aligned}
&(1+P_z)\left(\left|\mathcal{A}_{\frac{1}{2},\frac{1}{2}}\right|^2+\left|\mathcal{A}_{\frac{1}{2},-\frac{1}{2}}\right|^2\right)+(1-P_z)\left(\left|\mathcal{A}_{-\frac{1}{2},\frac{1}{2}}\right|^2+\left|\mathcal{A}_{-\frac{1}{2},-\frac{1}{2}}\right|^2\right)\\
&=(1+P_z)\left(\left|(G_1+G_2)\left(1+r_{\Lambda_b^0}e^{i(\delta_{\Lambda_b^0}+\gamma)}\right)\right|^2+\left|(\pm G_1\pm G_2)\left(1+r_{\Lambda_b^0}e^{i(\delta_{\Lambda_b^0}+\gamma)}\right)\right|^2\right)+\\
&+(1-P_z)\left(\left|(G_1+G_2)\left(1+r_{\Lambda_b^0}e^{i(\delta_{\Lambda_b^0}+\gamma)}\right)\right|^2+\left|(\pm G_1\pm G_2)\left(1+r_{\Lambda_b^0}e^{i(\delta_{\Lambda_b^0}+\gamma)}\right)\right|^2\right)\\
&=2\left(\left|(G_1+G_2)\left(1+r_{\Lambda_b^0}e^{i(\delta_{\Lambda_b^0}+\gamma)}\right)\right|^2+\left|(\pm G_1\pm G_2)\left(1+r_{\Lambda_b^0}e^{i(\delta_{\Lambda_b^0}+\gamma)}\right)\right|^2\right).
\end{aligned}\tag{2.67}$$

Considering that G_1 and G_2 are composed of a real and an imaginary part, denoted from here on with the subscripts r and i, it is possible to rewrite $G_n = G_{nr} + iG_{ni}$, then the first addendum of the last line in the equation above becomes

$$\begin{aligned}
&\left|(G_1+G_2)\left(1+r_{\Lambda_b^0}e^{i(\delta_{\Lambda_b^0}+\gamma)}\right)\right|^2\\
&=\left|(G_{1r}+G_{2r}+i(G_{1i}+G_{2i}))\left(1+r_{\Lambda_b^0}\cos(\delta_{\Lambda_b^0}+\gamma)+ir_{\Lambda_b^0}\sin(\delta_{\Lambda_b^0}+\gamma)\right)\right|^2\\
&=|\,(G_{1r}+G_{2r})\,(1+r_{\Lambda_b^0}\cos(\delta_{\Lambda_b^0}+\gamma))-(G_{1i}+G_{2i})\,r_{\Lambda_b^0}\sin(\delta_{\Lambda_b^0}+\gamma)+\\
&+i\,(G_{1i}+G_{2i})\,(1+r_{\Lambda_b^0}\cos(\delta_{\Lambda_b^0}+\gamma))+i\,(G_{1r}+G_{2r})\,r_{\Lambda_b^0}\sin(\delta_{\Lambda_b^0}+\gamma)|^2\\
&=(G_{1r}+G_{2r})^2\,(1+r_{\Lambda_b^0}\cos(\delta_{\Lambda_b^0}+\gamma))^2+(G_{1i}+G_{2i})^2\,r^2_{\Lambda_b^0}\sin^2(\delta_{\Lambda_b^0}+\gamma)+\\
&+(G_{1i}+G_{2i})^2\,(1+r_{\Lambda_b^0}\cos(\delta_{\Lambda_b^0}+\gamma))^2+(G_{1r}+G_{2r})^2\,r^2_{\Lambda_b^0}\sin^2(\delta_{\Lambda_b^0}+\gamma)\\
&=|G_1+G_2|^2\left[(1+r_{\Lambda_b^0}\cos(\delta_{\Lambda_b^0}+\gamma))^2+r^2_{\Lambda_b^0}\sin^2(\delta_{\Lambda_b^0}+\gamma)\right]\\
&=|G_1+G_2|^2\left[1+r^2_{\Lambda_b^0}+2r_{\Lambda_b^0}\cos(\delta_{\Lambda_b^0}+\gamma)\right].
\end{aligned}\tag{2.68}$$

The result for the second addendum is the same, so that the final result is

$$\begin{aligned}
\Gamma(\Lambda_b^0\to D_{CP}\Lambda^*)&\propto(1+P_z)\left(\left|\mathcal{A}_{\frac{1}{2},\frac{1}{2}}\right|^2+\left|\mathcal{A}_{\frac{1}{2},-\frac{1}{2}}\right|^2\right)+(1-P_z)\left(\left|\mathcal{A}_{-\frac{1}{2},\frac{1}{2}}\right|^2+\left|\mathcal{A}_{-\frac{1}{2},-\frac{1}{2}}\right|^2\right)\\
&=4\,|G_1+G_2|^2\left[1+r^2_{\Lambda_b^0}+2r_{\Lambda_b^0}\cos(\delta_{\Lambda_b^0}+\gamma)\right]=\mathrm{A}_{\Lambda_b^0}\left[1+r^2_{\Lambda_b^0}+2r_{\Lambda_b^0}\cos(\delta_{\Lambda_b^0}+\gamma)\right].
\end{aligned}\tag{2.69}$$

It is possible to compute the amplitude for the $\overline{\Lambda}_b^0$ decays in the same way, obtaining

$$\Gamma(\overline{\Lambda}_b^0\to D_{CP}\overline{\Lambda}^*)\propto\mathrm{A}_{\Lambda_b^0}\left[1+r^2_{\Lambda_b^0}+2r_{\Lambda_b^0}\cos(\delta_{\Lambda_b^0}-\gamma)\right].\tag{2.70}$$

It follows then, the computation for the observables of the measurement we are aiming to perform

$$\begin{aligned}
\mathrm{A}_{CP}&=\frac{\Gamma(\Lambda_b^0\to D_{CP}\Lambda^*)-\Gamma(\overline{\Lambda}_b^0\to D_{CP}\overline{\Lambda}^*)}{\Gamma(\Lambda_b^0\to D_{CP}\Lambda^*)+\Gamma(\overline{\Lambda}_b^0\to D_{CP}\overline{\Lambda}^*)}\\
&=\frac{\mathrm{A}_{\Lambda_b^0}\left[1+r^2_{\Lambda_b^0}+2r_{\Lambda_b^0}\cos(\delta_{\Lambda_b^0}+\gamma)\right]-\mathrm{A}_{\Lambda_b^0}\left[1+r^2_{\Lambda_b^0}+2r_{\Lambda_b^0}\cos(\delta_{\Lambda_b^0}-\gamma)\right]}{\mathrm{A}_{\Lambda_b^0}\left[1+r^2_{\Lambda_b^0}+2r_{\Lambda_b^0}\cos(\delta_{\Lambda_b^0}+\gamma)\right]+\mathrm{A}_{\Lambda_b^0}\left[1+r^2_{\Lambda_b^0}+2r_{\Lambda_b^0}\cos(\delta_{\Lambda_b^0}-\gamma)\right]}\\
&=\frac{r_{\Lambda_b^0}\left(\cos(\delta_{\Lambda_b^0}+\gamma)-\cos(\delta_{\Lambda_b^0}-\gamma)\right)}{1+r^2_{\Lambda_b^0}+2r_{\Lambda_b^0}\cos(\delta_{\Lambda_b^0}+\gamma)+2r_{\Lambda_b^0}\cos(\delta_{\Lambda_b^0}-\gamma)}=\frac{2r_{\Lambda_b^0}\sin\delta_{\Lambda_b^0}\sin\gamma}{1+r^2_{\Lambda_b^0}+4r_{\Lambda_b^0}\cos\delta_{\Lambda_b^0}\cos\gamma}.
\end{aligned}\tag{2.71}$$

The results just shown allow to conclude that considering the yields of the decays and not its angular distributions, it will not be the absence of polarization the factor limiting the sensitivity of the study.

2.5 State of art of the measurements of the γ angle at LHCb

The angle γ is, up to now, uniquely determined using B meson decays, particularly those involving $B \to DK$, where D meson can manifest as D^0 or $\overline{D}^0$. Historically, experiments such as BaBar and Belle at the B-factories have extensively utilized various strategies, like the GLW, ADS, and GGSZ methods, meaning that several multi-body D final states have been looked at, to measure γ with significant precision. The GGSZ method [36], named after Giri, Grossman, Soffer, and Zupan, involves studying $B^{\pm} \to DK^{\pm}$ decays where the D meson decays to multi-body, self-conjugate final states such as $D \to K_S\pi^+\pi^-$. By analyzing the interference patterns in the Dalitz plot of the D decay, the GGSZ method allows for a precise determination of the weak phase γ, exploiting the rich information available from the phase-space distribution of the decay products. Parallel to this main branch, other studies focused on B meson decays but with vector mesons in their final states, such as D^* and K^*. These methods leverage the different final states of the D meson to extract γ amidst varying degrees of statistical and systematic uncertainties. For instance, the two most recent analyses that published a γ measurement within the LHCb collaboration are a binned phase-space analysis in $B^{\pm} \to D[\to K^{\mp}\pi^{\pm}\pi^{\pm}\pi^{\mp}]h^{\pm}$ decays within the GGSZ framework [37], and the study of the decays $B^{\pm} \to Dh^{\pm}$, using $D \to h^{\pm}h'^{\mp}\pi^0$ final states [38]. In 2022 LHCb updated its official value of γ [39] obtained as a combination of all the channels the collaboration has explored and the methods previously explained, but also combining the b-sector with the charm one. Specifically, charm mixing parameters, which describe oscillations between D^0 and $\overline{D}^0$ mesons, were included [40]. Collecting the data from Run 1 and Run 2 of the LHC, coming from *pp* collision from a center-of-mass energy of 7 TeV, up to a center-of-mass energy of 13 TeV, the value obtained is

$$\gamma = (64.6 \pm 2.8)^{\circ}, \tag{2.72}$$

modulo 180°. Predictions from theoretical groups such as the CKMfitter group ($\gamma = (66.23^{+0.60}_{-1.43})^{\circ}$) [41] and the UTfit collaboration ($\gamma = (65.1 \pm 1.3)^{\circ}$) [42] are in perfect agreement with the experimental determinations coming from the flavour physics experiments around the world. At the moment, LHCb is undergoing its Run 3, running a brand new detector and collecting data with a statistics five times bigger than what was achieved in Run 2. For this reason, the amount of Λ_b^0 decays is expected to be enough to measure the γ angle with several final states, not only its favoured ones. In principle, this baryon just has a d quark as a spectator and a $u\overline{u}$ pair generated in the vacuum more than the B meson, so with the same matrix elements, the sensitivity to the angle should be the same. The real advantage, anyway of analysing a three body decay, is the chance to perform an amplitude analysis, which is not possible with a two-body B meson decay. Keeping this in mind, the purpose of this thesis is to prepare the measurement of the γ angle using the $\Lambda_b^0 \to DpK^-$ decay, applying the GLW method, so in particular detecting and isolating the D^0 *CP* eigenstates $D^0 \to K^-K^+$ and $D^0 \to \pi^-\pi^+$.

3

The LHCb experiment at the LHC

3.1 The Large Hadron Collider

The Large Hadron Collider (LHC) [43] is the most powerful proton-proton collider to date. It is built across-Swiss and French territories at the CERN site in Geneva. It consists of an accelerator ring of 27 km installed in the pre-existing tunnel of the Large Electron-Positron collider at CERN (LEP) [44] machine in which protons or heavy ions as Pb are accelerated nearly up to the designed energy of 7 TeV per beam (or 2.8 TeV per heavy ion nucleon), and forced to collide in 4 specific points, where four experiments ALICE, ATLAS, CMS and LHCb have been placed. LHC was completed in 2008 and started working in 2009 with a center of mass energy $\sqrt{s}$ of 7 TeV from 2010 to 2011, 8 TeV during 2012 and up to 13 TeV during Run 2 (2015-2018). At the moment, the LHC is undergoing its Run 3, in which a luminosity of $2 \times 10^{33}\text{cm}^2\text{s}^{-1}$ is expected to be reached at $\sqrt{s}$ = 13.67 TeV.

3.1.1 The accelerator complex and LHC structure

The accelerator comprises two rings in which protons travel the separate beamlines in opposite directions. Their path is kept constant thanks to a strong magnetic field of 8.33 T: dipole magnets keep the particles in an almost circular orbit, and quadrupole magnets focus the beam. The magnets are superconductive, a condition necessary to obtain high currents, and because of that, they work at 1.9K temperature, which is achieved thanks to superfluid helium.
The entire CERN acceleration complex and LHC structure are shown in Figure 3.1 and explained in the following. To provide a first acceleration to the beam, protons and ions are accelerated in four steps by a set of linear and circular accelerators:

1. To begin, protons are extracted from hydrogen gas and speeded up to 50 MeV by LINAC 2 (LINear ACcelerator);
2. Later, they are accelerated up to 1.4 GeV by the Proton Synchrotron Booster (PSB);
3. Then, the Proton Synchrotron (PS) accelerates them up to 25 GeV;
4. The Super Proton Synchrotron (SPS) accomplishes the last step, where protons reach 450GeV of energy and are injected into the LHC.

The acceleration in the LHC relies on radiofrequency (RF) cavities, which increase the beam energy by around 500 keV at each turn and to avoid collision between hadrons and gas particles

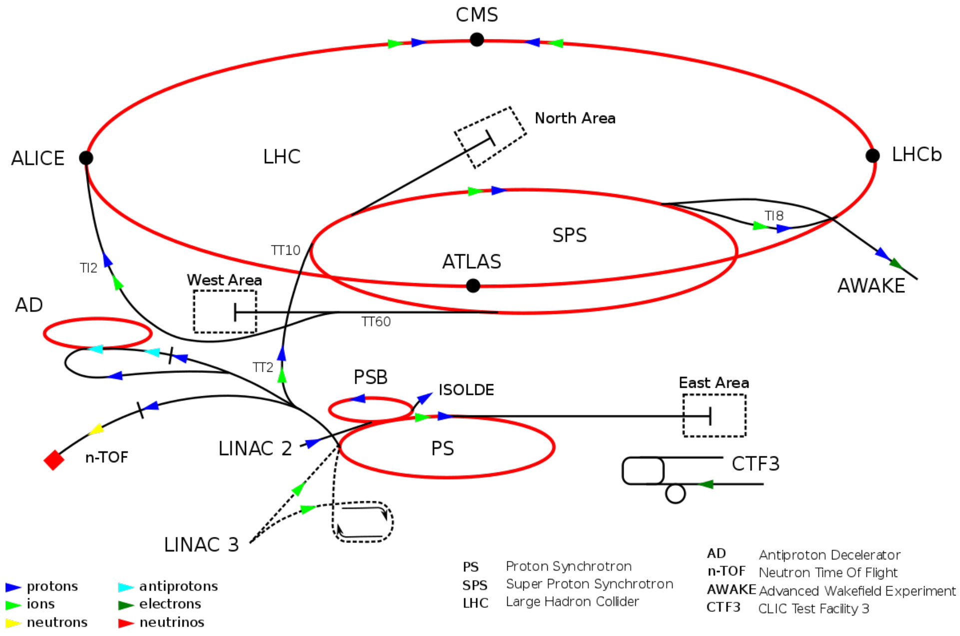

Figure 3.1: Accelerator complex at CERN and LHC structure

in the tubes, the vacuum has to be made in them down to a pressure of 10^{-13} bar. As said before, four experiments are placed in the LHC, each one with a different purpose:

- LHCb (Large Hadron Collider beauty experiment) studies decays of B hadrons looking for CP violation sources beyond the Standard Model and rare decays. In recent years, it has developed a heavy ion program, too.
- ALICE (A Large Ion Collider Experiment) observes heavy-ion collisions and studies strong interactions in quark-gluon plasma.
- ATLAS (A Toroidal LHC ApparatuS) and CMS (Compact Muon Solenoid) are general-purpose detectors designed to cover a broad range of physics measurements in proton-proton and heavy-ion collisions to investigate the SM and search for new physics Beyond the SM (BSM).

3.1.2 *pp* interaction and luminosity

Proton-proton collisions at high energies are studied at the LHC experiments to validate the predictions of SM and to explore BSM physics. Collisions can be classified into two different types:

- Soft collisions: long distance interactions with low momentum transfer. The protons behave as elementary particles, and the internal structure is not involved in the process. Since the momentum transferred is low, the scatter angles are small. This type of collision has a small transverse momentum compared to the beam line.
- Hard collisions: short distance interactions in which quarks and gluons, the inner part of the protons, take part. They are characterized by a large transferred momentum, in this way high-mass particles are produced at large angles with respect to the beam line.

Hard collisions are looked at with interest in particle experiments, but they are rare and difficult to produce. Investigating these events requires both high beam energy and high beam intensities to observe the production of massive particles and increase the cross-section, but also to have a large number of events to study. Given these elements, it is important to introduce a quantity typical of particle experiments: luminosity. The instantaneous luminosity is defined as

$$\mathcal{L} = \frac{f_{\text{LHC}} n N_{\text{bunch}}^2}{A}, \tag{3.1}$$

where f_{LHC} is the accelerator frequency, n is the number of colliding bunches, N_{bunch} is the number of particles for each bunch and A is the beamline cross-section. In particular, the number of events for a given process per second generated in the LHC collisions is given by:

$$\frac{dN_{\text{event}}}{dt} = \mathcal{L}\sigma_{\text{event}}, \tag{3.2}$$

where σ_{event} is the cross-section of the process. The integrated luminosity is obtained with an integral with respect to the time of the instantaneous one, it is expressed in inverse cross-section units (e.g. fb^{-1}). A correct estimation of luminosity is an important ingredient for comparing the Monte Carlo simulations and the theoretical expectations.

3.1.3 Production of b-hadrons at the LHC

Among the many particles generated in high-energy collisions at the LHC, b-quarks are particularly interesting. Besides the hints already given in the first chapter, a more extensive overview follows below.

In the high-energy *pp* collisions at the LHC, parton interactions are the most probable, with b-quarks primarily produced through gluon fusion ($gg \to b\bar{b}$) and quark-antiquark annihilation ($q\bar{q} \to b\bar{b}$). The distinct momenta of the interacting partons, coupled with the significant difference between the LHC's center-of-mass energy and the b-quark mass, results in a boost of the produced b-quarks towards the forward or backward direction, tangential to the beam axis at the collision point. This boost is fundamental as it causes a more significant displacement of b- and c-hadron decay vertices, aiding their identification in the LHCb detector. Unlike the other detectors at the LHC, the LHCb detector is designed as a forward spectrometer. This unique geometry is specifically tailored to capture the forward-boosted b-hadrons produced at the LHC, allowing it to contain approximately 27% of the produced b or $\bar{b}$ quarks and 24% of the $b\bar{b}$ pairs despite its reduced solid angle. The $b\bar{b}$ cross-section as a function of the polar angles and pseudorapidities is shown in Figure 3.2. This design enables LHCb to access an uncommon phase space with a pseudorapidity range of $2 < \eta < 5$, where η is defined as $\eta = -\ln(\tan\frac{\theta}{2})$, and θ represents the polar angle relative to the beam axis. The forward acceptance of LHCb offers a unique vantage point compared to the general-purpose detectors, with only a small overlap in phase space. The so produced b-quarks hadronize to form B mesons (such as B^0, B^+, B_s^0, B_c^+) and b-baryons. The subsequent decays of these hadrons provide rich information about their production mechanisms and the dynamics of their decays. Studying these decays, particularly in the context of LHCb, allows for precise measurements of production cross-sections and differential distributions. These are key elements for testing pQCD predictions and refining parton distribution functions (PDFs).

The LHCb experiment's ability to identify and reconstruct b-hadron decays relies on advanced detector technologies and sophisticated data analysis techniques. The VErtex LOcator (VELO)

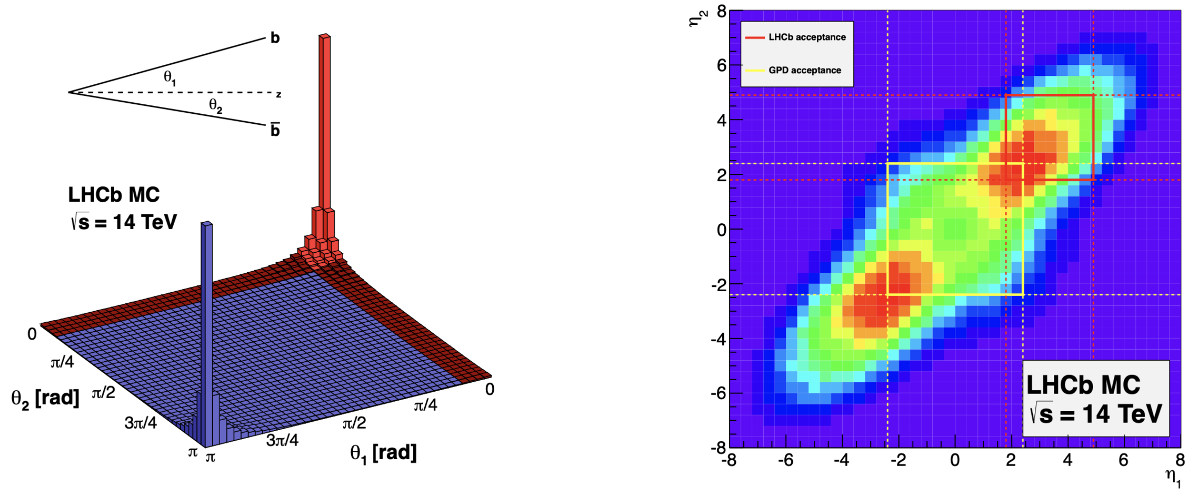

Figure 3.2: Left: production cross-section as a function of the polar angles of b and $\bar{b}$ with respect to the beam direction. Right: same cross-section as a function of the pseudorapidities. The yellow square delimits the ATLAS and CMS acceptance (General Purpose Detectors - ndr), while the red one the LHCb acceptance. The simulation uses PYTHIA8 [17] and CTEQ6 NLO parton density function.

is decisive in precisely reconstructing the decay vertices of b-hadrons, which typically occur at measurable distances of around 300–500 μm from the primary interaction point due to the relatively long lifetimes of B mesons. B mesons have lifetimes of the order of 1.5 picoseconds, allowing them to travel a few millimetres from the primary interaction point before decaying. This displacement is key to separating b-hadron decay vertices from the primary vertex, enabling accurate decay reconstruction and analysis. Additionally, particle identification systems, including the Ring Imaging Cherenkov (RICH) detectors, are essential for distinguishing between different particle species and accurately reconstructing decay products. These are only few of the detectors involved in the reconstruction of particles. LHCb has recently undergone an impressive update in both hardware and software due to the foreseen increase in the number of vertices per collision, expected to reach around five visible primary vertices per collision, as well as the increased center-of-mass energy in Run 3, which is now underway. In the following sections, the reader will find a description of the detector that has been running from 2011 until 2018 (Run 1 and Run 2) and the major changes that characterize the current detector, running from autumn 2022, other than some anticipations for Upgrade 2.

3.2 The LHCb Detector in Run 1 and Run 2

As mentioned before, LHCb is an experiment dedicated to flavour physics, whose primary goal is to look for indirect evidence of new physics in *CP* violation and rare decays of beauty and charm hadrons. It is equipped to separate particles based on their mass, momentum, and energy, as a series of specialized subdetectors is tailored to measure or assist in measuring these properties. The general layout of the detector is illustrated in Figure 3.3. The LHCb coordinate system is defined with its origin at the interaction point. The z-axis is aligned along the beam direction, extending from the interaction point toward the muon stations. The y-axis is vertical, perpendicular to the LHC plane, pointing upward at the surface. The x-axis, combined with the other two, forms a right-handed coordinate system. b-hadrons and other unstable particles are re-

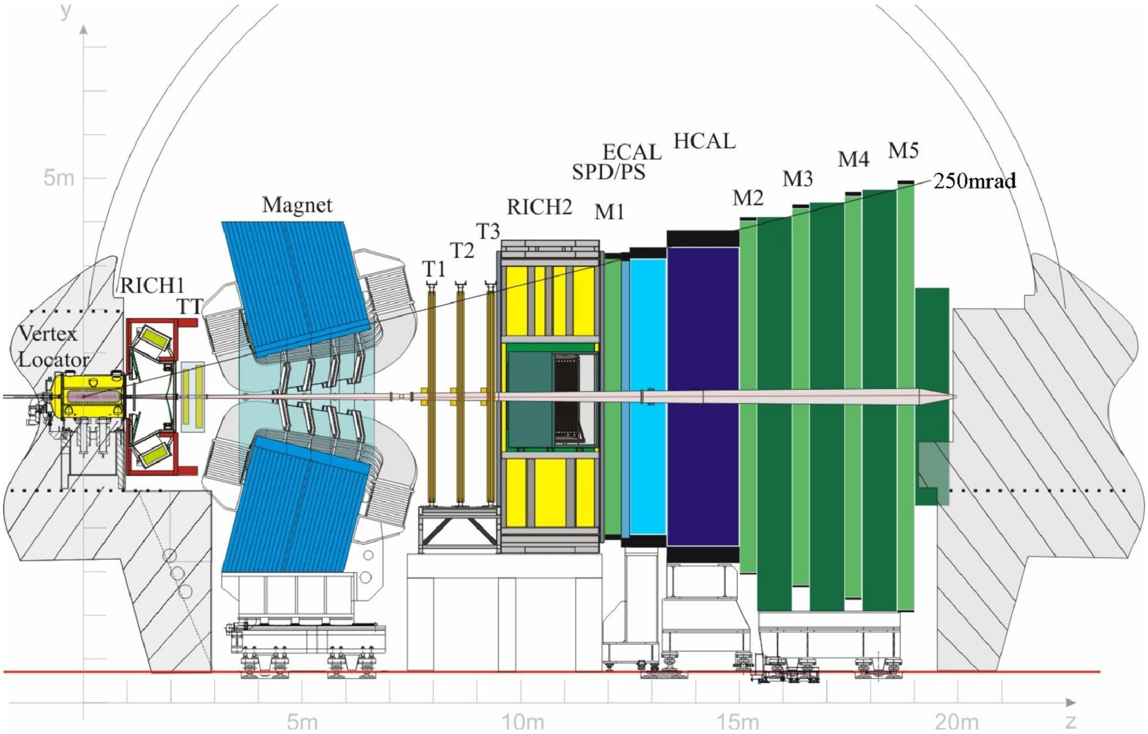

Figure 3.3: Side view of the LHCb detector [45].

constructed using their decay products, primarily charged leptons, hadrons, and photons. Some particles, like muons, traverse the entire detector and interact with almost all subdetectors. Others, termed "stable" particles within LHCb terminology, travel through most of the detector but are stopped before the end. These include charged pions ($\pi^{\pm}$), charged kaons ($K^{\pm}$), protons (p, $\bar{p}$), electrons ($e^{\pm}$), muons ($\mu^{\pm}$), and photons (γ). "Unstable" particles, which have short lifetimes and decay before crossing the detector, are detected only through their decay products. Among the unstable particles, some hadrons such as K^0, Λ, and Ξ^- have longer lifetimes and traverse some detectors before decaying; these are classified as "long-lived." Neutrinos, however, are not directly reconstructed in LHCb.

To provide a broad overview of the detector's design, the sequence of subdetectors is outlined here, with detailed descriptions provided in subsequent sections. Collisions occur within the VELO, a highly precise tracking detector that measures vertex coordinates near the interaction point. VELO is crucial for distinguishing between prompt particles (produced directly at the primary vertex) and secondary particles (resulting from displaced decays of other particles). This distinction is made using the Impact Parameter (IP), defined as the transverse Distance Of Closest Approach (DOCA) between the particle's trajectory and the vertex. The tracking system is further enhanced by two additional tracking detectors: the Tracker Turicensis (TT) located upstream of the dipole magnet, and three tracking stations (T1-T3) situated downstream of the magnet. The dipole magnet bends the paths of charged particles, allowing the determination of their charge sign and momentum through the curvature of their tracks. Charged particle identification is performed by two Ring Imaging CHerenkov Detectors (RICH1 and RICH2), positioned upstream and downstream of the magnet, respectively. These detectors utilize Cherenkov radiation to identify particles by measuring the angle of emitted light as particles pass through a medium at speeds exceeding the speed of light in that medium. Energy measurements are provided by two calorimeters: the Electromagnetic CALorimeter (ECAL) and the Hadronic CALorimeter (HCAL). These calorimeters also contribute to the Level-0 hardware trigger, which is essential for initial event selection. At the end of the detector, the muon detection system comprises muon chambers (M2-M5), with an additional station (M1) placed before the ECAL. As it could be understood by its name, this system is designed to identify muons. Detailed descriptions are following.

3.2.1 Tracking system

Tracking detectors are indispensable for measuring b- and c-hadron decays, as they provide the precise positions of primary and secondary vertices. The distance between these vertices can be expressed as flight distance or decay time, enabling efficient triggering on such decays and suppression of background noise. Additionally, charged particle tracks allow for momentum measurements through the curvature of their paths in a magnetic field, which, in the LHCb detector, is provided by a dipole magnet. The principle behind tracking detectors is based on the interaction of charged particles with the detector material, depositing energy in the sensitive layers, referred to as "hits". Tracking algorithms are optimized to identify patterns of hits from the same particle, reconstructing them into tracks. The VELO is the closest tracking detector to the pp interaction region, which provides vertex information to identify unstable particles. Long-lived particles may decay outside the VELO, necessitating hits from other tracking detectors for precise momentum measurements of stable charged particles and reconstruction of long-lived particle decays. The TT, located in front of the magnet, and the three tracking stations (T1-T3) positioned just after the magnet, complement the VELO in this task. Depending on their length, tracks are classified into several categories: long tracks, which have hits in both the VELO and the T1-T3 stations; downstream tracks, which have hits in the tracking system excluding the VELO; upstream tracks, which have hits in the VELO and TT but not in T1-T3; VELO tracks, which only have hits in the VELO; and T tracks, which are measured only in the T stations and typically result from secondary interactions. A representation of the just described tracks is reported in Figure 3.4. Long-tracks are preferred in physics analyses due to their superior momentum resolution, as long-tracks achieve a momentum resolution of around 0.5% for high-momentum particles, whereas downstream tracks have a resolution closer to 1%, and upstream tracks are typically less precise, with a resolution of approximately 1.5%. Downstream tracks are often used for analyzing long-lived particles, while VELO tracks are crucial for reconstructing the primary vertex (PV). If a particle is reconstructed more than once with different track types, the track traversing the most subdetectors is chosen. The number of unique long tracks in an event, nTracks, serves as a measure of event multiplicity.

VErtex LOcator

VELO [45] provides precise measurements of the track coordinates close to the interaction point, enabling the distinction between secondary displaced vertices and prompt vertices with exceptional accuracy. This detector is constructed from a series of silicon strip modules arranged along the beam direction. These modules are designed to measure either the radial (r) or azimuthal (ϕ) coordinates of particle tracks. The r-sensors measure the radial distance with circularly arranged strips, while ϕ-sensors determine the azimuthal angle with radially aligned strips. The third spatial coordinate is inferred from the known positions of these sensor planes. The high

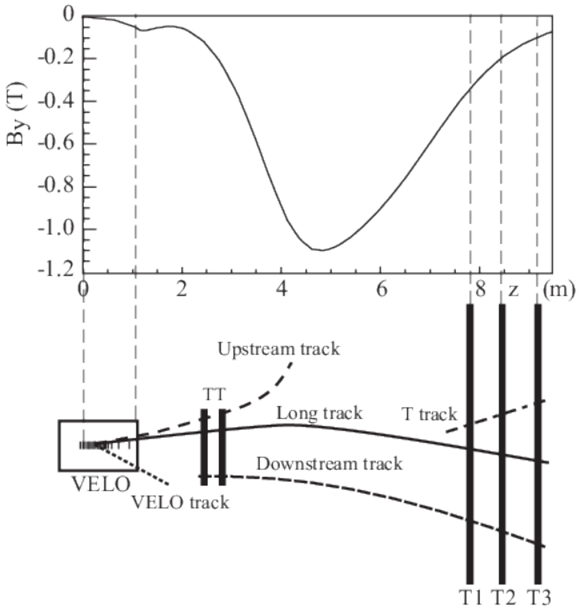

Figure 3.4: Track-type definitions in the LHCb tracking system. The main **B**-field component, along the y direction, is plotted above as a function of the z coordinate, along the beam axis.

granularity and precision of the VELO are achieved through small strip sizes and the large number of strips per module, enabling vertex and track position resolutions within the range of 5 to 25 micrometres. The VELO consists of two halves, referred to as the A-side and the C-side, each comprising 21 modules arranged in the z-direction, as shown in Figure 3.5. This configuration

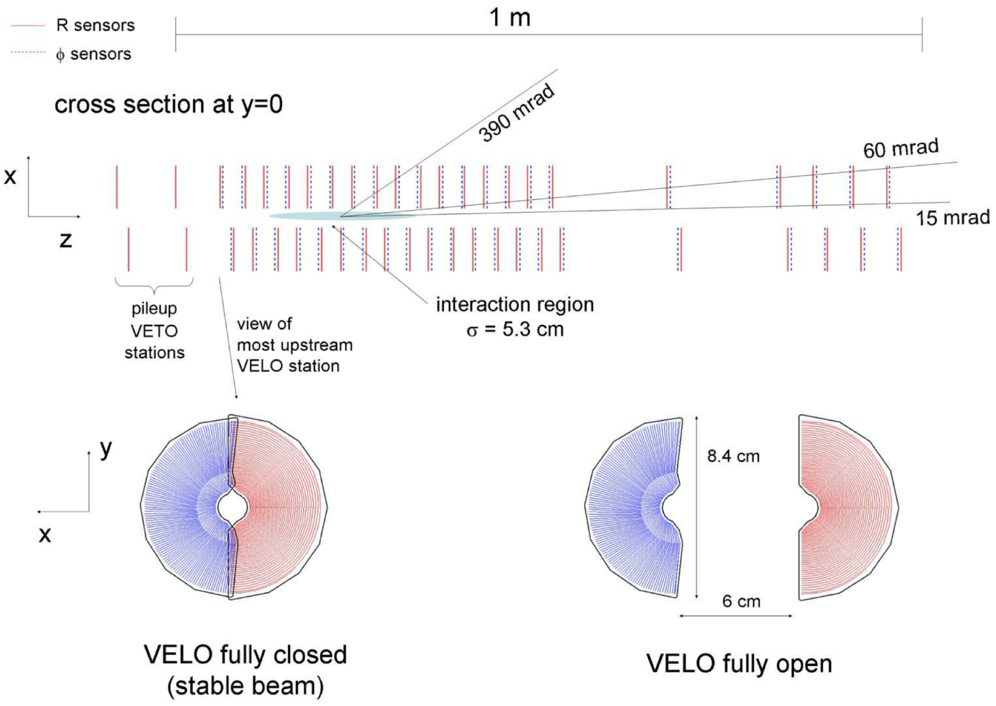

Figure 3.5: Scheme of the arrangement of the modules of which VELO is composed of. On the top Figure, it is possible to observe the pile-up veto system, later explained in 3.2.3. In the lower part, the front face of the modules is pictured, both in closed and open position.

ensures that charged particles produced at the interaction point (z = 0) and directed within the pseudorapidity range of $1.6 < \eta < 4.9$ cross at least six modules. Additionally, two supplementary veto stations are installed at negative coordinates (i.e. before the PV) to remove events with high multiplicity. To protect the VELO from radiation damage during beam injection and proton acceleration phases, the detector is initially placed in an "open" position, where the two halves are separated by 6 cm. Once stable beams are achieved, the VELO is "closed", reducing the inner distance between the sensor layers and the beam to just 8.2 mm, and the modules overlap, ensuring that a track within the LHCb acceptance crosses at least three stations, which is essential for accurate tracking and vertex reconstruction. This proximity enhances the detector's ability to precisely measure the IP of charged particles, a key parameter for distinguishing between prompt and secondary particles.

The VELO operates under vacuum conditions, with a secondary vacuum separating the detector from the beam vacuum. This separation is achieved using a thin aluminium RF foil, which shields the sensors from radio frequency interference emanating from the beam. The foil is kept as thin as possible, approximately 0.5 mm, to minimize the material budget and reduce multiple scattering effects that could degrade the vertex resolution. The overall material budget of the VELO corresponds to only about 1/6 of a radiation length X_0, ensuring a great momentum resolution within the LHCb experiment.

The VELO's performance has been validated in various runs, demonstrating an IP resolution of around 30 μm per track during Run 2. Its intrinsic resolution on the decay time is approximately 40 fs. The cooling system, which maintains the modules at temperatures between -10°C and 0 °C, further enhances the detector's longevity and performance by mitigating radiation-induced damage.

Silicon Tracker

The Silicon Tracker (ST) is comprised of two main detectors: the TT [46] and the Inner Tracker (IT). These detectors use silicon microstrip sensors to measure the positions and momenta of charged particles as they traverse the detector. The TT is placed at around z = 2.5 m upstream of the LHCb dipole magnet. It covers a large active area of approximately 8.4 m^2 and consists of four detection layers. A sketch can be found in Figure 3.6. Each layer is equipped with vertical strips in the first and last layers, and strips tilted by +5° and -5° in the second and third layers, respectively. This arrangement optimizes the spatial resolution and helps in accurately reconstructing particle trajectories. The TT's silicon microstrip sensors have a strip pitch of about 200 μm, providing a spatial resolution of approximately 50 μm. The working principle of the TT and the IT involve charged particles crossing the silicon p-n junctions, creating electron-hole pairs in the depletion zone. These pairs are then separated by an electric field, causing them to move towards the microstrips where they are collected, generating an electric signal that is read out by the detector electronics. This process allows the TT to precisely determine the positions of passing particles. The IT is located closer to the beam axis at the tracking stations T1 to T3 level. The IT is designed to cover the innermost region around the beam pipe, where the particle density is highest. With an active area of about 4.0 m^2, the IT plays a fundamental role for tracking particles that are produced at small angles relative to the beam direction. Similar to the TT, the IT consists of four detection layers with the same strip pitch of approximately 200 μm and a spatial resolution of about 50 μm. The IT's strategic placement allows it to capture tracks that might otherwise be missed by the Outer Tracker.

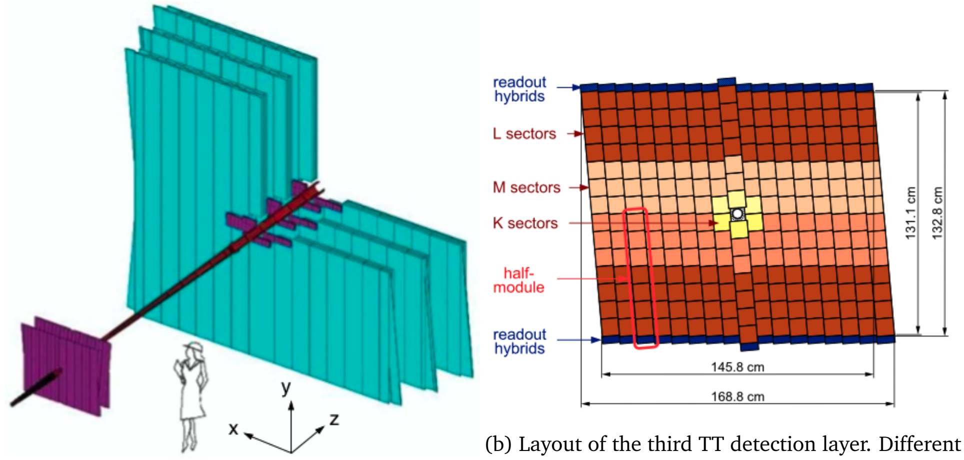

(a) Tracking station arrangement, with the ST in violet and OT in cyan. The magnet is located in the big gap.

(b) Layout of the third TT detection layer. Different readout sectors are indicated by different shadings.

Figure 3.6: Scketch of the TT and the T stations.

Outer Tracker

The Outer Tracker (OT) [47] is a component of the LHCb detector designed to complement the precision measurements provided by the Silicon Tracker. Positioned downstream of the dipole magnet and surrounding the IT, the OT is fundamental for extending the tracking capabilities to a larger radial and longitudinal coverage. The OT consists of straw tube detectors, which are lightweight and provide efficient tracking over a large area. Each straw tube is a gas-filled cylinder with a central anode wire, functioning as a drift tube detector. When a charged particle passes through a straw tube, it ionizes the gas, creating electron-ion pairs. The electrons drift towards the anode wire under the influence of an electric field, generating a signal that can be read out and processed. The OT is divided into three main stations, labelled T1, T2, and T3, located downstream of the IT and the LHCb dipole magnet. Each station is further segmented into several modules and layers, with the layers oriented in different directions. This arrangement allows the OT to effectively track particles that have been bent by the magnetic field, providing precise momentum measurements, as remarked in Figure 3.6a. Each module contains two staggered layers of drift tubes with inner diameters of 4.9 mm. As a counting gas, a mixture of Argon (70%) and CO_2 (30%) is chosen in order to guarantee a fast drift time, below 50 ns, and a sufficient drift-coordinate resolution (200 μm). The resolution obtained is lower than the IT, which achieves approximately 100–150 μm, but since the particle flux through OT is lower, the value achieved is sufficient for the purpose.

3.2.2 Particle identification system

In high-energy particle physics experiments such as LHCb, identifying the type of particles produced in collisions gives a hint for understanding the underlying physical processes. While the tracking system effectively reconstructs the trajectories of charged particles, it does not provide information about their identities or the presence of neutral particles. Particle identification (PID) involves assigning a hypothesis to the nature of these particles, which is essential for distinguishing between different decay modes. For instance, the distinction between a pion and a kaon is fundamental also in the analysis object of the thesis. LHCb employs several subdetectors that rely on different physical principles to identify particles. By combining the data from these subsystems, LHCb can optimize the PID variables and accurately determine the identity of the particles. The key subdetectors involved in the PID process include the RICH detectors, to perform a distinction between pions, kaons and protons, the calorimeter system, to distinguish between photons and electrons on one side, and hadrons on the other, and the muon chambers.

RICH Detectors

The particle identification [48] system uses two RICH detectors, RICH1 and RICH2, to achieve precise particle identification (PID). These detectors play an important role in distinguishing between different types of charged particles, such as protons, kaons, pions, muons, and electrons, by exploiting the Cherenkov radiation phenomenon. They cover the full momentum range, since at large polar angles the momentum spectrum is softer while at small polar angles the momentum spectrum is harder. RICH1 is positioned just downstream of the VELO and is optimized for low-momentum charged particles, covering a momentum range of approximately 1 to 60 GeV/c. Initially, RICH1 used both an aerogel and a fluorobutane (C_4F_{10}) gas radiator. However, the aerogel component was removed after Run 1 due to its decreased performance in high-multiplicity events. Currently, RICH1 uses only the C_4F_{10} gas with a refractive index of n=1.0014. The Cherenkov light produced in RICH1 is focused using a system of spherical and flat mirrors, which direct the light onto Hybrid Photon Detectors (HPDs). These HPDs convert the light into electronic signals that are then processed to reconstruct the Cherenkov angle. RICH2 is located further downstream, after the TT stations, and is designed to handle higher momentum particles, ranging from approximately 15 to 100 GeV/c. RICH2 uses a CF_4 gas radiator with a refractive index of n=1.0005, suitable for higher momentum thresholds. This detector covers a higher pseudorapidity range, focusing on areas where more energetic particles are expected. A schematic view is reported in Figure 3.7. Similar to RICH1, RICH2 employs a mirror system to direct the Cherenkov light to HPDs situated outside the detector acceptance. These HPDs are protected from the magnetic field and radiation damage by a metal shield. RICH1 has a wide acceptance, it covers the full LHCb acceptance from ±25 mrad to ±300 mrad (horizontal) and ±250 mrad (vertical) whereas RICH2 has a limited angular acceptance of $\sim \pm 15$ mrad to ±120 mrad (horizontal) and ±100 mrad (vertical). The technology used by RICH detectors is the Cherenkov light, which allows to identify particles; when charged particles travel through a medium at a speed greater than the phase velocity of light in that medium, they emit Cherenkov radiation. This radiation forms a cone of light with an opening angle θ_C, which is related to the particle's velocity v and the refractive index n of the medium by the equation

$$\cos\theta_C = \frac{1}{n\beta} \tag{3.3}$$

where β is ${}^{v}/_{c}$. By measuring the Cherenkov angle θ_C, one can deduce the velocity of the particle. The particle's mass can be calculated when combined with the momentum measurement provided by the tracking system, allowing for its identification, as in Figure 3.8.

Dedicated algorithms are employed to reconstruct the Cherenkov rings and compute the Cherenkov angle θ_C. A track is then assigned to the reconstructed rings, and a likelihood (DLL) is computed for each track, indicating the probability of the particle being of a certain type (e.g., pion, kaon, proton). Differences in these likelihoods (e.g., $(\mathrm{DLL})_K - (\mathrm{DLL})_\pi$) are used as discriminating variables in offline selection processes. Typically, a neural network is trained to

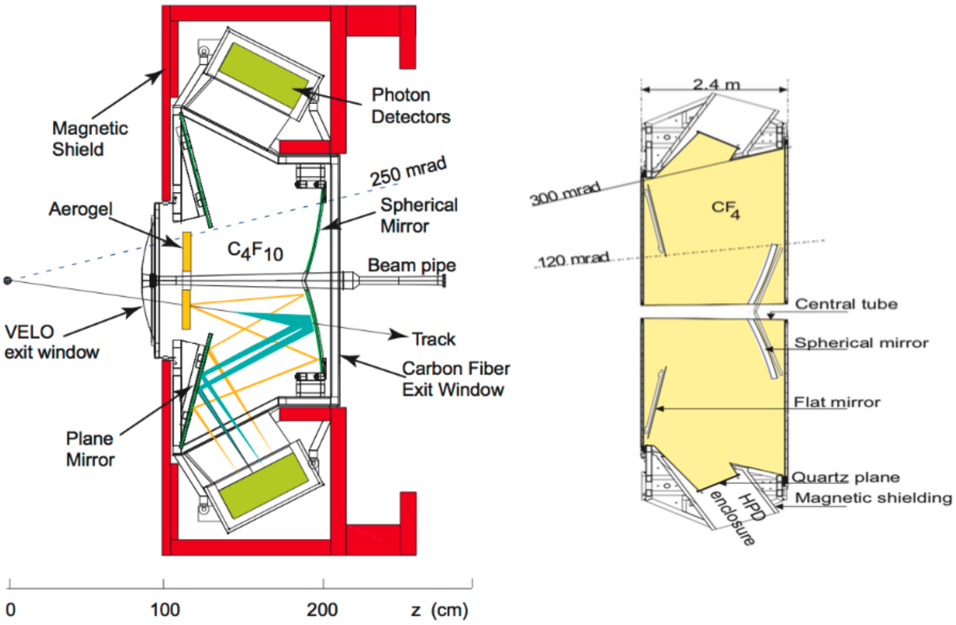

Figure 3.7: On the left a sketch of the side view layout of the RICH1 detector is pictured, with the optical path of the Cherenkov light emitted by a track. On the right, the top view of the RICH2 in the x-z plane.

combine the information from several subdetectors, providing a probability (ProbNN) for each charged particle candidate, which significantly enhances the discrimination power.

Calorimeters

In the particle identification system, there are two calorimeters [49]: the electromagnetic calorimeter, dedicated to the detection of photons and electrons, in general, particles that interact electromagnetically, and the hadronic calorimeter, used to measure energy and direction of hadrons, or particles whose interaction is weak or strong. The aim of the calorimeters is to measure the energy of the particles, but they also play an important role in the first level trigger (L0), which uses the measurement of transverse energy (E_T), to decide, within 4 μs, whether to keep or reject an event. The calorimeters are located downstream of the RICH2 and preceded by two auxiliary detectors: the PreShower (PS) and the Scintillator Pad Detector (SPD). All detectors are able to discriminate showers very efficiently thanks to their high granularity in the regions closer to the beam, granularity that decreases towards the outer ones.

The PS and the SPD are two identical layers of scintillating pads, with wavelength-shifting fibres that transmit scintillation light to photomultiplier tubes (PMTs), separated by 15 mm of lead, with an area of 7.6 m in width and 6.2 m in height as it can be seen in Figure 3.9, which is used as a converter, corresponding to 2.5 radiation lengths X_0 and 0.06 of the hadronic interaction length: consequently, electrons and photons start the shower in the lead whereas hadrons do not. This is the first element to discriminate the two typologies. A second one is the different interaction that the tracks have with the SPD, as electrons will leave hits in the detector, while photons will not.

The ECAL is built using the shashlik technology, i.e. a sampling scintillator/lead structure readout by plastic Wavelength-shifting (WLS) fibres along a 42 cm stack, equivalent to 25 radiation lengths. WLS fibres are used to transmit the scintillation light to the PMTs for the readout. This technology gives enough uniformity and an advanced monitoring system. The designed

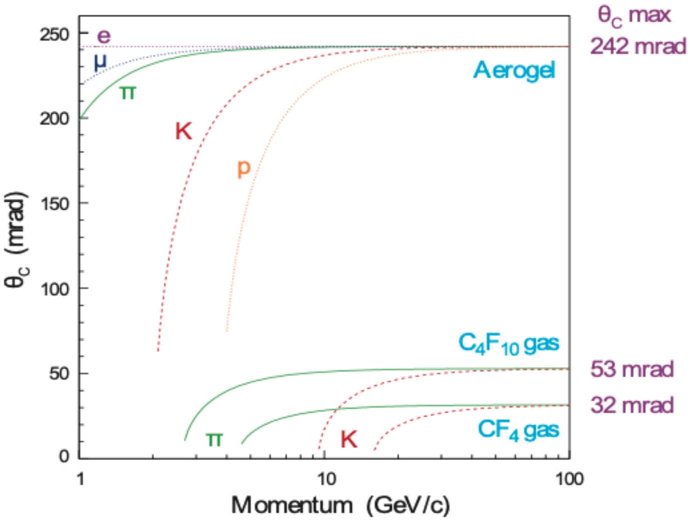

Figure 3.8: Cherenkov angle as a function of the particle momentum for the RICH detectors.

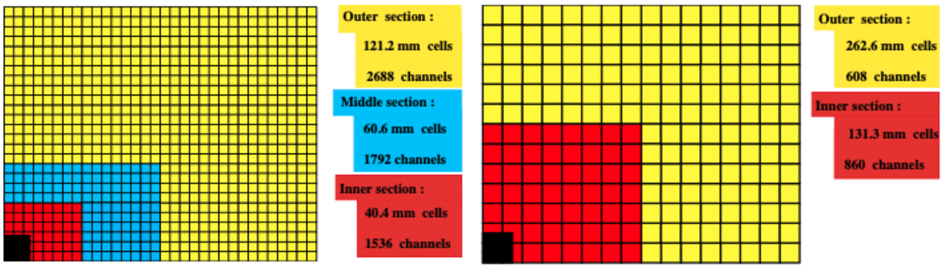

Figure 3.9: Lateral segmentation of the SPD/PS and ECAL (left) and the HCAL (right). One-quarter of the detector's front face is shown.

energy resolution of ECAL modules is

$$\frac{\sigma_E}{E} = \frac{10\%}{\sqrt{E}} \oplus 1\%, \tag{3.4}$$

where E is in GeV and $\oplus$ is the quadratic sum. This resolution translates to an expected B mass resolution of 90 MeV/c^2 for the $B^0 \to K^*\gamma$ decay and 75 MeV/c^2 for $B^0 \to \pi^+\pi^-\pi^0$ decay.

To induce showers in the HCAL, the iron is used as absorber material, while the scintillating tiles are the active material. The thickness corresponds to 5.6 hadronic interaction lengths (plus 1.2 interaction lengths from the upstream ECAL). The resolution is, accounting for E in GeV, is

$$\frac{\sigma_E}{E} = \frac{65\%}{\sqrt{E}} \oplus 9\%. \tag{3.5}$$

This lower resolution compared to the ECAL makes the HCAL primarily useful for the hardware trigger stage rather than detailed analysis.

Muon system

Muons correct identification [50] is fundamental for the experiment since they are present in many final states of B decays. The muon system provides fast information for the high-p$_T$ muon trigger at the L0 and muon identification for the high-level trigger (HLT) and offline analysis. The LHCb detector features a comprehensive muon system composed of five stations, labeled M1 through M5, which are strategically placed along the beam axis to ensure optimal muon detection and identification. It is located at the end of the detector since muons are not stopped by the calorimeters or any of the previous detectors, granting that their tracks pass through the whole structure. As it can be seen in Figure 3.10, the muon stations are arranged in a sequence, with M1 positioned before the calorimeter system and M2 to M5 located downstream of the calorimeters. The primary purpose of M1 is to provide an initial measurement of the muons'

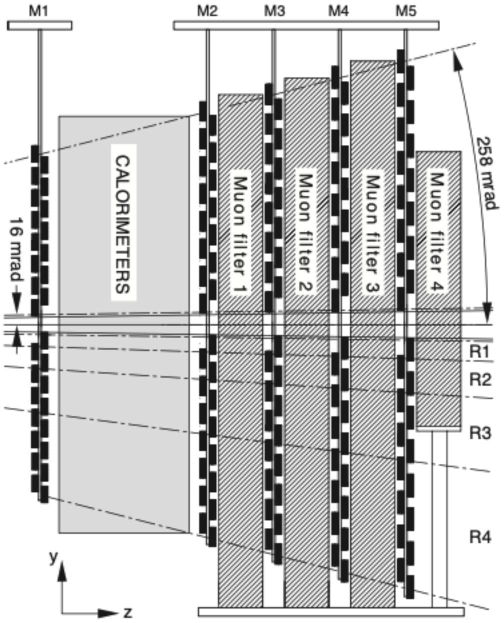

Figure 3.10: Side view of the muon system.

transverse momentum, which is crucial for the hardware trigger to select high-p_T particles. The remaining stations, M2 through M5, are interspersed with 80 mm thick iron absorbers, ensuring that only muons with sufficient momentum (greater than 6 GeV/c) can traverse all the stations. This setup results in a total absorber thickness equivalent to 20 interaction lengths, effectively filtering out non-muon particles. Most of the muon stations use multi-wire proportional chambers (MWPCs), except for the inner region (R1) of M1, which employs triple-GEM (Gas Electron Multiplier) detectors. GEM detectors are more resilient to high particle rates and radiation, providing reliable performance in the innermost regions. The system has a total of 1368 multi-wire proportional chambers holding four anode-wired sections filled with a gas mixture of Ar, CO_2 and CF_4. The muon stations cover a large area of 435 square meters to match the angular acceptance of the LHCb detector, which ranges from 20 (16) mrad to 306 (258) mrad in the bending (non-bending) plane. Each station is divided into four regions (R1 to R4), with a linear scale ratio of 1:2:4:8, in order to have the same flux of muons in each section. The granularity of the chambers changes similarly to the other sections of the detector: it is higher in the central region and poorer in the outer ones. The muon system is integral to the LHCb trigger system, particularly the HLT. The HLT algorithm, which uses the aforementioned identification variables, has been enhanced for Run 2 to take advantage of increased computing power, resulting in a 15% improvement in efficiency compared to Run 1. The muon identification efficiency is typically around 98%, with pion and kaon misidentification rates below 1%.

3.2.3 LHCb trigger

At the LHC, proton bunches cross every 25 ns, corresponding to a frequency of 40 MHz. However, at the LHCb interaction point, not all bunches are filled due to the forward geometry of the LHCb detector, which shifts the interaction point along the z-axis away from the center of the cavern. In each collision at LHCb, the reduced bunch filling and forward geometry result in a lower interaction rate, which reduces radiation damage and simplifies event reconstruction and triggering. Furthermore, the number of interactions per bunch crossing is dominated by single interactions, which facilitates the triggering and reconstruction by assuring low channel occupancy. The bunch crossing frequency reached is lower, about 30 MHz, and in each collision, the majority of the events are not of interest to the experiment. Here intervenes the trigger, whose role is to find and keep the events that may contain interesting physics and save them to disk while discarding the rest, saving an enormous amount of disk space. The system operates in two main stages, as shown in Figure 3.11, the hardware-based Level 0 (L0) trigger and the software-based HLT, which is further divided into HLT1 and HLT2, after which the rate of writing to storage has been reduced to 12.5 kHz.

Level-0 Trigger

The L0 trigger is implemented using custom made electronics, operating synchronously with the 40 MHz bunch crossing frequency. It aims to reduce the event rate from 30 MHz to 1 MHz within a decision time of 4 μs. This stage uses information from the VELO pile-up system, the calorimeters, and the muon stations. The L0 trigger identifies high-energy particles, such as those from b-hadron decays, which typically have large transverse momentum or transverse energy.

- Calorimeter Triggers: The calorimeters form clusters of 2×2 cells and select candidates

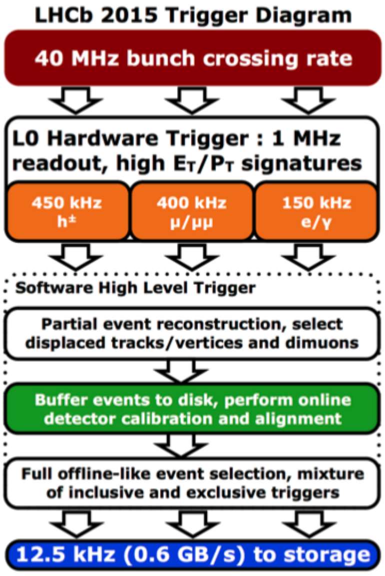

Figure 3.11: Run 2 trigger system scheme [51]

with the highest E_T. The information from the SPD, PS, ECAL, and HCAL is used to identify electrons, photons, pions, and hadrons. Events with high multiplicity, indicated by a large number of SPD hits, are vetoed to avoid overloading the subsequent stages.

- Muon Triggers: The muon trigger looks for tracks with high p_T that have hits in all five muon stations and point back to the interaction point. Dimuon triggers are also used to identify events with high-p_T muon pairs.

High-Level Trigger

After passing the L0 trigger, events are processed by the HLT, which is implemented as software applications running on the Event Filter Farm (EFF). The HLT further reduces the event rate from 1 MHz to 5 kHz in Run 1 and to 12.5 kHz in Run 2.

- HLT1: The first stage of the HLT performs a simplified track reconstruction, focusing on finding segments in the VELO and forming primary vertices. Tracks not associated with a PV or not matched to any hits in the muon stations are discarded. The remaining tracks are matched with hits in the T-stations to form long tracks. This stage reduces the rate to around 80 kHz.

- HLT2: In HLT2, a full reconstruction of events is performed using all available sub-detector information. This stage includes more detailed track reconstruction and particle identification using the calorimeters and RICH detectors. HLT2 is divided into inclusive and exclusive trigger lines. Inclusive lines select events based on generic signatures, while exclusive lines target specific decay channels. During Run 2, an automatic real-time calibration and alignment procedure was introduced, improving the online reconstruction quality to match the offline reconstruction.

3.3 LHCb Upgrade I

Intending to maintain and enhance its capabilities in the face of increased luminosity and data rates, the LHCb detector underwent a significant upgrade known as Upgrade I [52]. This upgrade, implemented in preparation for Run 3 and Run 4 of the LHC, is designed to handle an instantaneous luminosity levelled at $2 \times 10^{33}\mathrm{cm}^{-2}\mathrm{s}^{-1}$, significantly higher than in previous runs. The anticipated increase in the average number of visible interactions per bunch crossing (μ) to 5.2 necessitated substantial enhancements to the detector and its data acquisition systems. A detailed description will follow, while for a first glance, there is Figure 3.12.

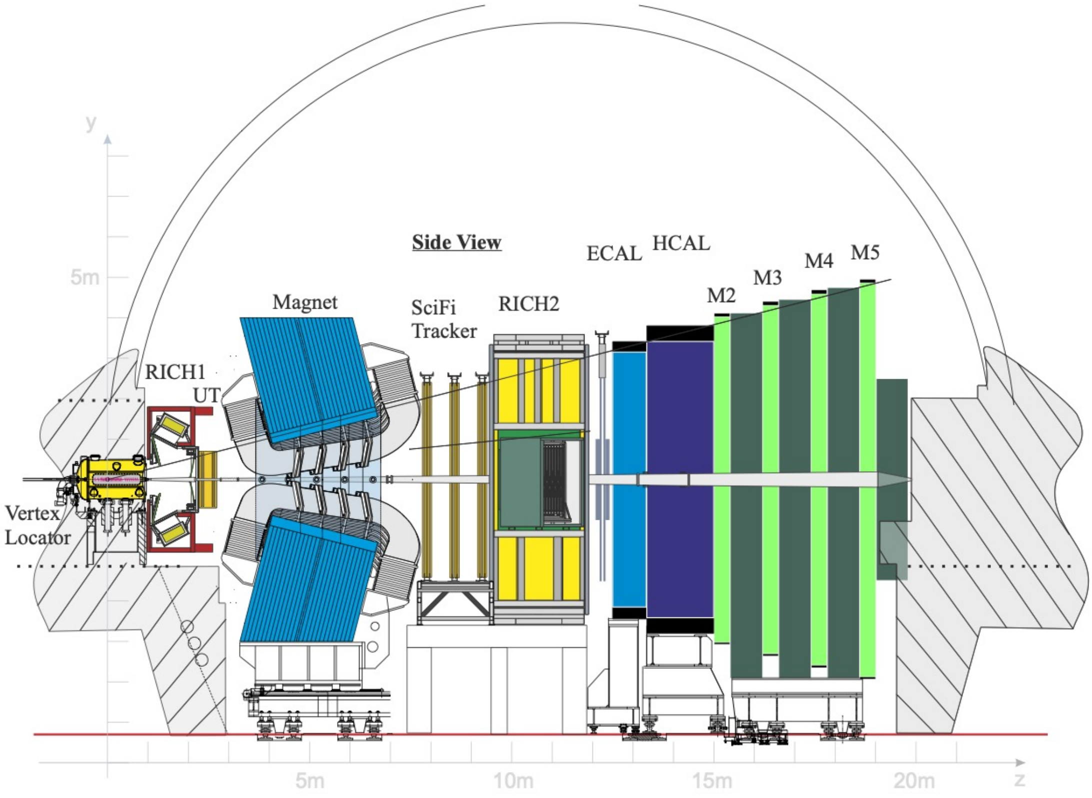

Figure 3.12: Schematic view of the LHCb detector after Upgrade I.

Trigger System

One of the most notable changes in Upgrade I is removing the hardware trigger (L0) and replacing it with a fully software-based trigger system. This new system aims to achieve higher efficiencies for both hadrons and leptons. The new trigger strategy is divided into two stages: HLT1 and HLT2. The HLT1 trigger, implemented using the Allen software on GPUs, performs partial event reconstruction, while the HLT2 trigger, using Moore software on CPUs, completes the full event reconstruction and makes the final selection. The real-time alignment and calibration are now integrated into the HLT1 stage, allowing for immediate application of these corrections in HLT2. This approach enables a higher quality of event reconstruction, reducing the need for offline processing. The transition to a software-based trigger allows for more flexible and comprehensive trigger decisions, maximizing the efficiency of selecting interesting events.

VELO Upgrade

The VELO [53] has been upgraded to improve granularity, cope with higher particle multiplicities, and increase ghost rates. The new VELO employs silicon pixels instead of silicon strips, enhancing the impact parameter resolution by 40% for tracks with a first hit at $z > 300$mm. The upgraded VELO consists of 26 planar stations, each positioned closer to the beam (5.1 mm distance) with a reduced aluminium foil thickness, minimizing material budget and further improving resolution.

Tracking System

The TT stations have been replaced by the Upstream Tracker (UT) [54], which features finer granularity silicon strips and improved radiation hardness. This upgrade is expected to reduce ghost tracks and enhance momentum resolution. The IT and OT have been replaced by the Scintillating Fiber Tracker (SciFi), comprising three stations with four layers of scintillating fibres each. This new tracker aims for a hit efficiency of 99% and a hit resolution in the xz plane of less than 10μm.

Calorimeter and Muon Systems Upgrades

While the existing ECAL and HCAL are retained, their front-end electronics is upgraded to handle the 40 MHz readout rate [55]. The PS and SPD detectors, previously part of the L0 trigger, have been removed. The gain of the PMTs in the calorimeters will be reduced by a factor of five to limit degradation, with the readout electronics upgraded accordingly. The muon system also sees significant changes. The M1 station is removed, as it was primarily used for the now-obsolete L0 trigger. The inner region of M2 is upgraded with Triple-GEM detectors to cope with increased particle flux, and the electronics across all muon stations are upgraded for 40 MHz readout.

RICH Detectors

The RICH detectors undergo an optical redesign to manage higher particle densities, with the HPDs replaced by multi-anode photomultipliers (MaPMTs) for improved granularity. The RICH front-end electronics are also updated for 40 MHz readout using the new CLARO chip.

Real-Time Analysis (RTA)

The new software trigger system, including the HLT, is designed to run in two stages. HLT1, operating on GPUs, performs initial track reconstruction and vertex fitting, significantly reducing the data rate. HLT2 then performs full event reconstruction, applying real-time calibration and alignment. This approach, termed Real-Time Analysis (RTA), eliminates the need for subsequent offline reconstruction, thus streamlining data processing and enhancing trigger efficiency. The Allen project has been embraced for HLT1, running on 500 GPUs to perform track reconstruction and selection. This setup reduces the global data volume significantly, optimizing computational resources and reducing costs. The expected data throughput is around 80 Gbit/s, facilitating efficient event filtering and storage.

3.4 LHCb Upgrade II and beyond

Following the successful implementation of Upgrade I, the LHCb collaboration is planning an even more ambitious project known as Upgrade II [56]. Scheduled to be implemented during the Long Shutdown 4 (LS4) of the LHC, Upgrade II aims to prepare the LHCb detector for operation at significantly higher luminosities and to extend its physics reach even further. Upgrade II is driven by the need to cope with an instantaneous luminosity increase to $2 \times 10^{34}\text{cm}^{-2}\text{s}^{-1}$, an order of magnitude higher than the luminosity levels for which the current detector (post-Upgrade I) is designed. This higher luminosity will enable LHCb to collect an unprecedented amount of data, up to 350 fb^{-1}, significantly enhancing the precision of measurements and allowing for the exploration of rare processes that are currently beyond reach. The increased data volume and higher radiation levels necessitate extensive upgrades to many components of the detector to maintain performance and reliability. The key upgrades can be visualised in Figure 3.13, and be read in the following:

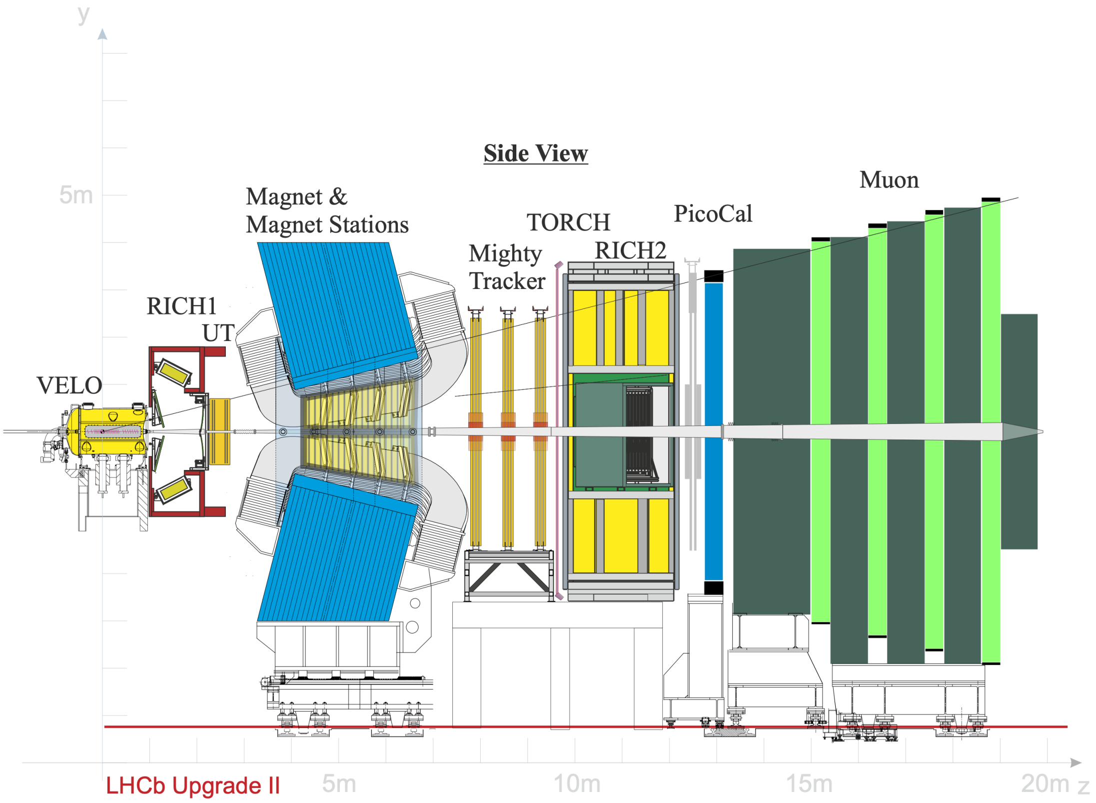

Figure 3.13: Schematic view of the LHCb detector after Upgrade II

- The VELO will undergo further improvements to handle higher particle densities and radiation levels. Enhancements will focus on further reducing the material budget, increasing the pixel granularity, and improving radiation hardness to maintain high-resolution vertex reconstruction.

- The tracking system, including the SciFi Tracker and the UT, will be upgraded to cope with higher occupancy and radiation. The goal is to improve spatial resolution and track reconstruction efficiency while minimizing ghost tracks.
- The ECAL will be optimized for better π^0, electron, and photon identification, with increased radiation hardness and an expanded Shashlik array. The HCAL will be adapted to maintain efficiency in the higher radiation environment. Technological upgrades include replacing photodetectors with multi-anode photomultiplier tubes (MaPMTs) and updating front-end electronics to handle the 40 MHz readout rate, ensuring the system can manage increased data throughput.
- Further upgrades to the RICH detectors will involve enhancing the optical systems and light detection mechanisms to handle higher event rates and maintain particle identification efficiency.
- The muon system will be upgraded with new technologies to ensure efficient muon detection despite the increased particle flux. This might involve further improvements to the GEM detectors and overall system readout speed.
- Building on the success of the RTA approach from Upgrade I, Upgrade II will further integrate real-time calibration and alignment. This will enhance the overall quality of the data collected and allow for immediate physics analysis.

4

Installation and commissioning of the UT detector

4.1 Silicon detectors in particle physics

Silicon detectors entered the field of particle physics aiming to augment the precision in tracking charged particles. Using silicon as a detection medium in particle physics dates back to the mid-20th century. Early experiments in the 1950s and 1960s demonstrated the potential of silicon diodes for radiation detection, primarily due to their excellent resolution and compact size compared to traditional gas-filled detectors [57], [58]. These early experiments laid the groundwork for developing more sophisticated silicon-based devices. The breakthrough in silicon detector technology came with the invention of the silicon strip detector. This innovation was driven by the need for higher precision in particle tracking, particularly in high-energy physics experiments. The first remarkable use of silicon strip detectors was in the NA11/NA32 experiment at CERN in the early 1980s, which marked the beginning of their widespread adoption in particle physics [59].

Silicon detectors operate based on the principle of ionization, exploited by the p-n junctions. A p-n junction is formed by bringing together p-type and n-type semiconductor materials, as silicon, which are doped to have an excess of holes and electrons, respectively. At the junction, electrons from the n-region diffuse into the p-region and recombine with holes, while holes from the p-region diffuse into the n-region and recombine with electrons. This diffusion results in a depletion region around the junction, where free carriers are absent, creating an electric field due to the ionized donor and acceptor atoms left behind. Applying an external reverse bias voltage across the p-n junction widens the depletion region, further reducing the number of free charge carriers in this region. This reverse bias condition is critical for semiconductor detectors, as it allows the junction to act as a sensitive volume for detecting ionizing radiation. When a charged particle or photon passes through the silicon detector, it creates electron-hole pairs in the depletion region. The strength and width of the depletion region can be controlled by adjusting the reverse bias voltage, optimizing the detector's sensitivity and resolution. The charge collection process begins when these electron-hole pairs are created. The electric field in the depletion region causes electrons to move towards the n-side and holes towards the p-side. This movement generates a current that can be measured as a signal, indicating the presence and intensity of the incident radiation. The efficiency of charge collection depends on the electric field strength, the mobility of the charge carriers, and the quality of the semiconductor material. The most common types of silicon detectors are silicon strip detectors and silicon pixel detectors. A schematic view of the two types can be found in Figure 4.1. The silicon wafer is divided

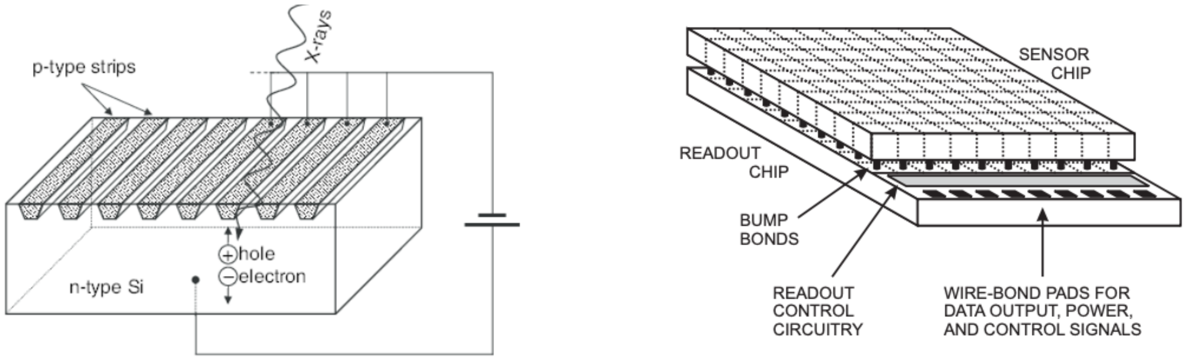

(a) Schematic view of a strip detector.

(b) Schematic view of a hybrid pixel detector.

Figure 4.1: Representations of two typologies of silicon detectors.

into narrow, parallel strips in silicon strip detectors, each acting as an independent detector. This configuration allows for precise determination of the particle's position in one dimension. Silicon pixel detectors, on the other hand, divide the silicon wafer into a grid of small, square pixels, providing two-dimensional position information [60]. Both detectors offer high spatial resolution, making them ideal for tracking charged particles in complex environments. The need for higher resolution, faster readout, and greater radiation hardness has driven the evolution of silicon detector technology. The development of integrated circuits and advances in semiconductor fabrication techniques have been fundamental in this evolution. One of the significant advancements in silicon detector technology is the transition from single-sided to double-sided detectors. Double-sided detectors have strips on both sides of the silicon wafer, allowing for the measurement of two-dimensional position information without needing multiple layers of detectors. This advancement significantly improved the spatial resolution and tracking efficiency of silicon detectors. In the context of the work performed in this thesis, a more detailed description of the working principle of the strip detectors is given. Recalling the schematic picture in Figure 4.1a, it is straightforward to see that the strips themselves are connected to readout electronics, which detect the movement of these charge carriers. Each strip acts as an individual detector, allowing for the precise localization of the particle's trajectory. The signal from each strip is processed to determine the position and energy release of the incident particle. This segmentation into strips provides high spatial resolution, as the position of the particle can be pinpointed to the width of the strip, which is typically a few tens of micrometers. A key aspect of strip detectors is the design of the readout electronics, which must handle the signals from a large number of strips simultaneously. This often involves the use of multiplexing techniques to reduce the number of required readout channels. The electronics must also minimize noise to ensure that the signals from the charge carriers are accurately measured.

Another significant development is the introduction of silicon pixel detectors. Pixel detectors provide even higher spatial resolution than strip detectors and can withstand high radiation doses. Today, silicon detectors are a critical component of many high-energy physics experiments. Among other applications, they are used in tracking detectors, vertex detectors, and calorimeters. The advancements in silicon detector technology have enabled experiments to achieve unprecedented precision and accuracy. In addition to high-energy physics, silicon detectors are used in medical imaging, space research, and industrial applications. Their ability to provide high-resolution imaging and their robustness in harsh environments make them suitable for various applications.

The future of silicon detector technology looks promising, with ongoing research and development aimed at further improving their performance. Innovations such as 3D silicon detectors, which have electrodes that penetrate the silicon wafer vertically, offer the potential for even higher resolution and faster readout speeds. Additionally, advancements in materials science and semiconductor fabrication techniques are expected to enhance silicon detectors' radiation hardness and longevity.

As particle physics experiments continue to push the boundaries of our understanding of the universe, the demand for more advanced silicon detectors will undoubtedly increase. These detectors will be the main protagonists in the next generation of experiments, enabling physicists to explore new frontiers and uncover the secrets of the fundamental particles and forces that govern our world.

4.1.1 Preamplifiers in Silicon detectors

As silicon detectors become more and more indispensable in particle physics, on the counterpart, the signals generated by these detectors are often weak and susceptible to noise. To address this challenge, the role of preamplifiers is essential in amplifying these weak signals, ensuring that they can be processed accurately.

A preamplifier is an electronic component designed to amplify the small electrical signals generated by silicon detectors before the main amplification and digitization electronics further process them. The primary function of a preamplifier is to boost the signal-to-noise ratio (SNR), ensuring that the subsequent stages of the data acquisition system can accurately capture and analyze the detector signals. The functioning of a preamplifier in a silicon detector system involves several key processes. When a charged particle traverses a silicon detector and creates electron-hole pairs in the silicon substrate, the movement of these charge carriers under an applied electric field generates a current pulse, which is collected by the detector electrodes, as previously described. The collected charge is typically minimal, often in the range of femtocoulombs (fC). Preamplifiers amplify this small charge signal to a more manageable level. The amplification process must be linear to ensure that the output signal accurately represents the input charge [58]. Silicon detectors are sensitive to various noise sources, including thermal noise, shot noise, and electronic noise from the readout circuitry. A preamplifier is designed to minimize these noise contributions, often by employing low-noise components and optimizing the circuit design. In addition to amplification, preamplifiers usually include signal shaping and filtering stages. Signal shaping adjusts the pulse shape to optimize the SNR and timing resolution. Filtering removes high-frequency noise components that could interfere with accurate signal measurement [59].

Several types of preamplifiers are used in silicon detector systems, each with its advantages and limitations:

- Charge-Sensitive Preamplifiers (CSPs) are widely used in silicon detectors. They convert the input charge signal into a voltage signal, with the output voltage proportional to the input charge. CSPs typically consist of a feedback capacitor and a high-gain amplifier. The charge collected by the detector is integrated over the feedback capacitor, producing a voltage pulse at the output.

- Voltage-Sensitive Preamplifiers amplify the voltage signal directly from the detector electrodes. These preamplifiers are simpler in design but can be more susceptible to noise

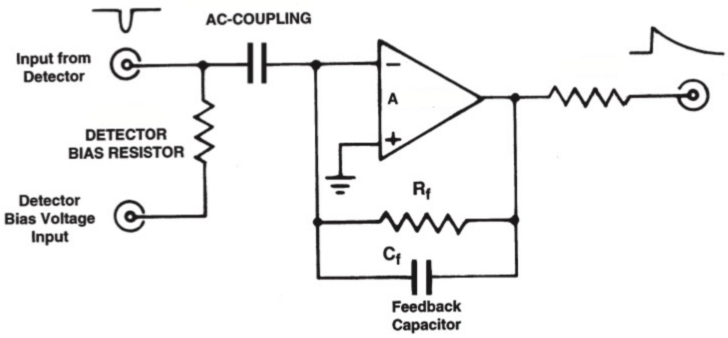

Figure 4.2: Simplified Schematic of a Charge-Sensitive Preamplifier.

compared to CSPs.

- Current-Sensitive Preamplifiers: also known as current amplifiers, amplify the current signal generated by the movement of charge carriers. These preamplifiers are less common in silicon detector systems due to their higher susceptibility to noise.

Given the importance for this thesis of CSPs, a detailed description follows. When these amplifiers convert the charge collected by the silicon strips into a measurable voltage signal, they also ensure minimal noise addition in order to preserve the signal integrity. A CSP typically consists of a Field-Effect Transistor (FET) at the input stage, fundamental component for maintaining low noise levels. The detector output, a current pulse, charges a feedback capacitor within the amplifier, ensuring the output voltage is directly proportional to the input charge, given by $V_{\mathrm{out}} = \frac{Q_{\mathrm{D}}}{C_{\mathrm{f}}}$, where V_{out} is the output voltage, Q_{D} is the charge from the detector, and C_{f} is the feedback capacitor. The feedback resistor R_{f}, connected in parallel with the capacitor, determines the decay time constant $\tau_{\mathrm{f}} = R_{\mathrm{f}} C_{\mathrm{f}}$ of the output signal (see Figure 4.2). Noise performance, quantified as Equivalent Noise Charge (ENC), is influenced by the FET, input capacitance, and leakage currents, and minimizing noise would lead to high-resolution measurements. Cooling the FET to cryogenic temperatures can significantly reduce noise. When designing a preamplifier for silicon detectors, one needs to consider several aspects. One of these is the gain, which must be carefully selected to ensure that the amplified signal falls within the dynamic range of the subsequent readout electronics. Too little gain may result in a weak signal, while too much gain can lead to signal saturation. In this context, the gain is primarily determined by the feedback capacitor, C_f, which plays an important role in converting the input charge from a detector into an output voltage. Recalling the definition of V_{out}, the voltage gain G_v of the preamplifier is inversely proportional to the feedback capacitance, $G_v = \frac{1}{C_f}$. This means that smaller feedback capacitors yield higher gains, while larger ones result in lower gains. For instance, if an input charge $Q_{in} = 10^{-12}\,\mathrm{C}$ is applied to a feedback capacitor $C_f = 10^{-12}\,\mathrm{F}$, the output voltage would be 1V, translating to a gain of $10^{12}\,\mathrm{V/C}$. The gain is influenced by factors such as input capacitance, which includes detector and parasitic capacitances affecting noise and bandwidth, and environmental conditions like temperature, which can alter the characteristics of the feedback capacitor. As one of the roles of the preamplifier is noise reduction, careful consideration of the noisy detector components needs to be taken, including the input transistors and feedback elements. Low-noise components and proper grounding techniques are essential. An important property of the preamplifier is its linearity; it has to provide a linear response to ensure that the output signal accurately represents the input charge. Non-linearities can distort the signal, leading to measurement errors. Last but not least, in our use case, the preamplifiers are often exposed to high radiation levels. The design must ensure that the components can withstand radiation without significant degradation in performance. Recent advances in preamplifier technology have focused on improving performance and integration with modern detector systems. One of these is the Application-Specific Integrated Circuits (ASICs) technology, which spread in the last decades. These custom-designed integrated circuits offer high performance, low noise, and compact size. ASICs can be tailored to the specific requirements of the detector system, providing optimized performance. Furthermore, advances in low-power design techniques have led to preamplifiers that consume less power while maintaining high performance. These designs are particularly important in large-scale detector systems, where power consumption can be a significant concern. There was also an effort in the development of radiation-hardened components that have improved the durability of preamplifiers in high-radiation environments. These components can withstand radiation without significant performance degradation, ensuring reliable operation in particle physics experiments.

4.2 The Upstream Tracker

As previously mentioned, the Upstream Tracker (UT) was designed to replace the Tracker Turicensis (TT) as part of the LHCb Upgrade I. This upgrade was motivated by the need to handle increased luminosity and interaction rates anticipated in Run 3 and beyond. The role of the UT is to enhance the tracking performance, reduce the ghost track rate, and improve momentum resolution, thereby contributing significantly to the overall physics performance of the LHCb experiment. Furthermore, UT is particularly critical for reconstructing decays such as $K^0_S \to \pi^+\pi^-$ and $\Lambda \to p\pi^-$, as most of these decays occur after the particles have passed through the VELO. In these scenarios, the decay tracks are identified using hits in the UT and the downstream tracking system. It is noteworthy that the majority of events, approximately 73%, are reconstructed from decays happening downstream of the VELO, utilizing both the UT and the downstream tracker (SciFi). The physics goals of the LHCb experiment require precise tracking and vertexing capabilities, especially in the high-radiation environment close to the LHC beamline. The UT is designed to meet these stringent requirements by providing high-resolution tracking and improved radiation hardness. As a recall, the UT is situated upstream of the LHCb dipole magnet and is divided into four detection layers. The layers are displaced with a $x - u - v - x$ configuration, as shown in Figure 4.3, where the *x* planes measure the *x* coordinate with strips along the *y* axis, while the *u* and *v* planes are titled by a stereo angle of $\pm 5^\circ$ with respect to the *y* axis to measure the *y* coordinate. These layers are equipped with silicon microstrip sensors offering high granularity and excellent spatial resolution. They have a strip pitch of 93.5 μm to 187.5 μm, depending on the region. The sensors are arranged in a layout that maximizes coverage and minimizes dead areas. They are of four typologies, Type A, Type B, Type C, and Type D, based on the expected occupancy linked to the occupied area. A representation is shown in Figure 4.4 and the details of each typology of sensor is summarised in Table 4.1. The smaller pitch in the regions closer to the beam pipe helps achieve higher resolution.

For an overlook of the whole detector complex with its electronics when installed in the LHCb cavern, see Figure 4.5. The detector is designed to withstand high radiation doses, indeed, the sensors and electronics are fabricated using radiation-hard materials and techniques, ensur-

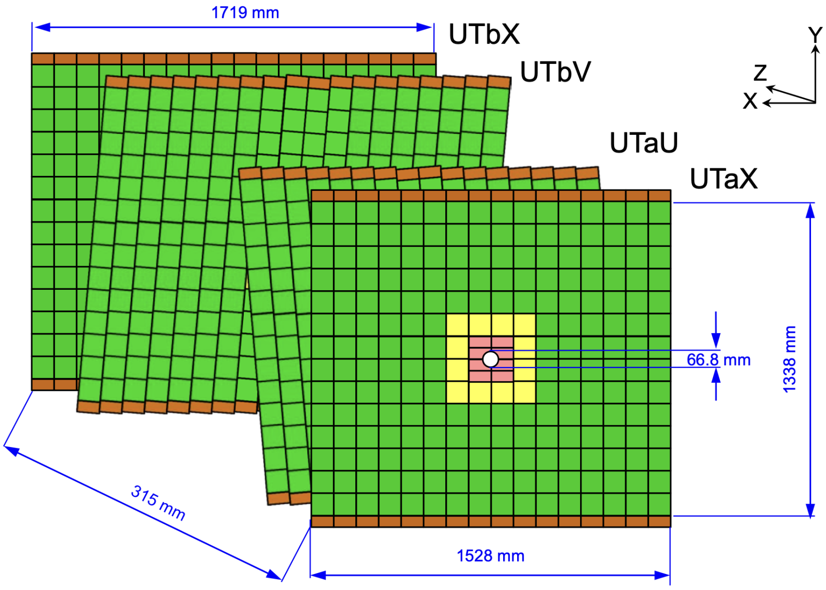

Figure 4.3: Overview of UT geometry looking downstream.

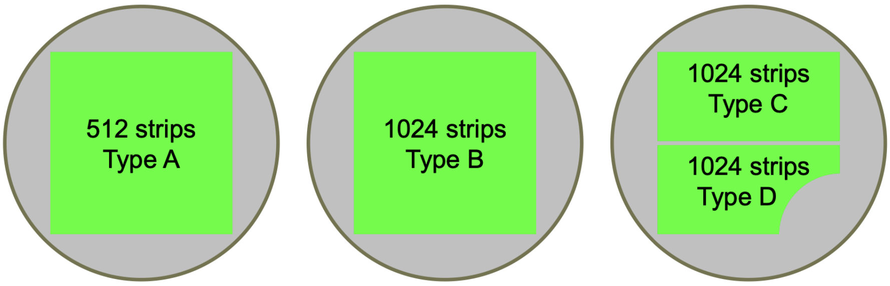

Figure 4.4: Sketch of the sensor designs for the UT upgrade.

Property	Sensors B,(C,D)	Sensors A
Technology	n^+-in-p	p^+-in-n
Thickness	320 (250) μm	320 μm
Physical dimensions	99.5 mm X 97.35 mm (51.45 mm X 97.35 mm)	99.5 mm X 97.5 mm
Length of read-out strip	99.5 (51.45) mm	99.5 mm
Number of read-out strips	1024	512
Read-Out strip pitch	93.5 μm	187.5 μm
Sensor number (needed)	48 (16,16)	888

Table 4.1: Properties of the sensors used in the detector.

ing long-term stability and performance. The UT sensors and electronics are designed using radiation-hard materials and processes to mitigate radiation damage. The cooling system is also optimized to maintain stable operating temperatures, further enhancing radiation tolerance, as high level doses of radiation can cause the silicon lattice structure to suffer of displacement damage, which results in defects in the material. These defects alter the electrical properties of the silicon, leading to increased leakage currents. The expected radiation dose for the UT over its operational lifetime is up to $1 \times 10^{15} 1{-}\mathrm{MeV}$ neutron equivalent $\frac{neq}{\mathrm{cm}^2}$. The UT uses the SALT

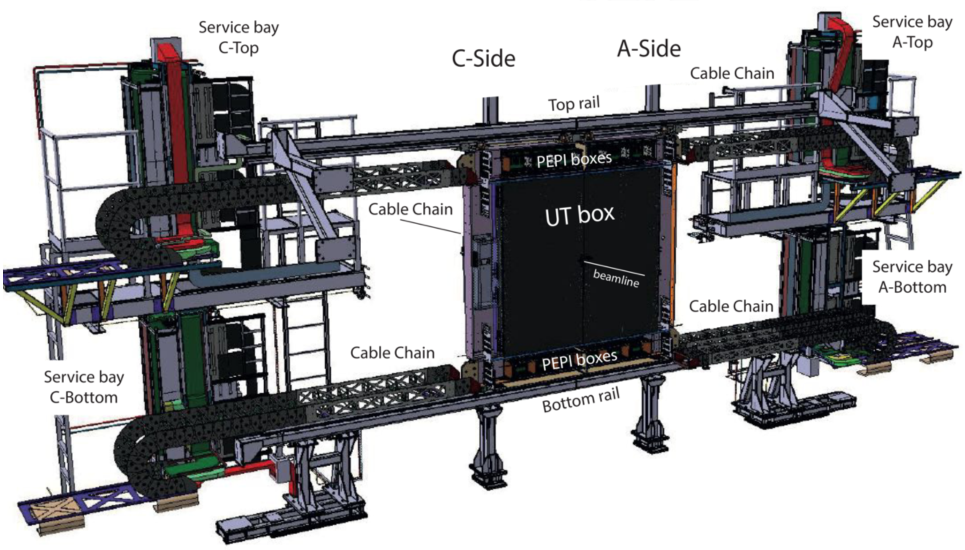

Figure 4.5: 3D representation of the detector installed in the cavern in its final configuration. The sensors are in the so-called UT box, which is positioned on up and bottom rails to move easily the two halves. Along the rails, the cable chains are accommodated, both the powering ones but also the low voltage and the optical fibres. On the sides, the service bays are placed.

(Silicon ASIC for LHCb Tracking) read-out chip, designed to operate at a 40 MHz bunch crossing frequency, reading the information transmitted by each of the 128 channels in each ASIC. The SALT chip integrates low noise, high-speed data processing, and zero-suppression features, ensuring that only relevant data is transmitted to the data acquisition system. The presence of this sub-detector in the whole detector complex serves several tasks in the tracking ecosystem. The UT provides initial track segments (seeds) extrapolated downstream to the other tracking stations (SciFi tracker) and upstream to the VELO. This helps reconstruct the complete trajectories of charged particles, and link hits across different detector layers. Furthermore, one of the significant improvements of the UT over the TT is its increased ability to reduce ghost tracks and its major coverage around the beampipe. Ghost tracks are spurious track candidates that do not correspond to any real particle. The high granularity and precision of the UT sensors help accurately identify and reject such ghost tracks, thereby improving the overall tracking efficiency. Moreover, the precise position measurements provided by the UT and the bending power of the LHCb dipole magnet allow for accurately determining the momentum of charged particles, as thanks to the UT the number of low momentum traces are reduced, speeding up the reconstruction at HLT1 level.

4.3 Installation

The commissioning of the UT involved several stages, including installation, calibration, and integration with the LHCb data acquisition system. The UT was installed in the LHCb detector cavern during the Long Shutdown 2 (LS2). The installation process required precise positioning and alignment of the detector modules to ensure optimal performance. It followed the calibration, which involved fine-tuning the sensor response, adjusting the gain and threshold settings of the read-out electronics, and ensuring uniform performance across all detector modules. To achieve these objectives, calibration runs with known particle sources and cosmic rays were conducted. The integration of the UT into the LHCb data acquisition system is currently ongoing and being completed in the time of the writing of this thesis, with the read-out electronics interfaced with the central trigger and data processing infrastructure. The integration process included extensive testing to ensure seamless data flow and synchronization with other detector components. I have been involved in each one of these phases throughout the past three years. My first contribution to the project was the assembly, testing, and installation of the data concentrator boards (DCBs). These objects are components of the UT's Data acquisition (DAQ) system, which is responsible for reading out data from the silicon microstrip sensors, processing this data, and transmitting it to the central data processing units. The overall system also consists of Front End Electronics (FEE) and Back-End Electronics, which handle further data processing and transmission to the data storage and analysis infrastructure. It combines the data received from Front End (FE) ASICs on several e-links (i.e. electrical links, high-speed serial data links) and transmits via optical fibres to TELL40 read-out boards in the counting rooms. After additional processing and filtering by the HLT, the data is transmitted to the data acquisition system. It is made of several components: Field-Programmable Gate Arrays (FPGAs), which collect data from multiple front-end chips, apply error correction, data compression, and format conversion before sending the data downstream to the back-end electronics, Data Transmission Modules, which utilize optical fibres for data transmission to ensure high bandwidth and low latency. Protocols such as GBT (GigaBit Transceiver) are employed for reliable data communication, and several other systems whose role is to regulate the voltage and monitor the circuits, monitor the radiation and the cooling system to adjust the temperature in case of need. A picture of a DCB can be found in Figure 4.6, and a scheme representing the data flux within a DCB is depicted in Figure 4.7. A careful observer may find some differences between the photograph (4.6) and the scheme (4.7): the VTTx/VTRx are not installed. These are assembled on optical mezzanines as in Figure 4.8. While there is always only one Versatile Transceiver (VTRx), which handles both transmitting and receiving data, the number of Twin-Transmitter (VTTx) modules varies throughout all the DCBs in the detector. This variation depends on the specific layer (x, u, v) and the distance from the beam pipe. The VTRx is essential for ensuring bidirectional communication between the detector and the control system, whereas the VTTx modules, which are responsible solely for data transmission, are used in differing quantities based on the data transmission requirements of each layer and the spatial constraints imposed by their proximity to the beam pipe. In layers closer to the beam pipe or with higher data transmission needs, more VTTx

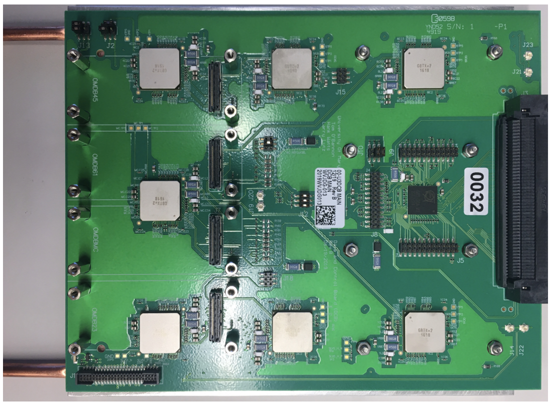

Figure 4.6: Picture of a DCB towards the completion of its assembly.

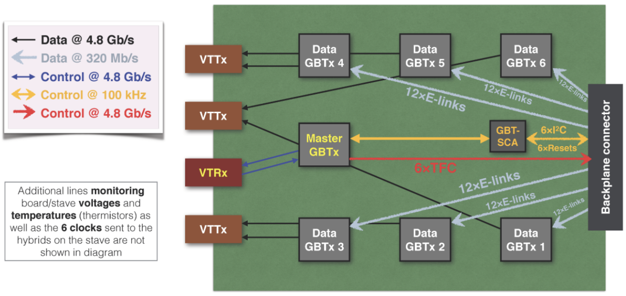

Figure 4.7: Diagram of the data flowing through a DCB.

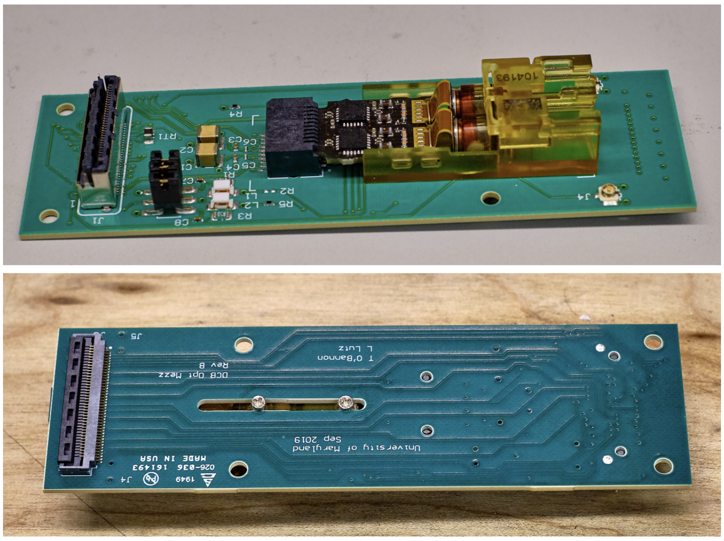

Figure 4.8: An assembled mezzanine, where the black component in a yellow casing is a VTTx.

modules are deployed to handle the increased data flow effectively. My task in this first phase was to assemble the DCBs with the correct number of mezzanines and test them to ensure the installation allowed communication with the board. The second step was populating the frame, which would have hosted the detector. A picture taken after filling up the frame can be found in Figure 4.9. The installation process consisted of placing the DCBs in the slot assigned based on how many VTTx they had and connecting them to the backplane, a large printed circuit board (PCB) with multiple connectors, serving as a communication highway for the DCBs, facilitating data transfer and power distribution. Subsequently, testing the powering system: each DCB is powered by two tensions, one at 1.5V powering the FPGAs on the boards, one at 2.5V I/O interfaces and other peripheral components. It allowed us to confirm that both the DCB installations were correctly performed and that the low-voltage circuits were well put in place. Another test performed with a board emulating a flex allowed us to confirm that the DCBs were correctly communicating with the future staves.

4.3.1 Noise study

Once the installation was completed, the noise produced by the sensors was analysed in two steps: directly after the assembly, and after the positioning in the cavern. The comparison between these two sets of data is needed to confirm that the conditions of a protected place, such as the clean room, are also preserved after the final installation. Noise in the UT can originate from several sources. The first and most irreducible one is the electronic noise generated by the front-end electronics, including thermal noise from resistors and flicker noise from transistors. This type of noise can affect the baseline signal levels and overall signal integrity. A slightly more reducible one is the radiation-induced noise: due to the high-radiation environment of the LHC, radiation can induce additional noise in the electronic components, potentially leading to spurious signals or fluctuations in the data. This is one of the reasons the sensors are cooled down to -10°C to fight against the inevitably increasing radiation damage of the sensors through time. Another source comes from electromagnetic interference (EMI) from other nearby electronic systems, which can couple into the UT electronics, introducing noise, but it is kept under control and is nevertheless not the biggest source of noise.

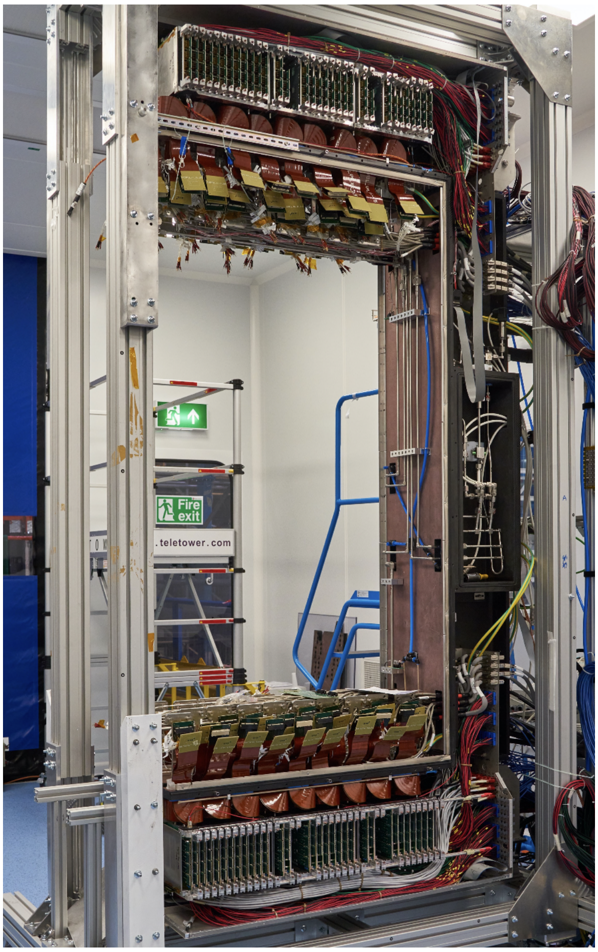

Figure 4.9: UT A-side frame after installing the DCBs in the clean room.

The two datasets are composed of ADCs (Analog to Digital Converter) values which result from the conversion of the analog signals received by the detector's readout. Another important concept is the pedestal, which refers to the baseline level of the signal when no particle interaction is detected. It is computed as

$$\text{Pedestal} = \frac{1}{N}\sum_{i=1}^{N} S_i,$$

where S_i is the signal from the readout channel in event i, and N is the total number of events. It represents the average noise level and offset without a true signal. Regular calibration runs are conducted to measure and update the pedestal values; the Mean Common Mode (MCM) refers to the average value of the ADC baseline shared across multiple channels of the detector, it is computed as

$$\text{MCM} = \frac{1}{M}\sum_{j=1}^{M}(S_j - \text{Pedestal}_j),$$

where S_j is the signal from the readout channel j in the event, Pedestal_j is the pedestal for readout channel j, and M is the number of readout channels in the group. This common mode noise can result from shared power supplies, ground loops, or external interference affecting multiple channels similarly. Finally, the study has been conducted on ADC Common Mode Subtracted (CMS), taking the result of the subtraction of the pedestal and the MCM to the raw ADCs. Tests involved the ASICs separately to find out whether one of their 128 channels was noisier than others or not sending any data, but also scans along the staves were performed to understand if there was a dependency on the position of the sensors on the *y*-axis or the *x*-axis. Finally, the behaviour of the sensors was also checked when a charge was injected.

By-ASIC study

Looking at Figure 4.10, it is possible to observe the behaviour of a fully functioning ASIC. The study was carried out comparing the ADC raw and the ADC CMS. As expected, the noise of the 128 channels is distributed as a Gaussian due to the central limit theorem, which states that the sum of many independent, random noise sources tends to form a normal distribution. A Gaussian fit has been used to discriminate channels of ASICs in which the noise was larger than expected. An example can be found in Figure 4.11. As a filter, channels were tagged as anomalous if their noise deviated from the Gaussian distribution for more than 5σ. This study allowed us to identify many anomalous channels and intervene to recover or mask them.

By position study

Another interesting observation that could have been made with the dataset at disposal has been the scan of the noise of the ASIC belonging to the same stave, so keeping the *x* coordinate fixed and moving along the *y* coordinate. This also verified how the chips on the same stave were behaving, as on the areas close to the beampipe, more than one typology of sensor was installed in the same stave (Figure 4.3). In Figure 4.12 it is possible to find the noise comparison of the closest stave to the beampipe (Figure 4.12a), where all the four types of sensors are installed, and of the stave the furthest from the beampipe (Figure 4.12b), where only Type A sensors are installed. The green histograms from both plots are filled with the noise coming from Type A sensors, while the peak at lower values in the blue histogram, reports the noise from the

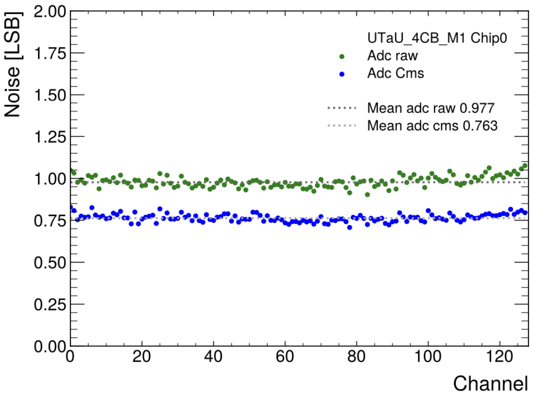

Figure 4.10: Noise distribution by the channels of the ASIC 0 of the sensor UTaU 4CB M1 in the clean room.

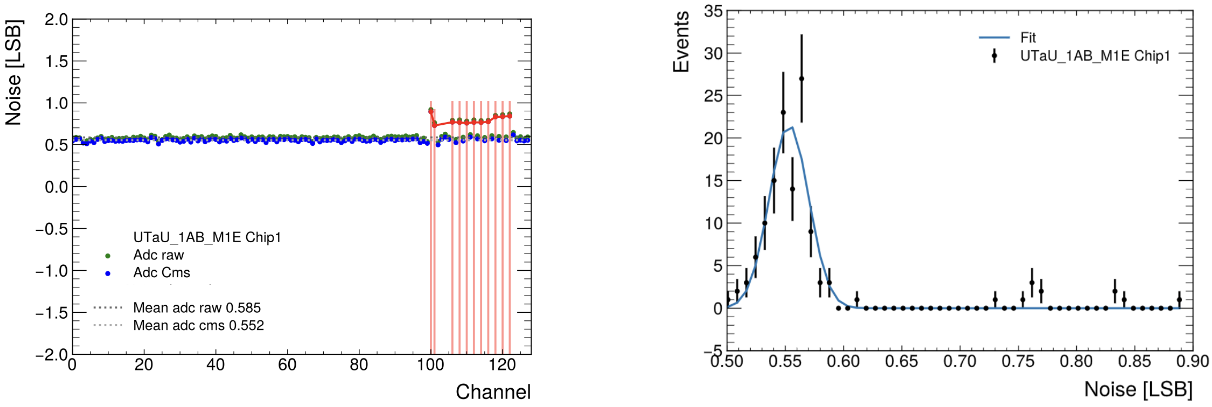

(a) Noise distribution as a function of the channels of the ASIC 1 of the sensor UTaU 1AB M1E in the clean room.

(b) Noise distribution of the ASIC 1 of the sensor UTaU 1AB M1E in the clean room.

Figure 4.11: Noise study performed by ASIC, example of an ASIC with anomalous channels.

sensors Type C and D, while the second peak collects the noise coming from the Type B sensors. The trend is expected as it follows the length of the sensors and the input capacitance to the preamplifier. The scan was also performed horizontally, i.e. keeping the y-axis fixed and moving along the x. The noise plots are reported in Figure 4.13. The same considerations reported for the previous case apply.

MIP injection study

One last set of data, as previously anticipated, was collected when an equivalent charge to a MIP (Minimum Ionizing Particle) was injected. This allowed us to test the charge amplification in the ASICs, one by one, and check whether it was properly working. The SALT chips, indeed, include an internal test pulse generator designed to facilitate this process. The test pulse generation mechanism simulates signal inputs by injecting a known charge into the front-end amplifier of the ASICs. By precisely controlling the amplitude and timing of these electrical pulses, we could mimic the signals produced by real particle interactions in the silicon strip detector. In Figure 4.14, a comparison of a fully working ASIC and a non-amplificating one is found. This study not only allowed us to flag channels that were not amplifying the signal correctly but also allowed us to observe if the amplification was happening uniformly. Some anomalous cases are reported

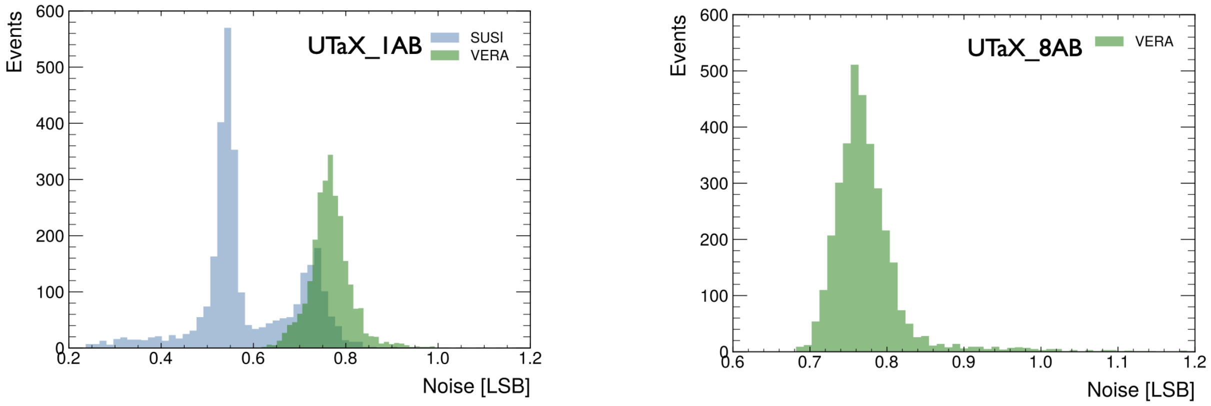

(a) Noise distribution by the stave, bottom part of the stave 1, installed on the straight layer closer to the interaction point.

(b) Noise distribution by the stave, bottom part of the stave 8, installed on the straight layer closer to the interaction point.

Figure 4.12: Noise study performed by the stave. The label "SUSI" and "VERA" refers to the chip, on which were positioned respectively 8 or 4 ASICs.

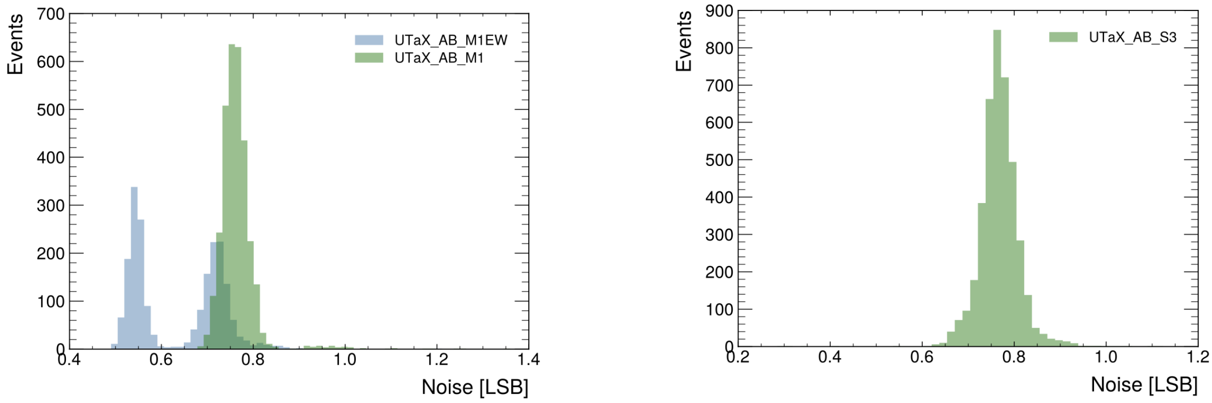

(a) Noise distribution by the module number, bottom part with respect to the beampipe, first row, straight layer, side closer to the interaction point.

(b) Noise distribution by the module number, bottom part with respect to the beampipe, last row, straight layer, side closer to the interaction point.

Figure 4.13: Noise study performed by the module number.

in Figure 4.15.

Comparison clean room and cavern

Noise datasets were collected also after the installation of the detector in the cavern, to check that the situation remained unchanged. No notable behaviour changes were observed. To complete the report and close this section, the reader can compare Figure 4.10 with Figure 4.16, as one plots the noise measured in the clean room and the second the noise measured in the cavern of the same ASIC.

4.3.2 Monitoring

The last task in which I was involved working for this sub-detector was helping develop the monitoring system. Continuous and precise monitoring helps in maintaining data quality, detecting anomalies, and ensuring that the collected data is reliable for further analysis. The software

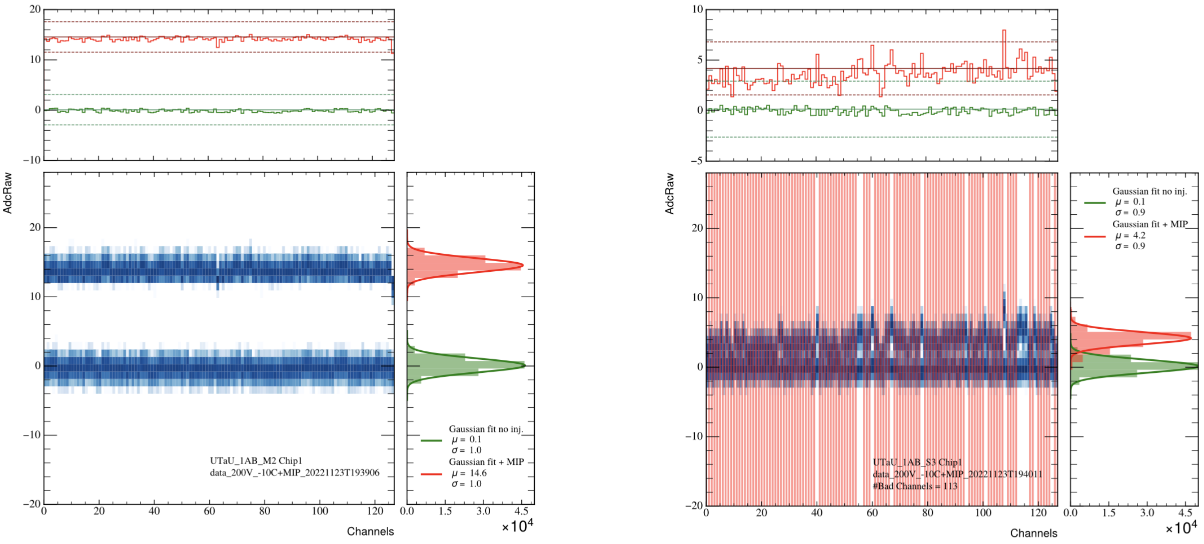

(a) Correctly working ASIC.

(b) Non-amplifying ASIC.

Figure 4.14: Noise distribution by ASIC. The blue bi-dimensional plots represent the behaviour of the ASIC when no charge is injected (lower stripe) and when a charge +MIP is injected (upper stripe). In the right side, the one-dimensional histogram representing the noise in the two cases is plotted, with the fitted value in the legend. In the upper side, is instead reported the noise by channel, where the dotted lines represent the $\pm 5\sigma$ limit.

used in LHCb is Monet [61]. Monet is designed to provide real-time monitoring of the data collected by the detector. It processes data from the detector into various types of histograms (1D, 2D, and profile histograms) and shows them online, such that they are available both for experts during software development for the sub-detectors, but also for the shifters in the control room, allowing to preserve high quality in data taking periods. Histograms are then saved and accessible anytime. My contribution was mostly technical, therefore, to save the reader from long and abstract technicalities, I will just show the result of what I contributed to. The plot in Figure 4.17 represents the hits in the UT during one of the runs in April.

4.4 UT performance in 2024

Since last year, substantial progress has been made in commissioning the UT detector at LHCb. After the installation of the detector, a period of intense firmware development was necessary to address initial DAQ instabilities encountered both with and without the beam. In October 2023, the team successfully collected 69 seconds of data with very high ADC thresholds, albeit with low efficiency, during the last day of Pb-Pb data taking. Significant advancements in firmware development helped cure the DAQ instabilities experienced without the beam. Enhancements were made to the Experiment Control System (ECS). The Front End (FE) SALT ASICs were extensively studied in local mode, resulting in significant setup improvements. Additionally, the detector safety monitoring system was improved and online monitoring enhancements were made. Coarse time alignment was achieved on 450 MeV beams in mid-March. Challenges with DAQ instabilities during the initial period of 6.8 TeV operation were addressed through firmware improvements and the implementation of the BxVeto, allowing Tell40s to recover during empty bunch crossings (BXs). Fine-time alignment was completed, followed by another round of FE

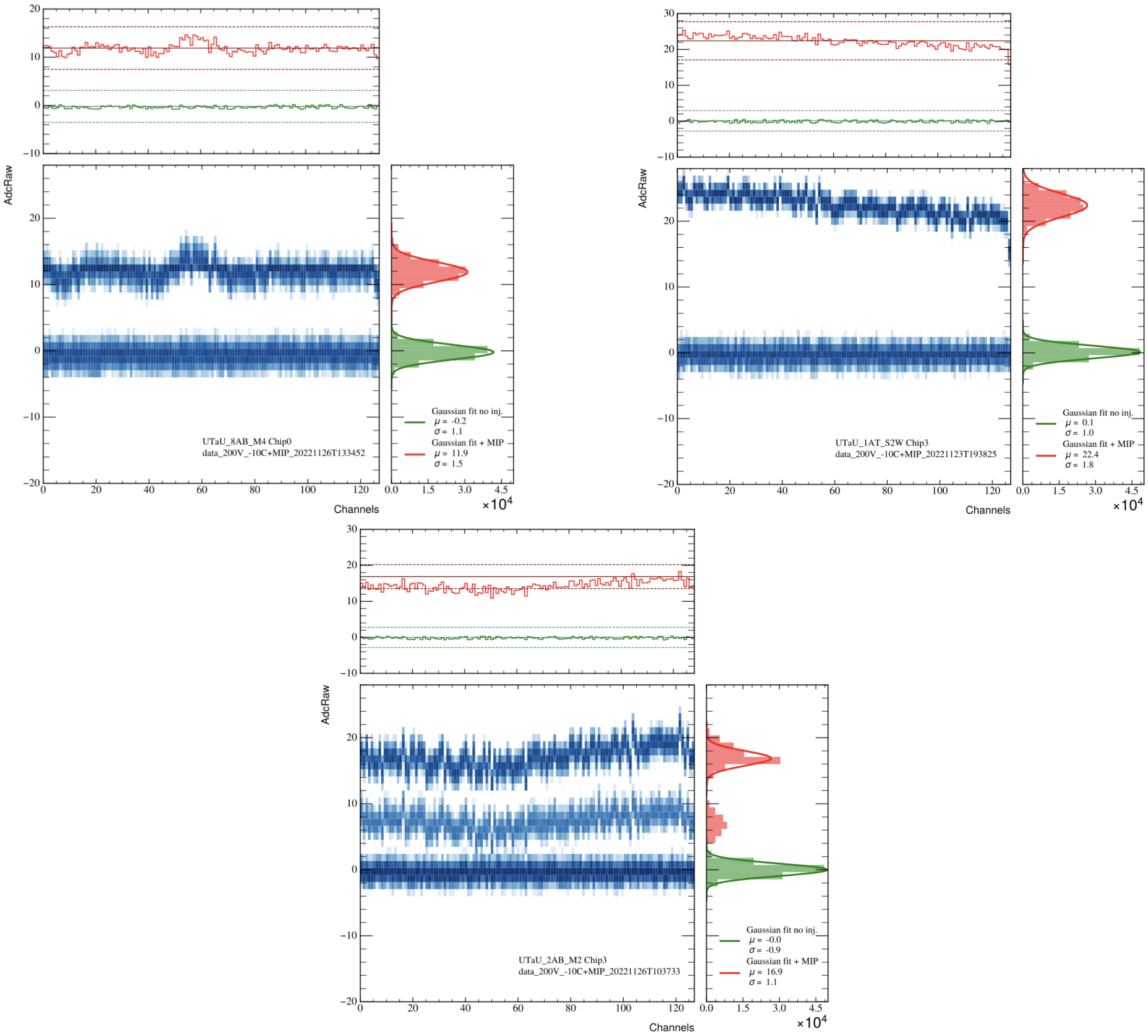

Figure 4.15: Anomalous amplifying behaviours.

retuning. Minor improvements were also made in offline software and Monte Carlo simulations. Regarding ADC baseline and signal, baseline noise and signal sizes were as expected, with a typical ADC threshold for a MIP, for an example run, a reference in Figure 4.18 is reported. ADC distributions obtained with low thresholds indicated that going below the Zero Suppressed threshold of 5 ADCs is useful, especially in the inner detector part with thinner sensors and smaller electronic noise. Stable DAQ was achieved thanks to the large density of Tell40s. The space alignment of the UT with respect to the Velo-SciFi was improved. Currently, space alignment does not limit UT efficiency except for the outermost sensors. However, there is room for improvement, with ongoing work to further refine the alignment. The result of a preliminary study can be found in Figure 4.19. Efforts to determine efficiency indicated that remaining inefficiencies could be reduced with further FE tune-ups. Extending the Hlt2 UT match to two or more layers would produce a more hardware fault-tolerant algorithm, leveraging the fine Y-segmentation of the UT. Efficiency versus DAQ stability showed that when almost all BXs were filled with beam, BxVeto became ineffective, leading to DAQ instabilities. The source of these instabilities was identified as Tell40 servicing outer hybrids, which occasionally overran firmware

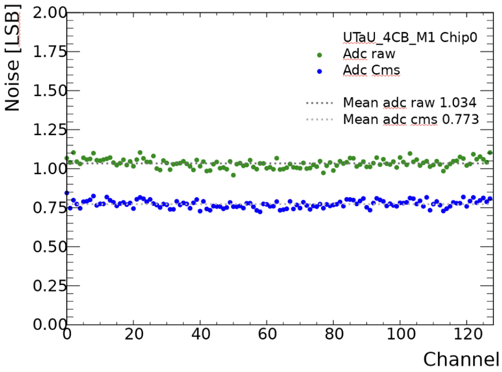

Figure 4.16: Noise distribution by the channels of the ASIC 0 of the sensor UTaU 4CB M1 in the cavern.

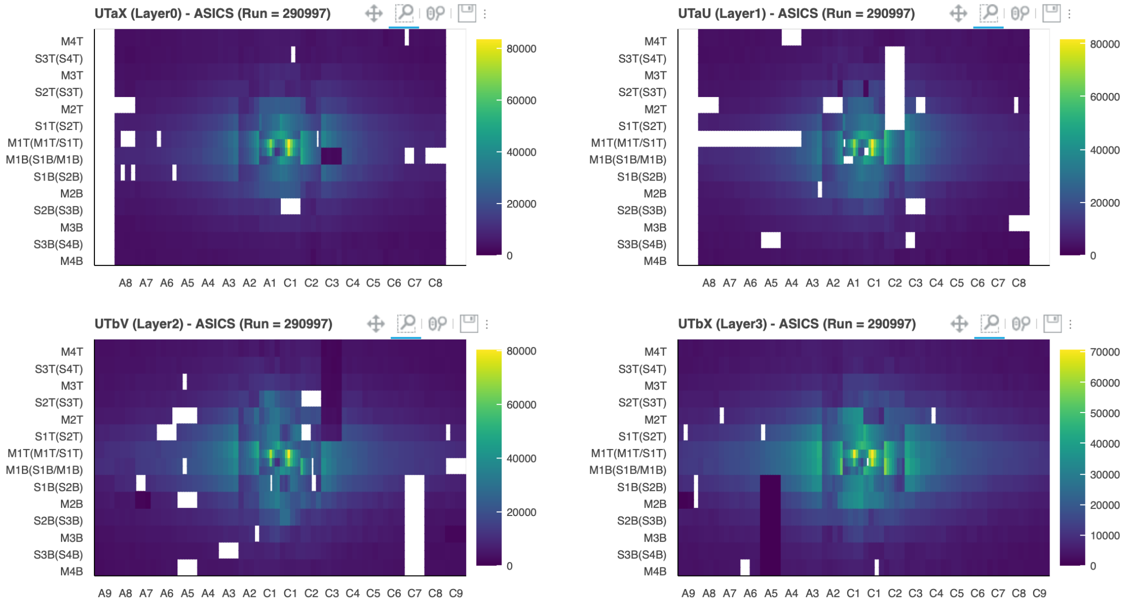

Figure 4.17: Screenshot of the Monet page containing the hit maps of the UT. The four layers are displayed.

buffers. In summary, the UT is operational, achieving about 95% efficiency on long tracks with standard software. Efficiency is expected to increase with pending Low Voltage Regulators repair and further FE tune-ups. The UT can operate in long runs up to μ=4.8, and firmware fixes or additional Tell40s could facilitate setup and operation, especially at higher mu. Integration with HLT triggers is planned to leverage the improvements in mass resolution and ghost track reduction. A representation of a typical event display in the UT is shown in Figure 4.20.

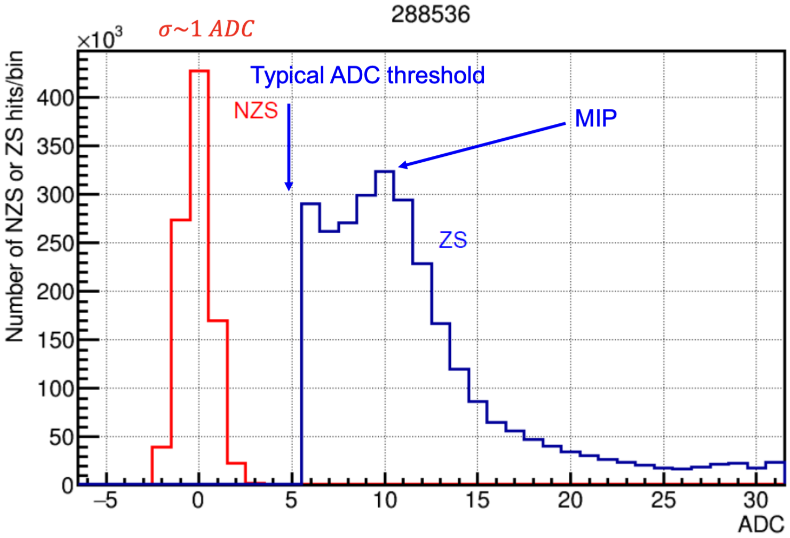

Figure 4.18: ADC values distribution collected during run 288536. It shows the expected value for the MIP in the Zero Suppressed (ZS) data, the typical threshold applied to reduce noise at 5 ADC, and the distribution of the Non-Zero Suppressed (NZS) ADCs.

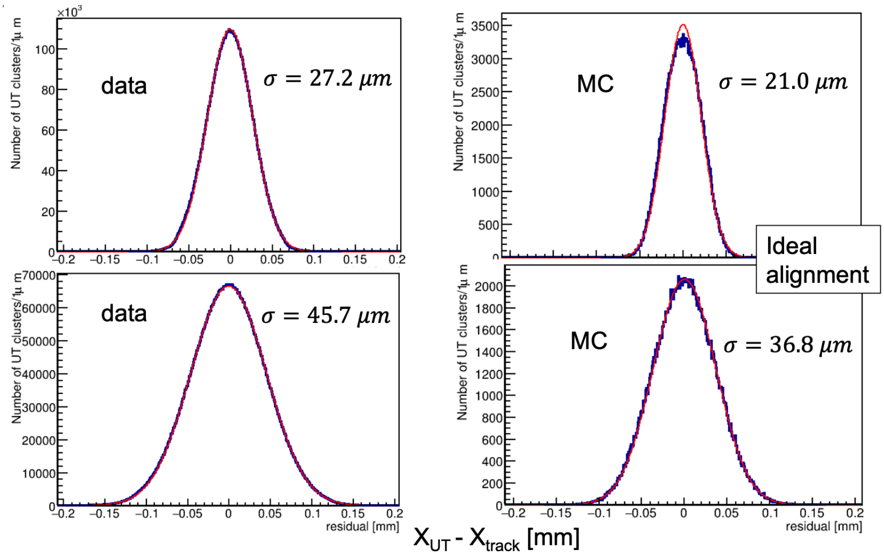

Figure 4.19: Study on space alignment performed comparing data and MC. The upper row concerns inner sensors, which have a smaller pitch, the lower row is for the outer sensors.

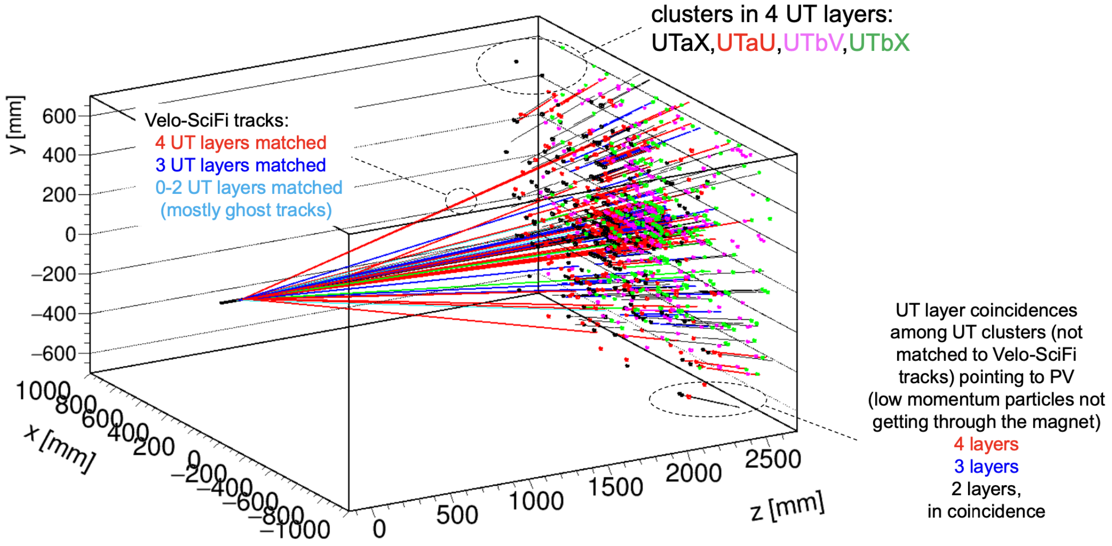

Figure 4.20: Event display showing the tracks being "seen" by the Velo, UT and SciFi, also reporting the number of layers activated by each event.

5

The $\Lambda_b^0 \to D^0 ph^-$ analysis

This chapter aims to present the strategy and work done towards studying the $\Lambda_b^0 \to D^0 ph^-$ decays. The dataset used comes from pp collisions recorded by the LHCb detector at center-of-mass energies of $\sqrt{s} = 7$, 8, and 13 TeV, totaling an integrated luminosity of $9\,\mathrm{fb}^{-1}$. The chapter begins with details on the preselection applied to the datasets, starting from the data processing stage, known as stripping, up to the first offline selection performed by maximising a Figure of Merit. A description of a fundamental tool used throughout the analysis, Monte Carlo simulations, is provided. Section 5.3.1 delves into classification algorithms used to suppress the most contaminating backgrounds. Finally, the efficiency of the applied selection is studied in preparation for the fit to data, performed on several samples, concluding with systematic uncertainties and the presentation of the results. It is important to highlight the significance of this measurement, as it not only presents previously unseen invariant mass spectra of these decays but also marks the first attempt to measure *CP* violation in these channels. Diving deeply into the quantities of interest, specifically, the measured *CP* asymmetries, are efficiency-weighted ones. This means that after extracting the yields of the decays of interest, as *sWeights* - detailed more in the following -, these are weighted by the efficiencies that the selection has on the sample. The observable becomes

$$A = \frac{\sum_i w_i^{\mathrm{GLW},\Lambda_b^0}/\epsilon_i^{\mathrm{GLW},\Lambda_b^0} - \sum_i w_i^{\mathrm{GLW},\overline{\Lambda}_b^0}/\epsilon_i^{\mathrm{GLW},\overline{\Lambda}_b^0}}{\sum_i w_i^{\mathrm{GLW},\Lambda_b^0}/\epsilon_i^{\mathrm{GLW},\Lambda_b^0} + \sum_i w_i^{\mathrm{GLW},\overline{\Lambda}_b^0}/\epsilon_i^{\mathrm{GLW},\overline{\Lambda}_b^0}}. \tag{5.1}$$

This formula will be applied to the decay processes $\Lambda_b^0 \to D^0 pK^-$, with D^0 subsequently decaying to either K^-K^+ or $\pi^-\pi^+$. Additionally, it will be applied to $\Xi_b^0 \to D^0 pK^-$, where the D^0 meson decays into the same final states. Moreover, the study incorporates $\Lambda_b^0 \to D^0 p\pi^-$ as a control channel, which allows for testing the analysis strategy in various steps before applying it to the signal channel. The reconstruction of Λ_b^0 candidates employs preprocessed stripping lines (see Section 5.1.1), which already provide candidates of the form $\Lambda_b^0 \to D^0 ph^-$, where h represents either K or π. Using the DaVinci framework, a versatile data processing and analysis tool used for event selection and classification in LHCb, we select $\Lambda_b^0 \to D^0 pK^-$ and $\Lambda_b^0 \to D^0 p\pi^-$candidates, with the D^0 decaying into $K\pi$, KK, or $\pi\pi$. The decay reconstruction is performed initially by the pattern recognition and track fitting algorithms that identify and refine track parameters from detector data. PID detectors then distinguish between different types of particles. Primary vertices (PVs) are reconstructed by clustering and fitting tracks from the collision point. Secondary vertices, where decays occur, are identified and fitted using displaced tracks. Decay candidates are formed by combining tracks and applying kinematic and geometric constraints to ensure consistency with expected decay patterns. Further constraints to the reconstruction are applied with the DecayTreeFit (DTF) tool [62], which uses a Kalman filter [63]. DTF is a tool designed for fitting decay chains and determining the kinematic properties of particles. This tool considers all particle information of the mother particle, its daughters, their momentum vectors, covariance matrices, and decay vertices. The Kalman filter is a mathematical algorithm for refining particle trajectories and improving precision. Events where the DTF fails or diverges are discarded; successful events are stored in ROOT [64] files. Constraints are applied to reduce the fit's degrees of freedom and improve the precision, including a constraint to the origin vertex. A second DTF is performed with an additional constraint on the Λ_b^0 mass, ensuring the Dalitz plot boundaries are respected. These software tools enable precise reconstruction and selection of decay events, which are essential for detailed analysis and accurate measurements.

5.1 Preselection

As mentioned in the introduction to this chapter, several meanings are hidden by preselection: the ones applied in the data processing, the ones applied to make the decays respect kinematic constraints and those obtained to reduce the data sample before using the classification algorithms. In this Section, a description of each one is presented.

5.1.1 Stripping Line

Stripping lines are a fundamental component of the LHCb experiment's data processing pipeline, designed to efficiently filter and select relevant events from the enormous amount of collision data produced at each Run. When protons collide at the LHC, the interaction results in many events, not all of which are pertinent to the specific physics analyses LHCb aims to perform. To manage this, the stripping process applies predefined selection criteria to the raw data, isolating events of interest and discarding less relevant ones. This significantly reduces the data volume, making it more manageable for storage and further analysis. The stripping lines come into play after the HLT performs the initial event selection. The HLT makes rapid decisions on whether an event should be retained based on high-level features. Once events pass this initial trigger, they undergo more detailed processing through the stripping lines. These lines are sophisticated algorithms embedded within the LHCb software framework, each tailored to target specific decay channels or physics phenomena. For example, a stripping line might be configured to identify events where a Λ_b^0 baryon decays into a D^0 meson, a proton, and a hadron, with the D^0 further decaying into kaons or pions: it is the case for the one adopted in this analysis, i.e. `Lb2D0PHD02HHBeauty2CharmLine` [65]. The selection criteria used in stripping lines are based on various physical properties and event topologies, such as invariant mass windows, PID probabilities derived from the RICH detectors, and the geometric topology of the decay. The ones for the adopted stripping line are reported in Table 5.1. Starting from charged particles, the reconstruction line builds up the decay chain to identify the mother particle Λ_b^0. Utilising two-body decays as components, it selects a $\Lambda_b^0 \to D^0\Lambda$ decay, where Λ further decays into ph. The Λ baryon is chosen also for its wide mass, not reducing the sensitivity to the signal. To prevent potential distortions in the physical variables during the DTF process, the Λ is substituted with a $\Lambda(1405)$, which has a reasonably short lifetime, ensuring more accurate results in the reconstruction and analysis.

Tracks	min p_{T}	0.1 GeV/c
	min p	1.0 GeV/c
	max $\chi^2_{\text{track}}/n_{\text{DoF}}$	3
	min χ^2_{IP}(PV)	4
D^0	min $\sum_{\text{daughters}} p_{\mathrm{T}}$	1.8 GeV/c
	min χ^2_{IP}(best PV)	36
	max DOCA (tracks)	0.5 mm
	max $\chi^2_{\text{vertex}}/n_{\text{DoF}}$	10
	max $\vert$m$_{D^0}$ - m$_{\text{PDG}}\vert$	0.1 GeV/c^2
Λ_b^0	min $\sum_{\text{daughters}} p_{\mathrm{T}}$	5.0 GeV/c
	min τ(best PV)	0.2 ps
	min χ^2_{IP}(best PV)	25
	max $\chi^2_{\text{vertex}}/n_{\text{DoF}}$	10
	min cosθ_{dira}(best PV)	0.999
	m$_{\Lambda_b^0}$	$[5.2, 7.0]$ GeV/c^2
p	min ΔLL$_{p\pi}$	-10
K	min ΔLL$_{K\pi}$	-10
π	max ΔLL$_{K\pi}$	20

Table 5.1: Selection criteria applied in the `Lb2D0PHD02HHBeauty2CharmLine` stripping line.

The cuts applied in a stripping line are intentionally loose to minimally impact the signal decay while significantly reducing background noise. These cuts ensure kinematically reasonable tracks and include a requirement on the χ^2/n_{DoF} (goodness of fit) to strengthen the decision. Additionally, a cut on χ^2_{IP}(PV), the significance of the impact parameter, is applied, calculated as the $\Delta\chi^2$ for the PV fit with and without the track, being small for prompt tracks, i.e particle tracks that originate directly from the PV without any significant displacement, indicating they are produced in the initial collision rather than from secondary decays. The D^0 particle's track is determined using similar criteria, with additional focus on the decay vertex of its daughters. A cut on the maximum DOCA for the daughter tracks a possible vertex, confirmed by the goodness of the vertex fit ($\chi^2_{\text{vertex}}/n_{\text{DoF}}$). A symmetric mass window around the true D^0 mass filters sensible D^0 candidates. For the Λ_b^0, a minimum lifetime τ relative to the best PV indicates that the Λ_b^0 has travelled a measurable distance. By best PV is defined the collision point that is most likely associated with a given decay, selected based on criteria such as spatial proximity to the decay vertex, track association, and statistical consistency. To ensure the Λ_b^0 originates from the best PV, its direction angle θ_{dira}, the angle between the Λ_b^0 momentum direction and the vector from the Λ_b^0 vertex to the best PV, must be close to zero.

5.1.2 Trigger

Given the extremely high collision rate at the LHC of 40 MHz, the LHCb detector cannot capture all events. Therefore, criteria are established to determine if an event is retained (because it holds “interesting” physics) or not. The LHCb trigger system manages this decision. The initial step in this process is the Level 0 hardware trigger, L0. As a hardware trigger, only events that meet its criteria are stored and proceed to the next processing phase. This makes the trigger a good ally to reducing background: by applying trigger flags offline to the dataset, one can significantly diminish the background events while maintaining a good quantity of signal events. Triggered Independent of Signal (TIS) and Triggered On Signal (TOS) are classifications used to describe how an event has been selected by the trigger system. An event is classified as TIS if it would have been triggered by particles or activity unrelated to the signal decay of interest. This ensures that the trigger condition does not bias the analysis of the signal decay, allowing for an unbiased measurement of the signal properties. Conversely, an event is classified as TOS if triggered directly by the particles from the signal decay, meaning the signal decay itself satisfies the trigger conditions. This is useful for studies where the properties of the signal need to be correlated with the trigger decision. Some events can overlap, being both TIS and TOS, allowing comprehensive data selection without bias. The L0Hadron trigger is a component of the L0 trigger system that identifies hadronic events. It is crucial for selecting events with high transverse energy (E_T) hadrons, which are significant for studying decays involving hadrons, such as $\Lambda_b^0 \to D^0 p K^-$. The L0Hadron trigger uses information from the HCAL to measure the E_T of hadronic clusters. The process involves forming clusters of energy deposits in the calorimeter corresponding to hadronic showers, calculating E_T of each cluster, and comparing it against a predefined threshold. Events with clusters exceeding this threshold are selected by the L0Hadron trigger and passed to the HLT for further processing. The selection used in this analysis for the L0 is `L0Global_TIS or L0HadronDecision_TOS`. At the HLT2 level, events are triggered by the `Hlt2(Topo2Body|Topo3Body|Topo4Body|Charm2Body)BBDTDecision` in Run 1 and `Hlt2Topo(2|3|4)BodyDecision` in Run 2. For an event to reach HLT2, it must first be triggered at HLT1 by `Hlt1TrackDecision` in Run 1, and by `Hlt1(Track|TwoTrack)MVADecision` in Run 2 for TOS. Alternatively, events can be triggered by `Hlt1(DiMuon|SingleMuon|Track)` in both Run 1 and Run 2 for TIS. The selection applied at HLT1 level can be found in Table 5.2. The

TrackMVA
$p_\mathrm{T} > 1000$ MeV$/c$
$p_\mathrm{T} < 25000$ MeV$/c$
$\chi^2_{IP} > 7.4$
$\chi^2_{track} > 2.5$
Ghost probability < 0.2

TwoTrackMVA
$p > 5000$ MeV$/c$
$p_\mathrm{T} > 500$ MeV$/c$
$\chi^2_{track} > 2.5$
$\chi^2_{IP} > 4$
$2 < \eta < 5$
$\chi^2_{vtx} < 10$
DIRA > 0
$m_{corr} > 1000$ MeV$/c^2$

Table 5.2: Selection applied by the chosen Hlt1 lines.

HLT2 lines mentioned (`Topo2Body`, `Topo3Body`, `Topo4Body`, and `Charm2Body` `BBDTDecision`) apply selections primarily based on the kinematic properties of the reconstructed particles and their decay topologies. These selections utilise Boosted Decision Trees (BDTs) to efficiently identify and select events with specific characteristics, such as decays involving multiple charged particles. For the `Topo2Body`, `Topo3Body`, and `Topo4Body` lines, the focus is on multi-body decays. These lines are trained to target decays involving at least two, three, or four charged particles, respectively. The selection criteria include minimal requirements on the transverse momentum, impact parameter, and vertex fit quality of the reconstructed decay products. The Charm2Body line targets two-body decays involving charm particles, so it is ad-hoc for the D^0 decay. It similarly employs BDTs to distinguish signal from background by evaluating kinematic variables such as momentum and decay vertex quality.

5.1.3 Particle identification

To ensure the validity and usefulness of the tracks, it is essential that all hadrons from the decay are registered in the RICH detectors, providing reliable PID information. Additionally, there are specific kinematic constraints to consider. Firstly, due to the detector acceptance, tracks with pseudorapidities (η) outside the interval [2.0, 4.5] are deemed unreasonable. Secondly, PID calculations are heavily dependent on the momentum of the particles. A minimum momentum (p_{min}) is required because particles must have sufficient energy to radiate Cherenkov light. Furthermore, a maximum momentum (p_{max}) can be useful because hadrons with momentum above a certain threshold become indistinguishable. This upper limit might not be necessary for two-body decays due to more precise kinematic constraints, but it is crucial for three-body decays to ensure discriminability. For instance, protons should have momenta within 9.0 GeV/c to 200.0 GeV/c, while kaons (K) and pions (π) should be within 3.0 GeV/c to 200.0 GeV/c. Ensuring tracks meet these criteria is essential for accurate reconstruction and analysis of decay events. The constraints help to filter out tracks that fall outside the detector's acceptance range or do not provide reliable PID information. This process improves the overall quality of the data used in subsequent analyses, leading to more precise measurements and a better understanding of the underlying physics.

5.1.4 Additional preselections

The preselection steps applied thus far have utilised relatively loose kinematic cuts. We now introduce additional, more stringent requirements to further refine the data and reduce background noise. In Figure 5.1, we compare the Monte Carlo distributions for the fit probability P_{fit} of the DecayTreeFit, the Λ_b^0 decay-length significance $S_{\text{decay length}}(\Lambda_b^0)$, and the D^0 decay-length significance $S_{\text{decay length}}(D^0)$, which is defined as the decay length divided by its error. For events resembling the signal, the fit probability is expected to follow a uniform distribution in the range [0.0, 1.0], whereas background events typically peak at zero. This background peak is extremely narrow and can be better visualised by applying the natural logarithm. Consequently, we implement a cut of $\ln(P_{\text{fit}}(\Lambda_b^0)) > -10$. Similarly, the logarithm is applied to the Λ_b^0 decay-length significance for improved discrimination, resulting in a cut of $\ln(S_{\text{decay length}}(\Lambda_b^0)) > 2.0$. Finally, also the $\ln(S_{\text{decay length}}(D^0))$ is selected, as first step in reducing a highly polluting background, of which there will be an extensive discussion in Section 5.3. In Figure 5.1, the distributions of the just mentioned variables and the impact of the selection are shown for the MC of $\Lambda_b^0 \to [K^-\pi^+]_{D^0} pK^-$, $\Lambda_b^0 \to [K^-\pi^+]_{D^0} p(\pi^-)_{K^-}$ misidentification, and $\Lambda_b^0 \to pK^-\pi^+K^-$ charmless. The notation used here for the misidentification implies that a certain rate of pions from the favoured $\Lambda_b^0 \to D^0 p\pi^-$ are misidentified as kaons, causing a shifted mass peak on the right sideband of the signal peak. By charmless events, throughout the whole document, I will refer to events in which the Λ_b^0 is directly decaying to a four-body final state, without the intermediate D^0 meson. Additionally, all daughter tracks must not have corresponding hits in the muon chambers to ensure the purity of the sample. These cuts are essential for enhancing the signal-to-noise ratio in our analysis, allowing for more precise measurements and reliable results. The chosen logarithmic transformations help in stretching narrow background peaks, thus facilitating more effective background suppression. By tightening the mass window and excluding tracks with muon chamber hits, we improve the accuracy of the reconstructed decay events, ultimately leading to a more robust analysis.

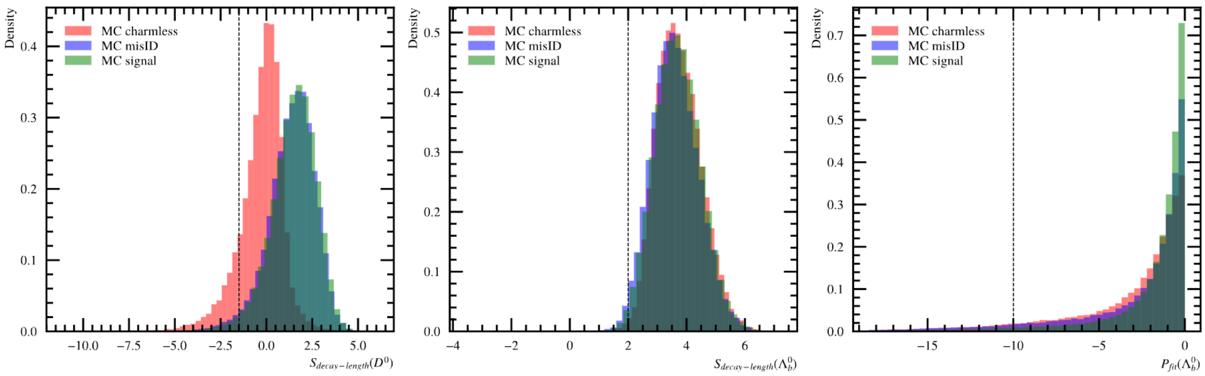

Figure 5.1: From left to right, the distributions of $\ln(S_{\text{decay length}}(D^0))$, $\ln(S_{\text{decay length}}(\Lambda_b^0))$ and $\ln(P_{\text{fit}}(\Lambda_b^0))$, for the Monte Carlo of $\Lambda_b^0 \to [K^-\pi^+]_{D^0}pK^-$, $\Lambda_b^0 \to [K^-\pi^+]_{D^0}p(\pi^-)_{K^-}$ mis-identification, and $\Lambda_b^0 \to pK^-\pi^+K^-$ charmless are shown.

5.2 Simulation

Monte Carlo (MC) simulations are an indispensable tool in the LHCb experiment, providing a detailed understanding of particle interactions and detector responses. These simulations play a crucial role in various aspects of data analysis, from detector design and optimisation to interpreting experimental results. MCs are employed for several reasons in high-energy physics (HEP). Firstly, they help understand how particles interact with the various components of the detector, enabling the calibration of detector responses. Secondly, simulations are used to calculate detection efficiencies and acceptance corrections, which are critical for determining cross-sections and branching ratios. Thirdly, MC simulations assist in estimating and modelling background processes, allowing for the separation of signal from noise. Fourthly, they enable the study of systematic uncertainties by varying parameters within the simulations and observing the effects on the results. Throughout this thesis, MCs have been used extensively for many of the listed reasons. The LHCb experiment utilises several specialised software packages for MCs. Pythia [17] is a general-purpose event generator used to simulate collisions at the LHC. It models the initial proton-proton interactions, generating the primary hard scatterings and subsequent parton showers. EvtGen [15] is a package specifically designed to simulate the decays of heavy-flavor hadrons, such as B mesons. It allows for detailed modelling of decay chains and incorporates various decay models and form factors. Geant4 [16] is a toolkit for the simulation of the passage of particles through matter. It is used to simulate the interactions of generated particles with the detector material, modelling processes such as electromagnetic and hadronic interactions. Gauss [14] is the LHCb-specific simulation framework integrating Pythia, EvtGen, and Geant4. It handles the entire simulation workflow, from event generation to tracking particles through the detector. MCs at LHCb rely on fundamental physical principles and probabilistic methods. The simulations of proton-proton collisions are based on QCD. Pythia models the parton distribution functions (PDFs) within protons, the hard scatterings, and the resulting parton showers. After parton showers, partons (quarks and gluons) undergo hadronisation, forming bound states known as hadrons. Pythia includes models for this non-perturbative process, generating mesons and baryons from the partons. EvtGen uses decay models based on the Standard Model of particle physics. It incorporates detailed angular distributions and form factors for decays, allowing an accurate representation of physical decay processes. Geant4 simulates the interactions of particles with the detector materials. This includes electromagnetic interactions (such as ionisation and Bremsstrahlung for charged particles) and hadronic interactions (such as scattering and absorption). The core of Monte Carlo methods is random sampling. Probabilities of various physical processes are used to randomly generate outcomes of interactions and decays, ensuring a realistic representation of possible events. The workflow of MCs at LHCb involves several stages. The initial proton-proton collisions are simulated using Pythia, producing a set of primary particles. The primary particles, especially heavy-flavor hadrons, are then decayed using EvtGen. This stage models the decay chains and generates secondary particles. Geant4 takes over to simulate the passage of these particles through the LHCb detector. This involves tracking each particle step-by-step and modelling their interactions with the detector materials. The physical interactions are then converted into electronic signals through a process known as digitisation, mimicking the response of the actual detector electronics. Finally, the simulated signals are processed using the same reconstruction algorithms as the real data, allowing for a direct comparison between simulation and experiment. MCs are vital for the LHCb experiment, providing a detailed and accurate representation of particle interactions and detector responses. By integrating various specialised software packages and relying on well-established physical principles, these simulations enable precise measurements and the validation of theoretical models.

5.2.1 MC matching

MCs are reconstructed similarly to actual experimental data, which can sometimes distort the distributions of the pure signal. To understand the true signal distributions, matching the reconstructed particle objects to their original true simulated particles is essential. This process, known as MC matching, is crucial for identifying and studying the true signal in HEP experiments like those conducted at LHCb. In LHCb analyses, a commonly used tool for this task is the `TupleToolMCBackgroundInfo` of the DaVinci framework. This tool facilitates the storage of flag-based information about different physics cases, enabling researchers to filter for true signal candidates effectively. The tool compares the user-defined decay sequence (decay descriptor) with the decay sequence information from the stripping line. It categorises the events into various background and signal categories (BKGCAT), which helps isolate the true signal from background noise. The two primary signal categories defined by `TupleToolMCBackgroundInfo` are:

- **BKGCAT-0** (Signal): This category includes events where the decay $\Lambda_b^0 \to D^0 pK^-$ and its subsequent D^0 decays are fully reconstructed as described in the decay descriptor. All final state particles in this category are matched to their true simulation counterparts.

- **BKGCAT-10** (Quasi-Signal): This category includes events that fulfil the BKGCAT-0 conditions but do not necessarily match the exact decay topology defined in the decay descriptor. Intermediate states may not match, allowing for pseudo Λ particles from the stripping line.

While this tool efficiently classifies events, it can sometimes misclassify the $\Lambda_b^0 \to D^0[pK^-]_\Lambda$ decay structure from the stripping line, mixing BKGCAT-0 and BKGCAT-10 categories. To address this, the analysis employs a custom algorithm where the particle types of the particles themselves, their mothers, and grandmothers (if existent) are matched to ensure accurate classification. The MC matching process is vital for several reasons. First, it helps in understanding the efficiency of the detector and the reconstruction algorithms in identifying and reconstructing various types of particles. It is possible to calculate detection efficiencies and acceptance corrections by comparing reconstructed events with known Monte Carlo truth information, a fundamental process for determining cross-sections and branching ratios. Second, MC matching assists in estimating and modelling background processes, allowing for the separation of signal from noise. This is essential for background estimation and helps improve the precision of the measurements. Third, it enables the study of systematic uncertainties by providing a benchmark against which different reconstruction and analysis strategies can be tested.

5.2.2 MC weighting

MC reweighting is a technique for ensuring that simulated data accurately represents real experimental data. This process involves adjusting the MC events to correct for discrepancies between the simulated and observed data distributions. The primary goal of reweighting is to improve the agreement between MC simulations and actual data, leading to more accurate and reliable physics results. MC reweighting is particularly important because the conditions and environments in which particles are detected can vary, leading to differences in the detector response. Reweighting the MC samples can minimise these differences, ensuring that the simulated data matches the real experimental conditions more closely. This improves the accuracy of efficiency calculations, background estimations, and systematic uncertainty studies. The weights computed are used to correctly compute the efficiencies on the Dalitz plot, and for this reason, it is imperative to have the MC corrected on the Dalitz variables, as the resonances seen in data are not correctly reproduced in the MC samples. In this analysis, the reweighting process was carried out by fitting the selected data with the nominal model - the procedure to reach this stage will be explained later in the document - and using the sPlot technique to extract the signal distribution from the data. The sPlot technique [18] is a statistical tool used to disentangle signal and background components in a dataset. It leverages a multivariate fit to separate the contributions of different processes based on discriminating variables. By applying sPlot, we can obtain a pure signal distribution, free from background contamination, which is essential for accurate reweighting. Once the signal distribution was obtained, the next step involved using the Dalitz plot variables, i.e. $\mathrm{m}^2(D^0p)$ and $\mathrm{m}^2(ph^-)$ as the reweighting variables. The actual reweighting was performed using the BDTReweight library [66]. This library employs Boosted Decision Trees (BDT), a machine learning technique, to compute the reweighting factors. BDTs are a type of ensemble learning method that combines multiple decision trees to improve prediction accuracy. They are particularly well-suited for handling complex, non-linear relationships in the data, making them an ideal choice for reweighting purposes. In the BDTReweight procedure, the BDT algorithm is trained on the $\mathrm{m}^2(D^0p)$ and $\mathrm{m}^2(ph^-)$ distributions of the control channel, learning the differences between the MC simulation and the real data. Once trained, the BDT can be used to compute weights for the MC events, effectively correcting the $\mathrm{m}^2(D^0p)$ and $\mathrm{m}^2(ph^-)$ distributions to match those observed in the real data, see Figure 5.2. Applying these weights to the MC data ensures that the reweighted simulated events have the same kinematic properties as the real events, reproducing the resonances observed in data. This improved agreement between the MC and data enhances the accuracy of the analysis, as now MC can be used to discriminate several types of background, more to follow in the next paragraph.

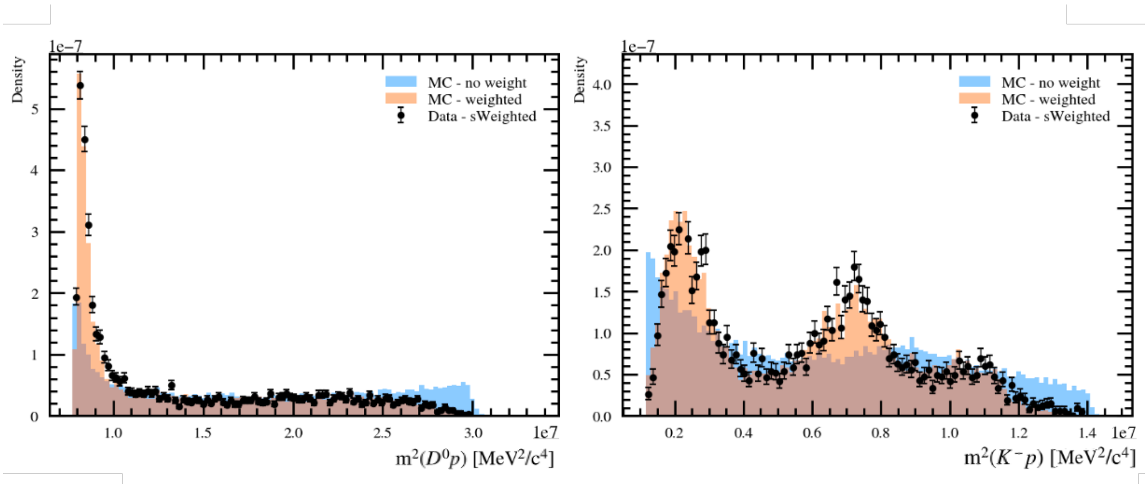

Figure 5.2: Comparison between MC without weights applied, MC with weights applied computed from data using the method explained in the text, and *sWeighted* dataset. Example of $\Lambda_b^0 \to [K^-\pi^+]_{D^0} pK^-$ candidates, coming from 2018 data taking, magnet up polarity, only preselection applied.

5.2.3 MC PID calibration

The simulation does not perfectly reproduce the PID response, so calibration is necessary. Within LHCb, a few approaches are available, as described in [67] and [68], all based on dedicated calibration samples recorded in parallel to the data taking. The PIDCorr package, described in [69] and provided within the LHCb collaboration, is used in this analysis. The PID correction process involves resampling the PID response from the MC simulation based on the distributions obtained from calibration samples. This approach uses a variable transformation technique to adjust the PID variables in the MC data, aligning them with the experimental data. The PID resampling technique replaces the original MC PID response with a response generated from parameterised PID distributions derived from real data. This method is particularly useful for analyses that require PID information in multivariate analyses (MVA). The resampling tool can handle both binned and unbinned probability density functions (PDFs), depending on the specific analysis needs. However, there are some limitations to this approach. The PID variables depend on several parameters, such as momentum (p), pseudorapidity (η), and the number of tracks (Ntracks), which can introduce correlations that are often ignored in simpler resampling methods. Moreover, the PID variables for a given track are correlated; for instance, a kaon-like track is less likely to be pion-like, and these correlations need to be preserved during resampling to maintain the accuracy of the simulation. To address these challenges, a variable transformation technique is used. Instead of using a random resampling method, the transformation adjusts the PID variables based on their distribution in the calibration sample. If a PID variable x_{MC} in the MC data follows a certain distribution $p_{\text{MC}}(x|p,\eta,Ntr)$, the corrected variable x_{corr} is obtained through a transformation that ensures it follows the distribution $p_{\text{exp}}(x|p,\eta,Ntr)$ observed in the experimental data. The transformation process ensures that the corrected PID variables x_{corr} remain strongly correlated with the original MC variables x_{MC}. This preservation of correlations is crucial because it ensures that any systematic uncertainties and correlations present in the MC data are retained after the PID correction.

5.3 Reducing backgrounds

Machine learning (ML) has become an indispensable tool in HEP, offering powerful techniques to analyse vast amounts of data and uncover subtle patterns that traditional methods might miss. The integration of ML in HEP has significantly enhanced our ability to perform complex tasks such as particle identification, event reconstruction, and background discrimination, thereby improving the precision of measurements and the discovery potential of experiments like those conducted at LHCb.

Classification algorithms are a fundamental ML component used extensively in HEP to distinguish between different types of events. These algorithms are trained on labelled datasets where each event is identified as a signal or background(s). The goal is to develop a model to classify events based on their features accurately. Standard classification algorithms used in HEP include decision trees, random forests, support vector machines (SVM), and neural networks. These algorithms analyse various event features — such as momentum, energy deposition, and particle trajectories — to assign probabilities to each event being a signal or background. For example, in a search for a rare decay process, a classification algorithm would learn the characteristic signatures of the decay (signal) and differentiate them from the more common processes (background). Discriminating backgrounds is one of the uses of ML algorithms in this thesis, as it allows us to isolate the signal events from different sources of background noise. During the training phase, the algorithm identifies patterns and correlations in the data that are indicative of background events and learns to distinguish these while enhancing the signal. One of the key metrics used to evaluate the performance of classification algorithms in this task is the Receiver Operating Characteristic (ROC) curve. The ROC curve is a graphical representation that illustrates the trade-off between the true positive rate (signal efficiency) and the false positive rate (background rejection) for different decision thresholds. The area under the ROC curve (AUC) is often used as a summary statistic to quantify the overall performance of the classifier — the closer the AUC is to 1, the better the classifier. Overtraining, or overfitting, is a significant concern when using ML. It occurs when a model learns the noise in the training data rather than the underlying signal pattern. An overtrained model performs exceptionally well on the training dataset but poorly on independent test datasets because it has essentially memorised the training data rather than generalising from it. There are several techniques to avoid it and tests that can be performed to ensure one is not incurring overtraining. Cross-validation is one such method, where the data is divided into multiple subsets, and the model is trained and validated on different combinations of these subsets. Visual inspection of the ROC curves on both training and validation datasets can also help identify overtraining: if the performance on the training set is significantly better than on the validation set, overtraining is likely.

5.3.1 Boosted Decision Tree

Boosted Decision Trees (BDTs) are a powerful ML technique widely used for tasks such as classification and regression. They combine the simplicity of decision trees with the robustness of ensemble learning to create accurate and efficient models. A decision tree is a model that uses a tree-like structure to make decisions based on input features, but it can suffer from overfitting, becoming too complex and performing poorly on unseen data. Boosting is an ensemble learning technique that aims to improve the performance of weak learners—models that are only slightly better than random guessing—by combining multiple weak learners to create a strong learner.

In the context of decision trees, boosting involves training several trees sequentially, where each new tree focuses on correcting the errors made by the previous ones. The boosting algorithm most commonly used with decision trees is AdaBoost (Adaptive Boosting) or Gradient Boosting. The process starts by training an initial decision tree, then increases the weight of the misclassified instances, and trains a new tree on this weighted dataset. This process is repeated for a specified number of iterations or until the performance improvement plateaus. The final model is a weighted sum of all the individual trees, with more emphasis placed on trees that performed well. BDTs are particularly effective for large sets of data due to their ability to handle large and complex datasets with many features.

Binary vs multi-class classification

One of the standout features of XGBoost (Extreme Gradient Boosting) [70] is its ability to handle multiclass classification tasks effectively. This capability is particularly advantageous in HEP, where it is often necessary to discriminate between multiple sources of background noise while identifying signal events. XGBoost's robust framework allows it to classify more than one category simultaneously, significantly enhancing its utility in complex datasets. In this analysis, XGBoost's multiclass classification feature is used to discriminate between two distinct sources of background. This approach proved highly effective, significantly improving the precision of our results. The key to this success lies in XGBoost's implementation of the softmax function for multiclass classification. The softmax function is a generalisation of the logistic function to multiple classes. In binary classification, the logistic function outputs a probability that a given input belongs to a particular class. In contrast, the softmax function outputs a probability distribution over multiple classes, ensuring that the probabilities sum to one. Mathematically, for an input vector z with elements z_i representing the raw output scores (logits) for each class i, the softmax function is defined as:

$$\text{softmax}(z_i) = \frac{e^{z_i}}{\sum_j e^{z_j}}$$

This function transforms the raw scores into a normalised probability distribution, allowing the classifier to handle multiple categories simultaneously. Using XGBoost with the softmax function, the model is trained on a labelled dataset containing signal events and two background sources. The model's ability to output a probability distribution for each event category allowed for nuanced decision-making, improving the classification accuracy. This approach was particularly beneficial in identifying subtle differences between background sources that traditional binary classifiers might miss. The performance of XGBoost in this multiclass setup was outstanding. It effectively discriminated between the two sources of background, significantly enhancing the signal-to-noise ratio. This improvement is crucial for the subsequent analysis stages, where precise background subtraction is essential for accurate measurements. By leveraging XGBoost's multiclass classification capability and the softmax function, I was able to achieve a more refined and accurate classification.

5.3.2 Training

As previously mentioned, the training method used in this analysis is supervised learning, where labelled datasets are provided as inputs to the algorithm. To achieve this, MC emulating signal candidates and the charmless background are given. For training the BDT to identify the combinatorial background, real data from the right sideband of the Λ_b^0 mass distribution is utilised.

Specifically, data with $m(D^0pK^-) > 5850$ MeV/c^2 is used for this purpose. Choosing the right variables for training a BDT is fundamental for the model's performance in discriminating between signal and background events. The selection process involves identifying features that effectively capture the underlying differences between these events. This analysis used a combination of kinematic and geometric variables to train the BDT, ensuring a comprehensive representation of the events' characteristics. The variables chosen for the analysis can be grouped into three categories: variables directly used as inputs, variables transformed into their logarithmic equivalent, and variables of which the cosine has been computed.

Direct Variables

- `VTX_SIG`: The vertex significance, which indicates the distance between the reconstructed vertices of Λ_b^0 and D^0, divided by the uncertainty of this measurement.
- `myDTF_Lb_ctau_sig`: The decay time significance of the Λ_b^0 baryon, variable computed containing the decay vertices.
- `myDTF_D0_ctau_sig`: The decay time significance of the D^0 meson, variable computed containing the decay vertices.
- `myDTF_Lb_PT`: The transverse momentum of the Λ_b^0 baryon, variable computed containing the decay vertices.
- `myDTF_D0_PT`: The transverse momentum of the D^0 meson, variable computed containing the decay vertices.
- `myDTF_Xm_PT`: The transverse momentum of the h^- meson (K^- or π^-, depending on the channel), variable computed containing the decay vertices.
- `myDTF_D0_Xm_PT`: The transverse momentum of a decay product from the D^0 meson (K^- or π^-, depending on the channel), variable computed containing the decay vertices.
- `myDTF_D0_Xp_PT`: The transverse momentum of a decay product from the D^0 meson (K^+ or π^+, depending on the channel), variable computed containing the decay vertices.
- `myDTF_Lb_Eta`: The pseudorapidity of the Λ_b^0 baryon, variable computed containing the decay vertices.

Logarithmic Variables

- `Lb_IPCHI2_OWNPV`: The χ^2 of the impact parameter of the Λ_b^0 baryon with respect to the primary vertex (PV), indicating the significance of its displacement.
- `Xm_IPCHI2_OWNPV`: The χ^2 of the impact parameter of the h^- meson (K^- or π^-, depending on the channel).
- `pplus_IPCHI2_OWNPV`: The χ^2 of the impact parameter of the proton.
- `D0_IPCHI2_OWNPV`: The χ^2 of the impact parameter of the D^0 meson.
- `D0_Xm_IPCHI2_OWNPV`: The χ^2 of the impact parameter of a decay product from the D^0 meson (K^- or π^-, depending on the channel).

- `D0_Xp_IPCHI2_OWNPV`: The χ^2 of the impact parameter of a decay product from the D^0 meson (K^+ or π^+, depending on the channel).

Cosine of Variables

- `Lb_DIRA_OWNPV`: The direction angle, representing the cosine of the angle between the Λ_b^0 momentum and the vector from the PV to the decay vertex, which indicates alignment with the primary vertex.

Each variable plays a significant role in differentiating between signal and background events. The kinematic variables (transverse momentum and pseudorapidity) help in understanding the motion and spatial distribution of particles. The geometric variables (impact parameter χ^2 values and decay time significances) provide insights into the vertex quality and lifetime of particles, to identify long-lived particles such as Λ_b^0 and D^0 hadrons. The angular variable (direction angle) helps in assessing the alignment of the particle's momentum with the primary vertex, aiding in the identification of genuine decay events. The variables just listed are displayed in Figure 5.3. By training the BDT with these carefully selected variables, the aim is to maximise the separation between signal and background distributions. The BDT's ability to handle complex, multi-dimensional data allows it to capture subtle differences in these variables, leading to an effective discrimination of background noise and enhancing the purity of the signal sample. The performance of the BDT is evaluated by comparing the distributions of each variable across different event categories, ensuring that the model accurately reflects the physical characteristics of the data. The datasets are split into training and testing samples to ensure robust training. The BDT is trained on the training sample, and its performance was evaluated on the testing sample. This approach helps in assessing the model's generalisation capability. Furthermore, the potential overtraining of the BDT is evaluated by comparing the scores obtained on the training and testing samples, ensuring that the model performs consistently well on the data that is not used for the training. In Figure 5.4, the comparison of BDT scores for training and testing samples can be found for Run 2 $\Lambda_b^0 \to [K^-\pi^+]_{D^0}p\pi^-$. The results for all the other decays can be found in Appendix A. As previously mentioned, the ROC curve helps assessing the robustness of the BDT model. The plots presented here show the ROC curves for different comparisons: charmless background vs. signal, combinatorial background vs. signal, and charmless vs. combinatorial background. Figure 5.5a demonstrates the ROC curve for charmless background versus signal. The mean AUC for this comparison is 0.92, indicating a strong ability to discriminate between these two categories. When treating charmless as the positive class, the AUC is 0.93, whereas treating the signal as the positive class yields an AUC of 0.90. Figure 5.5b shows the ROC curve for signal versus combinatorial background. Here, the mean AUC is 0.93, with the AUC being 0.91 when the signal is the positive class and 0.94 when the combinatorial background is the positive class. This high AUC value signifies excellent discriminative power of the BDT between signal and combinatorial background. Figure 5.5c illustrates the ROC curve for charmless versus combinatorial background. The mean AUC for this comparison is 0.97, with the charmless as the positive class yielding an AUC of 0.98 and combinatorial as the positive class yielding an AUC of 0.97. This indicates an almost perfect discrimination capability between charmless and combinatorial backgrounds. Finally, evaluating the importance of the variables in a BDT model helps in understanding which features contribute most significantly to the classification process. This evaluation involves analysing how each variable impacts the decision-making process of the BDT. Typically, the importance of a variable is measured by the total reduction in the Gini

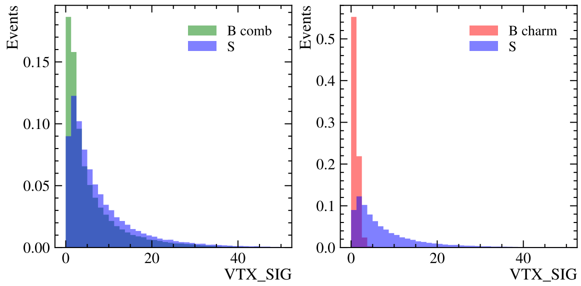

(a) On the left, comparison of the `VTX_SIG` distribution of the combinatorial background and the MC signal candidates. On the right, comparison of the `VTX_SIG` distribution of the charmless background and the MC signal candidates.

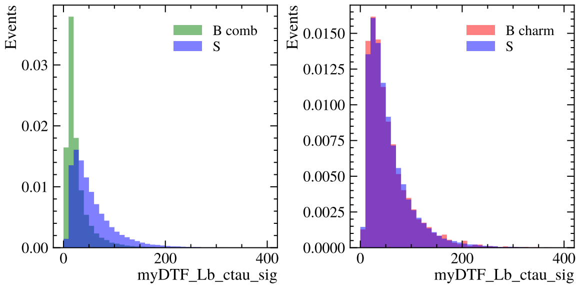

(b) On the left, comparison of the `myDTF_Lb_ctau_sig` distribution of the combinatorial background and the MC signal candidates. On the right, comparison of the `myDTF_Lb_ctau_sig` distribution of the charmless background and the MC signal candidates.

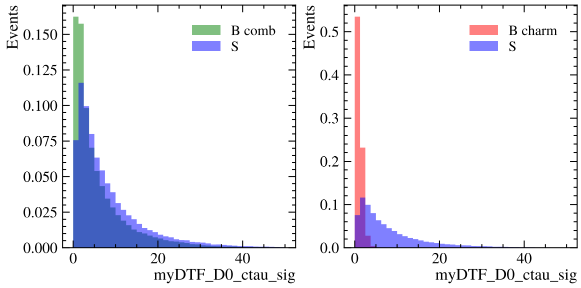

(c) On the left, comparison of the `myDTF_D0_ctau_sig` distribution of the combinatorial background and the MC signal candidates. On the right, comparison of the `myDTF_D0_ctau_sig` distribution of the charmless background and the MC signal candidates.

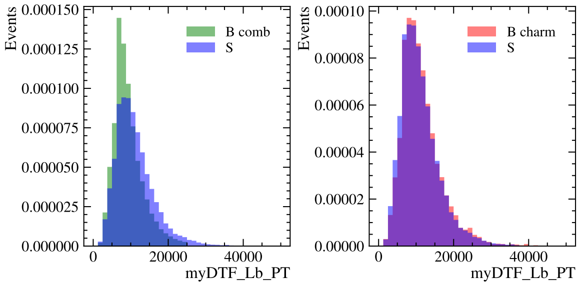

(d) On the left, comparison of the `myDTF_Lb_PT` distribution of the combinatorial background and the MC signal candidates. On the right, comparison of the `myDTF_Lb_PT` distribution of the charmless background and the MC signal candidates.

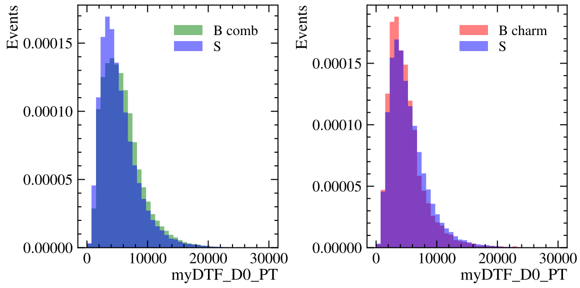

(e) On the left, comparison of the `myDTF_D0_PT` distribution of the combinatorial background and the MC signal candidates. On the right, comparison of the `myDTF_D0_PT` distribution of the charmless background and the MC signal candidates.

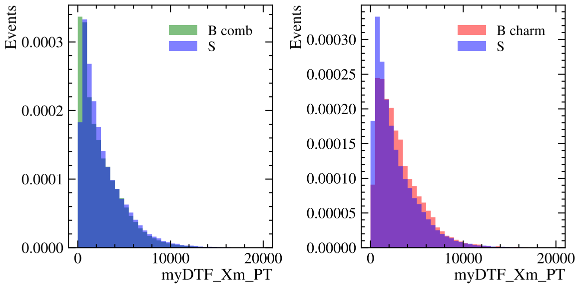

(f) On the left, comparison of the `myDTF_Xm_PT` distribution of the combinatorial background and the MC signal candidates. On the right, comparison of the `myDTF_Xm_PT` distribution of the charmless background and the MC signal candidates.

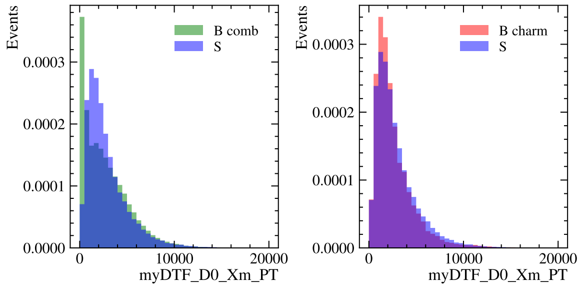

(g) On the left, comparison of the `myDTF_D0_Xm_PT` distribution of the combinatorial background and the MC signal candidates. On the right, comparison of the `myDTF_D0_Xm_PT` distribution of the charmless background and the MC signal candidates.

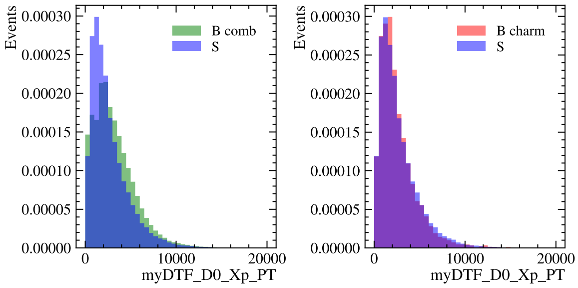

(h) On the left, comparison of the `myDTF_D0_Xp_PT` distribution of the combinatorial background and the MC signal candidates. On the right, comparison of the `myDTF_D0_Xp_PT` distribution of the charmless background and the MC signal candidates.

Figure 5.3: Part 1 of Variables used for the BDT training, normalised in the same range.

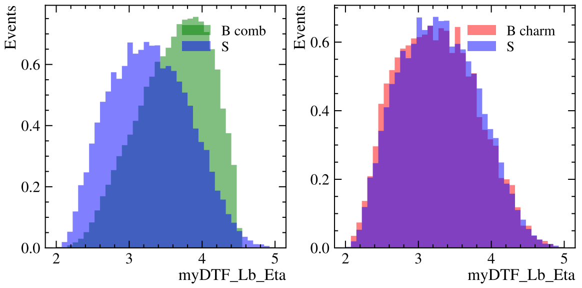

(i) On the left, comparison of the `myDTF_Lb_Eta` distribution of the combinatorial background and the MC signal candidates. On the right, comparison of the `myDTF_Lb_Eta` distribution of the charmless background and the MC signal candidates.

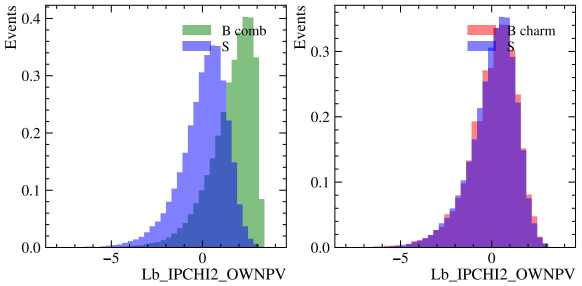

(j) On the left, comparison of the `Lb_IPCHI2_OWNPV` distribution of the combinatorial background and the MC signal candidates. On the right, comparison of the `Lb_IPCHI2_OWNPV` distribution of the charmless background and the MC signal candidates.

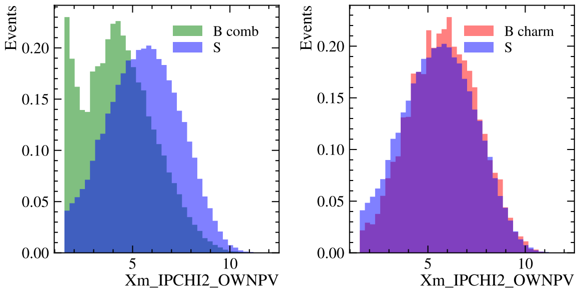

(k) On the left, comparison of the `Xm_IPCHI2_OWNPV` distribution of the combinatorial background and the MC signal candidates. On the right, comparison of the `Xm_IPCHI2_OWNPV` distribution of the charmless background and the MC signal candidates.

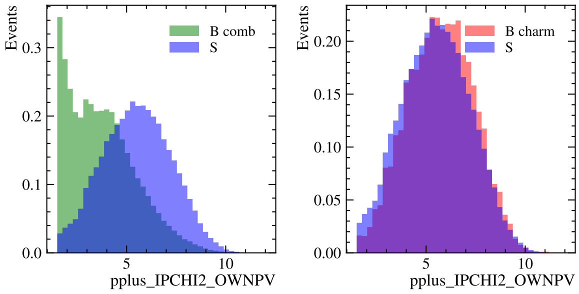

(l) On the left, comparison of the `pplus_IPCHI2_OWNPV` distribution of the combinatorial background and the MC signal candidates. On the right, comparison of the `pplus_IPCHI2_OWNPV` distribution of the charmless background and the MC signal candidates.

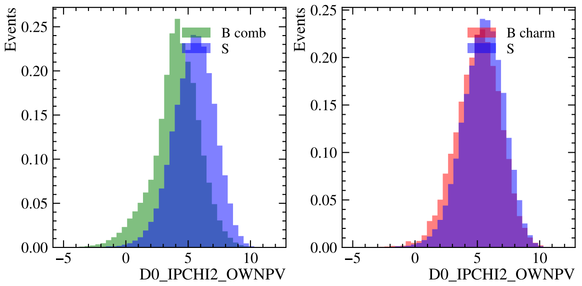

(m) On the left, comparison of the `D0_IPCHI2_OWNPV` distribution of the combinatorial background and the MC signal candidates. On the right, comparison of the `D0_IPCHI2_OWNPV` distribution of the charmless background and the MC signal candidates.

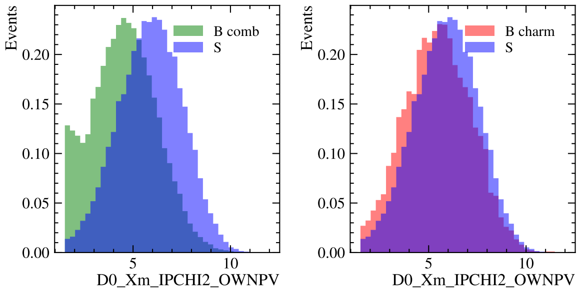

(n) On the left, comparison of the `D0_Xm_IPCHI2_OWNPV` distribution of the combinatorial background and the MC signal candidates. On the right, comparison of the `D0_Xm_IPCHI2_OWNPV` distribution of the charmless background and the MC signal candidates.

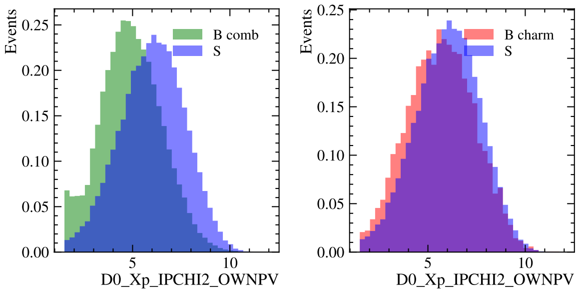

(o) On the left, comparison of the `D0_Xp_IPCHI2_OWNPV` distribution of the combinatorial background and the MC signal candidates. On the right, comparison of the `D0_Xp_IPCHI2_OWNPV` distribution of the charmless background and the MC signal candidates.

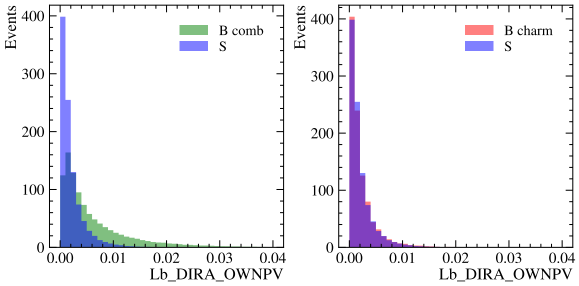

(p) On the left, comparison of the `Lb_DIRA_OWNPV` distribution of the combinatorial background and the MC signal candidates. On the right, comparison of the `Lb_DIRA_OWNPV` distribution of the charmless background and the MC signal candidates.

Figure 5.3: Part 2 of Variables used for the BDT training, normalised in the same range.

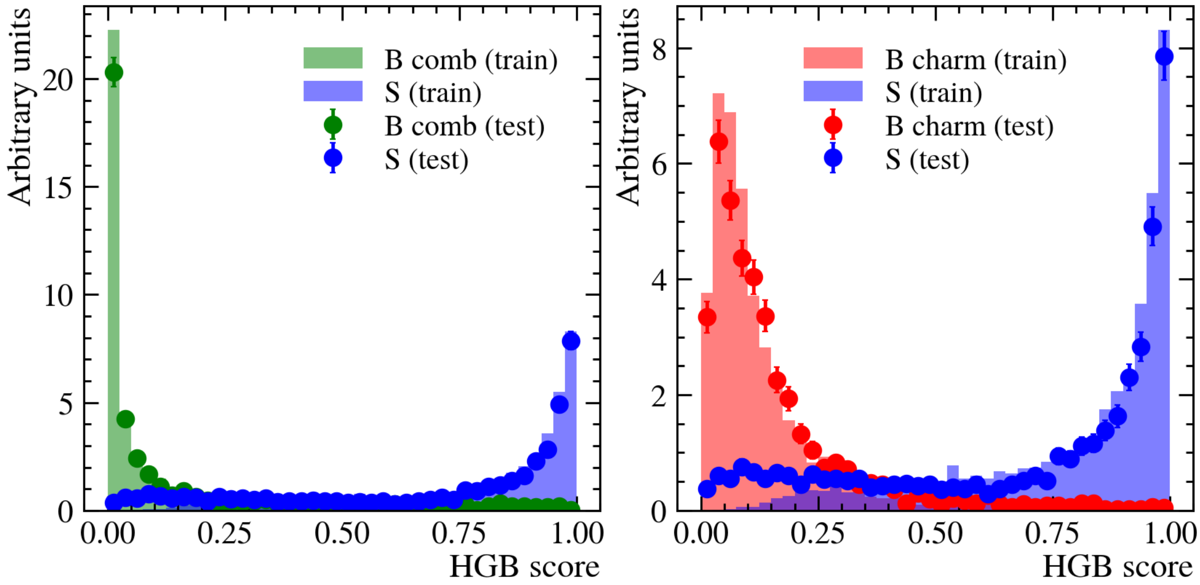

Figure 5.4: Comparison of BDT scores for training and testing samples. The left plot shows the score distribution for the combinatorial background (green) and signal (blue) for both training and testing datasets. The right plot illustrates the score distribution for the charmless background (red) and signal (blue) for both training and testing datasets. The close agreement between the training and testing distributions indicates no significant overtraining, validating the robustness of the BDT model.

impurity or entropy it provides across all the trees in the ensemble. Variables that frequently appear in the top splits of the trees or provide significant impurity reduction are considered more important. This insight allows us to refine the model by focusing on the most influential variables and potentially simplifying the feature set, enhancing the model's performance and interpretability. The ranking of the variables which had a higher impact on the classification skills of the model can be found in Figure 5.6. The results presented here pertain specifically to the Run 2 control channel, which is Cabibbo-favored. However, it is important to note that a separate BDT was trained for each decay channel and for each data-taking period (Run 1 and Run 2). This approach ensures that the classification models are finely tuned to the specific characteristics of each dataset, allowing for optimised performance in discriminating between signal candidates and various background sources. By training individual BDTs for each channel and run, we achieve robust and reliable classification across all analyses, enhancing the overall precision and effectiveness of the study.

5.3.3 Optimisation of the selection

In this paragraph, further details about the strategy adopted to enhance signal events over background events are presented. The approach to achieving this result has been using a Figure of Merit (FOM). The FOM is a quantitative metric that balances the trade-off between maximising signal efficiency and minimising background contamination. By evaluating different selection cuts based on the FOM, it is possible to identify the optimal set of criteria that improves the signal-to-background ratio. The choice of FOM depends on the specific goals and context of the analysis. A widely used FOM in particle physics is the signal significance, often defined as $S/\sqrt{S+B}$, where S represents the number of signal events and B represents the number of background events passing the selection cuts. This FOM aims to maximise the statistical signifi-

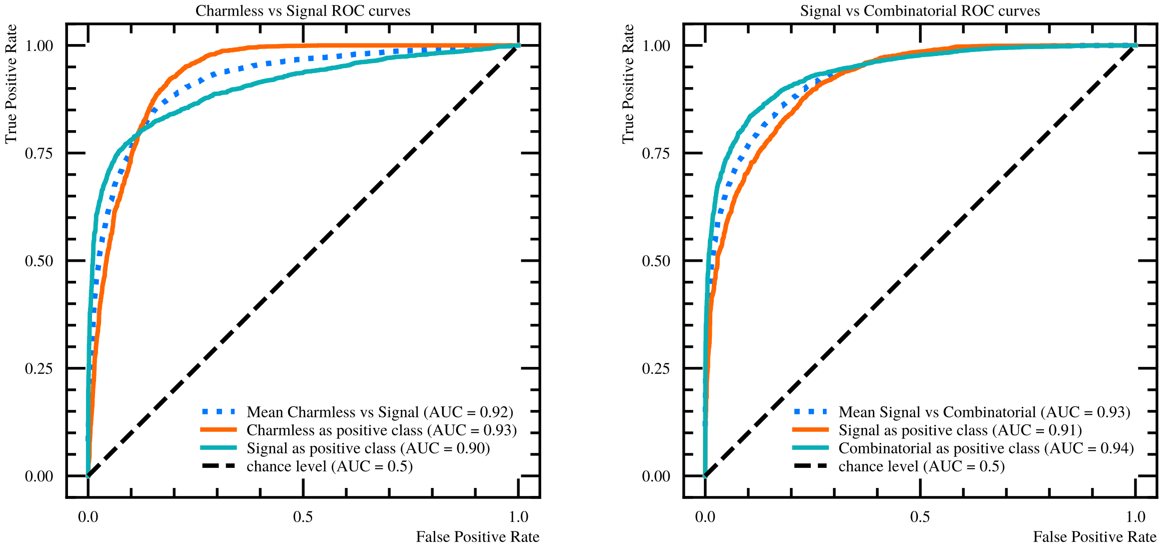

(a) ROC curve for charmless background versus signal.

(b) ROC curve for combinatorial background versus signal.

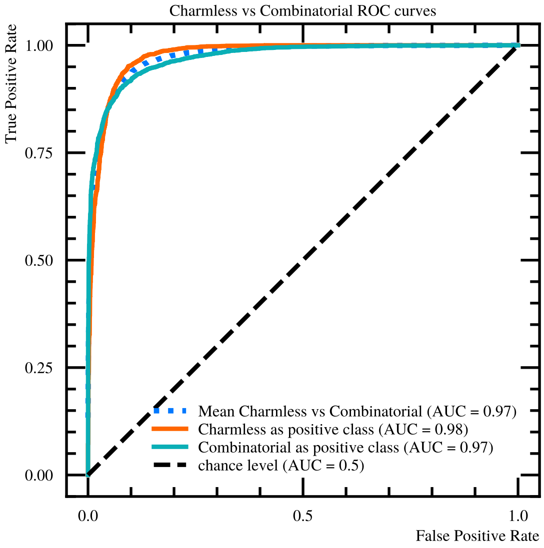

(c) ROC curve for charmless background versus combinatorial background.

Figure 5.5: Collection of ROC curves of the multiclass training for Run 2 $\Lambda_b^0 \to [K^-\pi^+]_{D^0} p\pi^-$.

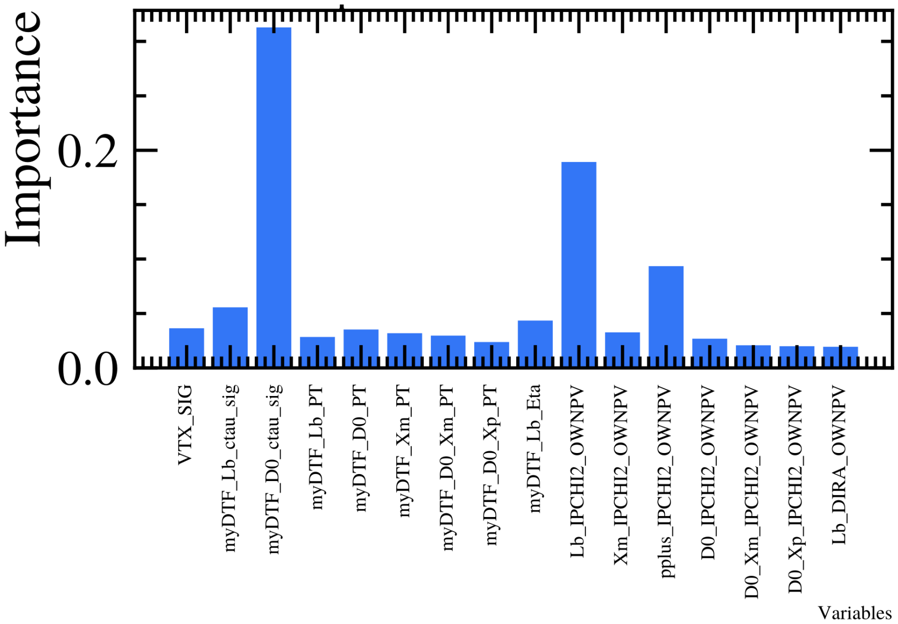

Figure 5.6: Variable importance plot for the BDT used in the analysis. The x-axis lists the variables considered, while the y-axis represents the importance score, indicating how significantly each variable contributes to the BDT's decision-making process.

cance of the signal over the background, ensuring that the selected signal events are statistically distinguishable from the background. To implement this optimisation, the analysis begins with applying loose kinematic and quality cuts, optimised on the control channel using PID variables of final state particle common to the control channel and the signal, managing to transport the selection from one to the other. As previously explained, these initial cuts reduce the dataset to a manageable size while retaining most of the signal. The next step involves varying the selection thresholds for different variables, such as particle identification variables, from here on called ProbNN*x*, where *x* is the probability of a given particle to be identified by the reconstructing algorithm as *x*, and the classifier variable. For each set of cuts, the signal and background yields are estimated, the first one computed taking into account parameters of the experiment and the efficiency of the previous selections as it follows $2{\cdot}\mathrm{L}{\cdot}f_{\Lambda_b}{\cdot}\sigma_{b\bar{b}}{\cdot}\mathrm{BR}(\Lambda_b){\cdot}\mathrm{BR}(D^0){\cdot}\epsilon_{\text{MCfilter}}{\cdot}\epsilon_{geom}{\cdot}\epsilon_{presel}$, scaled by the efficiency of the selection at each step. The background is computed as the amount of the background events in the signal region extracted by the *sPlot* technique, fitting the dataset with a simple Gaussian. The FOM is then calculated for each set of cuts, and the optimal selection is determined by the set that maximises the FOM. This process can be visualised using plots of the FOM as a function of the selection thresholds, helping to identify the most effective cuts. A visual example of the work done to optimise the selection of the proton PID variable can be found in Figure 5.7a. The strategy adopted to identify the negatively charged hadron coming from Λ_b^0 is a 2D FoM, as at the same time, the enhancement of the signal and the suppression of the misidentification background is achieved. Such a FoM can be found in Figure 5.7b. When the time to optimise the selection of the classifier variable came, a different FoM was adopted. Since the BTD was trained to discriminate another source of background, this needs to be taken into account in the FoM, which now becomes $S/\sqrt{S+B_{comb}+B_{charm}}$. The amount of charmless background has been estimated using the same formula as for the signal, substituting the branching fraction. To assess the final discrimination power of the BDT and check the remaining

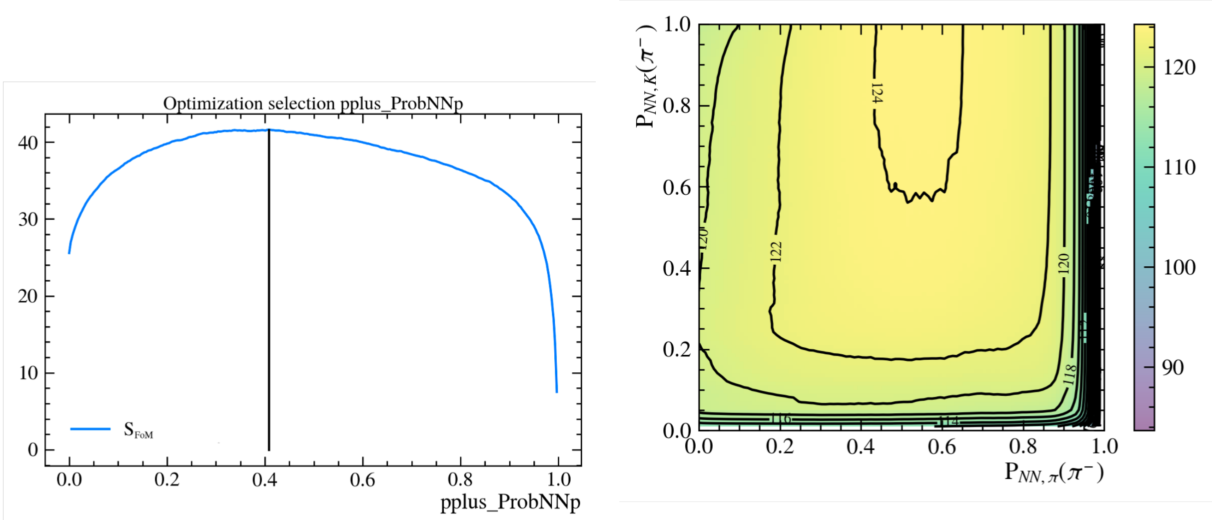

(a) Example of Figure of Merit maximised to optimise the selection for the PID variable of the proton.

(b) Example of Figure of Merit maximised to optimise the selection for the PID variable of the negative hadron coming from Λ_b^0.

Figure 5.7: Figures of Merit adopted in this analysis.

contributions of charmless events, a fit of the Λ_b^0 invariant mass distribution is performed in the right sideband of the distribution of the D^0 invariant mass, i.e. $\mathrm{m}(D^0) > 1910$ MeV$/c^2$. The number of remaining events is estimated by a proportion of the interval width of the charmless-only range and the signal one. This assumption is solid as we carefully checked that the BDT was not distorting the D^0 invariant mass distribution and keeping it flat, as shown in Figure 5.8. After this estimation, the remaining charmless events are comparable, if not less, to the statistical uncertainty on the signal yield, as one can see from the Λ_b^0 invariant mass represented in Figure 5.9, therefore this background can be considered removed.

5.4 Physical backgrounds studies

Combinatorial background refers to events arising from random combinations of particles that mimic the signal of interest. These are not genuine signal events but rather accidental associations of particles from different sources within the same event. This background has been mitigated using a BDT. Other backgrounds resulting from incorrect particle identification processes have been largely removed, but the specific contributions still require careful treatment.

5.4.1 Misidentification

When speaking about misidentification, one refers to the incorrect classification of a particle's identity based on the detector's measurements. This occurs when a particle is wrongly identified as another type of particle due to the overlapping properties of different particle species. This is quite common for pions and kaons, as they have relatively similar masses and can have overlapping ranges of momentum and energy, making them hard to distinguish based on these measurements alone. Additionally, their energy loss per unit length (dE/dx) in detector materials can be similar, especially in certain momentum ranges, complicating differentiation by ionisation energy loss. Moreover, both particles produce Cherenkov radiation, and their Cherenkov angles

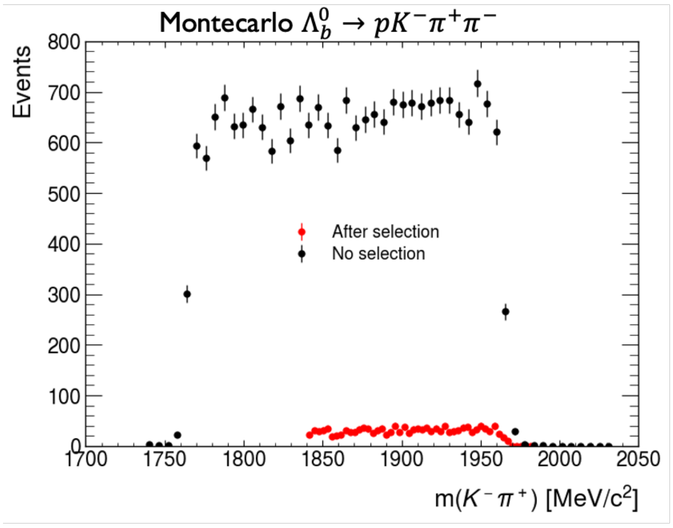

Figure 5.8: Invariant mass distribution of the D^0 meson for $\Lambda_b^0 \to pK^-\pi^+\pi^-$ Monte Carlo events. The black points represent the events before any selection criteria are applied, the red points depict the events after applying the selection criteria, showing the distribution to remain as flat as before the selection on the BDT variable is applied.

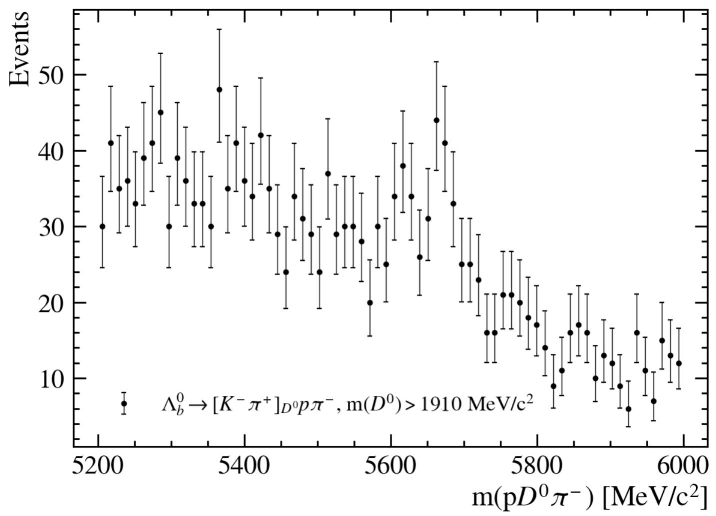

Figure 5.9: Λ_b^0 invariant mass distribution in the sideband of the D^0 mass. Run 2 of $\Lambda_b^0 \to [K^-\pi^+]_{D^0}p\pi^-$.

can be very close at overlapping momenta, leading to potential confusion in RICH detectors. For these reasons, misidentification backgrounds can still be visible in the datasets analysed. Furthermore, as the control channel $\Lambda_b^0 \to D^0 p\pi^-$ has an order of magnitude larger branching fraction compared to $\Lambda_b^0 \to D^0 pK^-$, the misidentification of $D^0 p\pi^-$ is well visible and needs to be well modelled given its proximity to the signal peak. Following the optimised selection in the previous step, the amount of misidentified events is estimated using the `PIDCalib2` package [71], a software used in the LHCb experiment for calibrating particle identification performance. It provides tools to create calibration samples by selecting well-identified particles from data, which are then used to determine PID efficiencies and misidentification rates. This calibration is used to correct biases in PID and specifically to estimate the number of misidentified candidates with the applied selection, which is fixed for later use in the fit. Kaons and pions are also final

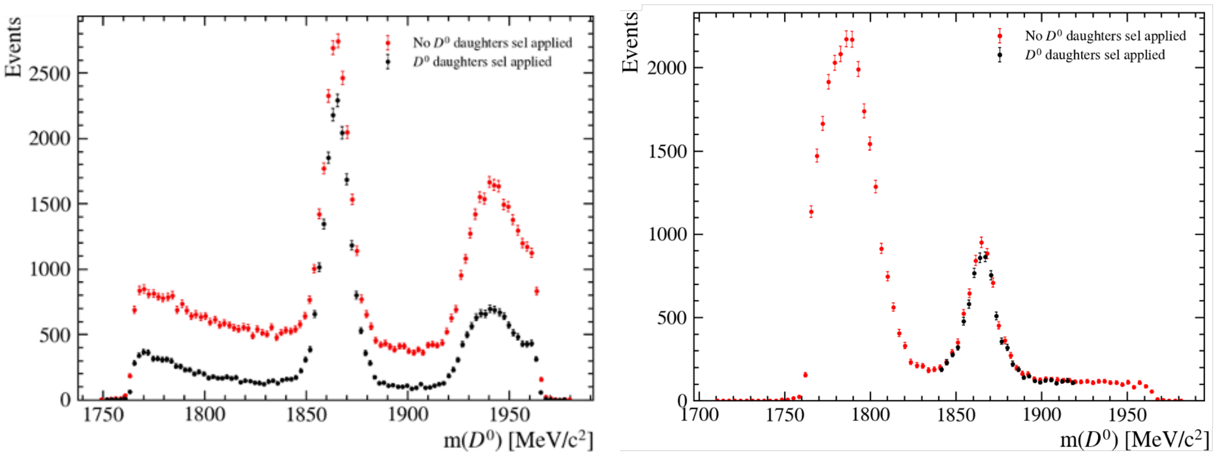

(a) Invariant mass of D^0 meson, with $D^0 \to K^-K^+$.

(b) Invariant mass of D^0 meson, with $D^0 \to \pi^-\pi^+$.

Figure 5.10: Invariant mass of D^0 meson in the channel $\Lambda_b^0 \to D^0 p\pi^-$, the clear misidentification peak of $D^0 \to K^-\pi^+$ is visible.

state particles in the D^0 decay, but rather than act on PID variables, as the invariant mass peak of misidentified particles is well separated from the signal peak, to reduce the background a selection on the invariant mass of the D^0 is adopted, i.e., 1840 MeV/c^2 <m$(D^0) < 1900$ MeV/c^2. Examples of this strategy can be found in Figure 5.10. Given how favoured $D^0 \to K^-\pi^+$ is with respect to the GLW modes, the misidentification is driven by this decay. It is possible to see how a further PID selection to reduce the baseline background is applied in the $D^0 \to K^-K^+$ case and how it is not effective in the $D^0 \to \pi^-\pi^+$ case.

5.4.2 $\Lambda_c^+ \to ph^-h^+$ background

In this analysis, potential backgrounds from Λ_c^+ decays could contribute, as these have significantly higher branching fractions with respect to the signal and control channels. For instance, the branching fractions of two-body Λ_b^0 decays, such as $\Lambda_b^0 \to \Lambda_c^+(\to ph^-h^+)h^-$, are approximately 10^2 to 10^3 times greater than that of $\Lambda_b^0 \to D^0 pK^-$, making them a significant source of background. This necessitates a careful examination for Λ_c^+ peaks in the invariant mass distributions. To mitigate this background, a veto is applied against Λ_c^+ in the invariant mass range $[2260, 2300]$ MeV/c^2 for all $\Lambda_b^0 \to D^0 pK^-$ decays except for the $D^0 \to K^-K^+$ mode. This veto is also applied for $D^0 \to \pi^-\pi^+$ in $\Lambda_b^0 \to D^0 p\pi^-$ decays. By implementing this Λ_c^+ veto, we effectively reduce the contamination from Λ_c^+ decays, which would otherwise overlap and obscure the Λ_b^0 signal. The specific vetoed regions for Λ_c^+ are illustrated in Figure 5.11. Additionally, it has been observed that when using both D^0 daughters, the invariant mass $m(D^0 ph^-)$ is consistently above the nominal Λ_c^+ mass. Therefore, a Λ_c^+ decay is only possible for a mixture of kaon and pion mesons from Λ_b^0 and D^0 and when the favoured Λ_c^+ decay was not possible in terms of final state particles coming from Λ_b^0, a misidentification was forced, and the veto was then applied. Forcing a misidentification implies changing the mass hypothesis of the particle and recomputing its energy.

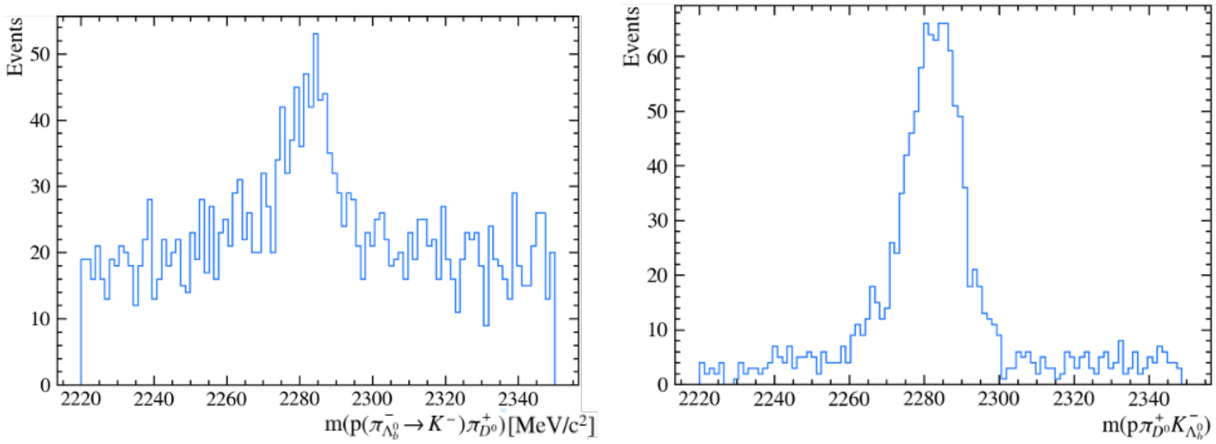

(a) Reconstructed invariant mass of Λ_c baryon, forcing the misidentification on π^-.

(b) Reconstructed invariant mass of Λ_c baryon, no forced misidentifications.

Figure 5.11: Reconstructed invariant mass of $\Lambda_c^+ \to pK^-\pi^+$ decay in the channel $\Lambda_b^0 \to [K^-\pi^+]_{D^0}p\pi^-$ and $\Lambda_b^0 \to [K^-\pi^+]_{D^0}pK^-$.

5.4.3 Partially reconstructed background

Partially reconstructed backgrounds presented a significant challenge in this analysis. These backgrounds arise from events where not all particle decay products are detected or reconstructed, resulting in an incomplete picture of the original decay process. This typically occurs in decays involving multiple particles, where one or more of the final-state particles are either undetected or fall outside the detector's acceptance range. Several factors can contribute to partially reconstructed backgrounds. Limited detector coverage can mean that some particles are emitted at angles or energies that are not within the sensitive regions of the detector. Additionally, particle interactions with detector materials can lead to energy loss, making the particles difficult to detect or reconstruct accurately. Furthermore, neutral particles often leave no direct signature in tracking detectors, complicating the full reconstruction of the decay event. Even if all the particles are reconstructed, then looking at the D^0ph^- invariant mass, the energy is lower, not considering extra particles to the final state, forming then the peculiar shape at lower masses. Given the wide invariant mass spectrum scanned in this analysis, we must also deal with this background. For $\Lambda_b^0 \to D^0p\pi^-$, the partially reconstructed candidates are visible below m$(D^0p\pi^-) < 5550$ MeV/c^2, and correspond to $\Lambda_b^0 \to D^{*0}p\pi^-$, and the lost particle is a photon or a π^0 coming from $D^{*0} \to D^0\gamma$ or $D^{*0} \to D^0\pi^0$. It was not possible to rely on the MCs to model this contribution, as the available ones did not consider the resonances in the channels; in fact, they were produced as `PHSP`, which stands for Phase Space. It assumes that the decay products are distributed uniformly in phase space, meaning that all kinematically allowed configurations of the decay products are equally probable, which, in reality, we know that they are not. For this reason, the adopted strategy has been to use `EvtGen` [15] to produce the events of interest but correct them with the weighted MCs. The first step has been to reproduce partially reconstructed events with the `PHSP` model to compute the corrections for the ones we will use. It was possible to separate from the MC the contributions coming from the decay chain of $D^{*0} \to D^0\gamma$ and $D^{*0} \to D^0\pi^0$, as it is possible to observe in Figure 5.12, to compute separate corrections. Then, the samples were produced using `EvtGen` using the `HELAMP` model, as it was taken into account the contributions of the several resonances, and this model allows to simulate particle decays by parameterising the decay amplitudes in terms of helicity amplitudes. In the case

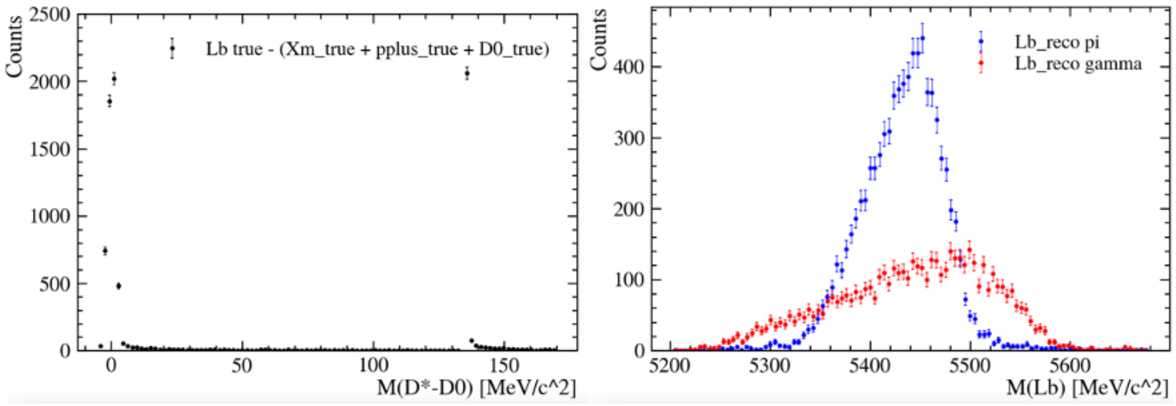

Figure 5.12: MC $\Lambda_b^0 \to D^{*0}p\pi^-$, $D^0 \to K^-\pi^+$. On the left is the reconstructed mass of the missing particle. On the right, based on the mass of the reconstructed particle, division in components of the Λ_b^0 invariant mass distribution.

analysed, the resonances considered are $(p\pi^-)_{N^*}$ and $(pD^0)_{\Lambda_c^*}$. the N^* resonances studied are $N(1440)$, with $J^P = (\frac{1}{2})^+$, $N(1520)$, with $J^P = (\frac{3}{2})^-$, $N(1535)$, with $J^P = (\frac{1}{2})^-$, and $N(1675)$, with $J^P = (\frac{5}{2})^-$. They all have different parity and helicity, as looking at the invariant mass distributions, only a few different shapes appeared. As an example, it is possible to look at the study performed on $N(1535)$ in Figure 5.13. The resonances studied are only four as it was checked that the shapes that repeat are always the same, so it was possible to merge the two chains considering their branching fraction, obtaining the invariant mass distribution for Λ_b^0 as in Figure 5.14. The same procedure was followed for the Λ_c^* resonances, and only one shape was found. The shapes adopted to model the Λ_b^0 invariant mass distribution can be found in Figure 5.15. The $\Lambda_b^0 \to D^0pK^-$ is slightly more complicated because as in the invariant mass spectrum, the misidentification of the $\Lambda_b^0 \to D^0p\pi^-$ and $\Xi_b^0 \to D^0pK^-$ appear, each one contributes with their partially reconstructed background, specifically $\Xi_b^0 \to D^{*0}pK^-$ being under the signal peak. Possible shape changes are evaluated in the systematics.

5.4.4 B contamination

Another possible background is the one coming from the misidentification of the proton into a kaon or a pion, which means having the signal being contaminated by B or B_s meson decays. When a proton is misidentified as a kaon, the decay $B_s^0 \to \overline{D}^0K^-K^+$ can mimic the signal $\Lambda_b^0 \to D^0pK^-$. The branching fraction of $B_s^0 \to \overline{D}^0K^-K^+$ is approximately 5.7×10^{-5} [72]. This decay has a higher branching fraction compared to the signal decay $\Lambda_b^0 \to D^0pK^-$, which has a branching fraction of about 3.5×10^{-6} when $D^0 \to K^-\pi^+$, so even one order of magnitude lower when considering the Cabibbo suppressed modes. Misidentification of the proton as a pion can also lead to significant background from decays like $B^0 \to \overline{D}^0K^-\pi^+$. The branching fraction for $B^0 \to \overline{D}^0\pi^-\pi^+$ is around 8.46×10^{-4} [73], so even a low misidentification rate could lead to a substantial number of background events. To investigate this background it was first used the control channel $\Lambda_b^0 \to D^0p\pi^-$, and a forced misidentification was applied on the proton on the selected data and looked at m(D^0p) to identify possible resonances observed in B decays. The representation of this misidentification can be found in Figure 5.16. The peaking $D_{s1}(2536)^+$ resonance brought to continue the investigation and look at the reconstructed invariant mass of the B_s^0 sectioning on the Λ_b^0 mass, highlighting the partially reconstructed range and the signal.

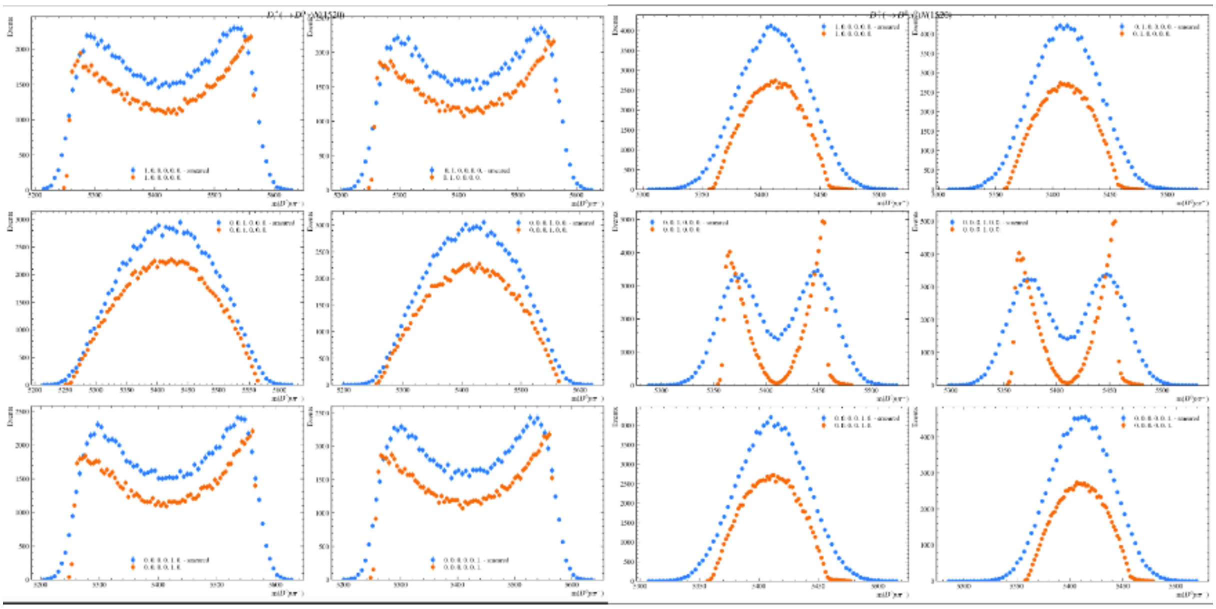

Figure 5.13: Comparison of the invariant mass distributions for the decay channel $\Lambda_b^0 \to D^{*0} p\pi^-$ using the `HELAMP` model for various helicity configurations. The orange points represent the unsmeared `HELAMP` model, while the blue points represent the smeared `HELAMP` model. Each plot shows the reconstructed mass distribution of the final state particles. The two left-most columns illustrate the decay chain involving a photon, while the two right-most columns show the decay chain involving a π^0.

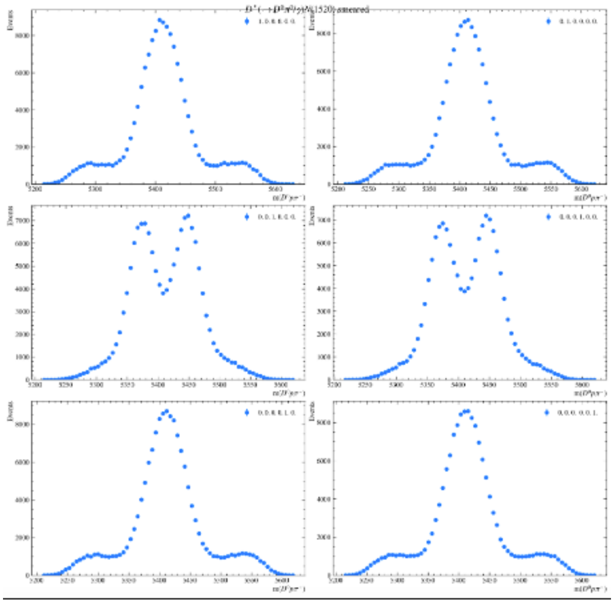

Figure 5.14: Λ_b^0 invariant mass distributions in the partially reconstructed background having as intermediate resonance $N(1535)$.

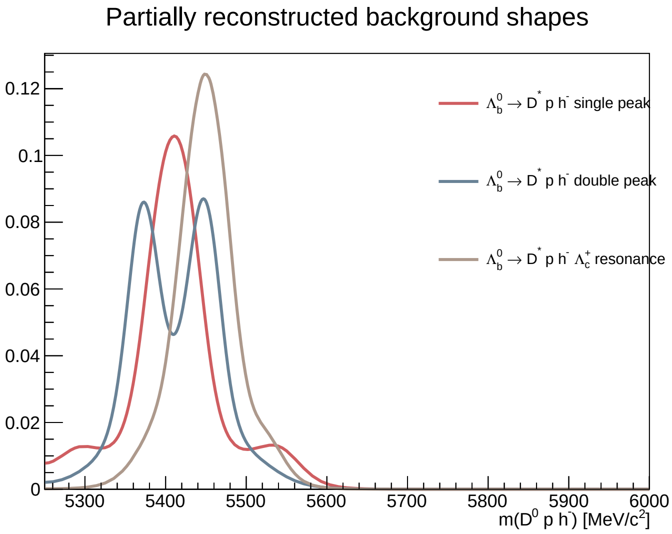

Figure 5.15: Shapes adopted to fit the partially reconstructed background.

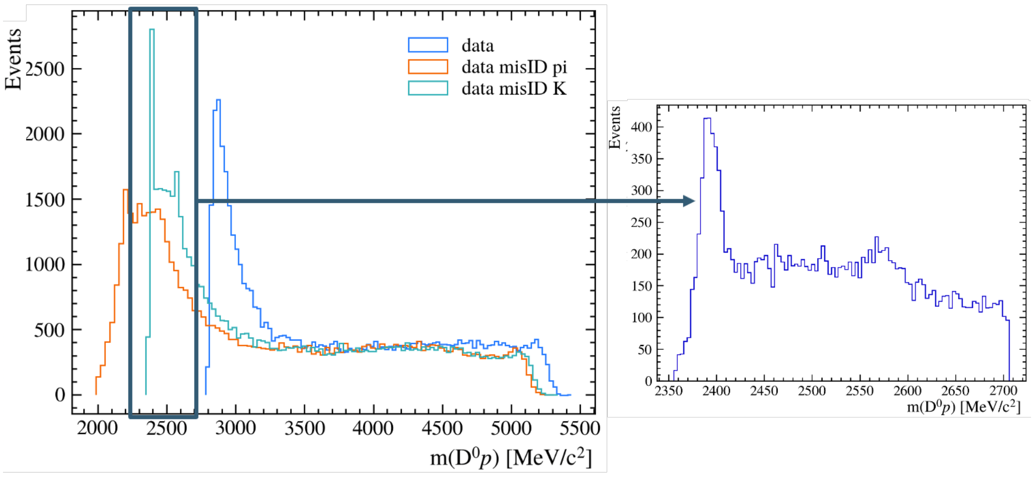

Figure 5.16: On the left, m(D^0p) with the proton being a proton and also forcing the misidentification of a kaon and a pion. A first study is performed on the m$(D^0(p \to K^+))$, zoomed on the right side of the image. A peak is clearly visible, corresponding to $D_{s1}(2536)^+$, as found in other B^0 analyses.

A clear B_s^0 mass peak is visible in Figure 5.17. Then, with EvtGen, it was possible to simulate the decay $B_s^0 \to D_{s1}(2536)^+\pi^-$, and imposing the misidentification of the kaon into the proton, it was possible to see where this decay lays in the Λ_b^0 invariant mass, as it is reported in Figure 5.18. The study continued as several other resonances were observed in the misidentification of the proton, leading to the population of Figure 5.19. The contributions are not in scale, just superimposed, but well underline the possible contamination situation. The result of this study is that a veto on the invariant mass of the B with the proton misidentified is applied, a selection that still granted 96% of efficiency on the signal MC.

5.5 Efficiencies

The measurement that this analysis aims to perform is an efficiency-weighted one. This means that once the MC samples are PID corrected and weighted, the selection's efficiency is computed

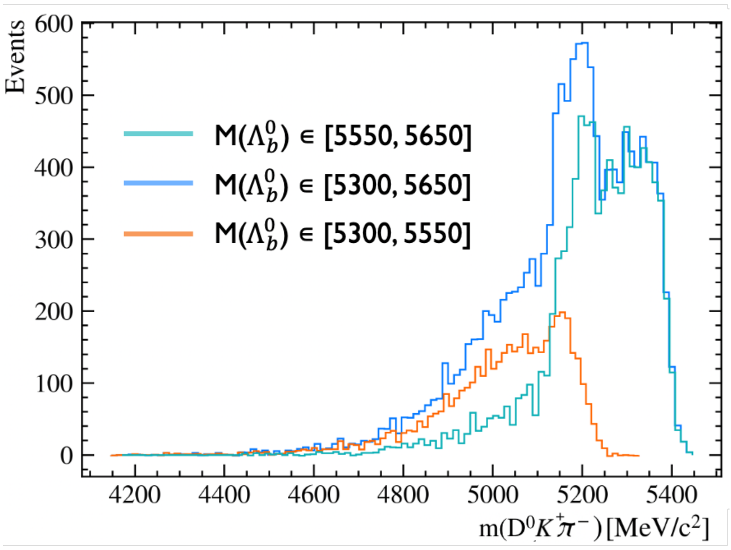

Figure 5.17: Reconstructed B_s^0 invariant mass. Each histogram corresponds to a different range in the Λ_b^0 invariant mass.

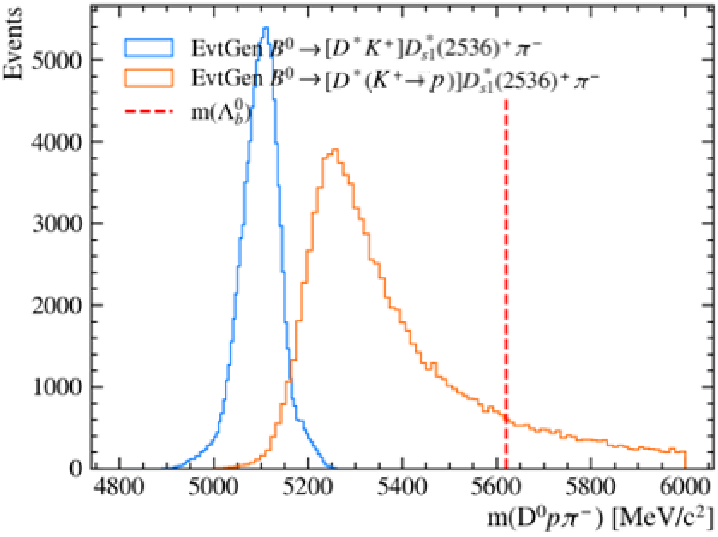

Figure 5.18: EvtGen simulations of the decay $B_s^0 \to D_{s1}(2536)^+\pi^-$, also with a forced misidentification of the kaon into a proton.

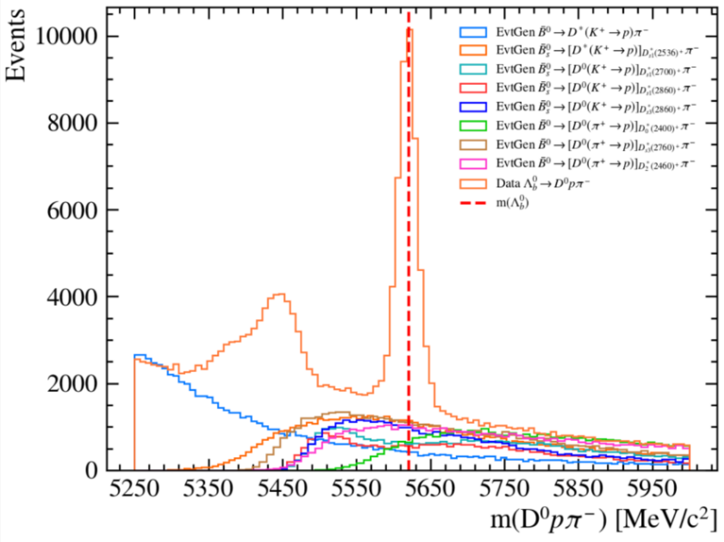

Figure 5.19: Run 2 $\Lambda_b^0 \to D^0 p\pi^-$ invariant mass, with all the superimposed possible contributions that could come from the misidentification of the proton into a kaon or a pion. Contributions not in scale.

to accomplish the measurement. For simplicity, the efficiencies are assumed to be factorisable so that the final efficiency is given by

$$\epsilon_{\text{tot}} = \epsilon_{\text{gen}} \cdot \epsilon_{\text{filt}} \cdot \epsilon_{\text{sel}}, \tag{5.2}$$

where each efficiency is computed as the number of events after the selection, divided by the number of events before the selection. ϵ_{gen} refers to the fraction of generated events that fall within the acceptance of the detector. This efficiency is determined by the detector's geometry and coverage, reflecting the likelihood that a generated event will be within the spatial region where the detector can effectively register it. It is computed as the ratio of the number of events within the detector's acceptance to the total number of generated events. ϵ_{filt} is the fraction of events that pass through a series of selection criteria or filters applied during the MC production process, i.e. when the MC is produced directly filtered by the stripping line. Filtering efficiency is calculated as the number of events that pass the filters divided by the number of events that were input to the filters. These quantities are represented Figure 5.20.

5.5.1 Selection

The efficiency of the offline selection ϵ_{sel} optimised and explained in the previous section is reported in Table 5.3, with the efficiencies collected in Table 5.4 and shown in Figure 5.21.

5.6 Invariant mass fit

In this chapter, the RooFit framework [74] is used to fit the mass distributions $m(D^0 ph^-)$ of the Λ_b^0 candidates to extract signal yields, ratios, and integrated *CP* asymmetries for the decays $\Lambda_b^0 \to D^0 pK^-$ and $\overline{\Lambda}_b^0 \to \overline{D}^0 \overline{p} K^+$. Our strategy involves applying an initial fit to the entire dataset, allowing us to constrain various parameters in subsequent fits to datasets split for Λ_b^0 and $\overline{\Lambda}_b^0$. All fits are conducted as simultaneous maximum likelihood fits to unbinned data.

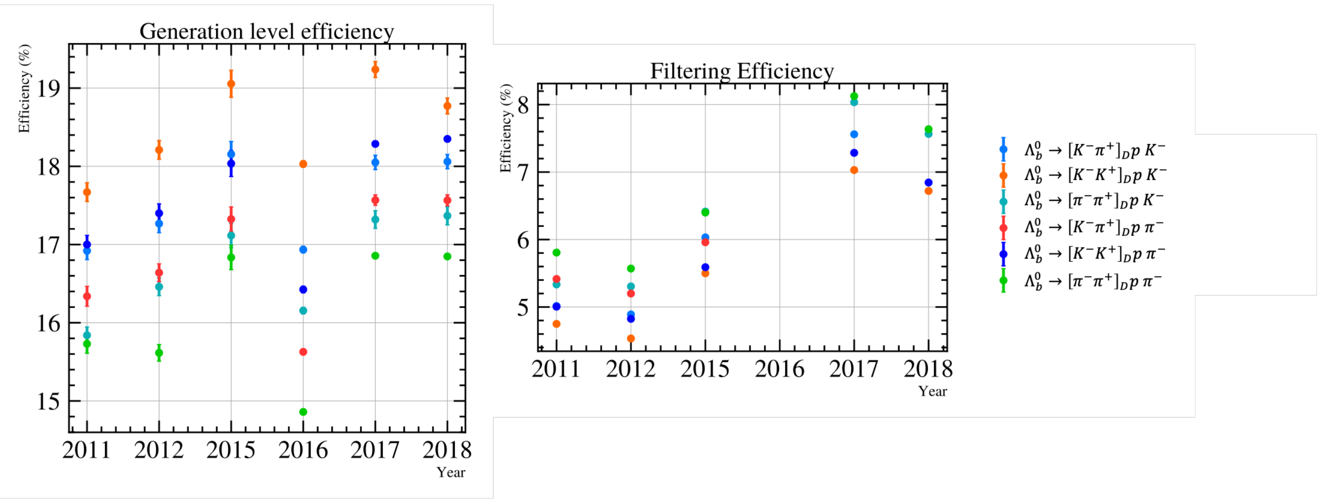

Figure 5.20: Efficiencies of the MC samples at the generation level (on the left) and of the stripping (on the right) for all the MC mimicking the signal. In the right plot, the missing points belong to MC samples which were produced unfiltered, and that were passed through the stripping line afterwards in the tuple creation.

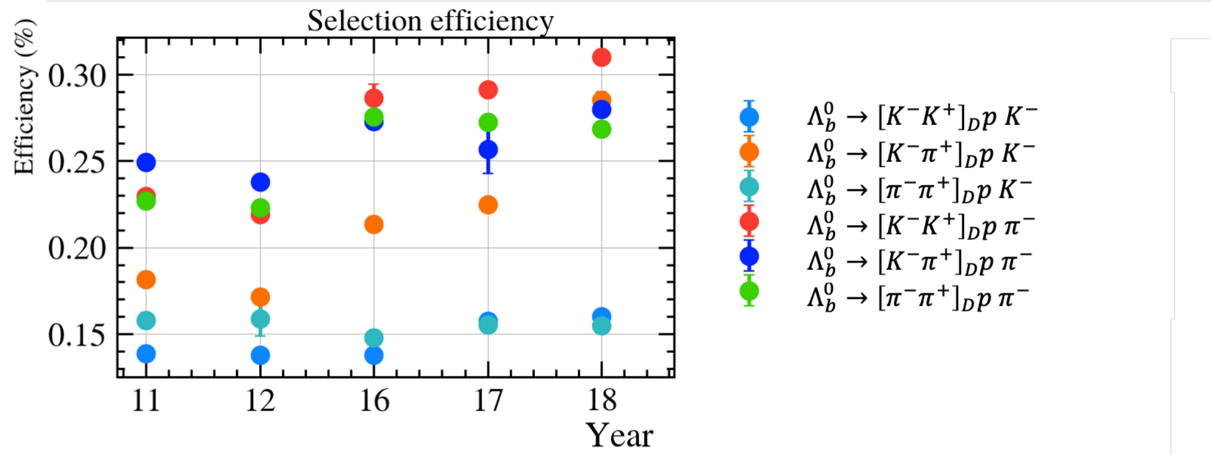

Figure 5.21: Efficiencies of the MC samples computed on the offline selection applied.

		`PID D0_Xm`	`PID D0_Xp`	`PID p`	`PID Xm`	`PID Xm misID`	`BDT`	`m(D)`	`m(Lc)`
$\Lambda_b^0 \to D^0 p K^-$									
$D^0 \to K^-\pi^+$	Run 1	> 0.15	> 0.15	> 0.35	> 0.3	< 0.95	> 0.45	$[1840, 1905]$	< 2260 or > 2300
	Run 2	> 0.15	> 0.15	> 0.75	> 0.54	< 0.95	> 0.56	$[1840, 1905]$	< 2260 or > 2300
$D^0 \to K^-K^+$	Run 1	> 0.07	> 0.07	> 0.35	> 0.3	< 0.95	> 0.4	$[1840, 1905]$	< 2260 or > 2300
	Run 2	> 0.1	> 0.1	> 0.85	> 0.2	< 0.6	> 0.6	$[1840, 1905]$	< 2260 or > 2300
$D^0 \to \pi^-\pi^+$	Run 1	$> 0.$	$> 0.$	> 0.45	> 0.4	< 0.6	> 0.2	$[1840, 1905]$	< 2260 or > 2300
	Run 2	$> 0.$	$> 0.$	> 0.8	> 0.75	< 0.6	> 0.7	$[1840, 1905]$	< 2260 or > 2300
$\Lambda_b^0 \to D^0 p \pi^-$									
$D^0 \to K^-\pi^+$	Run 1	> 0.15	> 0.15	> 0.3	> 0.2	< 0.75	> 0.42	$[1840, 1905]$	< 2260 or > 2300
	Run 2	> 0.25	> 0.25	> 0.65	> 0.57	< 0.93	> 0.52	$[1840, 1905]$	< 2260 or > 2300
$D^0 \to K^-K^+$	Run 1	> 0.1	> 0.1	> 0.35	> 0.2	< 0.86	> 0.35	$[1840, 1905]$	< 2260 or > 2300
	Run 2	> 0.15	> 0.15	> 0.45	> 0.2	< 0.87	> 0.45	$[1840, 1905]$	< 2260 or > 2300
$D^0 \to \pi^-\pi^+$	Run 1	$> 0.$	$> 0.$	> 0.3	> 0.1	< 0.6	> 0.6	$[1840, 1905]$	< 2260 or > 2300
	Run 2	$> 0.$	$> 0.$	> 0.6	> 0.36	< 0.74	> 0.65	$[1840, 1905]$	< 2260 or > 2300

Table 5.3: Selection implemented per each decay, per each Run.

		`PID D0_Xm`	`PID D0_Xp`	`PID p`	`PID Xm`	`PID Xm misID`	`BDT`	`m(D)`	`m(Lc)`
$\Lambda_b^0 \to D^0 p K^-$									
$D^0 \to K^-\pi^+$	Run 1	99	99	68	81	99	66	95	99
	Run 2	96	99	85	87	99	68	96	99
$D^0 \to K^-K^+$	Run 1	97	98	61	81	99	69	98	99
	Run 2	98	98	63	96	93	62	98	99
$D^0 \to \pi^-\pi^+$	Run 1	100	100	55	80	92	95	94	99
	Run 2	100	100	69	98	80	64	95	99
$\Lambda_b^0 \to D^0 p \pi^-$									
$D^0 \to K^-\pi^+$	Run 1	93	97	74	99	95	65	97	99
	Run 2	92	99	86	99	91	64	96	99
$D^0 \to K^-K^+$	Run 1	96	97	64	99	94	65	98	99
	Run 2	94	94	88	99	97	64	98	99
$D^0 \to \pi^-\pi^+$	Run 1	100	100	66	99	97	56	94	99
	Run 2	99	99	86	99	94	57	94	99

Table 5.4: Efficiency of the selection implemented per each decay, per each Run in %.

Unbinned maximum likelihood estimation (MLE) is a statistical technique that, unlike binned methods that aggregate data into discrete intervals, leverages the full information contained in each individual data point. This approach is particularly valuable in situations where data samples are limited or where the process of binning could introduce significant biases and loss of information. This technique constructs a likelihood function that directly incorporates each observed data point. Specifically, the likelihood function is formulated as the product of the probability density function evaluated at each observed data point. Mathematically, if we have a set of independent data points $x_1, x_2, \ldots, x_n$, and a model with a pdf $f(x; \theta)$ that depends on parameters θ, the likelihood function $L(\theta)$ is given by:

$$L(\theta) = \prod_{i=1}^{n} f(x_i; \theta).$$

The objective of unbinned MLE is to find the parameter values $\hat{\theta}$ that maximise this likelihood function, i.e.,

$$\hat{\theta} = \arg\max_{\theta} L(\theta).$$

In practice, it is often more convenient to work with the natural logarithm of the likelihood function, known as the log-likelihood, due to its additive properties and numerical stability:

$$\ln L(\theta) = \sum_{i=1}^{n} \ln f(x_i; \theta).$$

Maximising the log-likelihood provides the same parameter estimates as maximising the likelihood function but simplifies the computational process. Unbinned MLE is especially powerful in complex datasets with continuous underlying distributions where each data point provides critical information. By not grouping data into bins, this method avoids the arbitrary choices of bin edges and sizes, thereby preventing the distortion of the statistical properties of the data. This results in more accurate and reliable parameter estimates. The shape models for the different contributions are derived from fits to MC samples and fixed in the fits to the real data. This analysis has three main types of fits: the first is applied to unweighted data. This fit is proof of concept, involving *sWeight* calculation and fit validation with pseudo-experiments. This method allows us to verify the robustness of our fitting procedure and ensures that the efficiency corrections will then be accurately applied. The same fit is performed to unweighted data in the phase space region of Λ^* resonances. It provides deeper insights into the decay process dynamics and helps refine our measurement of *CP* asymmetries. Later on, after the model has been validated as mentioned above, a simultaneous fit is performed, as described below. Last but not least, the datasets are then refitted, weighted on the efficiency.

5.6.1 Shape study and validation

The first and most important step is to define a model that describes all the mass spectrum components. In particular, to wrap up, those are, in ascending mass order:

- For $\Lambda_b^0 \to D^0 p \pi^-$:
  - $\Lambda_b^0 \to D^{*0} p \pi^-$ double peak shape coming from N^* resonances.
  - $\Lambda_b^0 \to D^{*0} p \pi^-$ single peak shape coming from N^* resonances.
  - $\Lambda_b^0 \to D^{*0} p \pi^-$ single peak shape coming from Λ_c^{+*} resonances.
  - $\Lambda_b^0 \to D^0 p \pi^-$, the signal.
  - the combinatorial background.
- For $\Lambda_b^0 \to D^0 p K^-$:
  - $\Lambda_b^0 \to D^{*0} p K^-$ double peak shape coming from Λ^* resonances.
  - $\Lambda_b^0 \to D^{*0} p K^-$ single peak shape coming from Λ^* resonances.
  - $\Lambda_b^0 \to D^{*0} p K^-$ single peak shape coming from Λ_c^+ resonances.
  - $\Lambda_b^0 \to D^{*0} p \pi^-$, i.e. misidentified partially reconstructed decays.
  - $\Lambda_b^0 \to D^0 p K^-$, the signal.
  - $\Lambda_b^0 \to D^0 p \pi^-$, the misidentified signal.
  - $\Xi_b^0 \to D^{*0} p K^-$.
  - $\Xi_b^0 \to D^0 p K^-$.

  - the combinatorial background.

The main difference between the two decays is, as explained already, the absence of the misidentification component and also the absence of the Ξ_b^0 baryon decay, as in the $D^{*0}p\pi^-$ final state it is not allowed. The available MC sample on which it was possible to study the shape were, $\Lambda_b^0 \to D^0pK^-$, $\Lambda_b^0 \to D^0p\pi^-$, $\Lambda_b^0 \to D^0p\pi^-$ misidentification, $\Xi_b^0 \to D^0pK^-$, and the partially reconstructed $\Lambda_b^0 \to D^{*0}ph^-$, which as mentioned, was used to compute the corrections for the `EvtGen` simulations. The shapes adopted are the following:

- Johnson's distribution [75]. It comes from the re-adaptation of a Gaussian distribution and is adopted more and more in particle physics models. It is described by:

$$f(x) = \frac{\delta}{\lambda\sqrt{2\pi}} \frac{1}{\sqrt{1+\left(\frac{x-\xi}{\lambda}\right)^2}} \exp\left(-\frac{1}{2}\left(\gamma + \delta \sinh^{-1}\left(\frac{x-\xi}{\lambda}\right)\right)^2\right)$$

- Gaussian distribution. In this analysis, it is never used alone, always summed to another function. It is described by:

$$f(x) = \frac{1}{\sqrt{2\pi\sigma^2}} \exp\left(-\frac{(x-\mu)^2}{2\sigma^2}\right)$$

- Crystal ball distribution [76]. It is derived from a Gaussian distribution, adding exponential tails. It is described by:

$$f(x) = \begin{cases} \exp\left(-\frac{(x-\mu)^2}{2\sigma^2}\right) & \text{for } \frac{x-\mu}{\sigma} > -\alpha \\ A\left(B - \frac{x-\mu}{\sigma}\right)^{-n} & \text{for } \frac{x-\mu}{\sigma} \leq -\alpha \end{cases}$$

After several tests on the MC samples, the shapes adopted per each contribution are

- $\Lambda_b^0/\Xi_b^0 \to D^{*0}ph^-$: smeared `RooKeysPDFs` distributions, the shapes are reproduced thanks to a kernel estimator.
- $\Lambda_b^0 \to D^0ph^-$: sum of a Gaussian and a Johnson's distribution. The parameters describing the shapes are fixed by the fit on the MC samples, those that are left free to float on data are:
  - Mean μ: common to the two functions.
  - Standard deviation σ_G: the standard deviations of the 2 functions are linked via the ratio $\frac{\sigma_G}{\lambda_J} = f_\sigma$, where f_σ is fixed by the MC fit.
- $\Xi_b^0 \to D^0pK^-$: sum of a Gaussian and a Johnson's distribution. The shape adopted is the same as for the signal, also the free parameters are shared. The only parameter that is left free to be fitted is the mean difference $\Delta m = \mu_{\Xi_b^0} - \mu_{\Lambda_b^0}$.
- $\Lambda_b^0 \to D^0p\pi^-$, the misidentified background: sum of two Crystal balls, both with all the parameters constrained by the fit on MC.
- Combinatorial background: exponential function, whose coefficient is left free to float.

Some of the yields are fixed to give more stability to the fit, considering the poor information at disposal for some components: given that there are no studies on the partially reconstructed decays for the baryons, no accurate branching fraction is available. For this reason, a proportion was established for the partially reconstructed of the Ξ_b and of the misidentification. To be more specific, they were linked by these relations:

$$\frac{N_{\Xi_b^0 \to D^0 p K^-}}{N_{\Lambda_b^0 \to D^0 p K^-}} = \frac{N_{\Xi_b^0 \to D^{*0} p K^-}}{N_{\Lambda_b^0 \to D^{*0} p K^-}}, \qquad \frac{N_{\Lambda_b^0 \to D^0 p \pi^-}}{N_{\Lambda_b^0 \to D^0 p K^-}} = \frac{N_{\Lambda_b^0 \to D^{*0} p \pi^-}}{N_{\Lambda_b^0 \to D^{*0} p K^-}}.$$

As a reminder, the yield of the partially reconstructed background has also been fixed using `PIDCalib2` inputs.

5.6.2 Fit to the full dataset

Once the fitting strategy is established, the unbinned maximum likelihood fit is performed on the selected datasets. The results of the fit are shown in Figure 5.22 for $\Lambda_b^0 \to D^0 p K^-$ and in Figure 5.23 for $\Lambda_b^0 \to D^0 p \pi^-$, and the yields are reported in Table 5.5. The parameters extracted from the fit can be found instead, in Table 5.6.

	$\Lambda_b^0 \to D^0 p K^-$		$\Xi_b \to D^0 p K^-$		$\Lambda_b^0 \to D^0 p \pi^-$	
	Run 1	Run 2	Run 1	Run 2	Run 1	Run 2
$D^0 \to K^-\pi^+$	540 ± 40	1948 ± 97	262 ± 20	1105 ± 42	7958 ± 104	30982 ± 199
$D^0 \to K^-K^+$	115 ± 21	299 ± 28	27 ± 10	96 ± 13	853 ± 38	4482 ± 89
$D^0 \to \pi^-\pi^+$	115 ± 19	112 ± 18	24 ± 8	27 ± 9	397 ± 27	1406 ± 49

Table 5.5: Sample yields for different decay channels.

5.6.3 Toys validation

Toy validation, often referred to as toy Monte Carlo studies, is a technique used to statistically validate fits. This method involves generating many synthetic datasets (toys) based on a known or hypothesised probability distribution, which mirrors the expected behaviour of the data under study. These toy datasets are then analysed using the same fitting procedures applied to the real data, allowing to assess the performance and robustness of the fit models. The primary goal of toy validation is to ensure the fitting algorithm can reliably extract the correct parameters from the data. By comparing the fitted parameters obtained from the toy datasets with the true values used to generate these datasets, one can evaluate the bias, uncertainty, and coverage properties of the fit. This process helps identify systematic errors and potential biases in the fitting procedure, ensuring that the results are accurate and reliable. In this analysis, the size of the generated samples is the same as the dataset that is fitted, and the free values of the model are Gaussian generated from the fitted value, within three standard deviations. For the fit to be stable and pass the validation, the pulls of the toys need to be centred at zero and have a standard deviation equal to one. In Figure 5.24 and 5.25 the toy study performed on Run 1 dataset of $\Lambda_b^0 \to [K^-\pi^+]_{D^0} p K^-$ and $\Lambda_b^0 \to [K^-\pi^+]_{D^0} p \pi^-$, respectively, is shown.

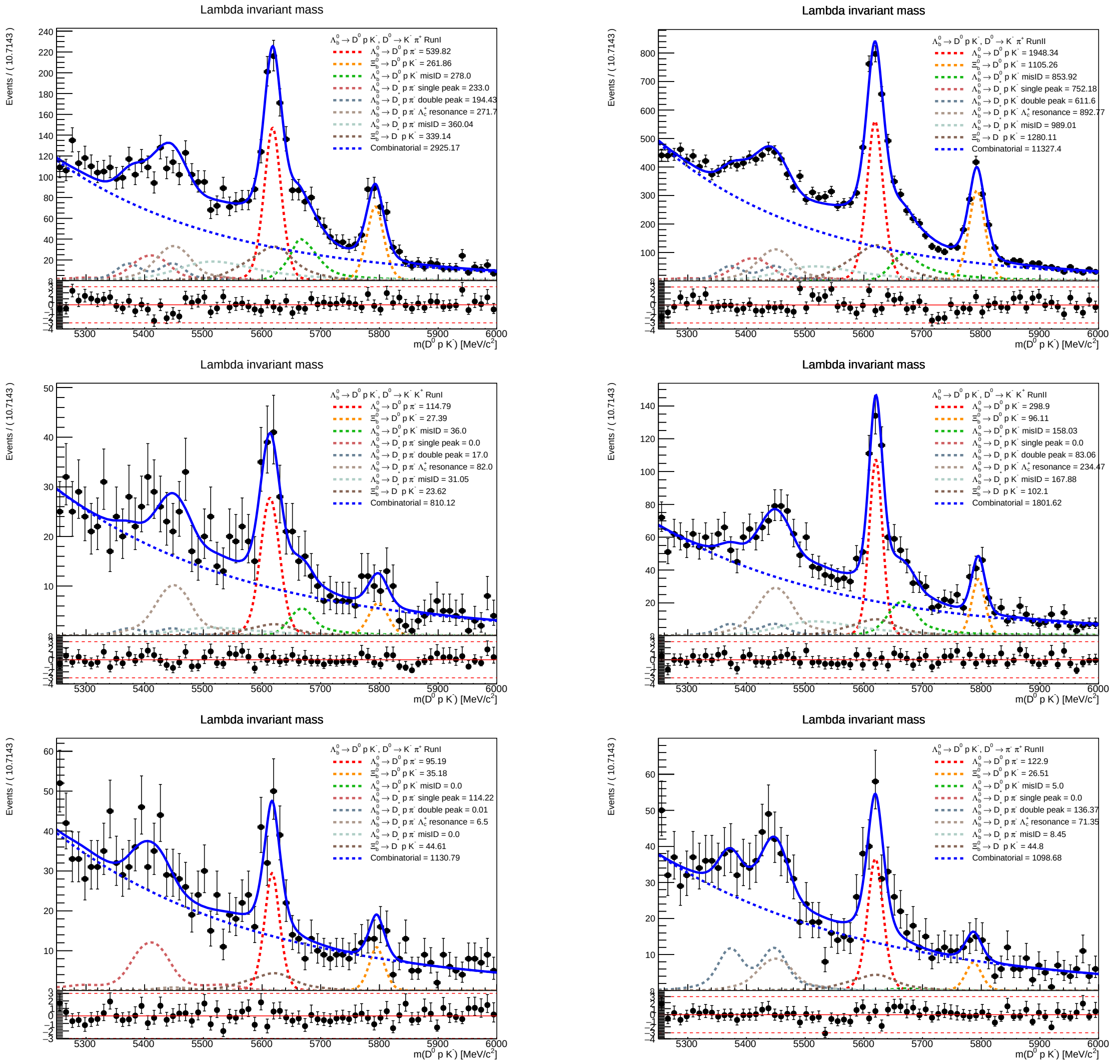

Figure 5.22: Unbinned maximum-likelihood fit for $\Lambda_b^0 \to D^0 p K^-$ decays, on the left column, the results for the Run 1 are shown, on the right column, the results for the Run 2 are shown.

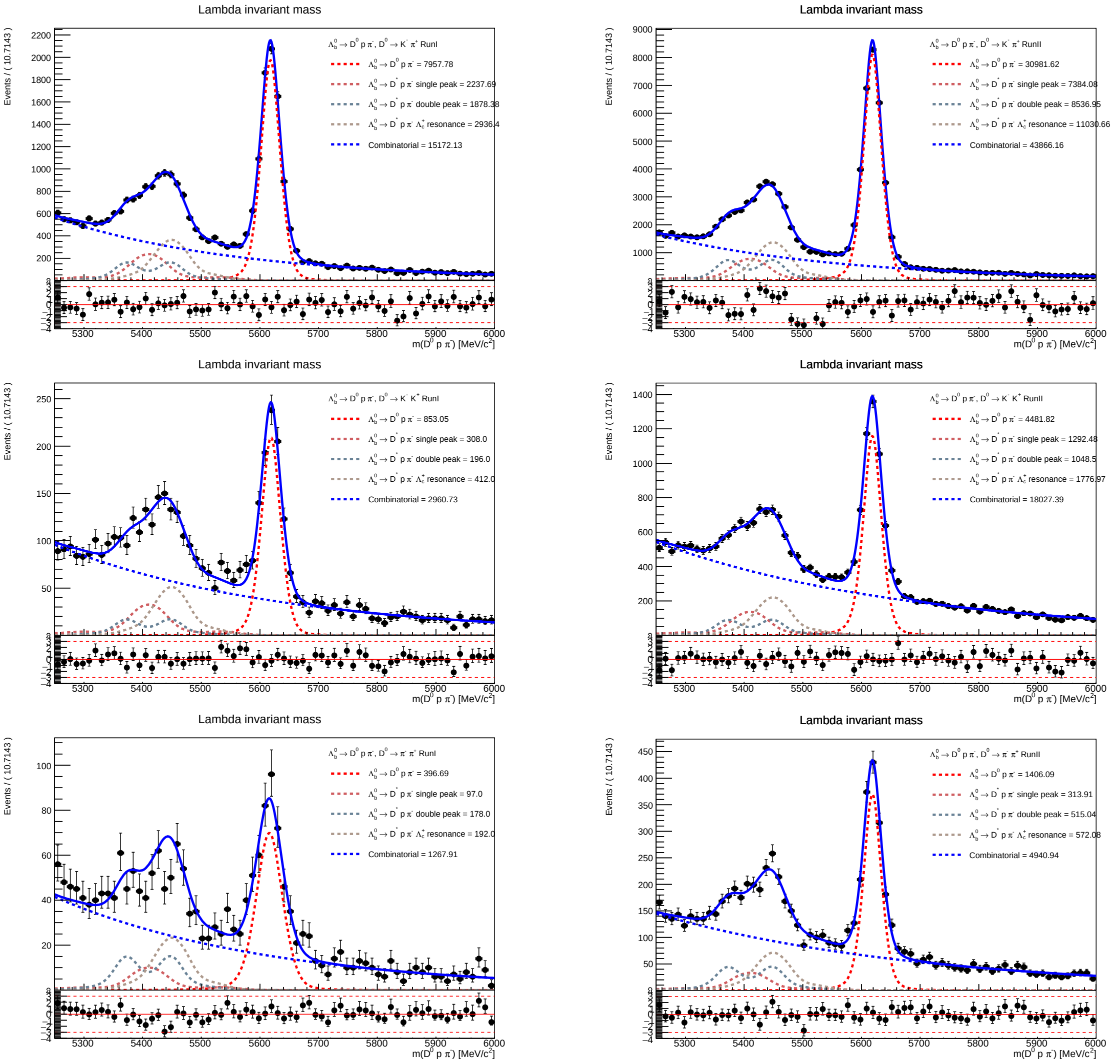

Figure 5.23: Unbinned maximum-likelihood fit for $\Lambda_b^0 \to D^0 p\pi^-$ decays, on the left column, the results for the Run 1 are shown, on the right column, the results for the Run 2 are shown.

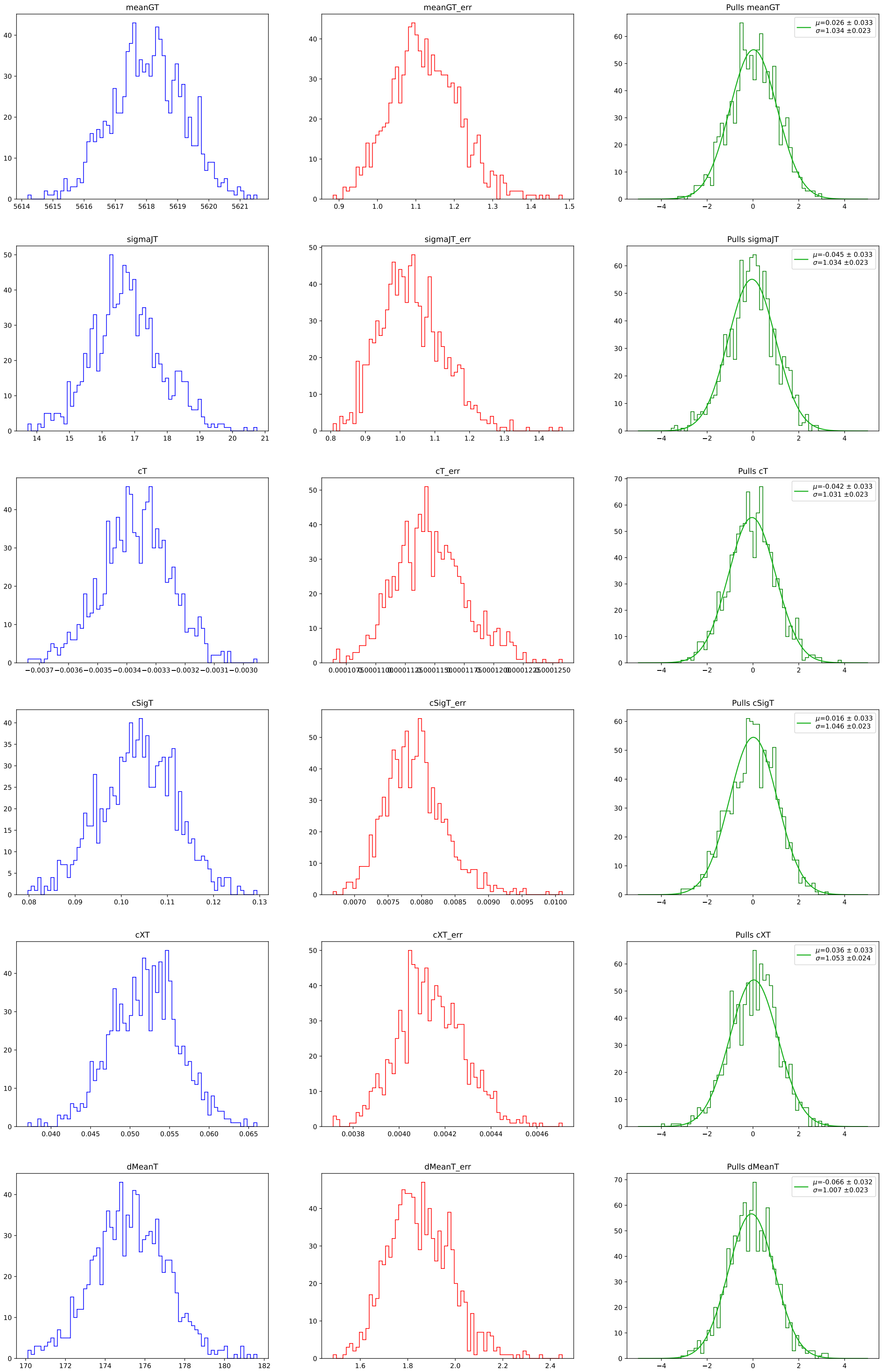

Figure 5.24: Results of toy study on the parameters of an unbinned maximum likelihood fit for the decay $\Lambda_b^0 \to [K^-\pi^+]_{D^0} pK^-$. The floating parameters are the mean of the signal mass distribution (`meanG`), the standard deviation of the signal distribution (λ_J), the exponential coefficient (`c`), the signal yield (`cSig`) and the yield of Ξ_b^0 (`cX`), along with the mass difference of the two baryons (Λ_b^0 and Ξ_b^0) (`dMean`). The distribution of the generated values, their uncertainty, and the pulls are shown for each of them. No significant deviation from the expected pull values is shown, ensuring the stability of the fit model.

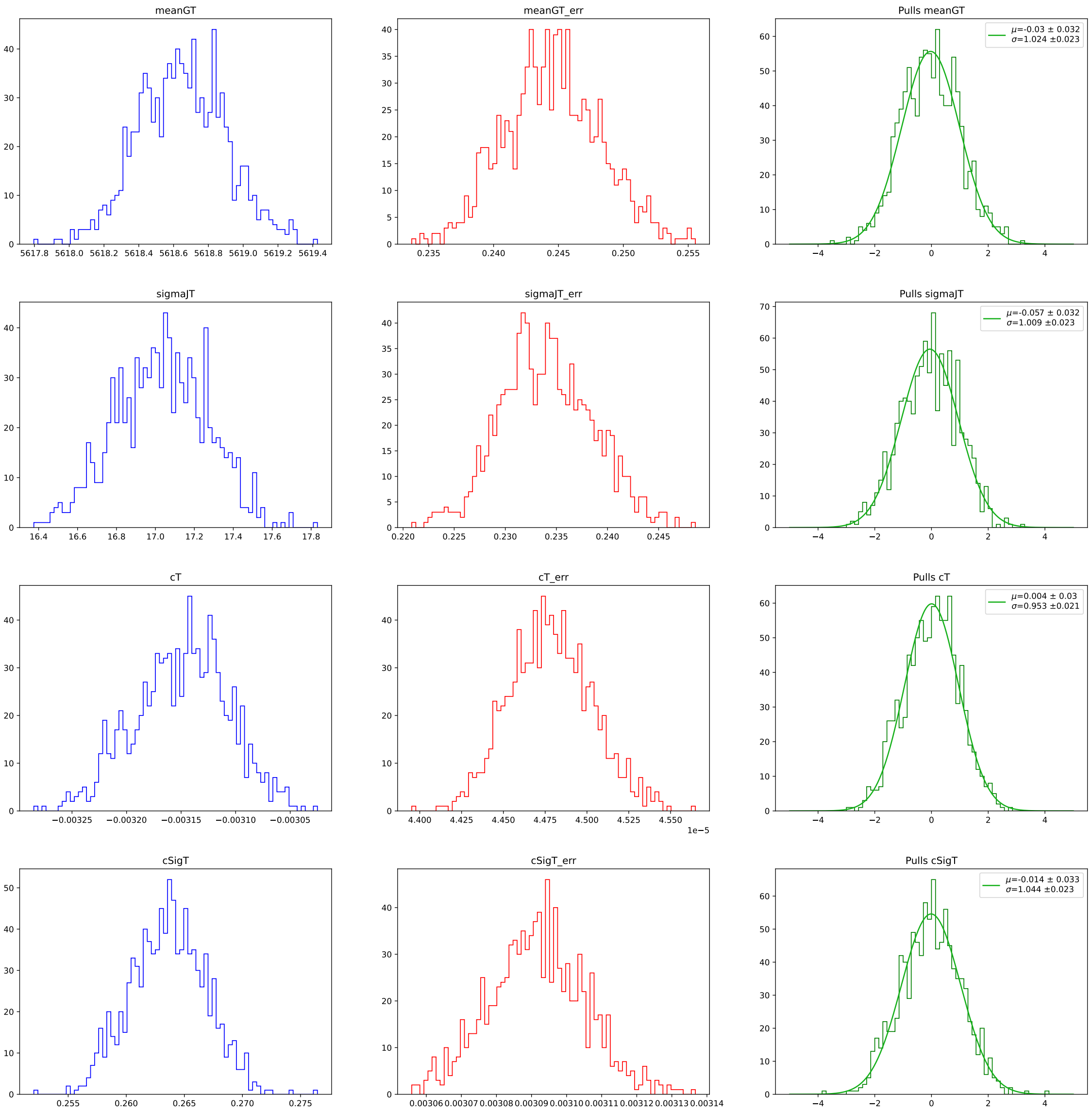

Figure 5.25: Results of toy study on the parameters of an unbinned maximum likelihood fit for the decay $\Lambda_b^0 \to [K^-\pi^+]_{D^0} p\pi^-$. The floating parameters are the mean of the signal mass distribution (`meanG`), the standard deviation of the signal distribution (λ_J), the exponential coefficient (`c`), and the signal yield (`cSig`). The distribution of the generated values, their uncertainty, and the pulls are shown for each of them. No significant deviation from the expected pull values is shown, ensuring the stability of the fit model.

$\Lambda_b^0 \to D^0pK^-$					
		`meanG`	`lambdaJ`	`dMean`	`c`
$D^0 \to K^-\pi^+$	Run 1	5618.4 ± 1.2	17 ± 1.0	175 ± 2	-0.0035 ± 0.0001
	Run 2	5619.3 ± 0.6	14.6 ± 0.5	173.7 ± 0.9	-0.0038 ± 0.0001
$D^0 \to K^-K^+$	Run 1	5614 ± 3	18 ± 3	185 ± 9	-0.0031 ± 0.0002
	Run 2	5620.6 ± 1.1	12.3 ± 1.2	175 ± 2	-0.0032 ± 0.0002
$D^0 \to \pi^-\pi^+$	Run 1	5617 ± 2	12 ± 2	179 ± 6	-0.0028 ± 0.0002
	Run 2	5621 ± 3	19 ± 3	163 ± 8	-0.0030 ± 0.0002
$\Lambda_b^0 \to D^0p\pi^-$					
$D^0 \to K^-\pi^+$	Run 1	5618.7 ± 0.2	17.1 ± 0.2		-0.0032 ± 0.0001
	Run 2	5619.3 ± 0.1	14.4 ± 0.1		-0.0026 ± 0.0001
$D^0 \to K^-K^+$	Run 1	5619.7 ± 0.8	16.6 ± 0.8		-0.0026 ± 0.0001
	Run 2	5619.4 ± 0.3	16.5 ± 0.4		-0.0023 ± 0.0001
$D^0 \to \pi^-\pi^+$	Run 1	5617 ± 2	24 ± 2		-0.0027 ± 0.0002
	Run 2	5619.3 ± 0.6	16.1 ± 0.6		-0.0022 ± 0.0001

Table 5.6: Parameters extracted from the fit, divided per run and per decay. `meanG` is the mean of the signal function, joint between the Johnson's distribution and the Gaussian distribution, `lambdaJ` is the correspondent standard deviation in the Johnson's distribution, `dMean` is the difference between the means in the signal and the Ξ_b^0 shapes, and `c` is the exponential coefficient of the combinatorial background.

5.6.4 Fit to the split dataset

Once the fit model is stable and toy-validated, the following step is performing the fit to the split dataset of Λ_b^0 and $\overline{\Lambda}_b^0$. The two samples are separated by the charge of the final state hadron (K or π), defining the as "Λ_b^0-type" the decays in which the hadron is negative and as "$\overline{\Lambda}_b^0$-type" otherwise. The chosen fit is an unbinned simultaneous maximum likelihood fit, in which the free parameters of the model are shared between the two subsamples. Even though for the reader it is possible to read the yields, the strategy adopted to compute the asymmetry is not completely unblind. The observables aimed to be measured are weighted on the efficiency, more explanations will come, and the fits displayed here are not. Therefore, the yields shown here are used to compute what will be called raw asymmetry, which does not represent the final result. The fits are displayed in Figure 5.26 for $\Lambda_b^0 \to D^0pK^-$ and in Figure 5.27 for $\Lambda_b^0 \to D^0p\pi^-$ and the yields are reported in Table 5.7.

		$\Lambda_b^0 \to D^0pK^-$		$\Xi_b \to D^0pK^-$		$\Lambda_b^0 \to D^0p\pi^-$	
		Run 1	Run 2	Run 1	Run 2	Run 1	Run 2
Λ_b^0-type	$D^0 \to K^-\pi^+$	275 ± 29	1085 ± 61	134 ± 14	538 ± 29	3925 ± 72	15490 ± 138
	$D^0 \to K^-K^+$	43 ± 13	136 ± 17	16 ± 7	96 ± 13	404 ± 25	2156 ± 59
	$D^0 \to \pi^-\pi^+$	57 ± 13	87 ± 16	16 ± 6	13 ± 7	195 ± 19	669 ± 32
$\overline{\Lambda}_b^0$-type	$D^0 \to K^-\pi^+$	252 ± 26	889 ± 61	136 ± 14	564 ± 29	4037 ± 73	15489 ± 138
	$D^0 \to K^-K^+$	75 ± 15	166 ± 19	11 ± 6	96 ± 13	458 ± 27	2329 ± 61
	$D^0 \to \pi^-\pi^+$	55 ± 11	68 ± 15	9 ± 6	12 ± 7	183 ± 19	737 ± 34

Table 5.7: Sample yields for different decay channels, split dataset.

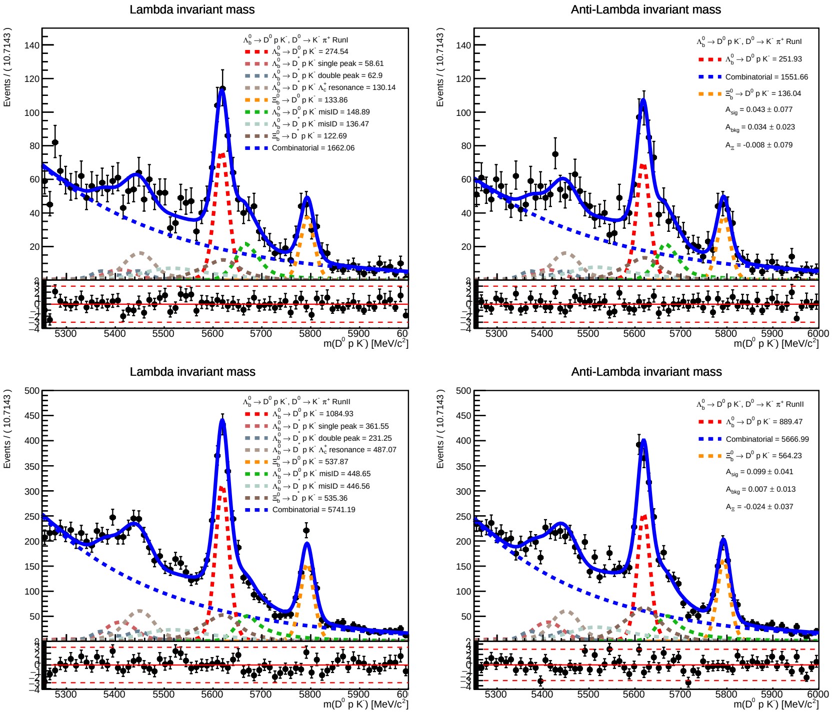

Figure 5.26: Simultaneous unbinned maximum-likelihood fit for $\Lambda_b^0 \to [K^-\pi^+]_{D^0} p K^-$ decays, on the left column, the results for Λ_b^0-type are shown, on the right column, the results for $\overline{\Lambda}_b^0$-type are shown. Top row is for Run I results, bottom row for Run II.

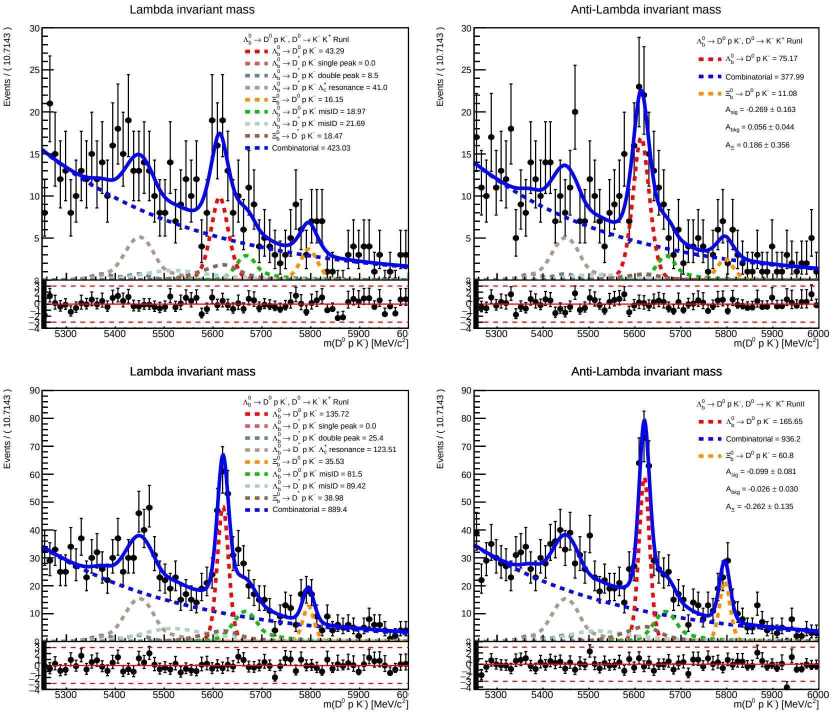

Figure 5.26: Simultaneous unbinned maximum-likelihood fit for $\Lambda_b^0 \to [K^-K^+]_{D^0} p K^-$ decays, on the left column, the results for Λ_b^0-type are shown, on the right column, the results for $\overline{\Lambda}_b^0$-type are shown. Top row is for Run I results, bottom row for Run II.

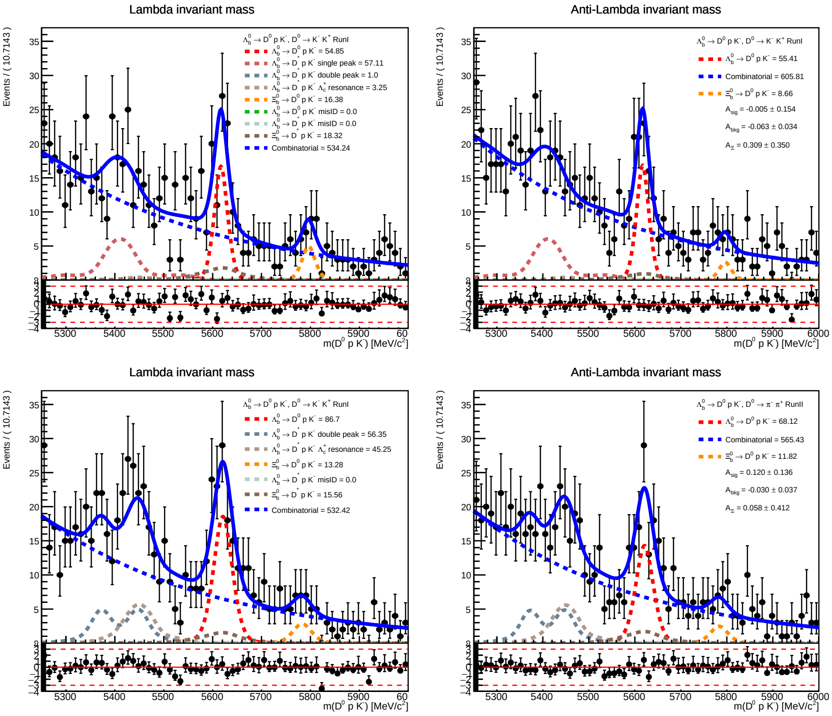

Figure 5.26: Simultaneous unbinned maximum-likelihood fit for $\Lambda_b^0 \to [\pi^-\pi^+]_{D^0} pK^-$ decays, on the left column, the results for Λ_b^0-type are shown, on the right column, the results for $\overline{\Lambda}_b^0$-type are shown. Top row is for Run I results, bottom row for Run II.

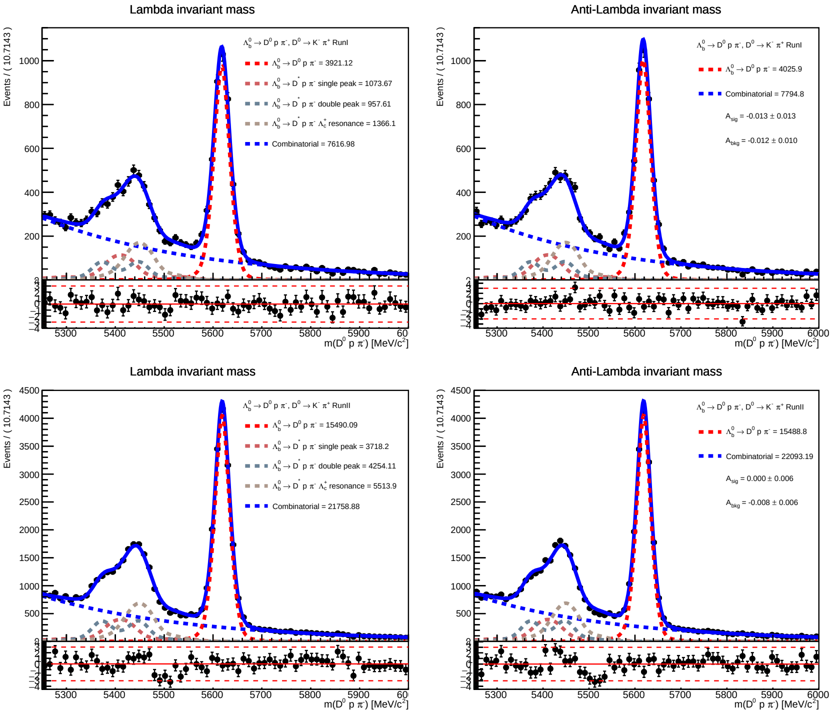

Figure 5.27: Simultaneous unbinned maximum-likelihood fit for $\Lambda_b^0 \to [K^-\pi^+]_{D^0} p\pi^-$ decays, on the left column, the results for Λ_b^0-type are shown, on the right column, the results for $\overline{\Lambda}_b^0$-type are shown. Top row is for Run I results, bottom row for Run II.

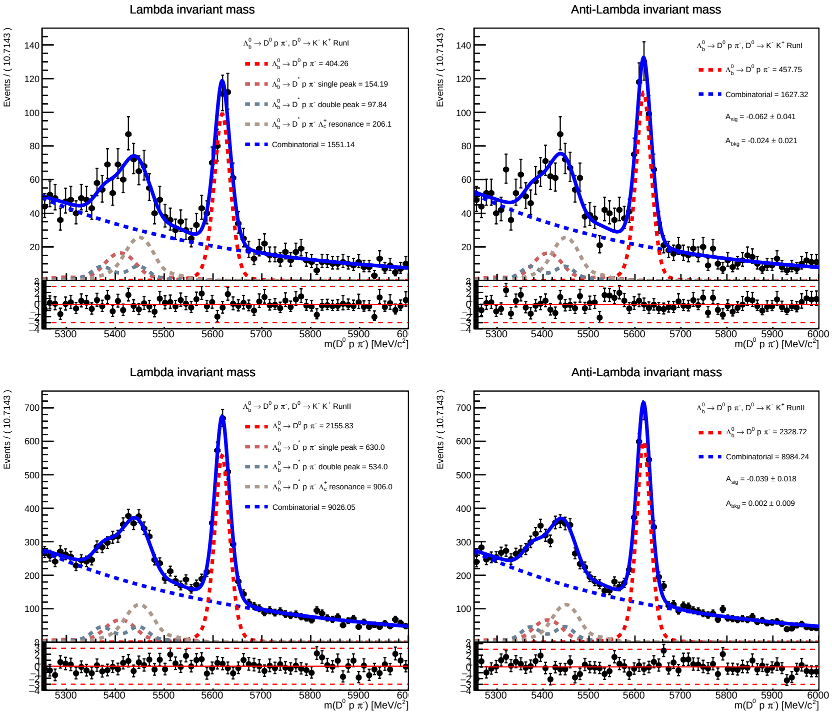

Figure 5.27: Simultaneous unbinned maximum-likelihood fit for $\Lambda_b^0 \to [K^-K^+]_{D^0}p\pi^-$ decays, on the left column, the results for Λ_b^0-type are shown, on the right column, the results for $\overline{\Lambda}_b^0$-type are shown. Top row is for Run I results, bottom row for Run II.

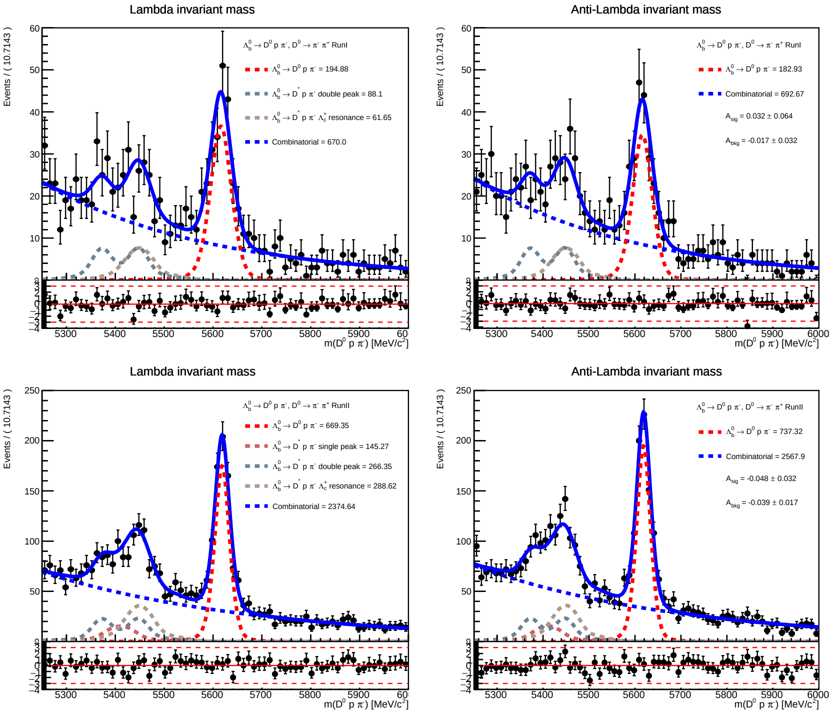

Figure 5.27: Simultaneous unbinned maximum-likelihood fit for $\Lambda_b^0 \to D^0p\pi^-$ decays, on the left column, the results for Λ_b^0-type are shown, on the right column, the results for $\overline{\Lambda}_b^0$-type are shown. Top row is for Run I results, bottom row for Run II.

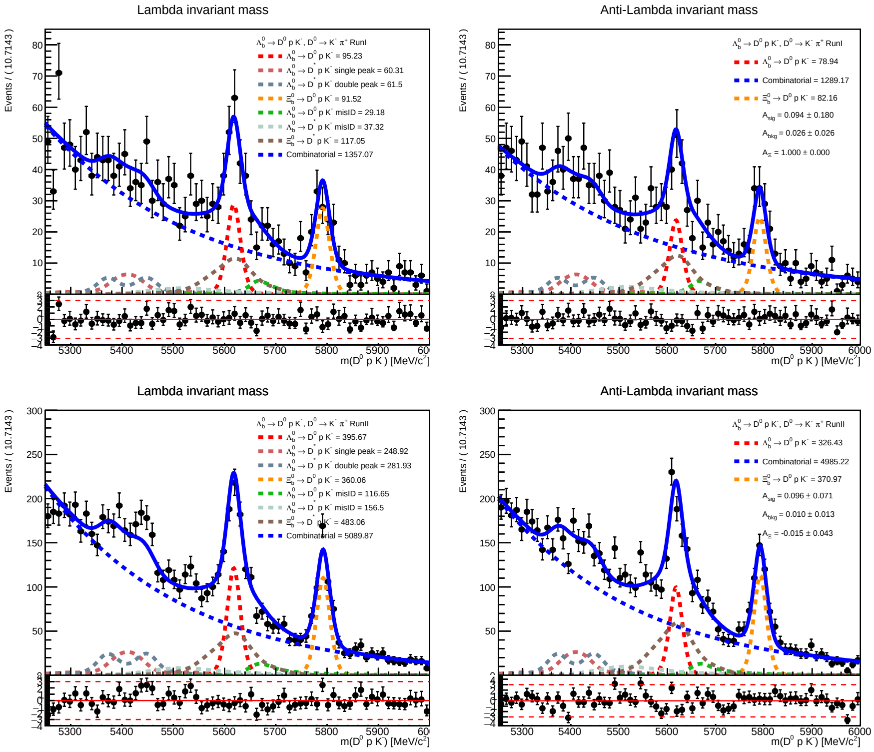

Figure 5.28: Simultaneous unbinned maximum-likelihood fit for $\Lambda_b^0 \to [K^-\pi^+]_{D^0}pK^-$ decays in the restricted Λ^* resonances phase space, on the left column, the results for Λ_b^0-type are shown, on the right column, the results for $\overline{\Lambda}_b^0$-type are shown.

5.6.5 Fit in the restricted phase space

As previously explained, the region in which more sensitivity is expected is the one in which the Λ^* resonances are dominant, and to access it, a selection on the m(D^0p) is applied, i.e. m$(D^0p) > 3100$ MeV/c^2. The fit performed is again a simultaneous one, same strategy as in the previous paragraph. The results are displayed in Figure 5.28 and reported in Table 5.8.

		$\Lambda_b^0 \to D^0pK^-$		$\Xi_b \to D^0pK^-$	
		Run 1	Run 2	Run 1	Run 2
Λ_b^0-type	$D^0 \to K^-\pi^+$	96 ± 30	396 ± 42	92 ± 12	360 ± 23
	$D^0 \to K^-K^+$	27 ± 11	53 ± 13	9 ± 6	22 ± 7
	$D^0 \to \pi^-\pi^+$	31 ± 10	37 ± 19	13 ± 5	11 ± 5
$\overline{\Lambda}_b^0$-type	$D^0 \to K^-\pi^+$	79 ± 16	326 ± 38	82 ± 12	371 ± 24
	$D^0 \to K^-K^+$	22 ± 12	82 ± 15	10 ± 4	37 ± 8
	$D^0 \to \pi^-\pi^+$	42 ± 10	43 ± 15	8 ± 5	7 ± 5

Table 5.8: Sample yields for different decay channels, split dataset, restricted phase space.

5.7 Systematic uncertainties

Several strategies are needed to compute systematic uncertainties as statistical uncertainties are extracted from the fit. Unlike statistical uncertainties, which arise from the finite size of

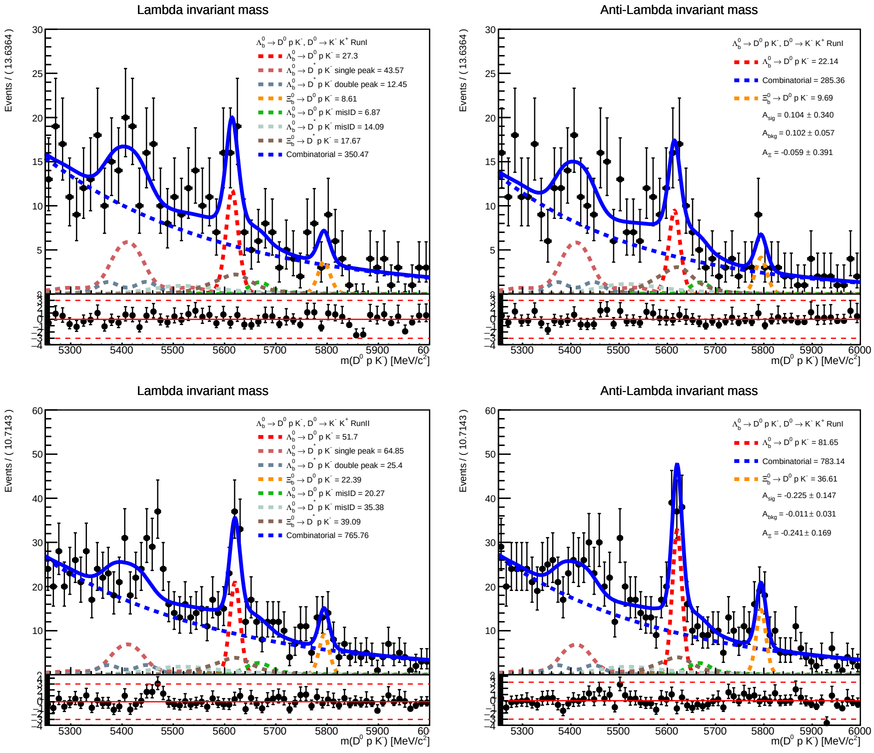

Figure 5.28: Simultaneous unbinned maximum-likelihood fit for $\Lambda_b^0 \to [K^- K+]_{D^0} p K^-$ decays in the restricted Λ^* resonances phase space, on the left column, the results for Λ_b^0-type are shown, on the right column, the results for $\overline{\Lambda}_b^0$-type are shown.

the data sample and decrease as more data are collected, systematic uncertainties originate from potential biases and inaccuracies in the measurement process itself. These can stem from various sources, such as detector performance, calibration errors, modelling assumptions, and external conditions that may affect the data. This section delves into identifying, estimating, and mitigating systematic uncertainties associated with the analysis, highlighting their impact on the measured observables and the overall conclusions. Overall, given the observables this analysis is aiming to measure, what is important to evaluate is the difference between $\epsilon^i_{\Lambda_b^0}$ and $\epsilon^i_{\overline{\Lambda}_b^0}$, where the apex i is for the sources that will be considered in the estimation of the systematics.

5.7.1 Fit Model

The first systematic uncertainties evaluated arise from the modelling assumptions that fit the data. Estimating these systematic uncertainties involves exploring the sensitivity of the fit results to variations in the model components. Specifically, we investigate the impact of different functional forms for the signal and background shapes on the extracted parameters. Several modifications are introduced, and their effects are quantified to evaluate the robustness of our fit model. We consider changing the signal shape from a combination of a Gaussian and a Johnson's distribution to a Gaussian and a Crystal Ball function. This adjustment allows us to examine how different representations of the signal peak affect the fit. The combinatorial background, described by an exponential function, is also varied. We explore the use of a second-order polynomial to understand the potential changes in the background modelling and its influence on signal extraction. Additionally, the shape of the misidentified contribution is modified from two

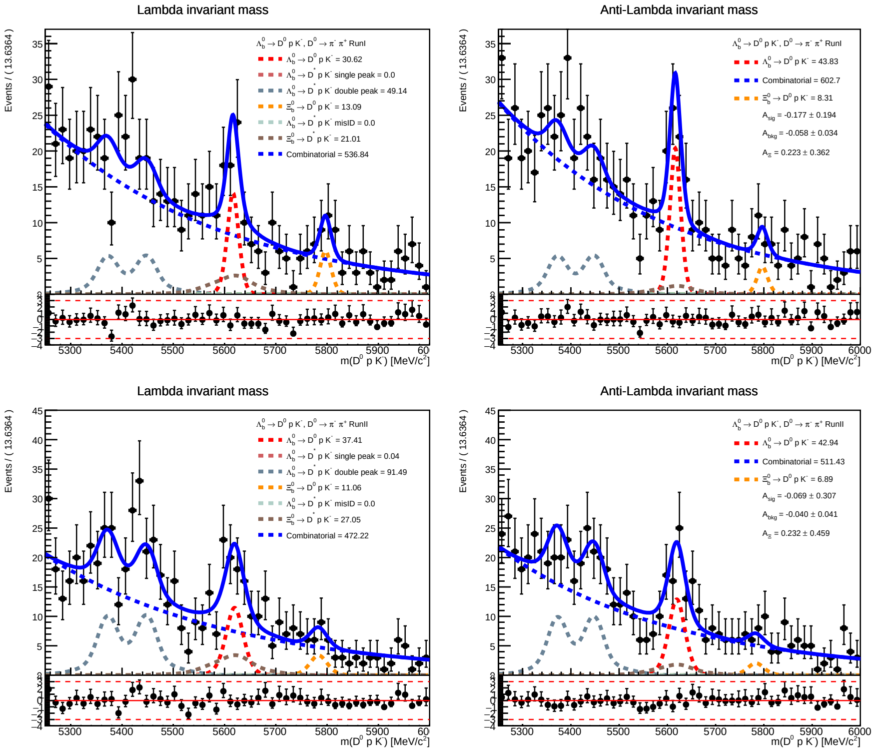

Figure 5.28: Simultaneous unbinned maximum-likelihood fit for $\Lambda_b^0 \to [\pi^-\pi+]_{D^0}pK^-$ decays in the restricted Λ^* resonances phase space, on the left column, the results for Λ_b^0-type are shown, on the right column, the results for $\overline{\Lambda}_b^0$-type are shown.

Crystal Ball functions to a single Crystal Ball function. For the partially reconstructed background from Ξ_b^0 decays, the current model employs a RooKeysPdf. We replaced this with a double Crystal Ball function to evaluate the impact of different functional forms on the fit, as this was the shape selected in a previous analysis performed within the collaboration [77]. This background is particularly challenging due to its complex structure, and accurate modelling is crucial to estimate the pollution of the signal. By systematically varying these components of the fit model, we can estimate the associated variation of the result and estimate the influence on our results. The contribution of this component to the total systematic uncertainty can be found in Table 5.9.

	$D^0 \to K^-\pi^+$		$D^0 \to K^-K^+$		$D^0 \to \pi^-\pi^+$	
Shape variation	Run I	Run II	Run I	Run II	Run I	Run II
Signal	-0.005	0.001	-0.009	-0.008	0.001	-0.006
Misidentification background	0.002	-0.001	-0.000	-0.01	0.000	0.000
Combinatorial background	0.004	-0.03	-0.007	-0.002	-0.025	-0.016
Total	$^{+0.004}_{-0.005}$	$^{+0.001}_{-0.03}$	$^{+0.000}_{-0.007}$	$^{+0.000}_{-0.01}$	$^{+0.001}_{-0.025}$	$^{+0.01}_{-0.006}$

Table 5.9: Variation of the Asymmetry depending on the shape used to describe the components in the first column.

5.7.2 Efficiency corrections

The efficiency corrections for the selection criteria are determined as a function of the Dalitz plot variables $\mathrm{m}^2(D^0p)$ and $\mathrm{m}^2(pK^-)$ using the simulated $\Lambda_b^0 \to D^0 pK^-$ sample. The candidates are set in a 20x20 bins grid, to which is assigned an efficiency value. Variations in the number of bins are used to assess the systematic uncertainty arising from the limited MC sample statistics. The impact of these variations is found to be below 1%.

5.8 Trigger induced asymmetries

This section discusses the procedure used to determine the asymmetries introduced by the trigger requirements. Trigger selection is necessary for the candidate events, but it can introduce asymmetry if the trigger's performance varies for oppositely charged D^0pK and $D^0p\pi$ pairs. Specifically, the trigger selection in this analysis involves `L0Global_TIS or L0HadronDecision_TOS` on L0 and `Hlt1(Track|TwoTrack)MVADecision_TOS` or`Hlt1(DiMuon|SingleMuon|Track)_TIS` on HLT1. Therefore, we must evaluate the impact of three components: the TOS component of L0, the TIS component of L0, and the same for HLT1. As HLT2 selection is applied after the full decay chain is reconstructed and the cuts do not differentiate between positively and negatively charged particles, we do not expect any asymmetry, which in any case is considered in the efficiency of the selection complementary to the PID efficiency and PID-induced asymmetry. The TIS part will be estimated using the control channel, $\Lambda_b^0 \to D^0 p\pi^-$ decays, whereas the TOS contribution will be assessed via efficiency tables used to calibrate the samples. The detailed procedure for this analysis will be explained in the following sections.

5.8.1 TIS asymmetry

A potential asymmetry from `L0Global_TIS` can arise due to the fact that TIS events are typically triggered by another beauty hadron in the event, which preferably decays semileptonically in a high-$\mathrm{p_T}$ muon that can trigger L0. Since the charge of the muon is related to the flavour of the b-hadron, an asymmetry between *CP* conjugate final states can be introduced. The `L0Global_TIS` term of the selection is not expected to give a noticeable effect on the raw asymmetry observed in the sample, as this trigger is activated independently of the signal decay by other particles coming from the pp collision; this correction will be nonetheless evaluated. In principle, any b-hadron decay with large enough statistics should serve the purpose of computing this asymmetry, since we have no way to know which decay was responsible for the trigger decision. We decide to use $\Lambda_b^0 \to D^0 p\pi^-$ decays. As it was checked that there are no dependencies of the asymmetry of the parent particle's kinematics, it is found that there is no need in performing the measurement as a function of the Λ_b^0 transverse momentum. The total value of the asymmetry on the signal $\Lambda_b^0 \to D^0 pK^-$ sample will be adopted by the result obtained because, as said, no kinematical dependencies are found. The procedure for computing the TIS asymmetry is the following:

- Apply the selection to the $\Lambda_b^0 \to D^0 p\pi^-$ sample.
- Divide the sample by charge of the Λ_b^0 and trigger category:
  - TIS: `L0Global_TIS and L0HadronDecision_TOS`;
  - !TIS: `!L0Global_TIS and L0HadronDecision_TOS`;

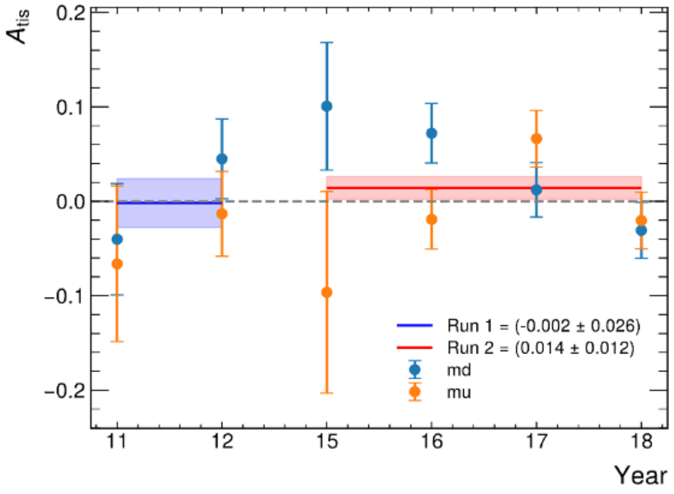

Figure 5.29: The figure displays the A_{TIS} values in each year for Run 1 and Run 2. The blue band represents the weighted average over the Run 1 period, and the red band represents the weighted average over the Run 2 period. Data points for Λ_b^0 decays into $D^0 p\pi^-$ are indicated with different markers for each year, distinguishing between the two magnet polarities.

- For each subsample, perform a maximum likelihood invariant-mass fit to extract the signal yields. The model adopted is the standard one.
- Compute the TIS efficiencies and asymmetry as:

$$\epsilon^+_{\text{TIS}} = \frac{N(\text{TIS}, \Lambda_b^0)}{N(\text{TIS}, \Lambda_b^0) + N(!\text{TIS}, \Lambda_b^0)}$$

$$\epsilon^-_{\text{TIS}} = \frac{N(\text{TIS}, \overline{\Lambda}_b^0)}{N(\text{TIS}, \overline{\Lambda}_b^0) + N(!\text{TIS}, \overline{\Lambda}_b^0)}$$

$$A_{\text{TIS}} = \frac{\epsilon^+_{\text{TIS}} - \epsilon^-_{\text{TIS}}}{\epsilon^+_{\text{TIS}} + \epsilon^-_{\text{TIS}}}$$

The resulting A_{TIS} values are shown in Figure 5.29 for Run 1 and Run 2. The total corrections amount to $(-0.2 \pm 2.6)\%$ for Run 1 and $(1.4 \pm 1.2)\%$ for Run 2.

5.8.2 TOS asymmetry

The calculation of TOS asymmetries for hadrons involves a systematic approach using calibration samples to ensure accurate and unbiased efficiency measurements [78]. The L0 hadron efficiency is determined using a sample of well-identified pions ($\pi^\pm$) and kaons ($K^\pm$) from $D^0 \to K^-\pi^+$ and $\overline{D}^0 \to K^+\pi^-$ decays, as well as protons ($p/\overline{p}$) from $\Lambda \to p\pi^-$ and $\overline{\Lambda} \to \overline{p}\pi^+$ decays. These calibration samples are specifically selected to be independent of any L0Calo candidates, ensuring that the determination of trigger efficiency is free from bias introduced by the trigger conditions themselves, as these events are triggered by L0Muon. The TOS efficiency is computed by evaluating the fraction of events that are TIS and also passing the L0 hadron trigger condition (TOS). This is done by calculating the ratio $\epsilon_{\text{hadron}} = \frac{N(\text{TIS and TOS})}{N(\text{TIS})}$, where $N(\text{TIS and TOS})$ is the number of events independent of the trigger that pass the L0 hadron trigger condition, and $N(\text{TIS})$ is the total number of events independent of the trigger. A charged

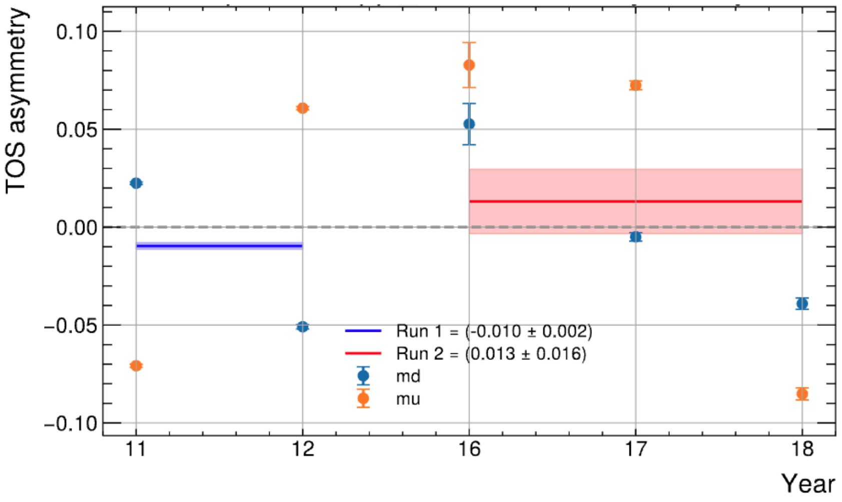

Figure 5.30: The figure illustrates the TOS asymmetry as a function of the years for Run 1 and Run 2. The blue band represents the weighted average of the TOS asymmetry during Run 1, and the red band represents the weighted average of the TOS asymmetry during Run 2. Data points are shown with different markers for each year, distinguishing between two magnet polarities.

track (either $\pi^\pm$, $K^\pm$, or $p/\overline{p}$) is classified as TOS if the 3×3 cell cluster built around the HCAL cell hit by the projection of the track shares at least one cell with a 2×2 cluster of an L0Calo hadron candidate with E_T above the trigger threshold. Additionally, the event is classified as TIS if it was triggered by the L0 Muon system (either Single or Di-Muon trigger conditions). This approach helps avoid bias from the efficiency computation and ensures that the L0 Muon trigger does not influence the hadron trigger efficiency measurement. To eliminate any residual bias from muons that punch through the HCAL and contribute to the L0 Muon trigger, the track is required not to be matched with any of the muon candidates responsible for the L0 Muon trigger. Only charged tracks within the acceptance of the HCAL and those with an SPD hit multiplicity below 600 are considered. The use of the efficiency tables so computed allowed to compute the asymmetry on the MCs $\Lambda_b^0 \to D^0 p K^-$, reported below. From the tables, an efficiency value is assigned to each event. Then, signal events are extracted using the *sFit* technique, after splitting the dataset into Λ_b^0 and $\overline{\Lambda}_b^0$ categories. The previously assigned efficiency values are then summed, allowing the computation of ϵ^+_TOS and ϵ^-_TOS for the two categories, respectively. Finally, the asymmetry is computed as

$$A_\mathrm{TOS} = \frac{\epsilon^+_\mathrm{TOS} - \epsilon^-_\mathrm{TOS}}{\epsilon^+_\mathrm{TOS} + \epsilon^-_\mathrm{TOS}}.$$

Figure 5.30 reports the results computed for Run 1 and Run 2 separately, which account for a correction respectively of $(1.0 \pm 0.2)\%$ and $(1.3 \pm 1.6)\%$.

5.8.3 L0 Trigger

Given the overlap of the TIS and TOS categories, a simple average of the asymmetries obtained for the two asymmetries is not possible. Therefore, to combine them, one needs to consider the efficiencies of the categories separately. The outcome is

$$A_{L0} = \frac{\epsilon_\mathrm{TIS} A_\mathrm{TIS} + \epsilon_\mathrm{TOS} A_\mathrm{TOS} - \epsilon_\mathrm{TIS}\epsilon_\mathrm{TOS}(A_\mathrm{TIS} + A_\mathrm{TOS})}{\epsilon_\mathrm{TIS} + \epsilon_\mathrm{TOS} - \epsilon_\mathrm{TOS}\epsilon_\mathrm{TIS}}, \tag{5.3}$$

resulting in $A_{L0} = (-0.57 \pm 0.3)\%$ and $A_{L0} = (1.14 \pm 0.4)\%$ respectively for RunI and RunII.

5.8.4 HLT1 asymmetry

The value of a possible asymmetry introduced by HLT1 selection is adopted from another analysis [79]. The method they used is the following: in order to compute the HLT1 asymmetry, a semileptonic sample is used, following a defined selection process. An efficiency map is created as a function of transverse momentum (p_{T}) and $\log(\chi^2_{IP})$ of the daughter particles by triggering on the muon and probing the hadron. This efficiency is computed with the formula:

$$\epsilon_h^{\pm}(p_{\mathrm{T}}, \log(\chi^2_{IP})) = \frac{N(\texttt{Hlt1TrackMVA\_TOS}(h^{\pm})\&\texttt{Hlt1TrackMuon\_TOS}(\mu)\&\texttt{L0\_TOS}(\mu))}{N(\texttt{Hlt1TrackMuon\_TOS}(\mu)\&\texttt{L0\_TOS}(\mu))}, \tag{5.4}$$

where h represents a proton, kaon, or pion. Using this, the efficiency for the $\Lambda_b^0 \to ph^-$ sample is calculated for each p_{T} bin and $\log(\chi^2_{IP})$ bin, and the two-body efficiency for Λ_b^0 is derived:

$$\epsilon^{p}_{\Lambda_b^0} = \epsilon_p^+(1-\epsilon_h^-) + (1-\epsilon_p^+)\epsilon_h^- \tag{5.5}$$

$$\epsilon^{\overline{p}}_{\Lambda_b^0} = \epsilon_p^-(1-\epsilon_h^+) + (1-\epsilon_p^-)\epsilon_h^+ \tag{5.6}$$

From this, the bin-per-bin asymmetry is obtained:

$$A_{\Lambda_b^0,i} = \frac{\epsilon^{p}_{\Lambda_b^0} - \epsilon^{\overline{p}}_{\Lambda_b^0}}{\epsilon^{p}_{\Lambda_b^0} + \epsilon^{\overline{p}}_{\Lambda_b^0}} \tag{5.7}$$

Finally, the overall HLT1 asymmetry is computed as the sum over all bins:

$$A_{\mathrm{HLT1}} = \sum_{i=1}^{N} f_i A_{\Lambda_b^0,i} \tag{5.8}$$

where f_i is the fraction of *sWeights* in the bin. Systematic uncertainty is added by comparing efficiencies from simulated samples with MC truth matched. The resulting asymmetry values for each year and magnet polarity are compatible to zero. Hence, for our analysis, we adopt this result, making HLT1 asymmetry negligible.

5.9 $\Lambda_b^0/\overline{\Lambda}_b^0$ production asymmetry

To measure the production asymmetry of the Λ_b^0 baryon in Run 1, we analysed $\Lambda_b^0 \to \Lambda_c^+\pi^-$ decays, with $\Lambda_c^+ \to pK^-\pi^+$, as documented in [80]. This analysis focused on Λ_b^0 rapidity and transverse momentum. The resulting maps facilitate the application to samples with different kinematic distributions. We utilised p_{T}-dependent values from Table 5.10 to calculate the production asymmetry for the $\Lambda_b^0 \to D^0ph^-$ sample in Run 1. For Run 2, it could not be possible to re-use the same table as production asymmetry scales with the center-of-mass energy, which has increased in Run 2 with respect to Run 1. Nonetheless, given that this analysis is statistically dominated, it can be acceptable to adopt the 2012 table remaining conservative on the final result. The calculation is performed using the following equation:

$$A_P(\Lambda_b^0) = \sum_i f_i A_{P,i}, \tag{5.9}$$

where $f_i = w_i/\sum_i w_i$, with i labeling the p_{T} bin and w_i representing the sum of the *sWeights* of the $\Lambda_b^0 \to D^0ph^-$ sample in bin i. $A_{P,i}$ is defined as $\frac{\sigma(pp\to\Lambda_b^0 Y)-\sigma(pp\to\overline{\Lambda}_b^0 Y)}{\sigma(pp\to\Lambda_b^0 Y)+\sigma(pp\to\overline{\Lambda}_b^0 Y)}$ per each p_{T} bin. The results of this computation are shown in Figure 5.31. The measured asymmetries are $(1.497 \pm 0.408)\%$ for Run 1 and $(1.106 \pm 0.211)\%$ for Run 2.

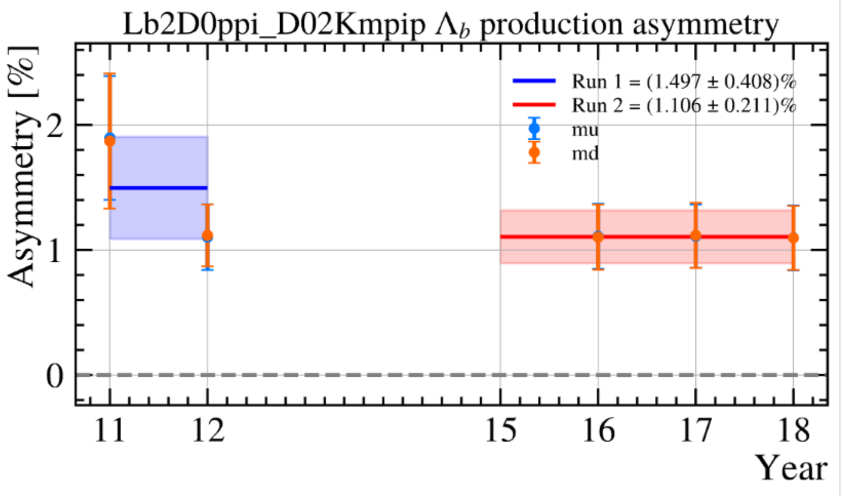

Figure 5.31: Production asymmetry of Λ_b^0 baryons as measured in Run 1 and Run 2. The asymmetry values are shown for different years, with the weighted average for Run 1 indicated in blue and Run 2 in red. The data points represent measurements for different years, with "mu" and "md" denoting different magnet polarities. The shaded areas represent the uncertainty in the measurements.

5.10 Detector interaction asymmetries

Final state particle interaction asymmetries are crucial phenomena that arise from differences in how particles and antiparticles interact with the detector material or the surrounding environment. These asymmetries can introduce significant biases in experimental measurements. When charged particles traverse the detector, they undergo various interactions such as energy loss, scattering, and absorption. These interactions can differ for particles and antiparticles due to their opposite charges. For instance, positive and negative particles might have different probabilities of ionising the detector material, leading to discrepancies in their energy loss rates. Additionally, the scattering angles might differ, causing particles and antiparticles to follow different trajectories through the detector. Magnetic fields present in the detector environment can further exacerbate these differences. Charged particles and antiparticles bend in opposite directions when exposed to a magnetic field. If the detector's acceptance or efficiency is not perfectly symmetric with respect to the magnetic field, it can result in different detection probabilities for particles and antiparticles. Hadronic interactions also play a significant role in final state interaction asymmetries. Particles such as protons, kaons, and pions can undergo strong interactions with the detector material. The cross-sections for these interactions can differ between particles and antiparticles due to differences in their quark content and interaction dynamics. This can

	$\sqrt{s} = 7$ TeV	$\sqrt{s} = 8$ TeV
$2 < p_{\mathrm{T}} < 4$ GeV/c	$1.28 \pm 1.08 \pm 0.29$	$1.58 \pm 0.74 \pm 0.35$
$4 < p_{\mathrm{T}} < 8$ GeV/c	$2.05 \pm 0.35 \pm 0.30$	$1.19 \pm 0.23 \pm 0.33$
$8 < p_{\mathrm{T}} < 12$ GeV/c	$1.89 \pm 0.34 \pm 0.24$	$1.21 \pm 0.22 \pm 0.24$
$12 < p_{\mathrm{T}} < 18$ GeV/c	$2.08 \pm 0.49 \pm 0.25$	$0.88 \pm 0.32 \pm 0.23$
$18 < p_{\mathrm{T}} < 27$ GeV/c	$0.49 \pm 1.11 \pm 0.34$	$-0.06 \pm 0.68 \pm 0.26$

Table 5.10: Λ_b^0 production asymmetry measured at $\sqrt{s} = 7$ TeV and $\sqrt{s} = 8$ TeV for different p_{T} bins.

lead to differences in their detection efficiencies, as antiparticles might be more likely to be absorbed or scattered out of the detector acceptance compared to their particle counterparts. The following will present the strategy of this analysis to estimate the final state particle detection asymmetries.

5.10.1 Kaon detection asymmetries

The kaon detection asymmetry, $A_D(K^-)$, is defined as

$$A_D(K^-) = \frac{\epsilon_{\text{reco}}(K^-) - \epsilon_{\text{reco}}(K^+)}{\epsilon_{\text{reco}}(K^-) + \epsilon_{\text{reco}}(K^+)}, \tag{5.10}$$

where ϵ_{reco} stands for the reconstruction efficiency of the given particle. This asymmetry can be obtained by measuring the two-body detection asymmetry $A_D(K^-\pi^+)$, as explained in [81]. Using $D^+ \to K^-\pi^+\pi^+$ and $D^+ \to K^0_S\pi^+$ control modes, the strategy involves selecting these decays from Run 1 and Run 2 data and dividing the samples into bins of kaon momentum. A kinematic reweighting is applied in each bin to equalise the kinematics of the two decays, performed over the p_{T} and η distributions of the D^+ and tag pion, i.e. the pion used for the flavour identification. A fiducial cut is added to avoid regions not sufficiently covered by either sample. After reweighting, a maximum-likelihood fit is performed in each bin to extract the raw asymmetries $A_{\text{raw}}(D^+ \to K^-\pi^+\pi^+)$ and $A_{\text{raw}}(D^+ \to K^0_S\pi^+)$. The fits model the signal shape with a Crystal Ball function for $D^+ \to K^0_S\pi^+$ and Gaussian functions for $D^+ \to K^-\pi^+\pi^+$, while the combinatorial background is modelled with an exponential function. The kaon detection asymmetry $A_D(K^-)$ is computed as the difference between the raw asymmetries, subtracting the known $A(K^0)$ asymmetry. This procedure is applied separately to sub-samples divided by year and magnet polarity. Kinematic reweighting ensures the cancellation of residual nuisance asymmetries between the decays. The resulting $A_D(K^-)$ values in each momentum bin are integrated over the non-tag pion (a pion present in the decay products but not used for the flavour identification) kinematic distributions to obtain a total asymmetry value per bin, which is then subtracted from the two-track asymmetry to get the single-track $A_D(K^-)$ asymmetry. The table obtained in this study, reported in Table 5.11, is then used to compute the asymmetry as a function of the kaon momentum for the decay $\Lambda^0_b \to D^0pK^-$. The result can be seen in Figure 5.32, and set to be $A_{det}(K) = (-0.776 \pm 0.693)\%$ in Run 1 and $A_{det}(K) = (-0.714 \pm 0.096)\%$ in Run 2.

5.10.2 Pion detection asymmetries

The pion detection asymmetry $A_D(\pi^+)$ is defined as:

$$A_D(\pi^+) = \frac{\epsilon_{\text{reco}}(\pi^+) - \epsilon_{\text{reco}}(\pi^-)}{\epsilon_{\text{reco}}(\pi^+) + \epsilon_{\text{reco}}(\pi^-)}.$$

Here, $\epsilon_{\text{reco}}(\pi^\pm)$ represents the reconstruction efficiency for π^+ and π^-, respectively. In Run 1, the pion detection asymmetry was measured using partially reconstructed $D^{*+} \to D^0(D^0 \to K^-\pi^+\pi^+\pi^-)\pi^+$ decays [82]. The key idea was to select events where one of the final-state pions was undetected and infer its momentum using the mass difference $\Delta M = m(\pi_s K^-\pi^+\pi^-) - m(K^-\pi^+\pi^-)$. This method leverages kinematic constraints to calculate the reconstruction efficiency. The reconstruction efficiency for pions, $\epsilon_{\text{reco}}(\pi^\pm)$, was defined as the ratio of the number

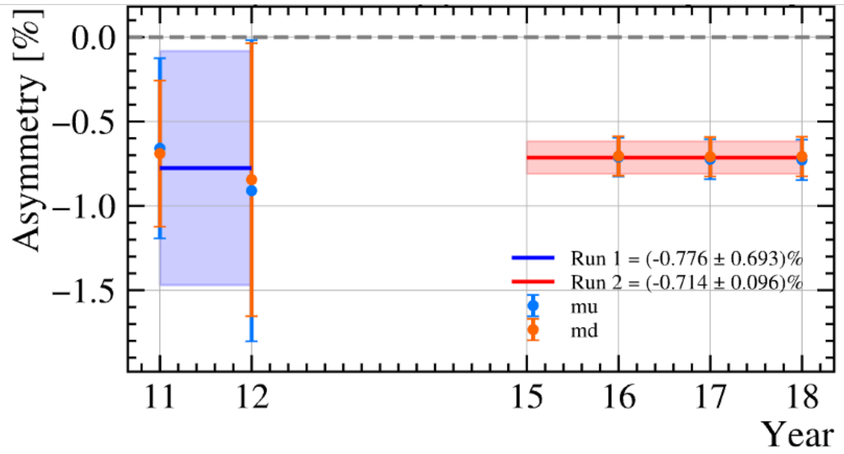

Figure 5.32: Detection asymmetry for $K^-_{\Lambda_b^0}$ mesons across different years. The asymmetry values are shown for different years, with the weighted average for Run 1 indicated in blue and Run 2 in red. The data points represent measurements for different years, with "mu" and "md" denoting different magnet polarities. The shaded areas represent the uncertainty in the measurements.

	$K^-\pi^+$		K^-	
Momentum [Gev/c^2]	Run 1 [%]	Run 2 [%]	Run 1 [%]	Run 2 [%]
$5 < p < 10$	-3.0 ± 2.4	-1.34 ± 0.20	-2.8 ± 2.4	-1.23 ± 0.20
$10 < p < 15$	-0.55 ± 0.30	-0.868 ± 0.093	-0.36 ± 0.31	-0.763 ± 0.095
$15 < p < 20$	-0.82 ± 0.22	-0.639 ± 0.090	-0.65 ± 0.23	-0.526 ± 0.092
$20 < p < 25$	-0.90 ± 0.24	-0.652 ± 0.095	-0.77 ± 0.25	-0.545 ± 0.097
$25 < p < 40$	-1.04 ± 0.16	-0.840 ± 0.082	-0.90 ± 0.17	-0.742 ± 0.085
$40 < p < 60$	-0.60 ± 0.21	-0.81 ± 0.12	-0.47 ± 0.22	-0.71 ± 0.12
$60 < p < 80$	-0.54 ± 0.36	-0.65 ± 0.14	-0.41 ± 0.37	-0.55 ± 0.14

Table 5.11: Comparison of $K^-\pi^+$ and K^- asymmetries for Run 1 and Run 2 in different momentum bins.

of partially reconstructed pions to the number of fully reconstructed pions:

$$\epsilon_{\text{reco}}(\pi^{\pm}) = \frac{N_{\text{partial}}(\pi^{\pm})}{N_{\text{full}}(\pi^{\pm})}.$$

By analysing the partially and fully reconstructed events, the efficiency as a function of pion momentum was measured. This approach allowed for a detailed comparison of the kinematics of pions from different samples. However, due to the momentum resolution being worse for the missing pion in partial reconstructions, an unfolding procedure was required to correct the momentum distribution. The result is reported in Table 5.12.

In Run 2, a different method was employed, involving K_S^0 decays from the bin-flip $D^* \to (D^0 \to K_S^0\pi^+\pi^-)\pi^+$ analysis [83]. This method combined one VELO track and a long track to reconstruct $K_S^0 \to \pi^+\pi^-$ decays. The efficiency to reconstruct a pion was determined by matching VELO tracks to long tracks and calculating the ratio:

$$\epsilon^{\pm} = \frac{N(\pi^{\pm}\text{VELO tracks matched to long tracks})}{N(\pi^{\pm}\text{VELO tracks})}$$

Momentum	2011		2012	
Gev/c^2	Down	Up	Down	Up
$p \in [2, 6]$	$(-0.59 \pm 0.36)\%$	$(-0.45 \pm 0.43)\%$	$(0.32 \pm 0.22)\%$	$(-1.21 \pm 0.21)\%$
$p \in [6, 15]$	$(0.34 \pm 0.24)\%$	$(-0.47 \pm 0.29)\%$	$(0.00 \pm 0.15)\%$	$(-0.52 \pm 0.15)\%$
$p \in [15, 20]$	$(0.14 \pm 0.34)\%$	$(-0.22 \pm 0.42)\%$	$(-0.12 \pm 0.21)\%$	$(0.08 \pm 0.21)\%$
$p \in [20, 30]$	$(0.18 \pm 0.37)\%$	$(-0.31 \pm 0.45)\%$	$(-0.12 \pm 0.22)\%$	$(0.04 \pm 0.22)\%$
$p \in [30, 40]$	$(0.04 \pm 0.56)\%$	$(-0.11 \pm 0.68)\%$	$(-0.73 \pm 0.33)\%$	$(0.15 \pm 0.33)\%$
$p \in [40, 50]$	$(0.04 \pm 0.80)\%$	$(0.88 \pm 0.96)\%$	$(-0.50 \pm 0.48)\%$	$(0.15 \pm 0.48)\%$
$p \in [50, 100]$	$(-0.49 \pm 0.88)\%$	$(0.6 \pm 1.1)\%$	$(-1.07 \pm 0.51)\%$	$(0.62 \pm 0.51)\%$
$p \in [100, 150]$	$(-0.5 \pm 1.8)\%$	$(0.6 \pm 2.1)\%$	$(-1.1 \pm 1.0)\%$	$(0.6 \pm 1.0)\%$

Table 5.12: Table of π^- detection asymmetry values for different momentum ranges for the years 2011 and 2012, separated by magnet polarity (Down and Up).

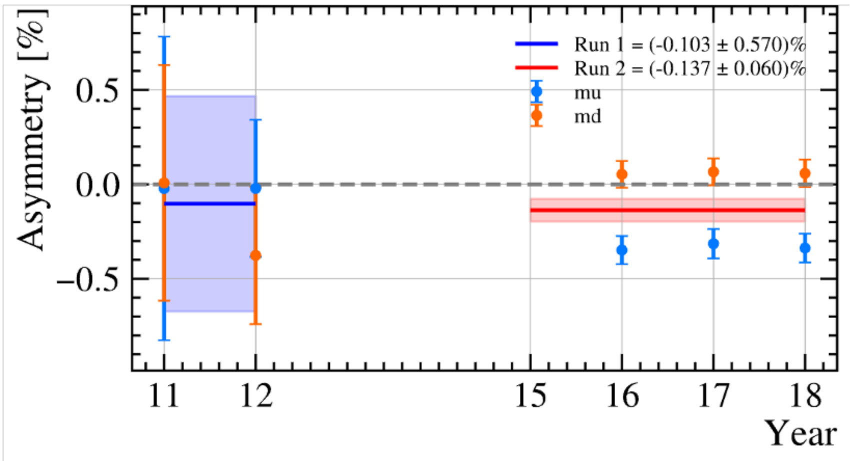

Figure 5.33: Detection asymmetry for pions over the years 2011 to 2018. The asymmetry values are shown for different years, with the weighted average for Run 1 indicated in blue and Run 2 in red. The data points represent measurements for different years, with "mu" and "md" denoting different magnet polarities. The shaded areas represent the uncertainty in the measurements.

The efficiencies were then obtained as functions of momentum and pseudorapidity. The asymmetry was calculated using the same formula as for Run 1. The kinematic reweighting was performed with the `hep_ml` package to equalise the p_T and η distributions of the D^+ and the tag pion (π^+) from the $D^+ \to K^-\pi^+\pi^+$ decay firing the `Hlt1TrackMVA` line. The overall asymmetry is calculated as $A_D(\pi^+) = (-0.10 \pm 0.57)\%$ for Run 1 and $A_D(\pi^+) = (-0.14 \pm 0.06)\%$ for Run 2, indicating compatibility between the two runs. A representation of the asymmetry computed per year can be found in Figure 5.33.

5.10.3 Proton detection asymmetries

Given the compatibility between Run 1 and Run 2 values of the interaction asymmetries of pions and kaons, it is reasonable to use the available Run 1 proton interaction asymmetry for both runs. This measurement was conducted during the Run 1 Λ_b^0 production asymmetry analysis, detailed as follows:

- For each proton (or antiproton) track in the $\Lambda_b^0 \to \Lambda_c^+(\to pK^-\pi^+)\mu\nu X$ sample, the total detector material encountered in the flight path, $d^{\pm}$, is computed using a simulation of the detector. This is expressed in units of the nuclear collision length $\lambda^{\pm}$. The latter is defined as the typical distance a hadron travels before undergoing an (in)elastic scatter with a nucleus in the material.

- Assuming the dependence of $\lambda^{\pm}$ on the particle's momentum in the detector material scales equally as the collision length for a deuterium target, a measurement from COMPASS [84] is used. This allows $\lambda^{\pm}$ for any atomic number A and momentum p to be factorised as:

  $$\lambda^{\pm}(A,p) = \lambda_{\text{avg}}(A, 20\,\text{GeV}/c)\frac{\sigma_{\text{avg}}(2H, 20\,\text{GeV})}{\sigma^{\pm}(2H,p)},$$

  where σ denotes the hadronic interaction cross-section and the avg subscript indicates a charge-averaged quantity.

- By computing the traversed thickness $d^{\pm}$ for each (anti)proton and considering the material collision length at a given momentum, the detection efficiency can be evaluated as:

  $$\epsilon^{\pm} \propto \exp\left(-\frac{d^{\pm}}{\lambda^{\pm}}\right).$$

  From this, a detection asymmetry can be readily computed:

  $$A_D(p) = \frac{\exp(-d^+/\lambda^+) - \exp(-d^-/\lambda^-)}{\exp(-d^+/\lambda^+) + \exp(-d^-/\lambda^-)}.$$

The measurement was performed as a function of the Λ_b^0 kinematics and proton momentum. The latter is used to reweight the kinematics of the protons in the signal $\Lambda_b^0 \to D^0 p h^-$ sample. The momentum distribution of the proton interaction asymmetry is reported in Table 5.13 and shown in Figure 5.34. For Run 1, the maps are used as they are, while for Run 2 samples, the 2012 map will be used for all years. The average values for $\Lambda_b^0 \to D^0 p K^-$ decays are found to be $(1.445 \pm 0.220)\%$ for Run 1 and $(1.484 \pm 0.182)\%$ for Run 2.

Momentum bin	2011		2012	
Gev/c^2	Down	Up	Down	Up
$10 < p < 15$	$(2.23 \pm 0.28)\%$	$(2.08 \pm 0.26)\%$	$(2.20 \pm 0.28)\%$	$(2.07 \pm 0.26)\%$
$15 < p < 25$	$(1.79 \pm 0.24)\%$	$(1.61 \pm 0.22)\%$	$(1.77 \pm 0.24)\%$	$(1.60 \pm 0.22)\%$
$25 < p < 40$	$(1.38 \pm 0.22)\%$	$(1.27 \pm 0.21)\%$	$(1.37 \pm 0.22)\%$	$(1.25 \pm 0.20)\%$
$40 < p < 60$	$(1.08 \pm 0.20)\%$	$(1.02 \pm 0.19)\%$	$(1.07 \pm 0.20)\%$	$(1.02 \pm 0.19)\%$
$60 < p < 80$	$(0.89 \pm 0.18)\%$	$(0.86 \pm 0.18)\%$	$(0.88 \pm 0.18)\%$	$(0.85 \pm 0.18)\%$
$80 < p < 125$	$(0.74 \pm 0.17)\%$	$(0.74 \pm 0.17)\%$	$(0.75 \pm 0.17)\%$	$(0.71 \pm 0.16)\%$

Table 5.13: Table of proton detection asymmetry values for different momentum ranges for the years 2011 and 2012, separated by magnet polarity (Down and Up)

5.11 PID induced asymmetry

PID induced asymmetries arise from the differences in the efficiency of identifying positively and negatively charged particles. These asymmetries can affect the measurements by introducing biases in the detection of particles like pions, kaons, and protons. The differences in efficiency can

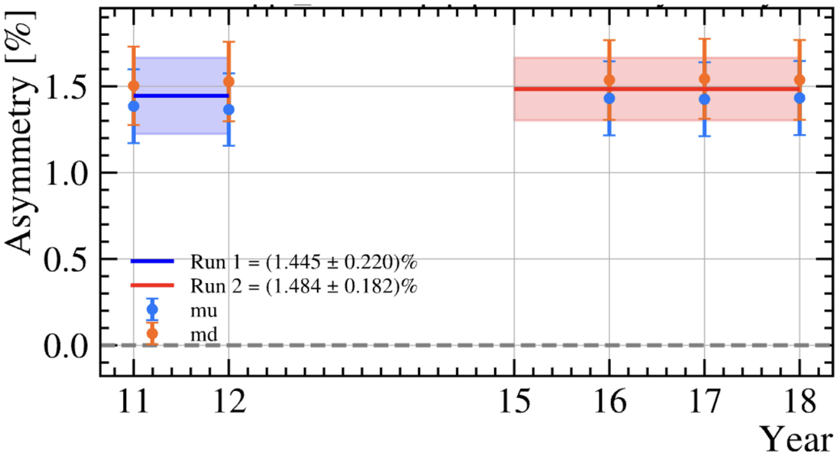

Figure 5.34: Detection asymmetry for protons over the years 2011 to 2018. The asymmetry values are shown for different years, with the weighted average for Run 1 indicated in blue and Run 2 in red. The data points represent measurements for different years, with "mu" and "md" denoting different magnet polarities. The shaded areas represent the uncertainty in the measurements.

stem from various sources, including detector geometry, magnetic field effects, and differences in the interaction of particles with the detector material. To quantify and correct for these PID induced asymmetries, this analysis employs the `PIDCalib2` package. The process to compute PID-induced asymmetries with `PIDCalib2` involves several steps:

1. Computation of the correction factors: Apply PID selection to compute the weights to be applied to the selected MCs.

2. Efficiency Determination: Calculate the PID efficiency for positively and negatively charged particles separately. The efficiency, ϵ, is obtained multiplying the PID efficiency of the final state particles.

3. Calculation of Asymmetry: The PID asymmetry, A_{PID}, is computed using the formula:

$$A_{PID}(h^+) = \frac{\epsilon_{PID}(\overline{D}^0 \overline{p} K^+) - \epsilon_{PID}(D^0 p K^-)}{\epsilon_{PID}(\overline{D}^0 \overline{p} K^+) + \epsilon_{PID}(D^0 p K^-)},$$

   where $\epsilon_{PID}(\overline{D}^0 \overline{p} K^+)$ and $\epsilon_{PID}(D^0 p K^-)$ are the PID efficiencies for positively and negatively charged particles, respectively. This asymmetry quantifies the difference in PID performance between particle and antiparticle.

The value obtained for each channel in both Run 1 and Run 2 is lower than 1%.

5.12 Summary of the uncertainties

Before presenting the results, in the following paragraph, it is possible to have a summary of the contributions that each source of uncertainty gives to the measurement in Table 5.14.

	$D^0 \to K^-\pi^+$		$D^0 \to K^-K^+$		$D^0 \to \pi^-\pi^+$	
Uncertainty	Run I	Run II	Run I	Run II	Run I	Run II
Statistical	0.08	0.04	0.16	0.08	0.15	0.14
Fit Model	$^{+0.004}_{-0.005}$	$^{+0.001}_{-0.003}$	$^{+0.000}_{-0.007}$	$^{+0.000}_{-0.001}$	$^{+0.001}_{-0.025}$	$^{+0.001}_{-0.006}$
Efficiency corrections	0.01	0.01	0.01	0.01	0.01	0.01
L0 Trigger	−0.006	+0.011	−0.006	+0.011	−0.006	+0.011
Production	+0.015	+0.011	+0.015	+0.011	+0.015	+0.011
Kaon detection	−0.008	−0.007	−0.008	−0.007	−0.008	−0.007
Proton detection	+0.014	+0.015	+0.014	+0.015	+0.014	+0.015
PID	0.01	0.01	0.01	0.01	0.01	0.01
Total systematic	$^{+0.03}_{-0.02}$	$^{+0.03}_{-0.02}$	$^{+0.03}_{-0.02}$	$^{+0.03}_{-0.02}$	$^{+0.03}_{-0.04}$	$^{+0.03}_{-0.02}$

Table 5.14: Influence of each contribution to the total uncertainty of the asymmetry measurement.

5.13 Results

This analysis aims to perform a measurement of the asymmetries as it follows:

$$A = \frac{\sum_i w_i^{\mathrm{GLW},\Lambda_b^0}/\epsilon_i^{\mathrm{GLW},\Lambda_b^0} - \sum_i w_i^{\mathrm{GLW},\overline{\Lambda}_b^0}/\epsilon_i^{\mathrm{GLW},\overline{\Lambda}_b^0}}{\sum_i w_i^{\mathrm{GLW},\Lambda_b^0}/\epsilon_i^{\mathrm{GLW},\Lambda_b^0} + \sum_i w_i^{\mathrm{GLW},\overline{\Lambda}_b^0}/\epsilon_i^{\mathrm{GLW},\overline{\Lambda}_b^0}}. \tag{5.11}$$

Here $w_i^{\mathrm{GLW},\Lambda_b^0}$ and $w_i^{\mathrm{GLW},\overline{\Lambda}_b^0}$ are the *sWeights* obtained from the invariant mass fit using the sPlot technique for the Λ_b^0 and $\overline{\Lambda}_b^0$ GLW events i, respectively, and ϵ_i are the corresponding efficiency correction weights. The sums go over all events in the datasets. The raw results are reported here as the weight-corrected ones will be computed after receiving the final approval from the working group within the LHCb Collaboration. Up to now, this document reported the measured values of the raw asymmetries for separate datasets of Run 1 and Run 2. The value for Run 1 and Run 2 combined is obtained by performing an unbinned maximum likelihood simultaneous fit between Run 1 and Run 2 for each GLW mode. The result, for Λ_b^0 and Ξ_b^0 decays can be found below

$$A_{\mathrm{CP}}^{K^-K^+}(\Lambda_b^0) = -0.15 \pm 0.07^{+0.03}_{-0.02}$$

$$A_{\mathrm{CP}}^{\pi^-\pi^+}(\Lambda_b^0) = 0.07 \pm 0.10 \pm 0.03$$

$$A_{\mathrm{CP}}^{K^-K^+}(\Xi_b^0) = -0.16 \pm 0.13^{+0.03}_{-0.02}$$

$$A_{\mathrm{CP}}^{\pi^-\pi^+}(\Xi_b^0) = 0.20 \pm 0.27 \pm 0.03,$$

where the first uncertainty is statistical and the second systematic. As expected, the result is mainly statistically dominated, given the small number of signal events. The same technique has been applied to the restricted phase space dataset, i.e. applying a mass cut m(D^0p)> 3100 GeV/c^2, giving the following results

$$A_{\mathrm{CP}}^{K^-K^+}(\Lambda_b^0) = -0.13 \pm 0.14^{+0.03}_{-0.02}$$

$$A_{\mathrm{CP}}^{\pi^-\pi^+}(\Lambda_b^0) = -0.11 \pm 0.19 \pm 0.03.$$

With the results obtained, the next step would be to measure the CKM angle γ. Unfortunately, recalling the formulas for the GLW modes observables and the discussion that followed, there is a non-negligible contribution from the parameter κ, which cannot currently be evaluated. This parameter is extracted from a full amplitude analysis of this decay, which has not yet been performed. I conclude this chapter by looking at the near future when also the *CP* violation measurements with the Λ_b^0 decays will be added and contribute to the γ measurement performed by the LHCb collaboration.

5.14 Future scenarios and prospects

After a difficult beginning, the LHCb experiment is now, in July 2024, completing the commissioning of the upgraded detector. Despite the impressive achievements, the data that have been collected until now, if analysed, would not allow to perform the same measurements as in Run 1 and Run 2, and therefore, the expected amount of data good for physics is diminished with respect to the foreseen one. In any case, given the higher center-of-mass energy, the increased luminosity, and the possible extension of the data-taking period expected, the goal of 23fb^{-1} of integrated luminosity is still achievable. If reached, the number of signal candidates for the decays of interest in this thesis should become roughly three times what was achieved now. With this scenario, the statistical uncertainty could go down to 0.02 for the $\Lambda_b^0 \to [K^- K^+]_{D^0} pK^-$ channel and down to 0.07 for the $\Lambda_b^0 \to [\pi^- \pi^+]_{D^0} pK^-$ channel, allowing for a much more clear evaluation of the asymmetry, if found. There are other searches with baryons performed within LHCb experiment, such direct *CP* asymmetries in decays as $\Lambda_b^0 \to pK^-$ and $\Lambda_b^0 \to p\pi^-$, which in Run 1 was limited to around 0.01 precision. However, as mentioned, achieving high sensitivity to the CKM angle γ is challenging due to the complex nature of hadronic parameters. Nonetheless, the precise determination of particle-antiparticle production asymmetries and detection asymmetries that could mimic *CP* violation effects remains a key experimental challenge, and the adoption of techniques like the difference of *CP* violating asymmetries in similar final states, triple-product asymmetries (TPA) [85], and energy tests (ET) are critical for the discovery of *CP* violation in multibody decays. Another promising area of research is the decay of beauty baryons to final states without a charm quark [86], influenced by $b \to d, s$ loop-level transitions. These decays are sensitive to new physics beyond the SM. Expected precisions of $\mathcal{O}(10^{-3})$ and $\mathcal{O}(10^{-2})$ for *CP* asymmetries in decays like $\Lambda_b^0 \to ph^-$ and $\Lambda_b^0 \to \Lambda h^+ h^-$ [87] highlight the potential of these studies. Large signal yields are also anticipated in multibody decays, enabling precise measurements across different phase spaces. While the theoretical understanding of these quantities remains challenging, future research is poised to fully exploit the potential of beauty baryons in elucidating *CP* violation and exploring physics beyond the SM.

6

Conclusions

In this thesis, the *CP* asymmetry for the Λ_b^0 baryon decaying to D^0pK^- has been measured in the full phase space and in a restricted one, where $m(D^0p) > 3100$ MeV/c^2. The data utilised come from proton-proton collisions within the LHCb detector in Run 1 and Run 2, i.e. from 2011 until 2018, at a center-of-mass energy of 7, 8, and 13 TeV. The main motivations for this measurement are the following: no *CP* violation has been measured in baryons yet, despite it is an expected phenomenon described by the SM. The LHCb collaboration itself published several attempted measurements, but compatibility with *CP* conservation has always been found. The aim of measuring *CP* violation in the selected decay served also to the measurement of the CKM angle γ, not the one known with the worst uncertainty within the three angles of the unitarity triangle, but nevertheless worth challenging the compatibility with the theoretical predictions computed by the UTfit [42] and the CKMfitter [41] collaborations. Furthermore, using baryons instead of the already exploited mesons to perform such a measurement would give access to a complementary search area, allowing access to side information, as b-baryon decays are sensitive to different manifestations of *CP* violation. Along with the Λ_b^0 *CP* violation measurement, this thesis presents the work done on the commissioning of the UT detector, beginning with the assembly, installation in the LHCb cavern, the characterization and monitoring, during the time of this thesis and taking data for the on-going Run 3.

The study performed on the Λ_b^0 baryon can be essentially broken into two steps: the selection and the fit. The selection on the dataset has been performed to remove sources of background polluting the signal, coming from the misidentification of final state particles, from the wrongful combination of the final state tracks, or from missing particles in the reconstruction of the signal. To cope with this amount of backgrounds, together with a selection on meaningful variables capable of discriminating the background events and the signal candidates, also a BDT was trained, with the peculiarity of being able to distinguish not only one type of background, as in the most common strategies of other analyses but being able to remove also the charmless background, a peaking polluting background whose reconstructed invariant mass, lays exactly under the signal peak. The selection on the variables was obtained by maximising a Figure of Merit, defined by $\frac{S}{\sqrt{S+B}}$, where S and B are respectively the number of estimated signal events and the number of background events underneath the signal peak. Once the selection has been fixed and the second part of the analysis began. Before performing the fit on the selected dataset, the shape of each component appearing in the investigated Λ_b^0 invariant mass range is chosen on the equally selected MC sample: it is the case for the signal, the misidentified background, and, for the $\Lambda_b^0 \to D^0pK^-$ model, the $\Xi_b^0 \to D^0pK^-$ contribution. The shape of the partially reconstructed backgrounds has been chosen through some simulations built with EvtGen and then smeared on MC. When the model was established, two different fit techniques were employed: an unbinned maximum likelihood fit on data and a simultaneous maximum likelihood fit on the split dataset. The same fitting strategies have been applied to the restricted phase space. With the toys validated model, the values for the *CP* asymmetry have been extracted for the $\Lambda_b^0 \to [K^-K^+]_{D^0}pK^-$ and $\Lambda_b^0 \to [\pi^-\pi^+]_{D^0}pK^-$ decays:

$$A_{\text{CP}}^{K^-K^+}(\Lambda_b^0) = -0.15 \pm 0.07^{+0.03}_{-0.02}$$

$$A_{\text{CP}}^{\pi^-\pi^+}(\Lambda_b^0) = 0.07 \pm 0.10 \pm 0.03$$

$$A_{\text{CP}}^{K^-K^+}(\Xi_b^0) = -0.16 \pm 0.13^{+0.03}_{-0.02}$$

$$A_{\text{CP}}^{\pi^-\pi^+}(\Xi_b^0) = 0.20 \pm 0.27 \pm 0.03,$$

and for the restricted phase space:

$$A_{\text{CP}}^{K^-K^+}(\Lambda_b^0) = -0.13 \pm 0.14^{+0.03}_{-0.02}$$

$$A_{\text{CP}}^{\pi^-\pi^+}(\Lambda_b^0) = -0.11 \pm 0.19 \pm 0.03,$$

having the first uncertainty statistical, and the second one systematic. Statistical uncertainties heavily dominate the measurement, and what is reported here is a result defined as raw, as the efficiency-weighted one will be extracted once the analysis strategy receives the final approval from the working group within the LHCb collaboration. The perspectives for the future include the goal of 23fb^{-1} of integrated luminosity at the end of Run 3. If reached, the number of signal candidates for the decays of interest in this thesis should become roughly three times what was achieved now, and also a factor 2 should be considered, coming from the removal of the L0 trigger. With this scenario, the statistical uncertainty of the full phase space could go down to 0.02 for the $\Lambda_b^0 \to [K^-K^+]_{D^0}pK^-$ channel and down to 0.07 for the $\Lambda_b^0 \to [\pi^-\pi^+]_{D^0}pK^-$ channel, allowing for a much more precise evaluation of the asymmetry, if found.

As mentioned previously, part of the work done in this thesis is linked to the commissioning of a new detector installed to contribute to the data taking of Run 3. As the luminosity and the center-of-mass energy are increasing, the experiment undergone major upgrades. One of these has been the change of the TT stations with the Upstream Tracker. My contribution begins with a more manual but essential task, the population of the DCBs with VTRx and VTTx, and their installation in the detector frame. The testing followed, to ensure correct powering, communication and data reception. I also contributed to the characterization of the silicon sensors, studying the noise in the clean room, testing the amplification capabilities when an MIP was injected, and comparing the results of the studies performed in the clean room and in the cavern, after the installation, to look for possible changes due to the change of operating environment. The result of this study allowed to identify components that were not behaving as expected, flag them, and study the source of the problem, either recovering or masking the specific channel. A final effort was made in working on the monitoring, as after the installation, it is fundamental to keep track of the behaviour of the detector when particles are running in the LHC. For this reason, quantities representative of the status of the detector are monitored, such as the number of hits per sensor, and the ADCs recorded by each module. These quantities filled both plots for experts to help them dive deeper into the issues encountered and for shifters in the control room of LHCb to ensure a continued and smooth running of the detector during data-taking periods.

A

BDT training results

The purpose of this Appendix is to report all the ROC curves, the Importances and the train/test comparison for all the decays for which a BDT was trained.

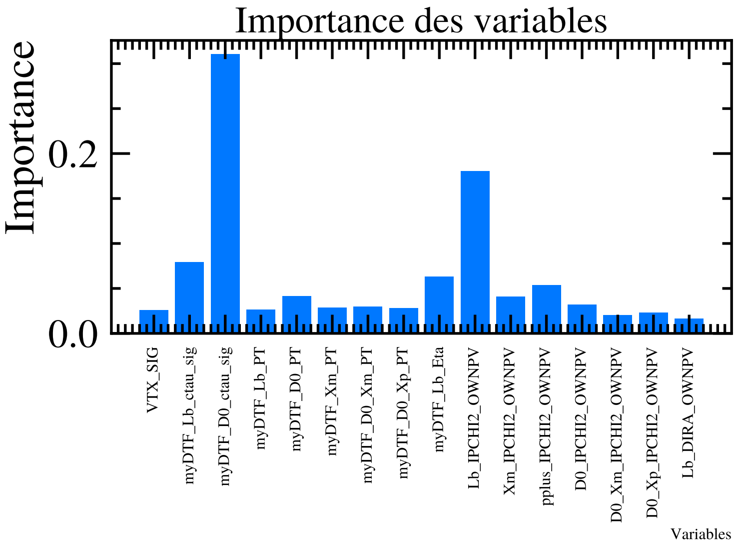

Figure A.1: Variable importance plot for the BDT trained for Run 2 $\Lambda_b^0 \to [K^-K^+]_{D^0}p\pi^-$. The x-axis lists the variables considered, while the y-axis represents the importance score, indicating how significantly each variable contributes to the BDT's decision-making process.

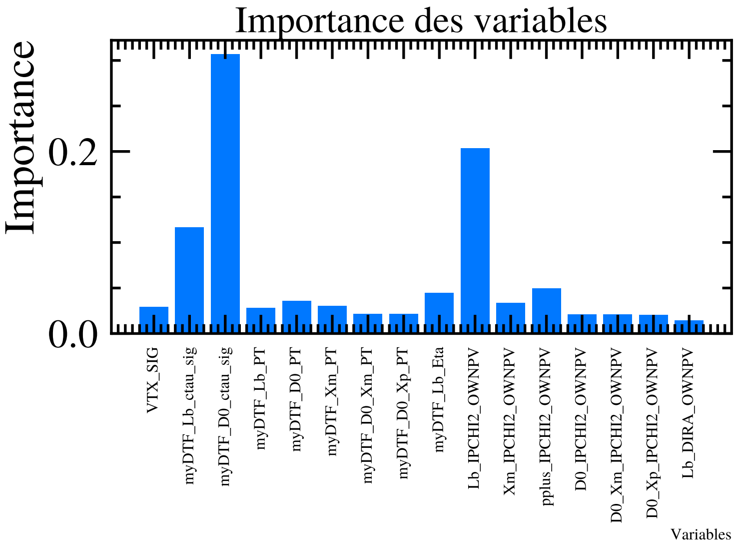

Figure A.2: Variable importance plot for the BDT trained for Run 2 $\Lambda_b^0 \to [\pi^-\pi^+]_{D^0}p\pi^-$. The x-axis lists the variables considered, while the y-axis represents the importance score, indicating how significantly each variable contributes to the BDT's decision-making process.

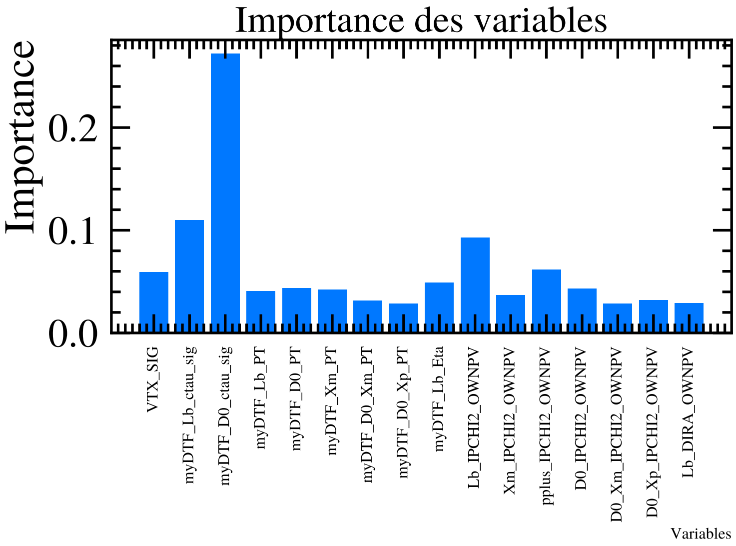

Figure A.3: Variable importance plot for the BDT trained for Run 1 $\Lambda_b^0 \to [K^-\pi^+]_{D^0}p\pi^-$. The x-axis lists the variables considered, while the y-axis represents the importance score, indicating how significantly each variable contributes to the BDT's decision-making process.

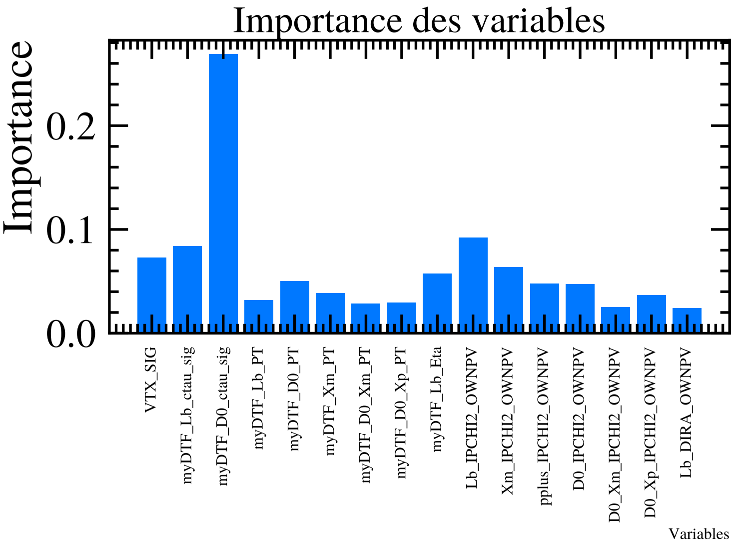

Figure A.4: Variable importance plot for the BDT trained for Run 1 $\Lambda_b^0 \to [K^- K^+]_{D^0} p \pi^-$. The x-axis lists the variables considered, while the y-axis represents the importance score, indicating how significantly each variable contributes to the BDT's decision-making process.

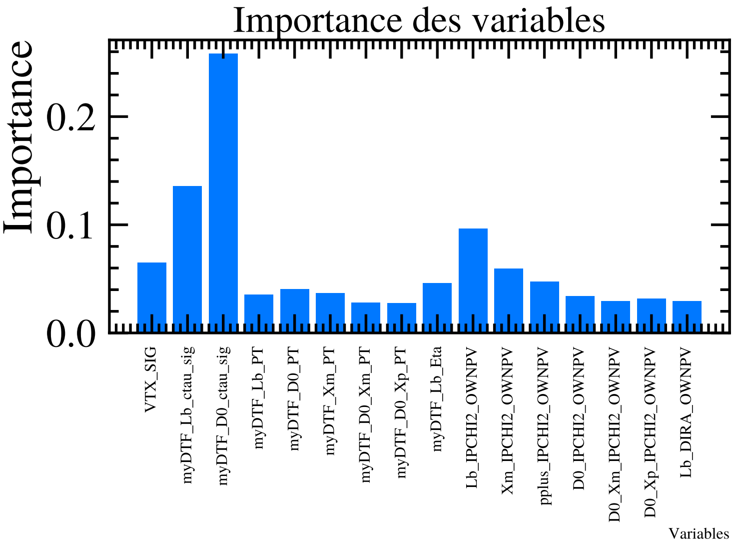

Figure A.5: Variable importance plot for the BDT trained for Run 1 $\Lambda_b^0 \to [\pi^- \pi^+]_{D^0} p \pi^-$. The x-axis lists the variables considered, while the y-axis represents the importance score, indicating how significantly each variable contributes to the BDT's decision-making process.

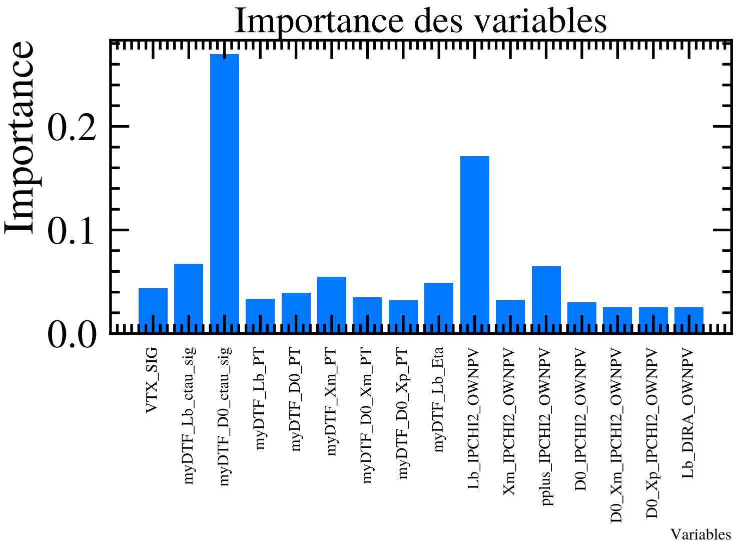

Figure A.6: Variable importance plot for the BDT trained for Run 2 $\Lambda_b^0 \to [K^-\pi^+]_{D^0} pK^-$. The x-axis lists the variables considered, while the y-axis represents the importance score, indicating how significantly each variable contributes to the BDT's decision-making process.

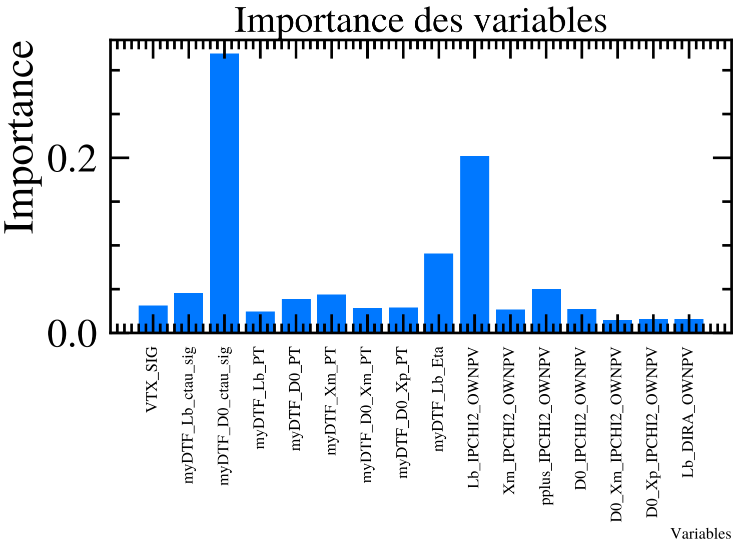

Figure A.7: Variable importance plot for the BDT trained for Run 2 $\Lambda_b^0 \to [K^-K^+]_{D^0} pK^-$. The x-axis lists the variables considered, while the y-axis represents the importance score, indicating how significantly each variable contributes to the BDT's decision-making process.

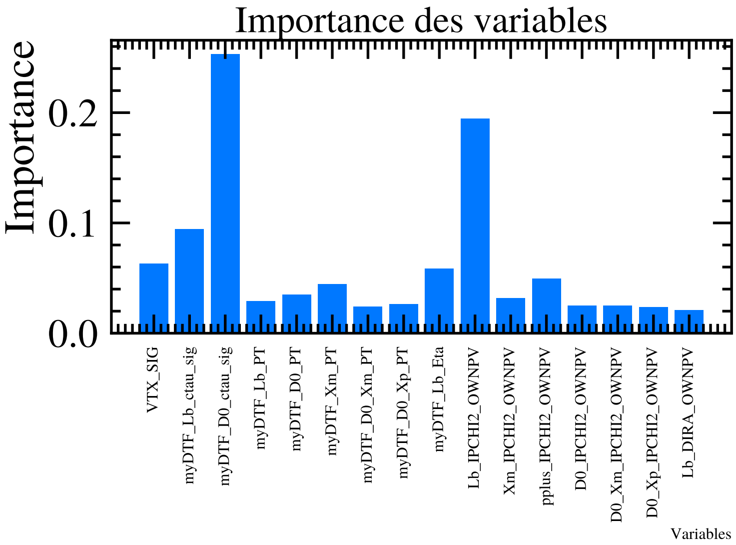

Figure A.8: Variable importance plot for the BDT trained for Run 2 $\Lambda_b^0 \to [\pi^-\pi^+]_{D^0}pK^-$. The x-axis lists the variables considered, while the y-axis represents the importance score, indicating how significantly each variable contributes to the BDT's decision-making process.

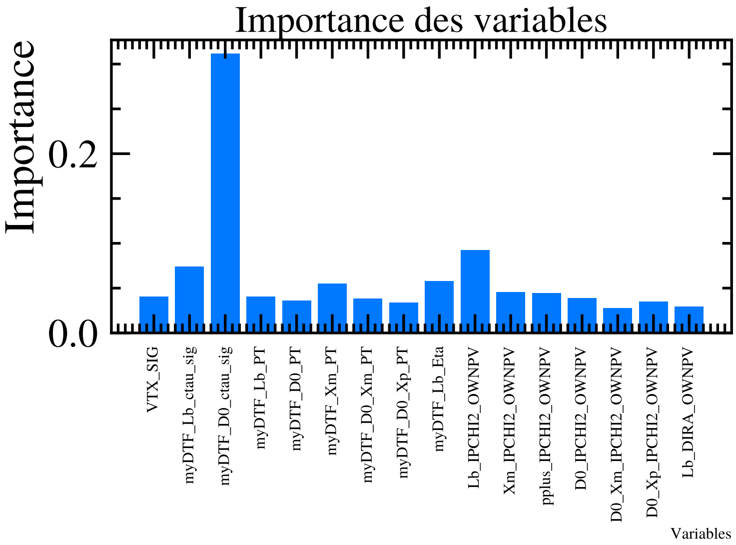

Figure A.9: Variable importance plot for the BDT trained for Run 1 $\Lambda_b^0 \to [K^-\pi^+]_{D^0}pK^-$. The x-axis lists the variables considered, while the y-axis represents the importance score, indicating how significantly each variable contributes to the BDT's decision-making process.

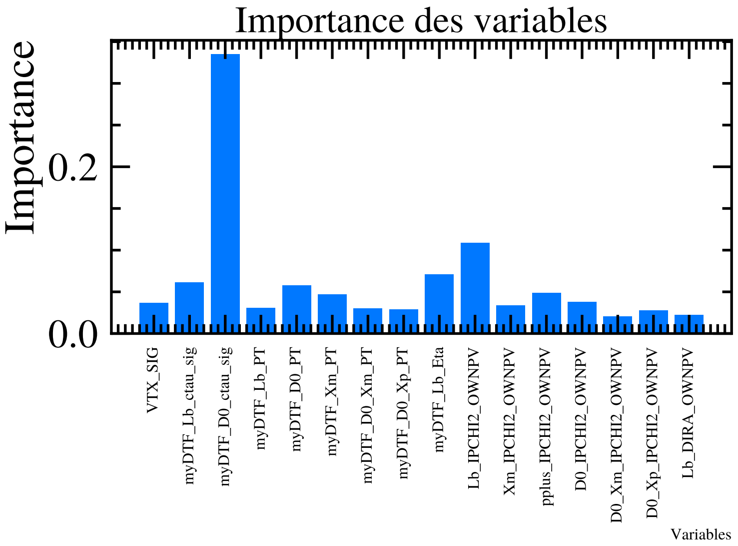

Figure A.10: Variable importance plot for the BDT trained for Run 1 $\Lambda_b^0 \to [K^- K^+]_{D^0} p K^-$. The x-axis lists the variables considered, while the y-axis represents the importance score, indicating how significantly each variable contributes to the BDT's decision-making process.

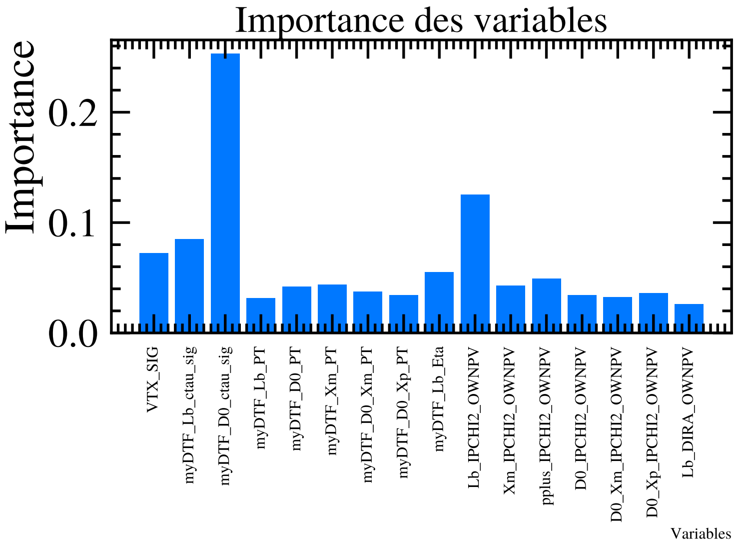

Figure A.11: Variable importance plot for the BDT trained for Run 1 $\Lambda_b^0 \to [\pi^- \pi^+]_{D^0} p K^-$. The x-axis lists the variables considered, while the y-axis represents the importance score, indicating how significantly each variable contributes to the BDT's decision-making process.

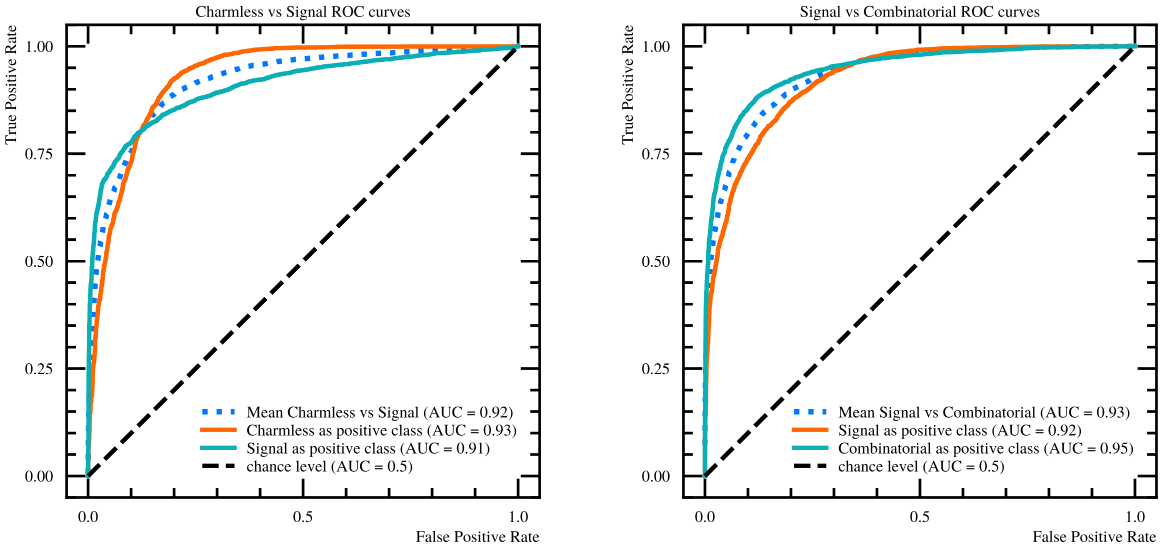

(a) ROC curve for charmless background versus signal.

(b) ROC curve for combinatorial background versus signal.

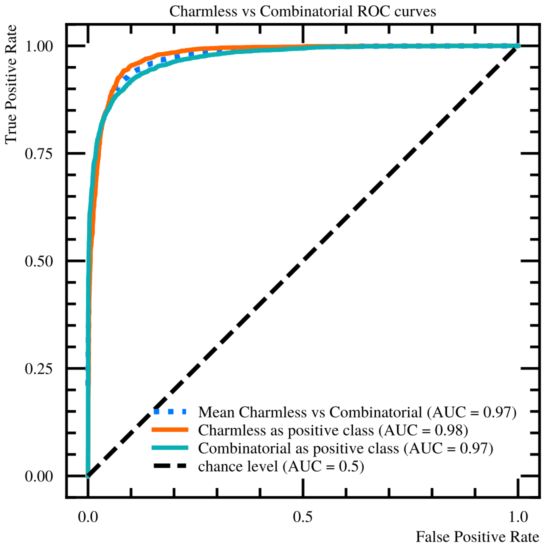

(c) ROC curve for charmless background versus combinatorial background.

Figure A.12: Collection of ROC curves of the multiclass training for Run 2 $\Lambda_b^0 \to [K^- K^+]_{D^0} p\pi^-$.

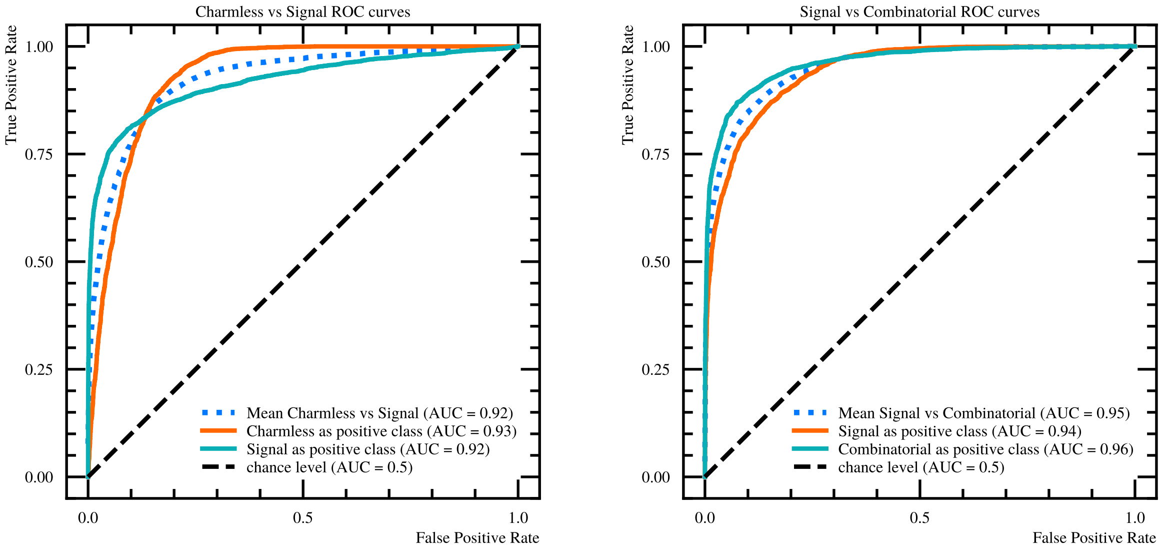

(a) ROC curve for charmless background versus signal.

(b) ROC curve for combinatorial background versus signal.

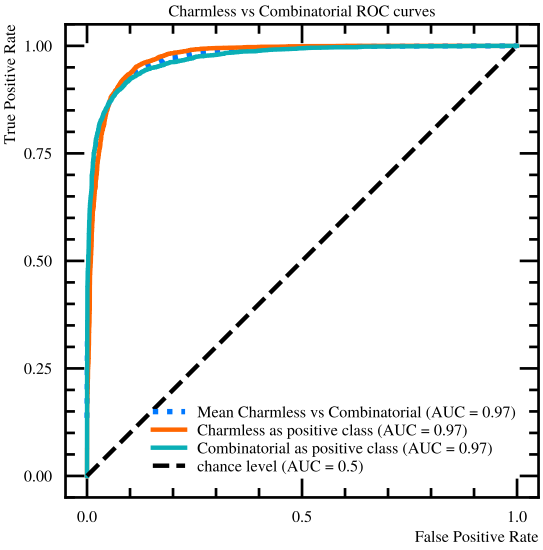

(c) ROC curve for charmless background versus combinatorial background.

Figure A.13: Collection of ROC curves of the multiclass training for Run 2 $\Lambda_b^0 \to [\pi^-\pi^+]_{D^0} p\pi^-$.

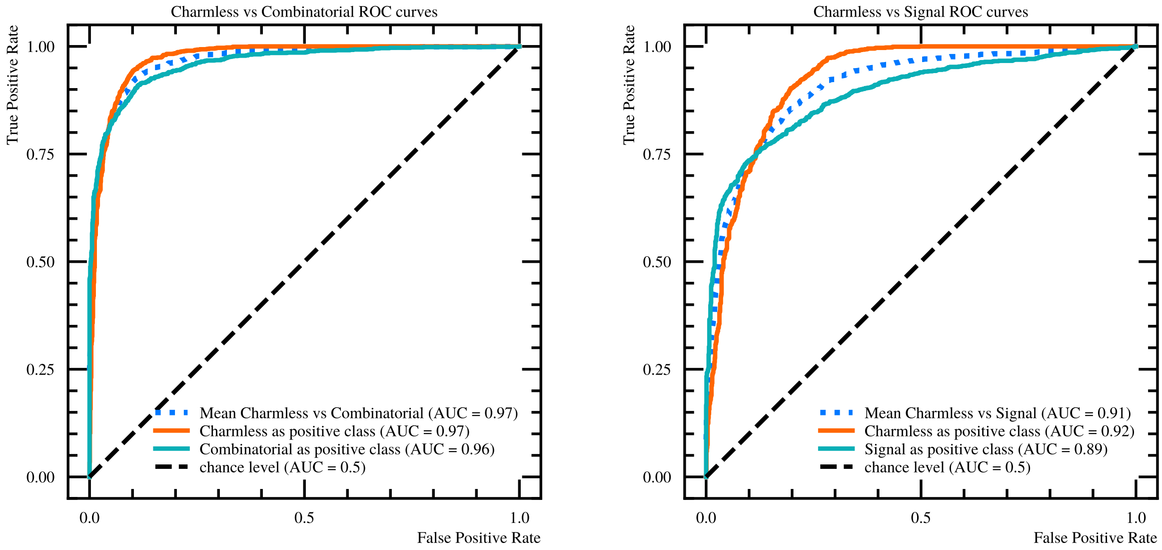

(a) ROC curve for charmless background versus signal.

(b) ROC curve for combinatorial background versus signal.

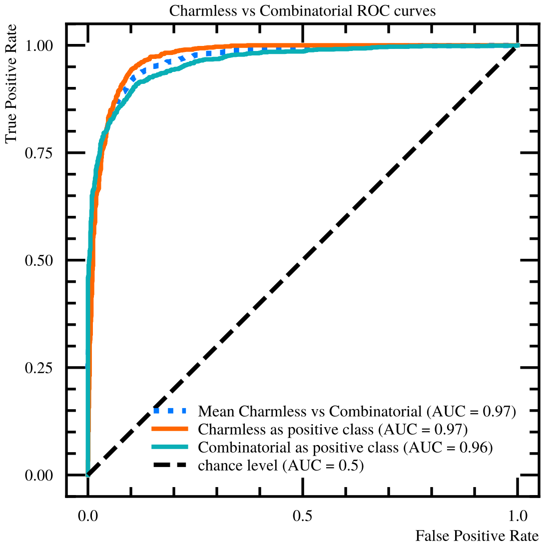

(c) ROC curve for charmless background versus combinatorial background.

Figure A.14: Collection of ROC curves of the multiclass training for Run 1 $\Lambda_b^0 \to [K^-\pi^+]_{D^0} p\pi^-$.

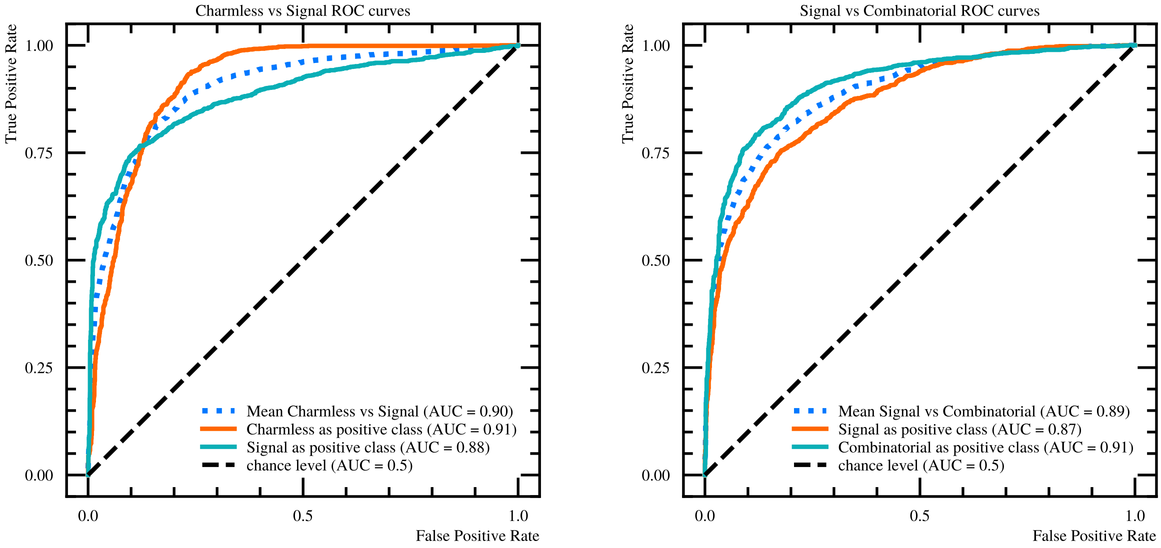

(a) ROC curve for charmless background versus signal.

(b) ROC curve for combinatorial background versus signal.

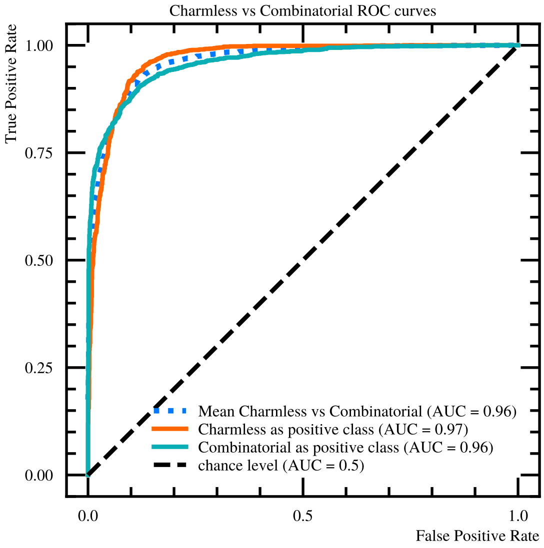

(c) ROC curve for charmless background versus combinatorial background.

Figure A.15: Collection of ROC curves of the multiclass training for Run 1 $\Lambda_b^0 \to [K^- K^+]_{D^0} p \pi^-$.

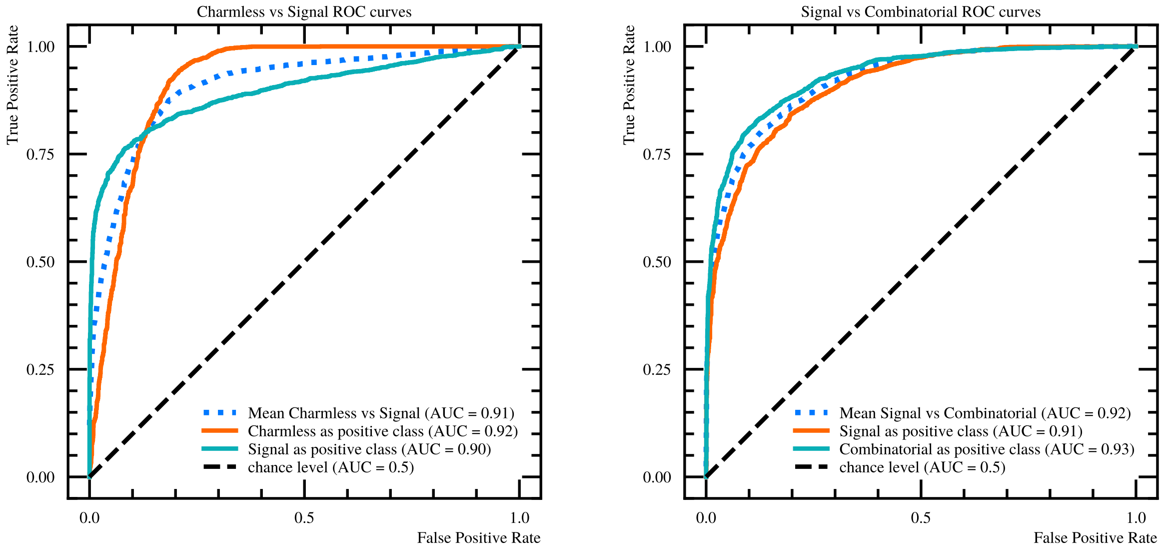

(a) ROC curve for charmless background versus signal.

(b) ROC curve for combinatorial background versus signal.

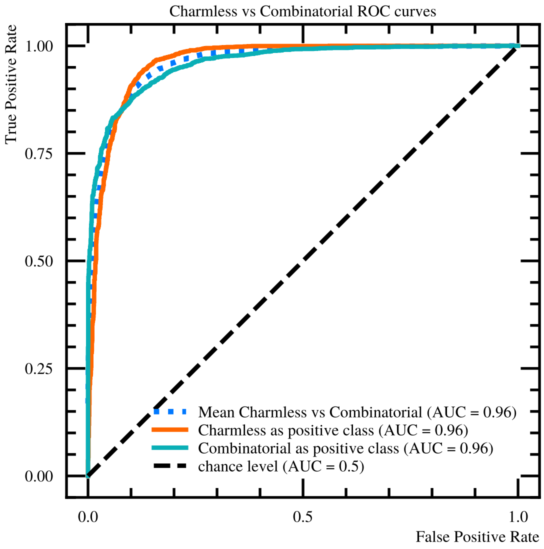

(c) ROC curve for charmless background versus combinatorial background.

Figure A.16: Collection of ROC curves of the multiclass training for Run 1 $\Lambda_b^0 \rightarrow [\pi^-\pi^+]_{D^0} p\pi^-$.

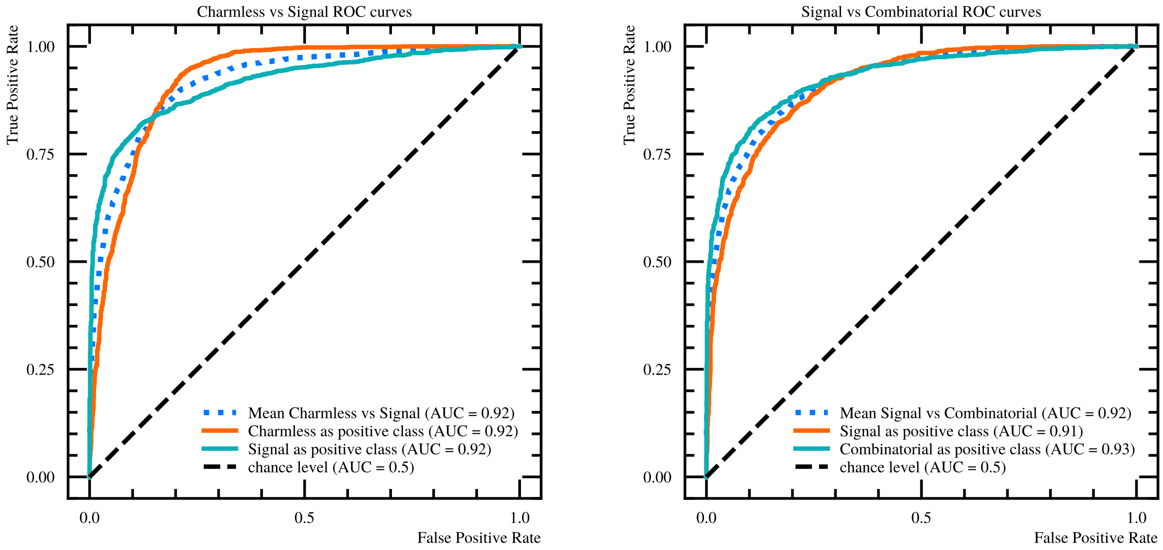

(a) ROC curve for charmless background versus signal.

(b) ROC curve for combinatorial background versus signal.

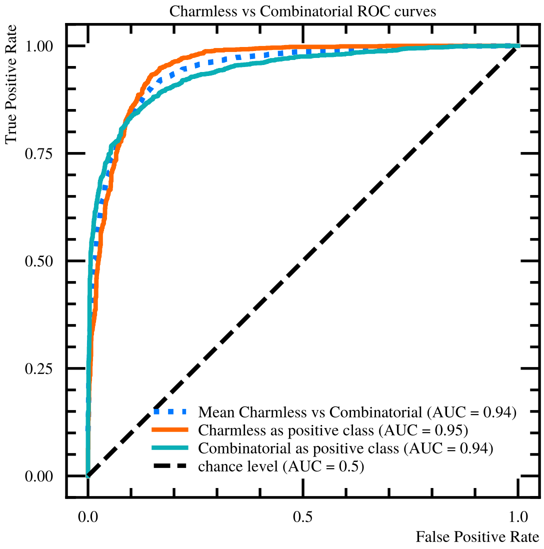

(c) ROC curve for charmless background versus combinatorial background.

Figure A.17: Collection of ROC curves of the multiclass training for Run 2 $\Lambda_b^0 \to [K^-\pi^+]_{D^0} p K^-$.

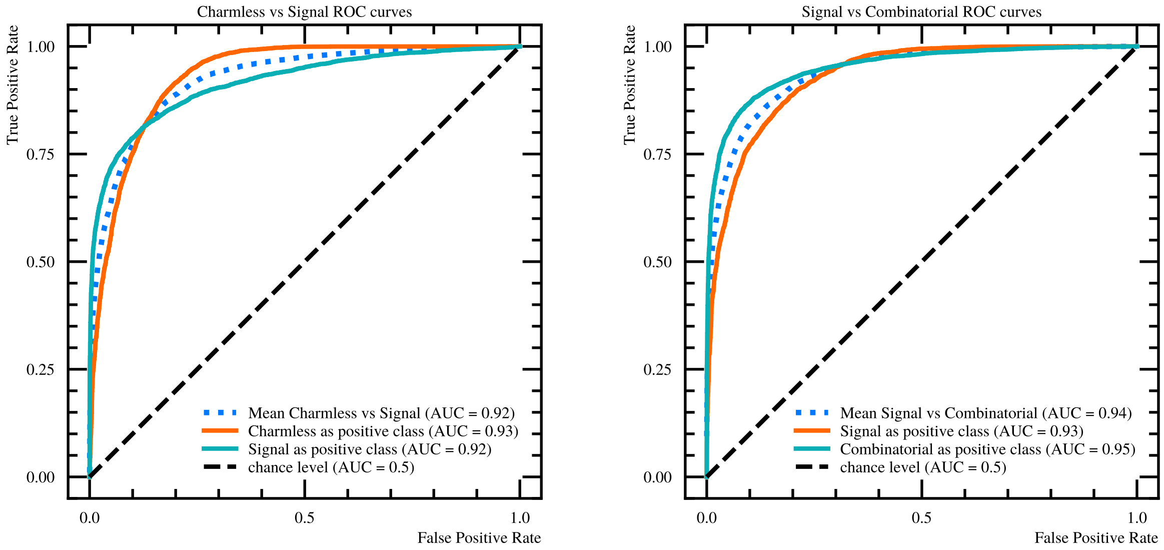

(a) ROC curve for charmless background versus signal.

(b) ROC curve for combinatorial background versus signal.

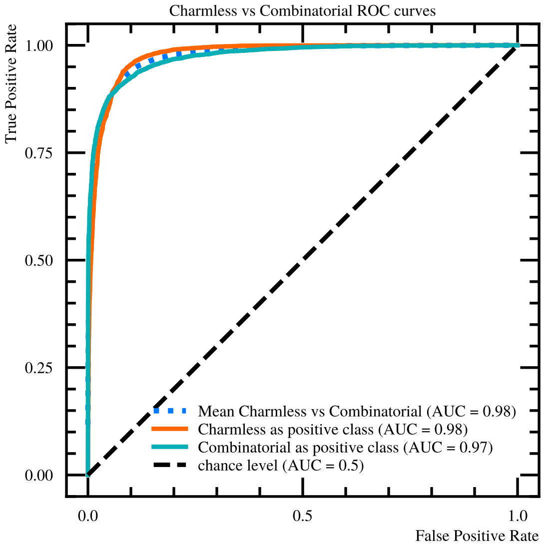

(c) ROC curve for charmless background versus combinatorial background.

Figure A.18: Collection of ROC curves of the multiclass training for Run 2 $\Lambda_b^0 \to [K^-K^+]_{D^0}pK^-$.

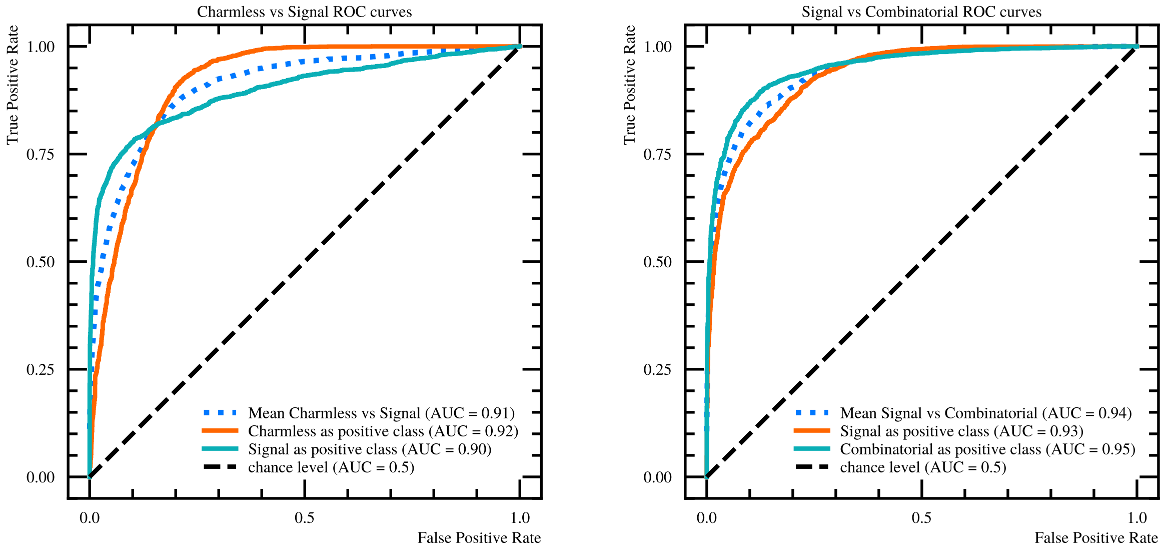

(a) ROC curve for charmless background versus signal.

(b) ROC curve for combinatorial background versus signal.

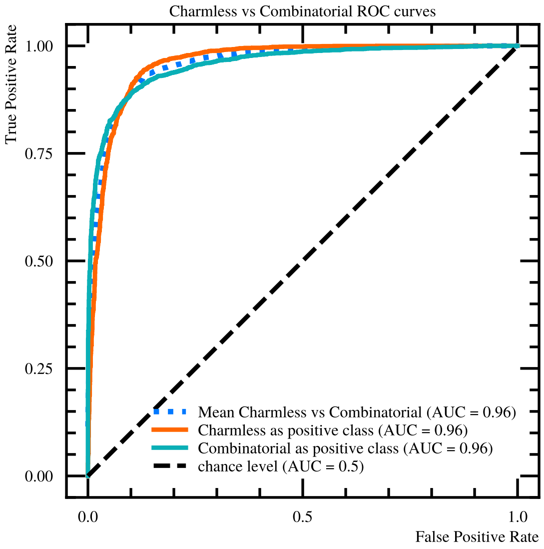

(c) ROC curve for charmless background versus combinatorial background.

Figure A.19: Collection of ROC curves of the multiclass training for Run 2 $\Lambda_b^0 \to [\pi^-\pi^+]_{D^0} p K^-$.

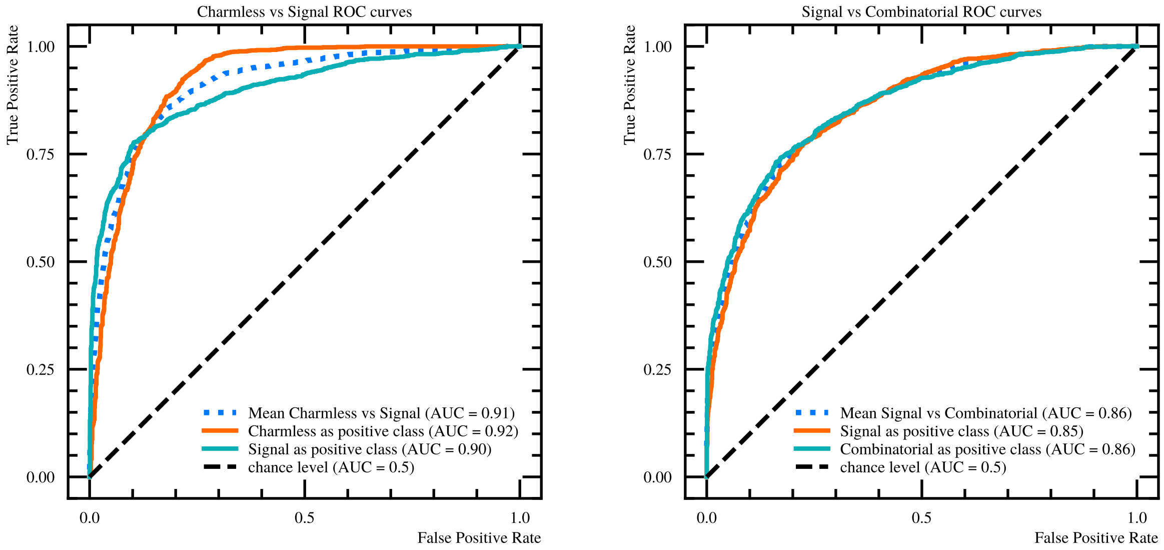

(a) ROC curve for charmless background versus signal.

(b) ROC curve for combinatorial background versus signal.

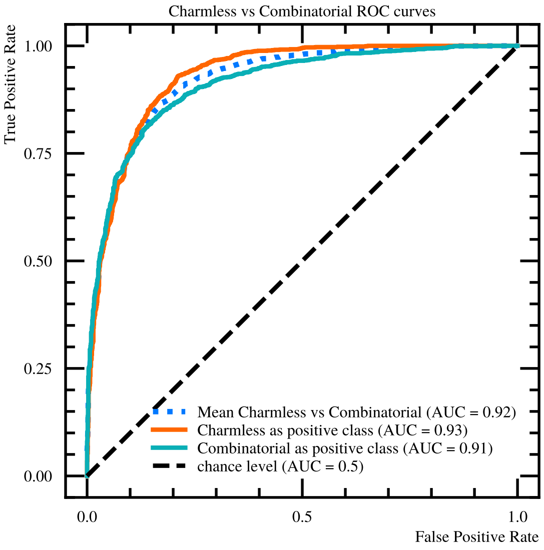

(c) ROC curve for charmless background versus combinatorial background.

Figure A.20: Collection of ROC curves of the multiclass training for Run 1 $\Lambda_b^0 \to [K^-\pi^+]_{D^0}pK^-$.

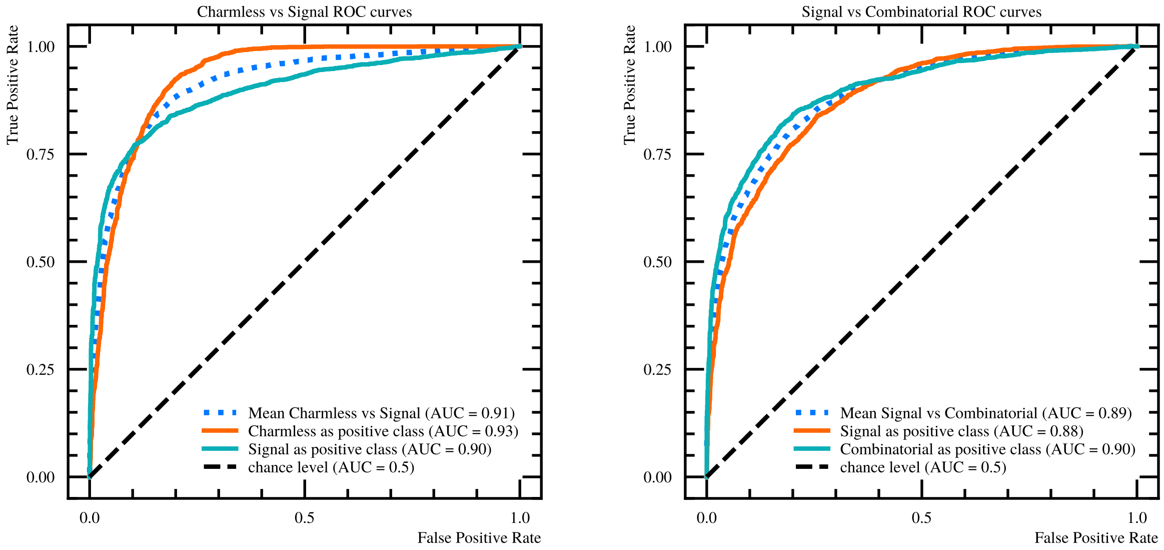

(a) ROC curve for charmless background versus signal.

(b) ROC curve for combinatorial background versus signal.

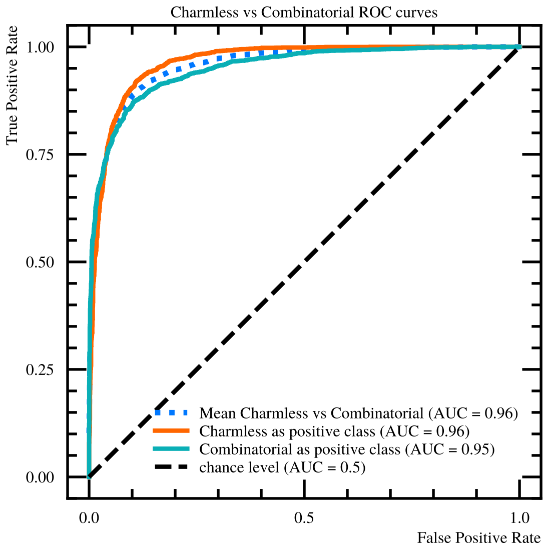

(c) ROC curve for charmless background versus combinatorial background.

Figure A.21: Collection of ROC curves of the multiclass training for Run 1 $\Lambda_b^0 \to [K^-K^+]_{D^0}pK^-$.

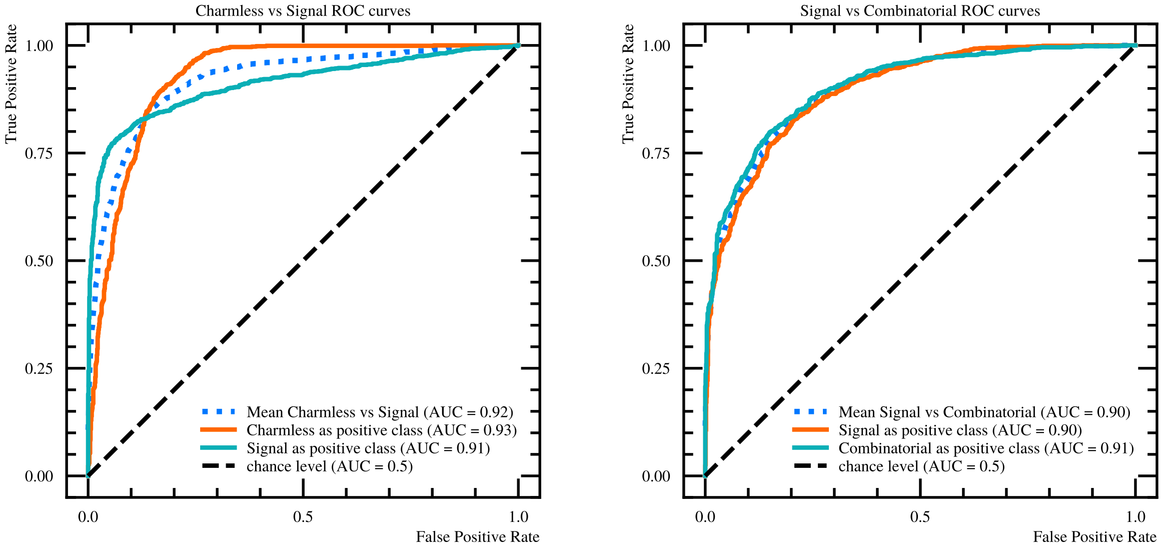

(a) ROC curve for charmless background versus signal.

(b) ROC curve for combinatorial background versus signal.

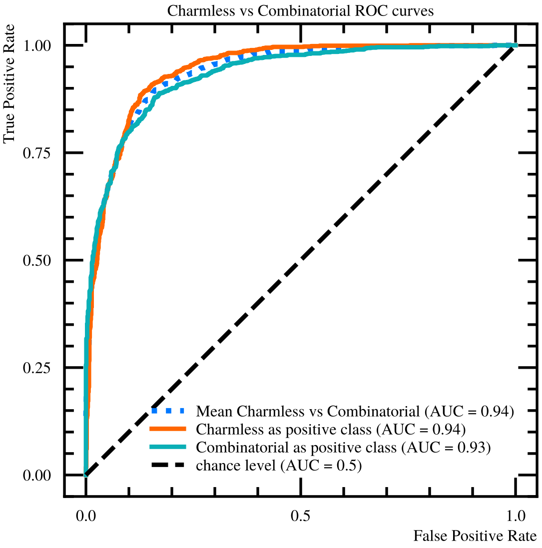

(c) ROC curve for charmless background versus combinatorial background.

Figure A.22: Collection of ROC curves of the multiclass training for Run 1 $\Lambda_b^0 \to [\pi^-\pi^+]_{D^0}pK^-$.

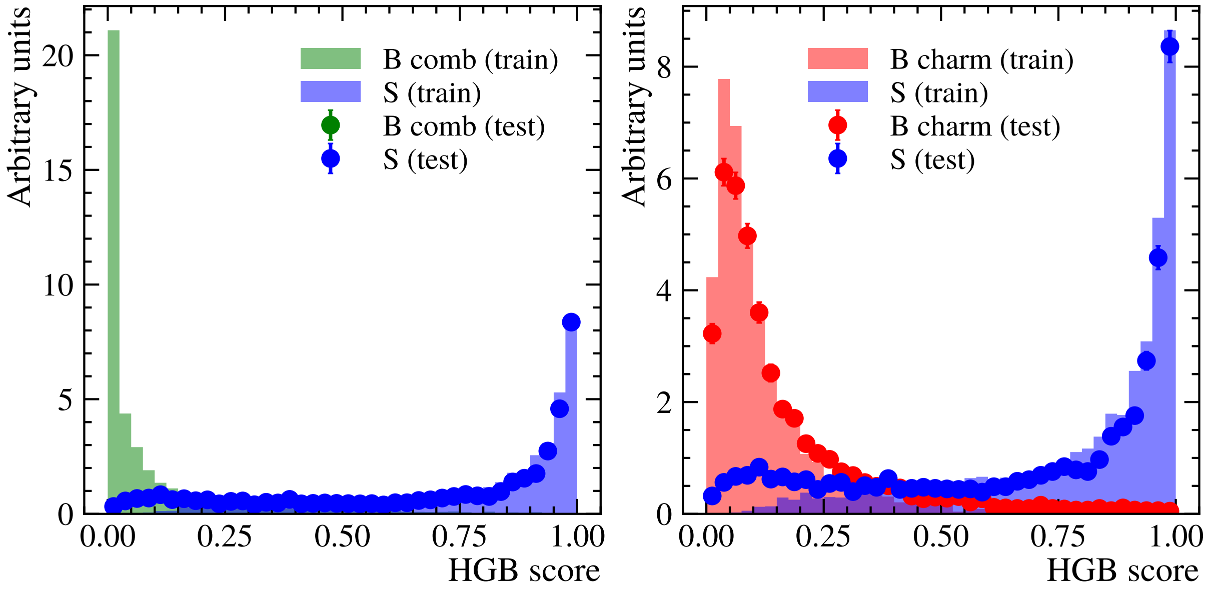

Figure A.23: Comparison of BDT scores for training and testing samples for Run 2 $\Lambda_b^0 \to [K^- K^+]_{D^0} p\pi^-$. The left plot shows the score distribution for the combinatorial background (green) and signal (blue) for both training and testing datasets. The right plot illustrates the score distribution for the charmless background (red) and signal (blue) for both training and testing datasets. The close agreement between the training and testing distributions indicates no significant overtraining, validating the robustness of the BDT model.

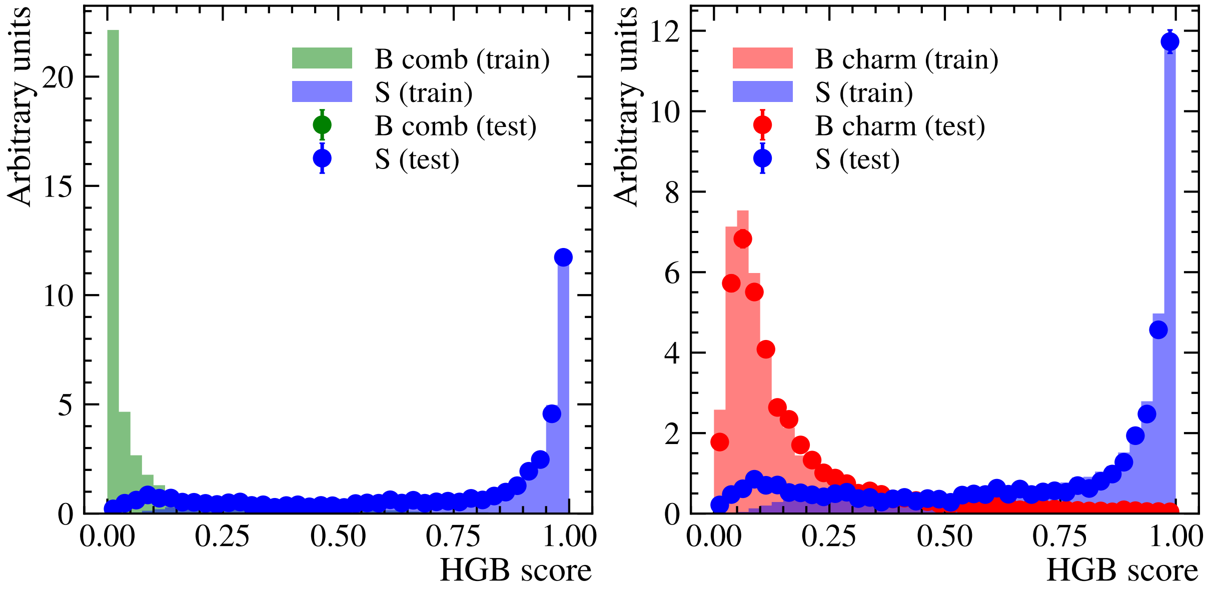

Figure A.24: Comparison of BDT scores for training and testing samples for Run 2 $\Lambda_b^0 \to [\pi^- \pi^+]_{D^0} p\pi^-$. The left plot shows the score distribution for the combinatorial background (green) and signal (blue) for both training and testing datasets. The right plot illustrates the score distribution for the charmless background (red) and signal (blue) for both training and testing datasets. The close agreement between the training and testing distributions indicates no significant overtraining, validating the robustness of the BDT model.

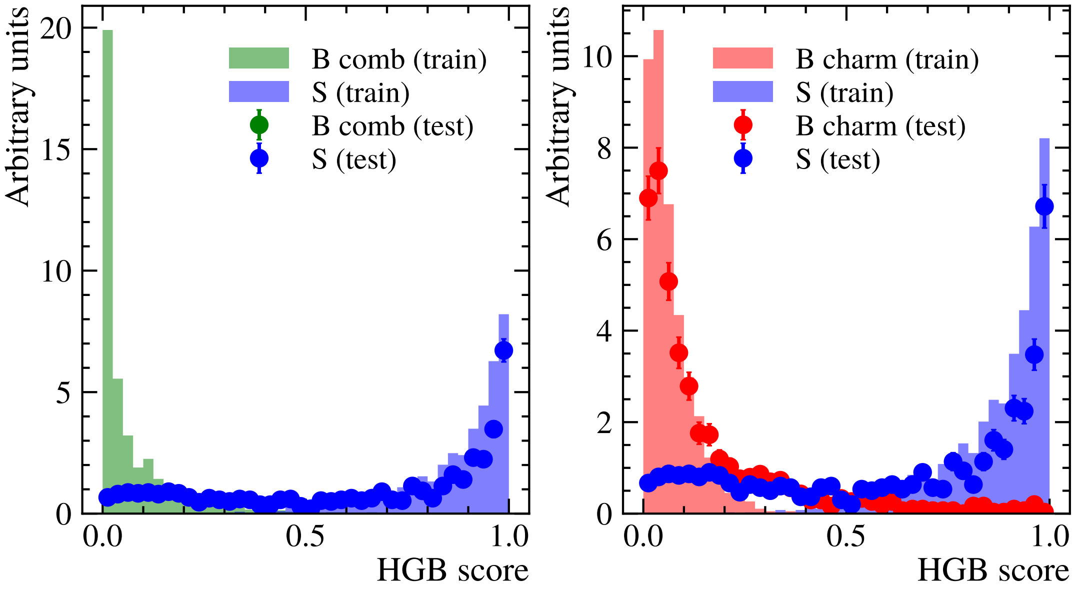

Figure A.25: Comparison of BDT scores for training and testing samples for Run 1 $\Lambda_b^0 \to [K^-\pi^+]_{D^0} p\pi^-$. The left plot shows the score distribution for the combinatorial background (green) and signal (blue) for both training and testing datasets. The right plot illustrates the score distribution for the charmless background (red) and signal (blue) for both training and testing datasets. The close agreement between the training and testing distributions indicates no significant overtraining, validating the robustness of the BDT model.

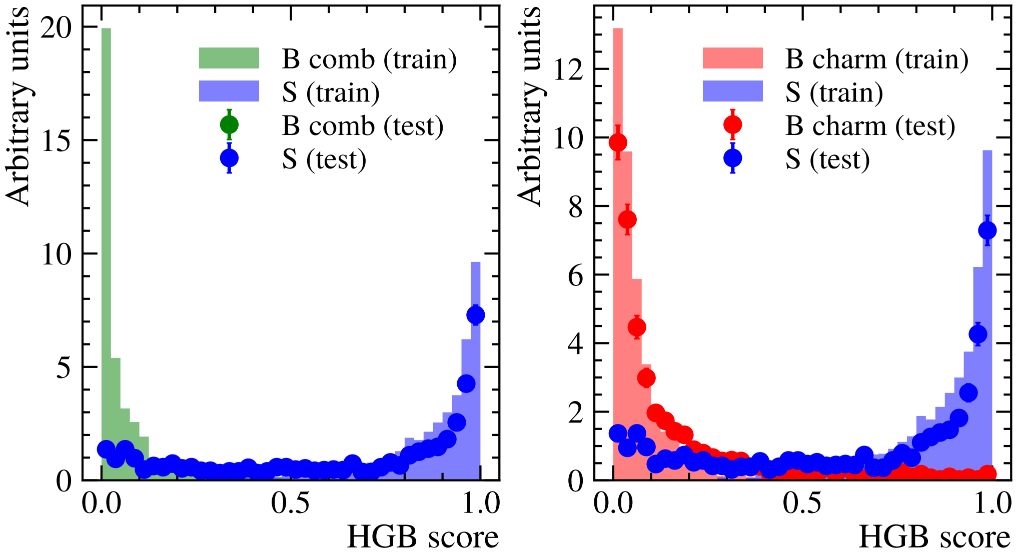

Figure A.26: Comparison of BDT scores for training and testing samples for Run 1 $\Lambda_b^0 \to [K^-K^+]_{D^0} p\pi^-$. The left plot shows the score distribution for the combinatorial background (green) and signal (blue) for both training and testing datasets. The right plot illustrates the score distribution for the charmless background (red) and signal (blue) for both training and testing datasets. The close agreement between the training and testing distributions indicates no significant overtraining, validating the robustness of the BDT model.

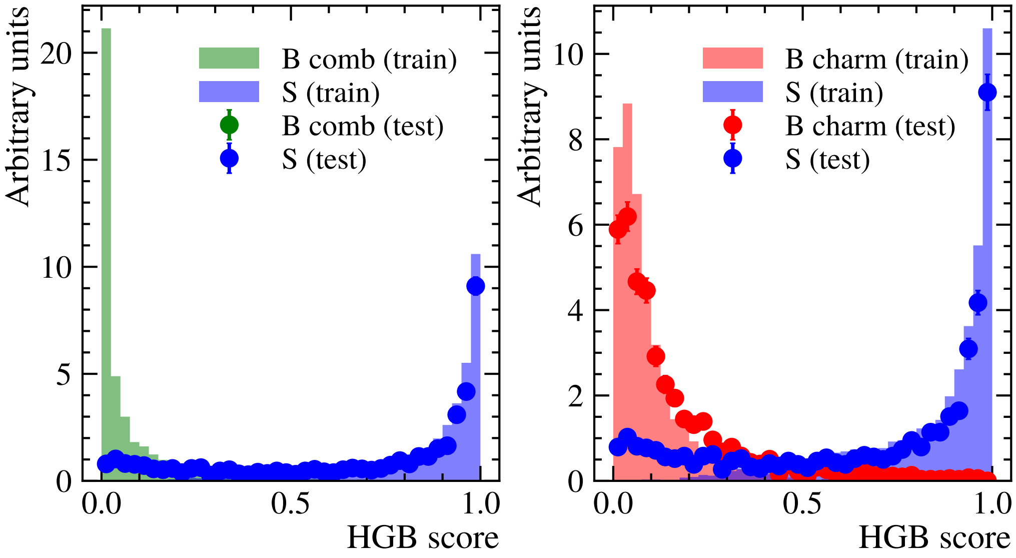

Figure A.27: Comparison of BDT scores for training and testing samples for Run 1 $\Lambda_b^0 \to [\pi^-\pi^+]_{D^0} p\pi^-$. The left plot shows the score distribution for the combinatorial background (green) and signal (blue) for both training and testing datasets. The right plot illustrates the score distribution for the charmless background (red) and signal (blue) for both training and testing datasets. The close agreement between the training and testing distributions indicates no significant overtraining, validating the robustness of the BDT model.

Bibliography

[1] M. Banner, R. Battiston, Ph. Bloch, et al. “Observation of single isolated electrons of high transverse momentum in events with missing transverse energy at the CERN pp collider”. In: *Physics Letters B* 122.5 (1983), pp. 476–485. ISSN: 0370-2693. DOI: `https://doi.org/10.1016/0370-2693(83)91605-2`. URL: `https://www.sciencedirect.com/science/article/pii/0370269383916052`.

[2] G. Arnison, A. Astbury, B. Aubert, et al. “Experimental observation of lepton pairs of invariant mass around 95 GeV/c2 at the CERN SPS collider”. In: *Physics Letters B* 126.5 (1983), pp. 398–410. ISSN: 0370-2693. DOI: `https://doi.org/10.1016/0370-2693(83)90188-0`. URL: `https://www.sciencedirect.com/science/article/pii/0370269383901880`.

[3] Peter W. Higgs. “Broken Symmetries and the Masses of Gauge Bosons”. In: *Phys. Rev. Lett.* 13 (16 Oct. 1964), pp. 508–509. DOI: `10.1103/PhysRevLett.13.508`. URL: `https://link.aps.org/doi/10.1103/PhysRevLett.13.508`.

[4] Nicola Cabibbo. “Unitary Symmetry and Leptonic Decays”. In: *Phys. Rev. Lett.* 10 (1963), pp. 531–533. DOI: `10.1103/PhysRevLett.10.531`.

[5] Makoto Kobayashi and Toshihide Maskawa. “CP-Violation in the Renormalizable Theory of Weak Interaction”. In: *Progress of Theoretical Physics* 49.2 (Feb. 1973), pp. 652–657. ISSN: 0033-068X. DOI: `10.1143/PTP.49.652`. eprint: `https://academic.oup.com/ptp/article-pdf/49/2/652/5257692/49-2-652.pdf`. URL: `https://doi.org/10.1143/PTP.49.652`.

[6] Lincoln Wolfenstein. “Parametrization of the Kobayashi-Maskawa Matrix”. In: *Phys. Rev. Lett.* 51 (21 Nov. 1983), pp. 1945–1947. DOI: `10.1103/PhysRevLett.51.1945`. URL: `https://link.aps.org/doi/10.1103/PhysRevLett.51.1945`.

[7] Bernard Aubert et al. “The BaBar detector”. In: *Nucl. Instrum. Meth. A* 479 (2002), pp. 1–116. DOI: `10.1016/S0168-9002(01)02012-5`. arXiv: `hep-ex/0105044`.

[8] S. Amato et al. “LHCb technical proposal: A Large Hadron Collider Beauty Experiment for Precision Measurements of CP Violation and Rare Decays”. In: (Feb. 1998).

[9] S. L. Olsen. “The BELLE experiment at KEKB”. In: *1994 Meeting of the American Physical Society, Division of Particles and Fields (DPF 94)*. Aug. 1994, pp. 1908–1913.

[10] J Kahn. “The Belle II Experiment”. In: (2017), pp. 45–54. DOI: `10.23727/CERN-Proceedings-2017-001.45`. URL: `https://cds.cern.ch/record/2301997`.

[11] Michael Gronau and Daniel Wyler. “On determining a weak phase from CP asymmetries in charged B decays”. In: *Phys. Lett. B* 265 (1991), pp. 172–176. DOI: `10.1016/0370-2693(91)90034-N`.

[12] David Atwood, Isard Dunietz, and Amarjit Soni. “Enhanced CP Violation with $\mathrm{B} \to \mathrm{KD0}(\mathrm{D}^0)$Modes and Extraction of the Cabibbo-Kobayashi-Maskawa Angle”. In: *Physical Review Letters* 78.17 (Apr. 1997), pp. 3257–3260. ISSN: 1079-7114. DOI: `10.1103/physrevlett.78.3257`. URL: `http://dx.doi.org/10.1103/PhysRevLett.78.3257`.

[13] Anjan Giri, Yuval Grossman, Abner Soffer, et al. “Determining γ using $B^{\pm} \to \mathrm{DK}^{\pm}$ with multibody D decays”. In: *Phys. Rev. D* 68 (5 Sept. 2003), p. 054018. DOI: `10.1103/PhysRevD.68.054018`. URL: `https://link.aps.org/doi/10.1103/PhysRevD.68.054018`.

[14] M Clemencic, G Corti, S Easo, et al. “The LHCb Simulation Application, Gauss: Design, Evolution and Experience”. In: *Journal of Physics: Conference Series* 331.3 (Dec. 2011), p. 032023. DOI: `10.1088/1742-6596/331/3/032023`. URL: `https://dx.doi.org/10.1088/1742-6596/331/3/032023`.

[15] David J. Lange. “The EvtGen particle decay simulation package”. In: *Nuclear Instruments and Methods in Physics Research Section A: Accelerators, Spectrometers, Detectors and Associated Equipment* 462.1 (2001). BEAUTY2000, Proceedings of the 7th Int. Conf. on B-Physics at Hadron Machines, pp. 152–155. ISSN: 0168-9002. DOI: `https://doi.org/10.1016/S0168-9002(01)00089-4`. URL: `https://www.sciencedirect.com/science/article/pii/S0168900201000894`.

[16] S. Agostinelli et al. “Geant4—a simulation toolkit”. In: *Nuclear Instruments and Methods in Physics Research Section A: Accelerators, Spectrometers, Detectors and Associated Equipment* 506.3 (2003), pp. 250–303. ISSN: 0168-9002. DOI: `https://doi.org/10.1016/S0168-9002(03)01368-8`. URL: `https://www.sciencedirect.com/science/article/pii/S0168900203013688`.

[17] Torbjörn Sjöstrand, Stephen Mrenna, and Peter Skands. “A brief introduction to PYTHIA 8.1”. In: *Computer Physics Communications* 178.11 (2008), pp. 852–867. ISSN: 0010-4655. DOI: `https://doi.org/10.1016/j.cpc.2008.01.036`. URL: `https://www.sciencedirect.com/science/article/pii/S0010465508000441`.

[18] M. Pivk and F.R. Le Diberder. “sPlot: A statistical tool to unfold data distributions”. In: *Nuclear Instruments and Methods in Physics Research Section A: Accelerators, Spectrometers, Detectors and Associated Equipment* 555.1-2 (Dec. 2005), pp. 356–369. ISSN: 0168-9002. DOI: `10.1016/j.nima.2005.08.106`. URL: `http://dx.doi.org/10.1016/j.nima.2005.08.106`.

[19] J. Chadwick. “The Existence of a Neutron”. In: *Proceedings of the Royal Society of London. Series A, Containing Papers of a Mathematical and Physical Character* 136.830 (1932), pp. 692–708. ISSN: 09501207. URL: `http://www.jstor.org/stable/95816` (visited on 07/18/2024).

[20] Sheldon L. Glashow. “Partial-symmetries of weak interactions”. In: *Nuclear Physics* 22.4 (1961), pp. 579–588. ISSN: 0029-5582. DOI: `https://doi.org/10.1016/0029-5582(61)90469-2`. URL: `https://www.sciencedirect.com/science/article/pii/0029558261904692`.

[21] A. Salam and J.C. Ward. “Electromagnetic and weak interactions”. In: *Physics Letters* 13.2 (1964), pp. 168–171. ISSN: 0031-9163. DOI: `https://doi.org/10.1016/0031-9163(64)90711-5`. URL: `https://www.sciencedirect.com/science/article/pii/0031916364907115`.

[22] Steven Weinberg. “A Model of Leptons”. In: *Phys. Rev. Lett.* 19 (21 Nov. 1967), pp. 1264–1266. DOI: `10.1103/PhysRevLett.19.1264`. URL: `https://link.aps.org/doi/10.1103/PhysRevLett.19.1264`.

[23] S. Abachi, B. Abbott, M. Abolins, et al. “Observation of the Top Quark”. In: *Physical Review Letters* 74.14 (Apr. 1995), pp. 2632–2637. ISSN: 1079-7114. DOI: `10.1103/physrevlett.74.2632`. URL: `http://dx.doi.org/10.1103/PhysRevLett.74.2632`.

[24] F. Englert and R. Brout. “Broken Symmetry and the Mass of Gauge Vector Mesons”. In: *Phys. Rev. Lett.* 13 (9 Aug. 1964), pp. 321–323. DOI: `10.1103/PhysRevLett.13.321`. URL: `https://link.aps.org/doi/10.1103/PhysRevLett.13.321`.

[25] James D. Bjorken and Sidney D. Drell. *Relativistic Quantum Mechanics*. Chapter 4 discusses Dirac matrices and their properties. New York: McGraw-Hill, 1964. ISBN: 978-0070054936.

[26] Francis Halzen and Alan D. Martin. *Quarks and Leptons: An Introductory Course in Modern Particle Physics*. Chapter 4 introduces the Gell-Mann matrices and their properties. New York: John Wiley & Sons, 1984. ISBN: 978-0471887416.

[27] E. Noether. “Invariant problem”. In: *Gott. Nachr.* (1918), pp. 235–237.

[28] Chien-Shiung Wu, Ernest Ambler, Raymond W Hayward, et al. “Experimental test of parity conservation in beta decay”. In: *Physical Review* 105.4 (1957), p. 1413.

[29] J. H. Christenson, J. W. Cronin, V. L. Fitch, et al. “Evidence for the 2π Decay of the K_2^0 Meson”. In: *Phys. Rev. Lett.* 13 (4 July 1964), pp. 138–140. DOI: `10.1103/PhysRevLett.13.138`. URL: `https://link.aps.org/doi/10.1103/PhysRevLett.13.138`.

[30] S. L. Glashow, J. Iliopoulos, and L. Maiani. “Weak Interactions with Lepton-Hadron Symmetry”. In: *Phys. Rev. D* 2 (7 Oct. 1970), pp. 1285–1292. DOI: `10.1103/PhysRevD.2.1285`. URL: `https://link.aps.org/doi/10.1103/PhysRevD.2.1285`.

[31] Makoto Kobayashi and Toshihide Maskawa. “CP-Violation in the Renormalizable Theory of Weak Interaction”. In: *Progress of Theoretical Physics* 49.2 (Feb. 1973), pp. 652–657. ISSN: 0033-068X. DOI: `10.1143/PTP.49.652`. eprint: `https://academic.oup.com/ptp/article-pdf/49/2/652/5257692/49-2-652.pdf`. URL: `https://doi.org/10.1143/PTP.49.652`.

[32] R. Aaij et al. “Opposite-side flavour tagging of B mesons at the LHCb experiment”. In: *Eur. Phys. J. C* 72 (2012), p. 2022. DOI: `10.1140/epjc/s10052-012-2022-1`. arXiv: `1202.4979 [hep-ex]`.

[33] R. Aaij, C. Abellán Beteta, T. Ackernley, et al. “Measurement of the $$ {\Lambda}_b^0 $$→J/angular distribution and the $$ {\Lambda}_b^0 $$polarisation in pp collisions”. In: *Journal of High Energy Physics* 2020.6 (2020), p. 110. DOI: `10.1007/JHEP06(2020)110`. URL: `https://doi.org/10.1007/JHEP06(2020)110`.

[34] R.L. Workman, V.D. Burkert, V. Crede, et al. *Review of Particle Physics: 2022*. Vol. 2022. Notes. Oxford: Oxford University Press, 2022. DOI: `10.1093/ptep/ptac097`. URL: `https://cds.cern.ch/record/2836514`.

[35] A. D. Martin and T. D. Spearman. *Elementary Particle Theory*. Amsterdam: North-Holland Publishing Co., 1970. ISBN: 978-0-7204-0157-8.

[36] Anjan Giri, Yuval Grossman, Abner Soffer, et al. "Determining γ using $B^{\pm} \to DK^{\pm}$ with multibody D decays". In: *Physical Review D* 68.5 (2003), p. 054018. DOI: `10.1103/PhysRevD.68.054018`. URL: `https://doi.org/10.1103/PhysRevD.68.054018`.

[37] R. Aaij, A. S. W. Abdelmotteleb, C. Abellan Beteta, et al. "Measurement of the CKM angle with B± → D[K±±]h± decays using a binned phase-space approach". In: *Journal of High Energy Physics* 2023.7 (July 2023). ISSN: 1029-8479. DOI: `10.1007/jhep07(2023)138`. URL: `http://dx.doi.org/10.1007/JHEP07(2023)138`.

[38] R. Aaij, A. S. W. Abdelmotteleb, C. Abellán Beteta, et al. "Constraints on the CKM angle from B± → Dh± decays using D → h±h0 final states". In: *Journal of High Energy Physics* 2022.7 (July 2022). ISSN: 1029-8479. DOI: `10.1007/jhep07(2022)099`. URL: `http://dx.doi.org/10.1007/JHEP07(2022)099`.

[39] LHCb collaboration. "Updated LHCb combination of the CKM angle γ". In: *Review of Scientific Instruments* 72.12 (Dec. 2020), pp. 4477–4479. URL: `http://cds.cern.ch/record/2743058/files/LHCb-CONF-2020-003.pdf`.

[40] *Simultaneous determination of the CKM angle γ and parameters related to mixing and CP violation in the charm sector*. Tech. rep. Geneva: CERN, 2022. URL: `https://cds.cern.ch/record/2838029`.

[41] CKMFitter group. "The Global CKM Fit". In: *Review of Scientific Instruments* 69.3 (Mar. 2019), pp. 1236–1239. URL: `http://ckmfitter.in2p3.fr/www/results/plots_summer19/num/ckmEval_results_summer19.html`.

[42] UTFit group. "Using Diode Lasers for Atomic Physics". In: *Review of Scientific Instruments* 62.1 (Jan. 2018), pp. 1–20. URL: `http://www.utfit.org/UTfit/ResultsSummer2018SM`.

[43] Lyndon Evans and Philip Bryant. "LHC Machine". In: *JINST* 2.3:S08001 (2008), 405:279–390.

[44] "LEP Design Report Vol.1: The LEP Injector Chain". In: (June 1983).

[45] et al. Barbosa-Marinho. *LHCb VELO (VErtex LOcator): Technical Design Report*. Technical design report. LHCb. Geneva: CERN, 2001. URL: `https://cds.cern.ch/record/504321`.

[46] P R Barbosa-Marinho, I Bediaga, F Barbosa-Ademarlaudo, et al. *LHCb inner tracker: Technical Design Report*. Technical design report. LHCb. revised version number 1 submitted on 2002-11-13 14:14:34. Geneva: CERN, 2002. URL: `https://cds.cern.ch/record/582793`.

[47] P R Barbosa-Marinho, I Bediaga, F Barbosa-Ademarlaudo, et al. *LHCb outer tracker: Technical Design Report*. Technical design report. LHCb. Geneva: CERN, 2001. URL: `https://cds.cern.ch/record/519146`.

[48] S et al. Amato. *LHCb RICH: Technical Design Report*. Technical design report. LHCb. Geneva: CERN, 2000. URL: `https://cds.cern.ch/record/494263`.

[49] S Amato, D Carvalho, P Colrain, et al. *LHCb calorimeters: Technical Design Report*. Technical design report. LHCb. Geneva: CERN, 2000. URL: `https://cds.cern.ch/record/494264`.

[50] P R et al. Barbosa-Marinho. *LHCb muon system: Technical Design Report*. Technical design report. LHCb. Geneva: CERN, 2001. URL: `http://cds.cern.ch/record/504326`.

[51] *Trigger Schemes*. URL: `http://lhcb.web.cern.ch/lhcb/speakersbureau/html/TriggerScheme.html`.

[52] LHCb collaboration, R. Aaij, A. S. W. Abdelmotteleb, et al. *The LHCb upgrade I*. 2023. arXiv: `2305.10515 [hep-ex]`. URL: `https://arxiv.org/abs/2305.10515`.

[53] LHCb Collaboration. *LHCb VELO Upgrade Technical Design Report*. Tech. rep. 2013. URL: `https://cds.cern.ch/record/1624070`.

[54] LHCb Collaboration. *LHCb Tracker Upgrade Technical Design Report*. Tech. rep. 2014. URL: `https://cds.cern.ch/record/1647400`.

[55] LHCb Collaboration. *LHCb PID Upgrade Technical Design Report*. Tech. rep. 2013. URL: `https://cds.cern.ch/record/1624074`.

[56] *Framework TDR for the LHCb Upgrade II: Opportunities in flavour physics, and beyond, in the HL-LHC era*. Tech. rep. Geneva: CERN, 2021. URL: `https://cds.cern.ch/record/2776420`.

[57] G. Lindström. "Radiation damage in silicon detectors". In: *Nuclear Instruments and Methods in Physics Research Section A: Accelerators, Spectrometers, Detectors and Associated Equipment* 512.1-2 (2003), pp. 30–43. DOI: `10.1016/S0168-9002(03)01842-9`.

[58] H. Spieler. *Semiconductor Detector Systems*. Oxford University Press, 2005. ISBN: 978-0198527848.

[59] F. Anghinolfi et al. "Nuclear electronics for the LHC experiments". In: *Nuclear Instruments and Methods in Physics Research Section A: Accelerators, Spectrometers, Detectors and Associated Equipment* 518.1-2 (2004), pp. 32–35. DOI: `10.1016/j.nima.2003.11.291`.

[60] G. Aad et al. "The ATLAS Experiment at the CERN Large Hadron Collider". In: *Journal of Instrumentation* 3.08 (2008), S08003. DOI: `10.1088/1748-0221/3/08/S08003`.

[61] M Adinolfi, F Archilli, W Baldini, et al. "LHCb data quality monitoring". In: *J. Phys.: Conf. Ser.* 898.9 (2017), p. 092027. DOI: `10.1088/1742-6596/898/9/092027`. URL: `https://cds.cern.ch/record/2298467`.

[62] Wouter D. Hulsbergen. "Decay chain fitting with a Kalman filter". In: *Nuclear Instruments and Methods in Physics Research Section A: Accelerators, Spectrometers, Detectors and Associated Equipment* 552.3 (Nov. 2005), pp. 566–575. ISSN: 0168-9002. DOI: `10.1016/j.nima.2005.06.078`. URL: `http://dx.doi.org/10.1016/j.nima.2005.06.078`.

[63] W.D. Hulsbergen. “The global covariance matrix of tracks fitted with a Kalman filter and an application in detector alignment”. In: *Nuclear Instruments and Methods in Physics Research Section A: Accelerators, Spectrometers, Detectors and Associated Equipment* 600.2 (Mar. 2009), pp. 471–477. ISSN: 0168-9002. DOI: `10.1016/j.nima.2008.11.094`. URL: `http://dx.doi.org/10.1016/j.nima.2008.11.094`.

[64] R. Brun and F. Rademakers. “ROOT: An object oriented data analysis framework”. In: *Nucl. Instrum. Meth. A* 389 (1997). Ed. by M. Werlen and D. Perret-Gallix, pp. 81–86. DOI: `10.1016/S0168-9002(97)00048-X`.

[65] LHCb Collaboration. *The STRIPPING project*. 2024. URL: `https://lhcbdoc.web.cern.ch/lhcbdoc/stripping/`.

[66] Alex Rogozhnikov. “Reweighting with Boosted Decision Trees”. In: *Journal of Physics: Conference Series* 762 (Oct. 2016), p. 012036. ISSN: 1742-6596. DOI: `10.1088/1742-6596/762/1/012036`. URL: `http://dx.doi.org/10.1088/1742-6596/762/1/012036`.

[67] Olli Lupton, Lucio Anderlini, Barbara Sciascia, et al. *Calibration samples for particle identification at LHCb in Run 2*. Tech. rep. Geneva: CERN, 2016. URL: `https://cds.cern.ch/record/2134057`.

[68] Roel Aaij, Lucio Anderlini, Sean Benson, et al. “Selection and processing of calibration samples to measure the particle identification performance of the LHCb experiment in Run 2”. In: *EPJ Techniques and Instrumentation* 6.1 (Feb. 2019). ISSN: 2195-7045. DOI: `10.1140/epjti/s40485-019-0050-z`. URL: `http://dx.doi.org/10.1140/epjti/s40485-019-0050-z`.

[69] Anton Poluektov. *Correction of simulated particle identification response in LHCb using kernel density estimation*. Tech. rep. Geneva: CERN, 2017. URL: `https://cds.cern.ch/record/2260281`.

[70] Tianqi Chen and Carlos Guestrin. “XGBoost: A Scalable Tree Boosting System”. In: *Proceedings of the 22nd ACM SIGKDD International Conference on Knowledge Discovery and Data Mining*. KDD ’16. ACM, Aug. 2016. DOI: `10.1145/2939672.2939785`. URL: `http://dx.doi.org/10.1145/2939672.2939785`.

[71] *The PIDCalib2 project*. `https://pypi.org/project/pidcalib2/`.

[72] Roel et al. Aaij. “Observation of the decay $B_s^0 \to \overline{D}^0 K^+ K^-$”. In: *Phys. Rev. D* 98.7 (2018), p. 072006. DOI: `10.1103/PhysRevD.98.072006`. arXiv: `1807.01891`. URL: `https://cds.cern.ch/record/2629428`.

[73] R. et al. Aaij. “Dalitz plot analysis of $B^0 \to \overline{D}^0 \pi^+ \pi^-$ decays”. In: *Phys. Rev. D* 92 (3 Aug. 2015), p. 032002. DOI: `10.1103/PhysRevD.92.032002`. URL: `https://link.aps.org/doi/10.1103/PhysRevD.92.032002`.

[74] Wouter Verkerke and David Kirkby. *The RooFit toolkit for data modeling*. 2003. arXiv: `physics/0306116 [physics.data-an]`. URL: `https://arxiv.org/abs/physics/0306116`.

[75] N. L. Johnson. “Systems of Frequency Curves Generated by Methods of Translation”. In: *Biometrika* 36.1/2 (1949), pp. 149–176. ISSN: 00063444, 14643510. URL: `http://www.jstor.org/stable/2332539` (visited on 07/17/2024).

[76] M. Oreglia. “A Study of the Reactions $\psi' \to \gamma\gamma\psi$”. Other thesis. Dec. 1980.

[77] LHCb collaboration and R. Aaij et al. *Observation of the suppressed $\Lambda_b^0 \to DpK^-$ decay with $D \to K^+\pi^-$ and measurement of its CP asymmetry*. 2022. DOI: `https://doi.org/10.1103/PhysRevD.104.112008`. arXiv: `2109.02621 [hep-ex]`. URL: `https://arxiv.org/abs/2109.02621`.

[78] Alexandra Martin Sanchez, Patrick Robbe, and Marie-Hélène Schune. *Performances of the LHCb L0 Calorimeter Trigger*. Tech. rep. Geneva: CERN, 2012. URL: `https://cds.cern.ch/record/1407893`.

[79] Laurent Dufour, Fabio Ferrari, Sascha Stahl, et al. *Measurement of integrated CP asymmetries in $\Lambda_b^0 \to ph^-$ decays with the full Run 1+2 dataset*. Tech. rep. Geneva: CERN, 2023.

[80] R. et al. Aaij. “Observation of a $\Lambda_b^0 - \overline{\Lambda}_b^0$ production asymmetry in proton-proton collisions at $\sqrt{s} = 7$ and 8 TeV”. In: *Journal of High Energy Physics* 2021.10 (Oct. 2021). ISSN: 1029-8479. DOI: `10.1007/jhep10(2021)060`. URL: `http://dx.doi.org/10.1007/JHEP10(2021)060`.

[81] Adam Davis, Laurent Dufour, Fabio Ferrari, et al. *Measurement of the $K^-\pi^+$ two-track detection asymmetry in Run 2 using the Turbo stream*. Tech. rep. Geneva: CERN, 2017. URL: `https://cds.cern.ch/record/2284097`.

[82] R. et al. Aaij. “Measurement of the CP Asymmetry in $B_s^0 - \overline{B}_s^0$ Mixing”. In: *Phys. Rev. Lett.* 117 (6 Aug. 2016), p. 061803. DOI: `10.1103/PhysRevLett.117.061803`. URL: `https://link.aps.org/doi/10.1103/PhysRevLett.117.061803`.

[83] R. et al. Aaij. “Observation of the Mass Difference between Neutral Charm-Meson Eigenstates”. In: *Phys. Rev. Lett.* 127 (11 Sept. 2021), p. 111801. DOI: `10.1103/PhysRevLett.127.111801`. URL: `https://link.aps.org/doi/10.1103/PhysRevLett.127.111801`.

[84] P. et al. Abbon. “The COMPASS experiment at CERN”. In: *Nuclear Instruments and Methods in Physics Research Section A: Accelerators, Spectrometers, Detectors and Associated Equipment* 577.3 (July 2007), pp. 455–518. ISSN: 0168-9002. DOI: `10.1016/j.nima.2007.03.026`. URL: `http://dx.doi.org/10.1016/j.nima.2007.03.026`.

[85] R. Aaij, B. Adeva, M. Adinolfi, et al. “Measurement of matter–antimatter differences in beauty baryon decays”. In: *Nature Physics* 13.4 (2017), pp. 391–396. DOI: `10.1038/nphys4021`. URL: `https://doi.org/10.1038/nphys4021`.

[86] R. et al. Aaij. “Search for CP violation using triple product asymmetries in $\Lambda_b^0 \to pK^-\pi^+\pi^-$, $\Lambda_b^0 \to pK^-K^+K^-$ and $\Lambda_b^0 \to pK^-K^+\pi^-$”. In: *Journal of High Energy Physics* 2018.8 (2018), p. 39. DOI: `10.1007/JHEP08(2018)039`. URL: `https://doi.org/10.1007/JHEP08(2018)039`.

[87] R. Aaij, C. Abellán Beteta, B. Adeva, et al. “Observations of $\Lambda_b^0 \to \Lambda K^+\pi^-$ and $\Lambda_b^0 \to \Lambda K^+K^-$ decays and searches for other Λ_b^0 and Ξ_b^0 decays to $\Lambda h^+h'^-$final states”. In: *Journal of High Energy Physics* 2016.5 (2016), p. 81. DOI: `10.1007/JHEP05(2016)081`. URL: `https://doi.org/10.1007/JHEP05(2016)081`.